Wet-chemistry synthesis and characterization of layered nanomaterials with tailored morphology

A report submitted to the University of Dublin, Trinity College

for the degree of

Doctor of Philosophy in Chemistry

by

Sonia Mętel

Supervisor: Prof. Valeria Nicolosi

Assistant Supervisor: Dr. Andrés Seral-Ascaso

I declare that this thesis has not been submitted as an exercise for a degree at this or any other university and it is entirely my own work.

I agree to deposit this thesis in the University's open access institutional repository or allow the Library to do so on my behalf, subject to Irish Copyright Legislation and Trinity College Library conditions of use and acknowledgement.

……

Sonia Metel (M.Sc)

Summary

This PhD Thesis addresses a comprehensive study on the application of wet-chemistry methods to the preparation of layered nanostructured materials; namely 2-dimensional Mg-Al and Ni-Fe layered double hydroxides and 1-dimensional layered amine-templated gallium chalcogenides. The size and the shape of the obtained materials were tailored by suitably choosing the reaction conditions and were subsequently tested in selected applications.

The wet-chemistry techniques used in this Thesis relied on the versatility of commonly used approaches, such as hydrothermal and colloidal processes, with simple modifications of the reaction and post-treatment conditions, which led to the formation of nanoparticles with defined morphology and composition.

Mg-Al layered double hydroxides were produced in the form of platelets with two different size ranges: 20-250 nm and 2-3 μm. The flakes with diameter below 50 nm were tested as plasmid-DNA delivery agents, while the bigger flakes (2-3 μm), in their exfoliated form, are proposed as catalysts. Also, ion-exchange was carried out to minimize the interlayer interactions and facilitate their further exfoliation.

On the other hand, Ni-Fe layered double hydroxides in the form of flower-like particles and platelet-like hexagons with high crystallinity were synthesized by the use of different capping agents. Both nanomaterials were tested as electrocatalysts in water splitting reaction showing promising results.

Finally, amine-templated gallium chalcogenide (sulfur and selenium) nanotubes were prepared by a heating-up method. Both nanomaterials presented a hollow tubular structure with lengths up to 500 nm and 2 μm for sulfur and selenium derivative, respectively. The long-chain amines acted as a template to produce a structure composed of alternating layers of amines and polymeric gallium chalcogenide. Preliminary tests of these compounds as active materials for lithium ion battery anodes showed their potential in energy storage.

In summary, the versatility of wet-chemistry methods was explored to synthesize several layered nanomaterials with controlled morphology. The obtained nanostructures showed promising behaviour in biological application (Mg-Al layered double hydroxide), water splitting (Ni-Fe layered double hydroxide) and energy storage (A_tGaS/Se nanotubes).

Table of Contents

Acknowledgments ..... **i**
List of figures ..... **ii**
List of tables ..... **viii**
Abbreviations ..... **ix**
List of publications ..... **xi**
List of Communications ..... **xii**
Awards: ..... **xiii**
1 Introduction and objectives **1**
Objectives **4**
1.1 Layered double hydroxides 5
1.1.1 Synthesis and exfoliation of LDH 8
1.1.2 Applications of LDH 10
1.2 Semiconducting gallium chalcogenides 14
1.2.1 GaS/Se-organic frameworks 18
2 Experimental techniques **20**
2.1 Electron microscopy 20
2.2 Atomic force microscopy 23
2.3 Infrared Spectroscopy 25
2.4 X-Ray diffraction 27
2.5 Inductively Coupled Plasma - Optical Emission Spectrometry 29
2.6 Elemental analysis 30
2.7 Thermogravimetric analysis 30
2.8 Ultraviolet–visible spectroscopy 31
2.9 Photoluminescence Spectroscopy 33
2.10 X-Ray Photoelectron Spectroscopy 34
2.11 X-ray fluorescence spectrometry 35
2.12 Nuclear magnetic resonance 36
2.13 Gas absorption and BET 38
3 Synthesis of magnesium-aluminium layered double hydroxides with tailored size and crystallinity for biological applications **41**

3.1 Homogenous precipitation of Mg_xAl_y LDH at increasing pH by thermal decomposition of urea and HMT 42
3.1.1 Temperature effect 43
3.1.1.1 Synthesis with urea 43
3.1.1.2 Synthesis with HMT 44
3.1.2 Reaction time 45
3.1.3 Encapsulation effect of organic solvents 46
3.1.4 Compositional and structural characterization 46
3.1.5 Ion exchange 51
3.2 Precipitation of $Mg_xAl_y(NO_3)_y \cdot nH_2O$ at constant pH 55
3.3 Precipitation of $Mg_xAl_y(OH)_2(NO_3)_y \cdot nH_2O$ at decreasing pH 57
3.3.1 Characterization of $Mg_xAl_y(OH)_2(NO_3)_y \cdot nH_2O$ with initial Mg^{2+}/Al^{3+} ratio 2:1 – Temperature effect 59
3.3.2 Characterization of $Mg_xAl_y(OH)_2(NO_3)_y \cdot nH_2O$ with initial Mg^{2+}/Al^{3+} ratio 4:1 – Concentration effect during aging 61
3.3.3 Characterization of $Mg_xAl_y(OH)_2(NO_3)_y \cdot nH_2O$ with initial Mg^{2+}/Al^{3+} ratio 3:1 – Temperature and time effect during aging 61
3.4 Plasmid DNA intercalation 67
3.4.1 LDH – LDO – LDH reconstruction with $NaNO_3$ 70
3.4.2 Synthesis of pDNA-LDH nanohybrids 72
3.4.3 Testing of the LDH as pDNA delivery agent 74
3.5 Conclusions 75
4 Synthesis of nickel-iron layered double hydroxides and their application as catalysts for oxygen evolution reaction 77
4.1 Synthesis of Ni_xFe_y LDH using trisodium citrate as capping agent 78
4.1.1 Characterization of flower-like Ni_xFe_y LDH synthesised at 150 ºC with TSC:Fe^{3+} ratio of 1:1 81
4.2 Synthesis Ni_xFe_y LDH with triethanolamine as capping agent 82
4.2.1 Characterization of Ni_xFe_y LDH obtained by homogeneous precipitation at 100 ºC with a TEA:Fe^{3+} ratio of 4:1 (sample NF7) 87
4.2.2 $Ni_{0.78}Fe_{0.22}(OH)_2A_x \cdot 0.6H_2O$ formation mechanism 91
4.2.2.1 Time-controlled precipitation of two-line ferrihydrite at RT 93

4.2.2.2 Ni^{2+} complex in the reaction mixture at RT 94

4.2.2.3 Ni_xFe_y LDH formation by thermal decomposition of urea at 100 ^oC 96

4.3 Electrocatalytic activity in OER 98

4.4 Conclusions 100

5 Synthesis of Amine-Templated Gallium Chalcogenide Nanotubes 102

5.1 Optimization of the synthesis of A_tGaS_x NT 104

5.2 Optimization of the synthesis of A_tGaSe_y NT 108

5.3 Synthesis of A_tGaTe_z NT 109

5.4 Characterisation of A_tGaS_x and A_tGaSe_y NT 112

5.4.1 Distribution of elements within the nanotubes 114

5.4.2 Composition of amine templated A_tGaS_x and A_tGaSe_y nanotubes 117

5.4.3 Optical properties of A_tGaS_x NT and A_tGaSe_y NT 124

5.5 Testing of the nanotubes as active materials for lithium ion battery anodes 126

5.6 Conclusions 129

6 Conclusions and future work 131

7 Supplementary information 134

7.1 Chapter 3 134

7.2 Chapter 4 135

8 References 136

Acknowledgments

Firstly, I would like to thank my supervisor Prof. Valeria Nicolosi, for encouraging my research and for allowing me to grow as a research scientist. Her guidance, motivation and knowledge are priceless. Moreover, I am thankful to my co-supervisor Dr. Andrés Seral-Ascaso, whose comments and suggestions gave the final shape of this thesis. His help with both experimental problems and data analysis let me understand and solve many problems faced during these three years. I would also like to acknowledge Christopher Hobbs for his help with TEM characterization and a lot of creative discussions. My grateful thank goes to my dear friend João Coelho for all the support he is giving me. Furthermore, I want to thank Daire Tyndall for all his time spent on reading this thesis.

I would also like to thank all my group members and Advanced Microscopy Laboratory, Trinity College Dublin, for their help and really nice time together. I want to especially recognise Carol McCaffrey, for all her help with the paperwork which sometimes turned out to be more complicated than science…

I am very grateful to all people who helped me with characterisation techniques, Edgar Muñoz (Instituto de Carboquímica, Spain) and Servicio General de Apoyo a la Investigación-SAI (Universidad de Zaragoza) for ICP-OES measurements, John O'Brien and Manuel Ruether for their help with NMR, and also Michael Finneran for invaluable help with solving many technical issues.

A big thanks go to the people from the office 4.22, who were taking all the failures and complains. It was also an unforgettable experience to re-discover Eastern Europe with you.

Finally, I must thank my fiancé for supporting me all the time and his patience during the last months. I am also very grateful to my family, who has never doubt I can do it.

In the end, I want to thank European Commission (ECFP7-MC-MoWSeS Marie Curie) for financial support.

List of figures

Figure 1.1.1 The schematic structure of LDH. Adapted from ref 27.[27] Copyright 2017 Elsevir (licence number 4119381417806). 5

Figure 1.1.2 a) Hexagonal and b) rhombohedral forms of LDH. Adapted from ref. 28. Copyright 2017 The Royal Society of Chemistry (licence number 4118170805181). 6

Figure 1.1.3 Flattening of $M(OH)_2$ octahedron in Zn-Al LDH (based on ref. 24).[24] 6

Figure 1.1.4 Proposed cellular uptake mechanism for the drug-LDH nanohybrid. Adapted from ref 86. Copyright 2017 The Royal Society of Chemistry (licence number 4118170466514).....10

Figure 1.2.1 The structure of GaS/GaSe, a) the stacking sequence in hexagonal GaS, b) rhombohedral GaS and c) the stacking sequence in hexagonal GaSe. Structures were generated in Mercury software.....14

Figure 1.2.2 The structure of the monoclinic GaTe. Structure was generated in Mercury software. 15

Figure 1.2.3 Energy diagram of materials with different electron conductivity.....15

Figure 1.2.4 Energy vs momentum in a) direct and b) indirect band gap semiconductors (based on ref. 109).[108].....16

Figure 1.2.5 The plot of density of states vs energy for nanomaterials depending on the nanoparticles dimensionality. Adapted from ref 113. Copyright 2017 John Wiley and Sons (licence number 4118190688913). 17

Figure 1.2.6 Quantum confinement of the 3D along z, xy and xyz directions. Adapted from ref 113. Copyright 2017 John Wiley and Sons (licence number 4118190688913). 17

Figure 1.2.7 a) A one-dimensional $[Ga_{10}S_{16}(NC_6H_7)_2(N_2C_{12}H_{12})]_2^-$ chain and b) schematic representation of a layer made of it's clusters. Reprinted from ref. 116. Copyright 2017 American Chemical Society. 18

Figure 2.1.1 Possible signals generated after electron-specimen interaction (based on ref. 128).[128].....20

Figure 2.1.2 Signals collected for generating TEM and SEM images (based on ref. 129).[129] 21

Figure 2.1.3 Signals generated after electron beam-sample interaction typical for SEM (based on ref. 130).[130].....21

Figure 2.1.4 Electron beam-atom interactions. 22
Figure 2.2.1 Schematic diagram of AFM (based on ref. 131).[131] 24
Figure 2.2.2 Intermittent-contact operating regime (based on ref. 132).[132] 25
Figure 2.3.1 Illustration of quantized discrete energy level in the atom/molecule. 26
Figure 2.3.2 Schematic representation of ATR technique (based on ref. 133).[133] 27
Figure 2.4.1 Schematic representation of the Bragg's law (based on ref. 136).[136] 28
Figure 2.5.1 Schematic Bohr model of atom and possible electron excitation/decay process (based on ref. 139).[139] 29
Figure 2.8.1 Electronic energy levels and possible transitions in UV-Vis spectroscopy (based on ref. 142).[142] 31
Figure 2.9.1 Joblonski diagram (based on ref. 146) representing difference between fluorescence and phosphorescence.[146] 33
Figure 2.10.1 Schematic of the XPS process showing the ejection of a 1s electron after interaction with X-Ray (based on ref. 149).[149] 34
Figure 2.11.1 Schematic representation of a) photon emission and b) Auger effect (based on ref. 109).[109] 36
Figure 2.12.1 NMR absorption process for the proton (based on ref. 142),[142] a spin change after interaction with electromagnetic radiation. 37
Figure 3.1.1 SEM micrograph of $Mg_xAl_y(OH)_2(CO_3)_{y/2}\cdot nH_2O$ obtained at a) 80 ^oC, b) 90 ^oC, c) 100 ^oC and d) 110 ^oC. 44
Figure 3.1.2 SEM micrograph of $Mg_xAl_y(OH)_2(CO_3)_{y/2}\cdot nH_2O$ obtained from HMT decomposition at a) 100 ^oC and b) 110 ^oC after 24 h. 45
Figure 3.1.3 SEM micrograph of $Mg_xAl_y(OH)_2(CO_3)_{y/2}\cdot nH_2O$ obtained at 90^oC after a) 48 and b) 72 hours. 45
Figure 3.1.4 SEM micrograph of $Mg_xAl_y(OH)_2(CO_3)_{y/2}\cdot nH_2O$ obtained at 80 ^oC in a) EG/water (1:1), b) EG/water (2:1) and c) EG/water (4:1). 46
Figure 3.1.5 FT-IR spectra of $Mg_xAl_y(OH)_2(CO_3)_{y/2}\cdot nH_2O$ obtained at a) 80 ^oC, b) 90 ^oC, c) 90 ^oC after 48 h, d) 90 ^oC after 72h, e) 100 ^oC, f) 110 ^oC, g) 80 ^oC in a mixture EG/water-1:1), h) 80 ^oC in a mixture EG/water-2:1, i) 80 ^oC in a mixture EG/water-4:1, j) 100 ^oC from HMT and k) 110 ^oC from HMT. 49
Figure 3.1.6 XRD patterns of $Mg_xAl_y(OH)_2(CO_3)_{y/2}\cdot nH_2O$ obtained at a) 80 ^oC, b) 90 ^oC, c) 90 ^oC after 48 h, d) 90 ^oC after 72h, e) 100 ^oC, f) 110 ^oC, g) 80 ^oC in a mixture EG/water-1:1), h) 80 ^oC in a mixture EG/water-2:1, i) 80 ^oC

in a mixture EG/water-4:1, j) 100 °C from HMT and k) 110 °C from HMT. 50

Figure 3.1.7 FT-IR spectra of $Mg_{0.65}Al_{0.35}(OH)_2(CO_3)_{0.175}\cdot nH_2O$ a) before acid-salt treatment, b) after treatment for 24 hours, c) after 48 hours and d) after 72 hours. 52

Figure 3.1.8 XRD pattern of $Mg_{0.65}Al_{0.35}(OH)_2(CO_3)_{0.175}\cdot nH_2O$ a) before acid-salt treatment, b) after treatment for 24 hours, c) after 48 hours and d) after 72 hours. Peaks marked by green * are related to the contamination of NaCl. 53

Figure 3.1.9 SEM micrograph of $Mg_{0.65}Al_{0.35}(OH)_2(CO_3)_{0.175}\cdot nH_2O$ a) before acid-salt treatment, b) after treatment for 24 hours, c) after 48 hours and d) after 72 hours. 53

Figure 3.1.10 TGA analysis of $Mg_{0.65}Al_{0.35}(OH)_2(CO_3)_{0.175}/(Cl)_{0.35}\cdot nH_2O$ corresponding to the samples before and after ion-exchange. 54

Figure 3.1.11 XRD pattern of the residue after thermogravimetric analysis of a) $Mg_{0.65}Al_{0.35}(OH)_2(Cl)_{0.35}\cdot nH_2O$ and b) $Mg_{0.65}Al_{0.35}(OH)_2(CO_3)_{0.175}\cdot nH_2O$. 55

Figure 3.2.1 a) SEM micrograph, b) FT-IR spectrum and c) XRD pattern of $Mg_{0.645}Al_{0.355}(OH)_2(NO_3)_{0.317}(CO_3)_{0.019}\cdot nH_2O$ obtained at constant pH…57

Figure 3.3.1 TEM micrograph of $Mg_{0.6}Al_{0.4}(NO_3)_{0.4}\cdot nH_2O$ aged at a) water at 150 °C, b) water at RT and c) EG/water (4:1) - 115 °C); d) EDX results of sample aged at RT. 60

Figure 3.3.2 TEM micrograph of $Mg_{0.78}Al_{0.22}(NO_3)_{0.22}\cdot nH_2O$ aged at 85 °C a) without dilution, b) diluted 1:10. 61

Figure 3.3.3 TEM micrograph (a-f) and corresponding particles diameter histograms (a'-f') of $Mg_{0.73}Al_{0.27}(NO_3)_{0.27}\cdot nH_2O$ a) without aging, b) aged for 3 days at RT, c) aged for 3 days at 50 °C, d) aged for 3 days at 85 °C, e) aged for 3 days at 115 °C (EG:H_2O-4:1) and f) aged for 3 days at 150 °C. 63

Figure 3.3.4 TEM micrograph of $Mg_{0.73}Al_{0.27}(NO_3)_{0.27}\cdot nH_2O$ aged for 7 days at a) RT, b) 50 °C, c) 85 °C. 64

Figure 3.3.5 TEM micrograph of $Mg_{0.73}Al_{0.27}(NO_3)_{0.27}\cdot nH_2O$ kept at RT for a) 14 days, b) 28 days, c) 42 days. 64

Figure 3.3.6 AFM image and height profile of $Mg_{0.73}Al_{0.27}(NO_3)_{0.27}\cdot nH_2O$ kept at RT for 7 days. The profiles 1, 2, 3 and 4 correspond to the numbered lines in the AFM image. 65
Figure 3.3.7 XRD pattern of $Mg_{0.73}Al_{0.27}(NO_3)_{0.27}\cdot nH_2O$ aged for 3 days at a) RT without washing, b) RT washed, c) 50 ºC, d) 85 ºC, e) 115 ºC (EG/water-4:1) and f) 150 ºC. 66
Figure 3.4.1 The intercalation mechanism of DNA into LDH via ion-exchange mechanism. Adapted from ref 83.[83] Copyright 2017 Taylor & Francis. ..68
Figure 3.4.2 Schematic representation of reconstruction method. Adapted from ref. 176 (licence number 4119400879469).[176] 68
Figure 3.4.3 XRD diffractogram of a) B1, b) LDO and c) B2. 70
Figure 3.4.4 FT-IR spectrum of a) B1, b) LDO and c) B2. 71
Figure 3.4.5 SEM micrograph of a) B1, b) LDO and c) B2. 72
Figure 3.4.6 FT-IR spectrum of a) B1, b) A1, c) A2 and d) A3. 72
Figure 3.4.7 a) STEM and b, c) STEM-EDX analysis of A2. 73
igure 3.4.8 a) STEM micrograph, b) Zoomed-in STEM micrograph and c) STEM-EDX spectrum of the pDNA-LDH nanohybrid inside the cell. 74
Figure 4.1.1 SEM micrographs of a) S1, b) S2, c) S3, d) S4, e) S5, f) S6, g) S7 and h) S8. 80
Figure 4.1.2 a) FT-IR spectra and b) XRD of TSC and $Ni_{0.75}Fe_{0.25}(OH)_2(C_6H_5O_7)_x(CO_3)_y\cdot nH_2O$. Peaks marked as * are attributed to the contamination of $NiFe_2O_4$. 82
Figure 4.2.1 Schematic representation of an atrane structure. 83
Figure 4.2.2 SEM micrographs of samples a) NF1, b) NF3, c) NF5, d) NF7, e) NF2, f) NF4, g) NF6 and h) NF8. 85
Figure 4.2.3 a) SEM micrograph and b) XRD pattern of the sample NF9. Peaks marked by * have been attributed to the contamination of iron(III) oxides and hydroxides. 86
Figure 4.2.4 SEM micrograph of a) NF10 and b) NF11. 87
Figure 4.2.5 a) FT-IR spectrum and b) X-Ray diffraction pattern of $Ni_{0.78}Fe_{0.22}(OH)_2A_x\cdot nH_2O$. In the inset it is shown the zoomed d-spacing region of 1.5-2.7 Å. 88
Figure 4.2.6 TGA analysis of $Ni_{0.78}Fe_{0.22}(OH)_2A_x\cdot 0.6H_2O$. 89
Figure 4.2.7 a) TEM micrograph and b) SAED of $Ni_{0.78}Fe_{0.22}(OH)_2A_x\cdot 0.6H_2O$. 90

Figure 4.2.8 AFM image and height profiles of $Ni_{0.78}Fe_{0.22}(OH)_2A_x \cdot 0.6H_2O$.....90
Figure 4.2.9 a) SEM electron image and distribution of b) nickel, c) iron and d) oxygen within a $Ni_{0.78}Fe_{0.22}(OH)_2A_x \cdot 0.6H_2O$ flake. 91
Figure 4.2.10 a) FT-IR spectrum, b) XRD pattern and c) TEM micrograph and SAED (in the inset) of the precipitate formed at RT. 92
Figure 4.2.11 Absorbance at 350 nm of the supernatant of the reaction mixture after different stirring time at RT. 93
Figure 4.2.12 UV-Vis spectrum of $Ni(NO_3)_2$ and the reaction mixture. 94
Figure 4.2.13 Comparison of the a) ^1H and b) ^{13}C NMR spectrum of the reaction mixture and TEA. 95
Figure 4.2.14 Evolution of the Fe^{3+} concentration and the pH value within 48 hours of heating the reaction mixture. 96
Figure 4.2.15 SEM micrographs of Ni_xFe_y LDH formed after a) 4 hours, b) 12 hours and c) 24 hours of heating the reaction mixture at 100 ^oC. 97
Figure 4.3.1 Linear sweep voltammetry curves for the Ni_xFe_y LDH hexagons, flowers and Ni foam at a scan rate of $5mVs^{-1}$ in 1M KOH. The horizontal dashed lines indicate the overpotential required to obtain a current density of 10 $mA \cdot cm^{-2}$. This value corresponds to a 10 % efficient solar water-splitting device and it has been commonly accepted as the figure of merit for OER catalysts.[221] In the inset it is shown a voltammogram revealing the typical peaks for the Ni^{3+}/Ni^{2+} redox couple. 99
Figure 5.1.1 SEM micrograph of the materials obtained at a) 175 ^oC and b) 200 ^oC...106
Figure 5.1.2 SEM image of A_tGaS_x NT obtained from Bz_2S_2.....107
Figure 5.2.1 SEM micrograph of A_tGaSe_y NT synthesised at a) 175 ^oC, b) 200 ^oC and c) 225 ^oC. 109
Figure 5.3.1 a) SEM micrograph and b) EDX spectrum of the precipitate isolated from the reaction FF, EDX signals of C, O and Al come from the SEM stub.111
Figure 5.3.2 a) SEM image and b) XRD pattern of the sample MM. 111
Figure 5.4.1 SEM and low magnification TEM micrographs of A_tGaS_x NT (a, b, c) and A_tGaSe_y NT (d, e, f). 112
Figure 5.4.2 TEM micrographs and corresponding intensity profiles taken in the places marked by a red line for a, b) A_tGaS_x NT and c, d) A_tGaSe_y NT. The insets in a and b show SAED taken in the places marked by red lines...113
Figure 5.4.3 XRD patterns of A_tGaS_x NT (black) and A_tGaSe_y NT (red). 114

Figure 5.4.4 EDX mapping performed under SEM of a) A_tGaS_x NT and b) A_tGaSe_y NT. 115
Figure 5.4.5 EDX mapping performed under high-resolution aberration-corrected STEM of a) A_tGaS_x NT and b) A_tGaSe_y NT. 116
Figure 5.4.6 EDX (TEM) spectra of a) A_tGaS_x NT and b) A_tGaSe_y NT. 117
Figure 5.4.7 FT-IR spectra of hexadecylamine, dodecylamine, A_tGaS_x NT and A_tGaSe_y NT. 118
Figure 5.4.8 TGA curve of A_tGaS_x NT (black line) and A_tGaSe_y NT (red line).....118
Figure 5.4.9 EDX (SEM) and XRD of the TGA residue of a, c) A_tGaS_x NT and b, d) A_tGaSe_y NT respectively. 119
Figure 5.4.10 T-XRF spectrum of a) A_tGaS_x NT and b) A_tGaSe_y NT. 120
Figure 5.4.11 XPS spectra of a) A_tGaS_x NT and b) A_tGaSe_y NT.....120
Figure 5.4.12 XPS of a) N 1s, b) Ga 3d, c) S 2p and d) Se 3d regions of A_tGaS_x NT and b) A_tGaSe_y NT. 121
Figure 5.4.13 SEM micrographs (left-SE and right BSE detector) of A_tGaSe_y NT a) fresh, b) after 1 day under air and c) after 1 week under air and d) XRD pattern of the sample kept for 1 week under air; peaks marked by green square are ascribed to the nanotubes. In the insets in the right corners it is shown the color changes of the samples after exposure to ambient conditions. 123
Figure 5.4.14 UV-Vis spectrum of a) A_tGaS_x NT and b) A_tGaSe_y NT dispersed in IPA; absorbance-red, extinction-black and scattering-blue. In the inset it is shown the zoomed in spectrum of A_tGaS_x NT in the region 2.5-4.5 eV.124
Figure 5.4.15 Photoluminescence (PL) excitation-emission contour plot of a) A_tGaS_x NT and b) A_tGaSe_y NT. 125
Figure 5.5.1 Pictures of free standing electrodes and SEM micrograph of a) A_tGaSe_y NT/SWCNT and b) A_tGaS_x NT/SWCNT. 127
Figure 5.5.2 Discharge curve of a) A_tGaS_x NT/SWCNT and b) A_tGaSe_y NT/SWCNT. 128
Figure 5.5.3 Rate performance of A_tGaS_x NT/SWCNT (black) and A_tGaSe_y NT/SWCNT (red).....128

List of tables

Table 3.1.1 Composition of the $Mg_xAl_y(OH)_2(CO_3)_{y/2}\cdot nH_2O$ produced by homogeneous precipitation, as obtained by ICP-OES and elemental analysis. 47

Table 3.3.1 Aging conditions of Mg_xAl_y LDH nitrate form with various starting Mg^{2+}/Al^{3+} ratios. 59

Table 4.1.1 Experimental details of the syntheses of Ni_xFe_y LDH with the addition of TSC. 79

Table 4.2.1 Synthesis conditions and pH of the reaction mixture before and after heating. 85

Table 4.3.1 Comparative table of the overpotential of synthesized Ni_xFe_y LDH versus other Ni_xFe_y LDH catalysts reported in the literature. 100

Table 5.1.1 Optimization of the synthesis conditions of A_tGaS_x NT: temperature study (samples A-E), gallium to sulfur molar ratio study (samples C, F and G), time optimization (samples G-K) and study of disulfides as alternative sulfur precursors (samples L-N).....105

Table 5.2.1 Optimization of the synthesis conditions of A_tGaSe_y NT: temperature study (samples O-S), gallium to selenium molar ratio study (samples Q, T and U), time optimization (samples Q and V-Y) and study of diselenides as alternative selenium precursors (samples Z and AA). 108

Table 5.3.1 Parameters changed during synthesis of A_tGaTe_z NT: reactions with elemental tellurium at different temperatures (sample BB-FF) and various Ga:Te molar ratio (samples GG and HH), temperature study with the use of Bz_2Te_2 (samples II-NN).....110

Abbreviations

0D/1D/2D/3D- zero/one/two/three dimensional

AFM- Atomic Force Microscopy

$A_tGaS_x/Se_y/Te_z$ NT- Amine-templated gallium sulphide/selenide/telluride nanotubes

ATR- Attenuated Total Reflection

BET- Brauner-Emmett-Teller

$Bz_2S_2/Se_2/Te_2$- dibenzyl disulfide/diselenide/ditelluride

CHN- carbon-nitrogen-hydrogen analysis

CVD- chemical vapour deposition

DNA- Deoxyribonucleic acid

DOS- Density of States

DRIFTs- Diffuse Reflection Infrared Spectroscopy

E_c- Energy of the conduction band

EDX- Energy-Dispersive X-Ray Spectroscopy

ED-XRF- Energy-dispersive X-Ray Fluorescence Spectroscopy

E_g- Energy gap

EG- Ethylene glycol

E_v- Energy of the valence band

FT-IR- Fourier Transform Infrared Spectroscopy

FWHM- Full width at half maximum

$Ga(acac)_3$- Gallium(III) acetylacetonate

HER- Hydrogen evolution reaction

HMT- Hexamethylenetetramine

HOMO- Highest Occupied Molecular Orbital

ICP-OES- Inductively Coupled Plasma Optical Emission Spectrometry

IEP- Isoelectric point

IPA- Isopropyl alcohol

$_iPr_2S_2/Se_2$- Diphenyl disulfide/diselenide

LDH- Layered double hydroxide

LDO- Layered double oxide

LiB- Lithium-ion batteries

LPE- Liquid-phase exfoliation

LUMO- Lowest Unoccupied Molecular Orbital

NMR- Nuclear Magnetic Resonance Spectroscopy

OER- Oxygen evolution reaction

pDNA- Plasmid deoxyribonucleic acid

pDNA-LDH- Plasmid DNA-LDH hybrid

Ph_2S_2/Se_2- Diphenyl disulfide/diselenide

PL- Photoluminescence Spectroscopy

RHE- Reversible hydrogen electrode

RT- Room temperature

SAED- Selected Area Diffraction pattern

SEM- Scanning Electron Microscopy

STEM- Scanning Transmission Electron Microscopy

SWCNT- Single walled carbon nanotubes

TEA- Triethanolamine

TEM- Transmission Electron Microscopy

TGA Thermogravimetric analysis

TSC- Trisodium citrate

T-XRF- Total Reflectance X-Ray Fluorescence Spectroscopy

UV-Vis- Ultraviolet-Visible Spectroscopy

WD-XRF- Wavelength-dispersive X-Ray Fluorescence Spectroscopy

XPS- X-Ray Photoelectron Spectroscopy

XRD- X-Ray Diffraction

XRF- X-Ray Fluorescence Spectroscopy

List of publications

- Xiaoling Zeng, Hippolyte Hirwa, Veit Wagner, **Sonia Metel**, and Valeria Nicolosi; *Solution Processed Thin Film Transistor from Liquid Phase Exfoliated MoS2 Flakes*; submitted to Journal of Applied Physics, 2017
- Andrés Seral-Ascaso, Clive Downing, Anuj Pokle, Hannah Nerl, **Sonia Metel**, Joao Coelho, Nina Berner, Andrew Harvey, Karsten Rode, Manuel Ruether, Georg Duesberg, Jonathan Coleman, Valeria Nicolosi; *Synthesis of 2D materials by self-assembly of rhenium-based clusters directed by long-chain amines*; npj 2D Materials and Applications 1.1 (2017): 11.
- Andres Seral-Ascaso, **Sonia Metel**, Anuj Pokle, Claudia Backes, John CF Zhang, Hannah Nerl, Karsten Rode, Nina Berner, Clive Downing, Nial McEvoy, Edgar Muñoz, Andrew Harvey, Zahra Gholamvand, Georg Duesberg, Jonathan Coleman, Valeria Nicolosi; *Long-chain amine-templated synthesis of gallium sulfide and gallium selenide nanotubes;* Nanoscale, 8(22), 11698-11706, 2016.
- **Sonia Metel**, Christopher Hobbs, Andrés Seral-Ascaso, João Coelho, Takayoshi Sasaki and Valeria Nicolosi; "*Hexagonal platelets of Ni-Fe Layered Double Hydroxide: formation mechanism* "; submitted to Nano research.

List of Communications

Oral Presentations:

- **Sonia Metel**, Andrés Seral-Ascaso and Valeria Nicolosi; "Size and shape controlled synthesis of semiconducting nanomaterials in long-chain amines"; 2016 E-MRS Fall Meeting (19-22 September 2016), University of Technology, Warsaw, Poland
- **Sonia Metel**, Andrés Seral-Ascaso, Christopher Hobbs and Valeria Nicolosi; "Layered double hydroxides for biological applications"; Flatlands beyond graphene (7-9 July 2015), Bar Ilan University, Israel

Posters:

- **Sonia Metel**, Christopher Hobbs, Andrés Seral-Ascaso, Fergal J. O'Brien and Valeria Nicolosi; "Layered double hydroxides for biological applications"; 2016 MRS Fall Meeting (27 November-2 December 2016), Boston, USA
- **Sonia Metel**, Andrés Seral-Ascaso and Valeria Nicolosi; "Size and shape-controlled synthesis of semiconducting nanomaterials"; Flatlands beyond graphene (5-8 July 2016), Bled, Slovenia.
- **Sonia Metel**, Andrés Seral-Ascaso, Christopher Hobbs and Valeria Nicolosi; "Synthesis and liquid-phase exfoliation of double layered hydroxides"; Flatlands beyond graphene (7-11 July 2014), Trinity College Dublin, Ireland

Awards:

- Best oral presentation on symposium E; 2016 E-MRS Fall Meeting (19-22 September 2016), University of Technology, Warsaw, Poland.

1 Introduction and objectives

During the last years, two-dimensional (2D) materials became the focus of an intensive scientific research due to their unique structure and enhanced physical properties.[1, 2, 3] 2D materials present important advantages in comparison with their bulk counterparts, including much higher surface area and transparency. Moreover, amazing changes in their physical properties, due to quantum effect, such as the appearance of superconductivity[4] or the change from indirect to direct band gap[5] have been reported. Therefore, 2D materials have been proposed for the fabrication of a new generation of smaller, more efficient and transparent devices.[6-10]

There are many compounds with a layered structures, each of which has its specific electronic, optical, mechanical and electrochemical properties.[2] These materials have a structure composed of layers arranged in stacks, which present a strong chemical bonds within the layer, while the layers are kept together via weak van der Waals interactions, which enables their separation by chemical and physical methods.[2, 8] Both bulk and exfoliated forms of layered compounds have been used in a variety of applications and every year new possibilities are reported.[2]

In 2004, Novoselov *et al*. announced the production of an atomically-thin layer of graphite (known as graphene) by a mechanical cleavage process, so-called scotch-tape technique.[1] Despite the improvement of this method,[11] the amount of produced material is very small, which highly restricts the development of industrial scale applications.

Liquid-phase exfoliation (LPE),[2, 7, 10] intercalation methods[2, 12] or shear mixing procedure[13] were subsequently developed to produce larger quantities of nanosheets from layered materials. All the techniques listed above follow the "*top-down*" approach, as they rely on decreasing the size of the existing bulk layered materials. On the contrary, the "*bottom-up*" techniques consist in the direct synthesis of atomically-thin nanosheets. Chemical vapour deposition (CVD) is the most common synthesis method to produce atomically thin flakes,[3, 10] although the requirement of very high temperatures and the small amount of the material obtained are still limiting factors to expand this process for industrial applications.

Direct synthesis of ultra-thin nanomaterials at relatively low temperature is a very attractive alternative;[14-18] synthesis of transition metal oxides[16] layered double hydroxides (LDH)[14, 17-19] and semiconducting nanocrystals[20] have been described but still the development of further synthesis methods represents a major scientific challenge.

One of the biggest advantages of the direct synthesis, in comparison to the "*bottom-up"* methods is the control over the composition of the nanoparticles and the ability to obtain novel materials presenting unique properties. Moreover, considering that the exfoliation techniques rely on breaking the bulk material into smaller/thinner pieces it is difficult to control their size and shape. In contrast, by direct synthesis, where the nanoparticles are formed in certain conditions, their formation can be controlled by changing the synthesis parameters.

Wet-chemistry methods are low cost and potentially scalable procedures to obtain nanomaterials with a high control over the nanoparticle's geometry (size and shape) and crystallinity. Moreover, the versatility of these techniques makes them applicable in the synthesis of various families of chemical compounds (metal chalcogenides, oxides, hydroxides, etc).[21, 22] Those techniques rely on the mixing of the precursors in a suitable solvent and their further reaction to produce nanoparticles with a controlled size and shape.[22] In general the process follows the scheme: decomposition of the precursors → precursors rearrangement to monomers → nuclei formation (nucleation) → crystal growth (by deposition of the monomers or Ostwald ripening).

In spite of more than 150 years of research in the field of nanoparticles formation in colloidal solution, the mechanism is still not clear. Xia *et al.*[23] described this situation very appropriately by saying that:

> *"at the current stage of development, it is not an exaggeration to say that the chemical synthesis of metal nanocrystals (as well as for other solid materials) remains an art rather than a science"*

In the presented Thesis wet-chemistry methods were used to obtain 2D flakes of Mg-Al LDH, Ni-Fe LDH and 1D amine-templated gallium chalcogenide nanotubes. Firstly, Mg-Al LDH platelets were designed for biological applications, in which the nanoparticles size plays a crucial role, as only particles below 200 nm in diameter can be uptaken by the cell in the endocytosis process. Moreover, the intercalation of DNA

between the LDH layers was also undertaken and the preliminary results of those nanohybrids uptake by the cell are presented as well. Secondly, regarding that Ni-Fe LDH was reported in the literature as a promising catalyst in oxygen evolution reaction (OER), but the preparation of the Ni-Fe LDH nanoparticles with well-defined morphology and high crystallinity still remains a challenge in the field, the synthesis of Ni-Fe LDH nanoparticles with regular shape was studied and the formation of those nanoparticles was carefully analysed. The catalytic activity of the obtained nanostructures in OER was preliminary tested. Finally, wet-chemistry methods were also applied in the synthesis of amine-templated gallium chalcogenide nanotubes. For the first time the heating-up procedure in long chain amines was applied to obtain layered 1D gallium chalcogenides nanostructures. The nanotubes were tested as active materials in lithium-ion batteries anodes.

A description of the materials under study and the synthesis methods used to produce them are briefly presented in this Chapter.

Objectives

The aim of this Thesis is the development of wet-chemistry synthesis methods to prepare different nanostructured layered materials and the study of the effects of different experimental parameters (reactants, temperature, pressure, time, etc) on the structure, crystallinity and purity of the obtained compounds.

The first section of this work pursues the preparation of Mg_xAl_y layered double hydroxides (LDH) nanoplatelets (Chapter 3) having a size in the range of 50-200 nm, and containing nitrates as counter anions. A material with these dimensions and characteristics should present optimum properties for further DNA intercalation process. The second aim of this project is the preparation of DNA-LDH nanohybrids being a part of bone-repairing therapy, performed in collaboration with Prof. Fergal O'Brien (Royal College of Surgeons in Ireland, RCSI).

The second part of this work seeks to achieve the preparation of Ni_xFe_y LDH well-crystallized platelets (Chapter 4) presenting a regular and well-defined geometry, which is expected to present enhanced electrocatalytic activity in oxygen evolution reaction (OER). The particles size must be in the nanometre scale, in order to increase surface area and make available maximum number of catalytically active sites, which should reduce the overpotential values in OER.

Furthermore, wet-chemistry methods will be also extended to the synthesis of amine-templated gallium chalcogenides (Chapter 5), which belong to the family of the inorganic-organic frameworks. Similarly as observed for other metal oxides and chalcogenides, it is expected that the long-chain amines template the growth of nanotubular structures. These nanostructures might present interesting properties as active material in energy storage (LiB anodes).

1.1 Layered double hydroxides

Layered double hydroxides (LDH) is a large family of layered materials which includes natural minerals and synthetically obtained compounds. The first discovered mineral belonging to this family was hydrotalcite ($Mg_6Al_2CO_3(OH)_{16}\cdot 4(H_2O)$), which was found in Sweden in mid-19th century,[24] albeit its properties were not described until almost a hundred years later.[25] The discovery of its structure started intensive research in the field of mixed metal hydroxides, so-called hydrotalcite-like materials.

LDH consist of positively charged layers and anions intercalated between them to compensate the positive charge. For this reason, LDH are also referred as anionic clays. Their structure is similar to that of brucite, $Mg(OH)_2$, where two-dimensional layers are made of $Mg(OH)_6$ octahedrons. These octahedral units form infinite layers by sharing edges. While for brucite the layers are electrically neutral, in LDH some divalent cations are exchanged to trivalent ones and the brucite-like layers become positively charged, and therefore, anions are intercalated between the layers in order to ensure the electrical neutrality of the structure.[26] Similarly to other layered materials, the host layers are stacked on top of each other by electrostatic interactions, van der Waals forces and hydrogen bonds, resulting in a three-dimensional structure (Figure 1.1.1).[26]

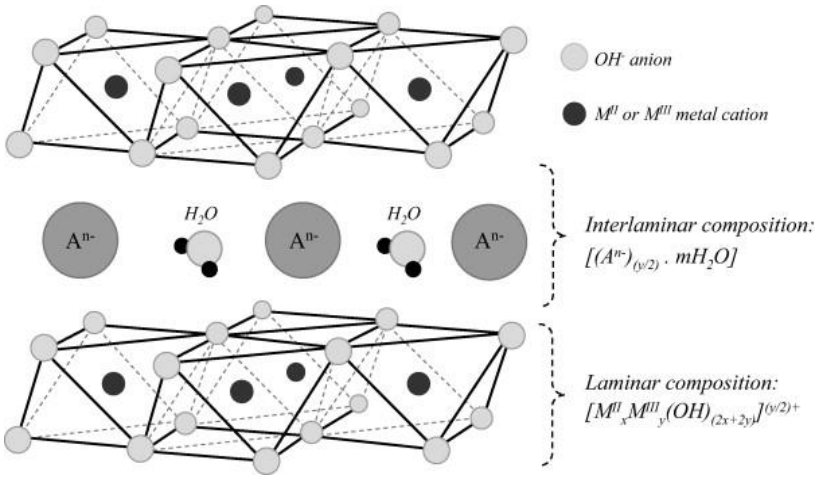

Figure 1.1.1 The schematic structure of LDH. Adapted from ref 27.[27] Copyright 2017 Elsevir (licence number 4119381417806).

The layers can stack on top of each other in two different symmetries: rhombohedral (3R) and hexagonal (2H). In rhombohedral polytype, if the three-fold

axis of OH groups is called ABC, the layers are stacked in the sequence AB-BC-CA-AB, resulting in three sheets per unit cell. In contrast, for hexagonal symmetry, there are only two sheets in a unit cell with a stacking sequence AB-BA-AB (Figure 1.1.2).[28]

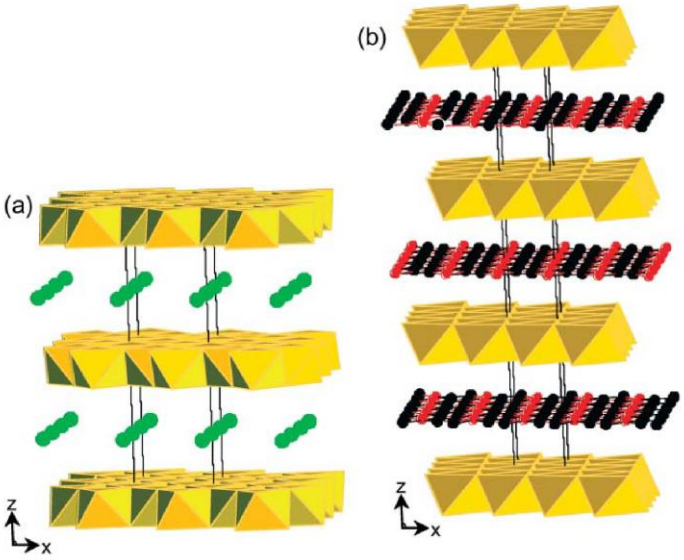

Figure 1.1.2 a) Hexagonal and b) rhombohedral forms of LDH. Adapted from ref. 28. Copyright 2017 The Royal Society of Chemistry (licence number 4118170805181).

Moreover, $M(OH)_2$ octahedrons are not perfect in LDH, since they are usually flattened along the c-axis, which results in lowering the symmetry from O_h to D_{3d}, as shown in the Figure 1.1.3 for Zn-Al LDH.

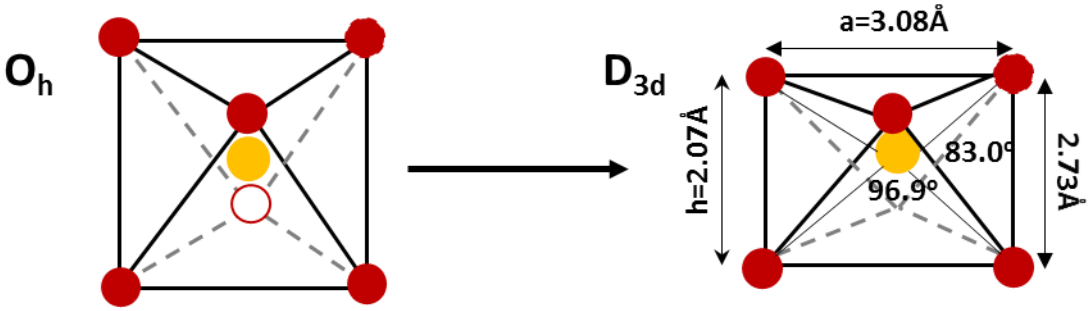

Figure 1.1.3 Flattening of $M(OH)_2$ octahedron in Zn-Al LDH (based on ref. 24).[24]

The degree of flattening depends on the metal ionic radius and leads to the decrease of the layer thickness and also an increase of the distance between the metal cations and, at the same time, the distance between OH groups on the same side of the

layer.[24] Furthermore, if the ionic radius of one of the cations is high enough, one side of the octahedron is opened and the symmetry is further decreased from D_{3d} to C_{3v}.

The general formula of LDH is:

$$[M^{II}_{1-x}M^{III}_{x}(OH)_2]^{x+}[A^{n-}_{x/n}\cdot yH_2O]^{x-}$$

where M^{II} is a divalent metal cation, M^{III} is a trivalent metal cation, A^{n-} is a charge balancing anion, n is the charge of the interlayer anion and x and y are fraction constants.[24, 26] The maximum replacement of divalent cations by trivalent ones is limited by the lattice parameters and the x value is usually in the range of $0.2 \leq x \leq 0.4$. Out of this range, other compounds such as hydroxides or metals salts are formed as a result of the electrostatic repulsions between trivalent cations[29] and also between interlamellar anions.[24]

Divalent and trivalent cations which form LDH belong mainly to the third, fourth and fifth periods of the periodic table, but some more exotic compounds containing rare earth metals have also been described.[30, 31] The only requirement about the cations nature is the size of the radii, which cannot be too different from those of Mg^{2+} and Al^{3+}. Interestingly, it is also possible to produce LDH with mono- and tetravalent cations.[32]

The nature of the anion is more versatile, as almost all negatively charged molecules can be intercalated: inorganic, organic, polymeric, complexes, macrocycling ligands or biochemical molecules have been used.[26, 33, 34] Moreover, these anions can be exchanged as long as the replacing counter anion establishes stronger interactions with the LDH, thus resulting in a more stable structure. The anion preference of LDH is established as:[26, 35, 36]

$$I^- < NO_3^- < Br^- < Cl^- < F^- < OH^- < SO_4^{2-} < HPO_4^{2-} < CO_3^{2-}$$

The relationship between the anion-exchange ability is very complex and depends on the size of the anion, its charge, charge density and its ability to create hydrogen bonds.[26, 35]

Another interesting property of the LDH is their “structure memory effect”. During calcination, LDH lose the hydroxyl groups, the interlayer water and the anions, which results in the formation of mix-metal oxides. These mix-metal oxides have an ability to reconstruct the layered structure when newly exposed to water and the anions. However, this ability is limited as overheating of the mix-metal oxides causes the formation of spinel structures which are resistant to rehydration.[26, 37]

1.1.1 Synthesis and exfoliation of LDH

The synthesis of LDH was intensively studied since their discovery, which resulted in the development of a large number of synthesis methods. The most common procedures include the precipitation at constant and variable pH (including the so-called homogeneous precipitation), which are described in the Sections 3.2, 3.3 and 3.1, respectively. Besides these techniques, there are many other methods to obtain LDH with various composition and morphology

Firstly, LDH can be obtained by sol-gel techniques, which rely on the hydrolysis and polymerization of alkoxides. These are dissolved in an organic solvent and then, cross-linking is induced upon water addition, thus leading to formation of LDH particles.[26, 38, 39] The materials prepared by this route usually present high homogeneity and porosity.

Secondly, LDH can be obtained by an induced hydrolysis method, which consists of two steps: the precipitation of the M^{3+} hydroxide and the slow addition of this precipitate to the solution of divalent metal salt under a fixed pH. A controlled release of M^{3+} takes place, which then combines with the M^{2+} and anions present in the solution, leading to the formation of the LDH.[24, 26]

Another route, which is similar to the induced hydrolysis, is the reaction of metal oxides/hydroxides with metal salts. The formed metal oxide/hydroxide is exposed to the metal salt solution and, due to dissociation of the solid, its surface becomes charged, which leads to the incorporation of the metal cations from the solution.[26]

LDH can be also produced by oxidation techniques, which are mostly applied in the preparation of transition-metal containing LDH. It this method, the divalent metal cations are precipitated and then oxidized to their higher oxidation states, leading to a positive charge of the brucite-like layers.[24, 26] The oxidation techniques can also be used in the preparation of LDH from metals, however this is not a common approach. The oxidation of the metals might be a disadvantage as well in the preparation of LDH, since under strongly basic conditions and in the presence of oxygen, divalent metals (especially manganese, cobalt, iron and vanadium) easily oxidize to their higher oxidation states.

Interestingly, it was demonstrated that not only the synthesis method, but also the processing (washing and aging conditions) define the size and morphology of the particles.[24, 26] The most common aging procedure applied to modify the particles

morphology and to constrict their size distribution is hydrothermal treatment,[40-42] which favours dissolution-recrystalization mechanism (Ostwald ripening). An alternative approach is microwave irradiation,[43-45] where microwaves induce a dipole reorientation, leading to uniform and volumetrically distributed heat. Due to the numerous water molecules in the interlamellar space, their fast reorientation might enhance Ostwald ripening.

Finally, LDH with the desired counter anions can be also obtained by using their ion-exchange ability[36, 46] and memory-effect property.[37, 47, 48] Noteworthy, by these techniques only the interlamellar space can be modified, and it is not possible to modify the composition of the brucite-like layers.

It is important to highlight here that the direct synthesis of LDH with counter anions different than carbonate requires a CO_2-free environment. The strong tendency of carbonate anions to intercalate between LDH layers is the result of their planar geometry and the presence of three oxygen atoms, which are able to create hydrogen bonds with hydroxyl groups in the layers.[24, 26]

Despite LDH being promising materials for several applications in their bulk form, positively-charged ultrathin nanosheets also present several important and interesting properties.[12, 19, 33, 49, 50] There are two main approaches to obtain ultrathin LDH flakes: *"top down"* and *"bottom up"*. The *"Top down"* approach is based on two steps: first, a "big molecule" is intercalated in the LDH structure in order to increase the distance between the layers and, thus, weaken the forces that keep the layers together. Then, a solvation process of this "big molecule" is induced by a polar solvent, which leads to the delamination. The intercalation of these molecules creates a hydrogen-bond network between the layers which causes the exfoliation.[51] The use of "big molecules" such as surfactants,[52] amino acids,[53] formamide[54] and dimethylformamide[55] for this procedure have been described in literature.

It must be highlighted here that exfoliation of LDH is a special case of delamination processes, because not only van der Waals forces and hydrogen bonds but also electrostatic interactions have to be broken to separate the single sheets.

The *"Bottom up"* approach is a one-step synthetic method in which monolayer LDH sheets are obtained. Normally, a two-phased environment (water and oil with surfactant) must be provided. In this system (so-called inverse-micelle), the aqueous phase where the crystal growth is occurring is surrounded by the oil and the surfactant (a kind of a nanoreactor) and its size limits the growth of the nanoparticles. The size of

this nanoreactor can be controlled by varying the water-surfactant ratio, and, thus, the size and the thickness of the particles.[50]

1.1.2 Applications of LDH

Hydrotalcite-like materials are easy to synthesise, relatively cheap, environmentally-friendly and potentially recyclable, which results in many applications in different research fields.

LDH are commercially used as antacids,[56, 57] selective adsorbents[58-60] or additives to cosmetics.[61] They are also potentially useful as ultra and nanofilters,[49, 62] biosensors or biocatalysts,[63-65] elastomer composites,[66, 67] ceramics[68] flame retardant nanocomposites,[69, 70] and electrode materials in energy storage devices.[71, 72]

Another area where LDH are intensively investigated is the biological field. Hydrotalcite (Mg-Al LDH), due to its low-toxicity, biocompatibility, high stability, enhanced cellular uptake behaviour, pH dependent solubility and anion exchange ability, has been successfully used as drugs and gene delivery agents.[73-84]

The intercalation of negatively charged molecules between the layers protects them from decomposition and permits their transport into cells, as presented in the Figure 1.1.4.

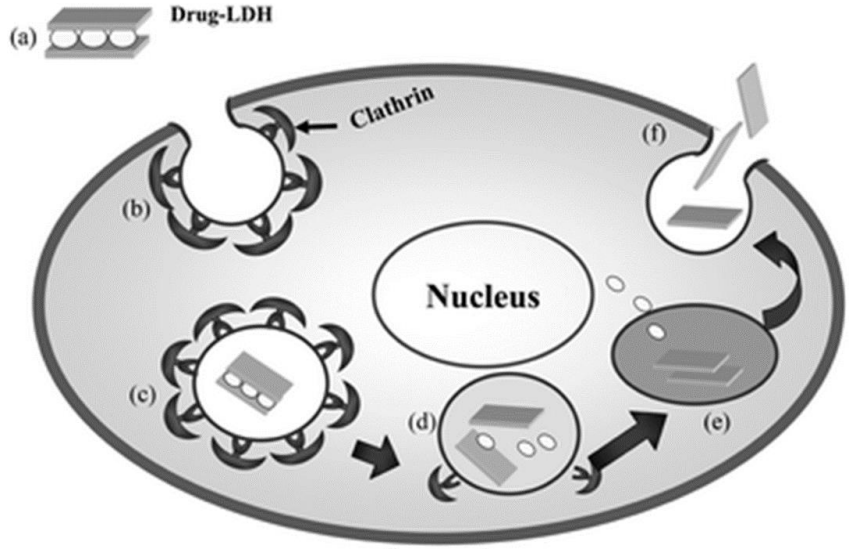

Figure 1.1.4 Proposed cellular uptake mechanism for the drug-LDH nanohybrid. Adapted from ref 86. Copyright 2017 The Royal Society of Chemistry (licence number 4118170466514).

The size and the shape of the LDH nanoparticles play a crucial role in the

cellular uptake mechanism, since only particles below 200 nm can be uptaken by the cell. Moreover, it was found that smaller particles (<100 nm), due to their higher effective surface area and lower sedimentation rate, are more effective in tissular diffusion mechanisms. Recent tests also proved that smaller LDH particles (<50 nm) have a higher gene capacity than larger ones (>100 nm).[81, 84-87] This fact is generally explained by a two-step gene-intercalation process where the biomolecule is firstly adsorbed on the nanoparticle surface and then it is inserted into the LDH interlayer space. This implies that, due to their higher surface area, this process is more efficient in the case of small particles, which results in a higher degree of intercalation.[87]

The process of drug/gene intercalation can be achieved by direct synthesis, ion exchange and reconstruction by the use of LDH memory effect (these processes are described in the Section 3.4), and then, due to the acidic pH within the cells, the hydroxide layers can be easily dissolved, thus releasing the biomolecules.[24, 74, 81, 87]

Gene therapy has been a great focus of interest since the second half of the last century, when Friedmann and Roblin published a paper about the potential use of gene therapy for the treatment of genetic disorders.[88] Since then, a huge progress has been made,[89] and there are many gene therapy treatments undergoing clinical trials. There are two main delivery systems: viral and non-viral. Viral vectors are viruses with very limited uses, due to their negative influence on the immune system. On the contrary, non-viral delivery agents are safer, and normally they consist of positively charged nanoparticles (for example LDH) able to carry negatively charged nucleic acids.[90] Moreover, gene therapy can be used in bone regeneration to deliver specific genes in a very precise way, which is much more effective than direct delivery of proteins.[91] Hybrids made of non-aggregated nanoparticles below 200 nm in size combined with collagen are very promising materials in tissue engineering.[92] In this Thesis, the synthesis of Mg_xAl_y LDH platelets with diameters below 200 nm and easily exchangeable nitrate as counter-anions by wet chemistry methods was proposed as a part of a project realized in collaboration with Prof. Fergal O'Brien (RCSI) and the results are detailed in Chapter 3.

Moreover, one of the main applications of LDH is catalysis, where they can perform as catalysts, catalyst precursors or catalyst supports. The first published work regarding the catalytic activity of LDH dates from 1924,[93] where the authors observed the high catalytic activity of Ni-Al LDH in the hydrogenation reactions, and, a few

years later, Zn-Cr mixed oxide was applied in the synthesis of methanol.[94] Since then, the catalytic applications of LDH expanded to the industrial scale.[26, 33, 60, 95-97]

The reason for the high catalytic activity of LDH is their high number of active sites within the brucite-like layers. Moreover, the great diversity of the cations forming these materials and their uniform distribution lead to a high control over the activity and selectivity.[33, 95]

Mixed-metal oxides obtained by thermal decomposition of LDH are also a group of compounds widely used as catalysts[95, 98-100] due to their high specific surface area, basic nature, homogenous dispersion of the metal cations within the structure and ability to reconstruct their layered structure. They are commonly used in photodegradation of organic pollutants,[33] reduction of NO_x and SO_x emissions and combustion of volatile organic compounds.[33, 95] Mixed-metal oxides are also used as a support for more catalytically active components like noble metals, titanates, niobates or tungstates.[33, 95, 98, 100]

Both hydrotalcite and mixed-metal oxides are used as a catalyst in numerous organic reactions, such as aldol and Knoevenagel condensations, epoxidation of olefins, halide exchanges, phenol hydroxylation, Michael additions, Fisher-Troposh synthesis, *trans*-estrifications and many others.[26, 33, 95, 96, 98]

Nowadays, hydrogen gas is regarded as one of the most promising and clean energy sources. Contrary to fossil fuels, hydrogen combustion in air does not result in the emission of pollutant or toxic gases:[101, 102]

$$2H_2 + O_2 \rightleftarrows 2H_2O \qquad \textbf{Eq.1.1.1}$$

As Equation 1.1.1 can be reversed (water electrolysis), hydrogen could, in principle, fuel our societies for an undefined amount of time. The electricity necessary to drive this reaction can be easily harvested from renewable energy sources, thus turning the overall process environmentally-friendly. Considering all the advantages of hydrogen gas as a clean energy carrier, several efforts have been made to produce it in large scale. However, for the water electrolysis to occur, it is necessary to overcome the hydrogen evolution reaction (HER) and oxygen evolution reaction (OER). Both electrochemical processes can be described by:[102, 103]

$$pH < 7 \begin{cases} 2H_2O \rightarrow O_2 + 4H^+ + 4e^- & (V_{OER} = 1.23\,V\ vs.\,RHE) \\ 4H^+ + 4e^- \rightarrow 2H_2 & (V_{HER} = 0\,V\ vs.\,RHE) \end{cases} \qquad \textbf{Eq. 1.1.2}$$

$$pH > 7 \begin{cases} 4OH^- \rightarrow O_2 + 2H_2O + 4e^- & (V_{OER} = 1.23\ V\ vs.\ RHE) \\ 4H_2O + 4e^- \rightarrow 2H_2 + 4OH^- & (V_{HER} = 0\ V\ vs.\ RHE) \end{cases} \quad \textbf{Eq. 1.1.3}$$

From Equation 1.1.2 and Equation 1.1.3 it is clear that HER is a very simple process and can easily occur in many metals at a very low overpotential (the potential difference between the thermodynamically determined potential and the potential at which the redox reaction is experimentally observed). On the contrary, OER requires a large overpotential to occur, thus limiting the overall water electrolysis process, or at least rendering it inefficient. Therefore, it is not surprising that several OER catalysts have been proposed during the last few years.[101, 102] In spite of their optimal electrocatalityc properties, RuO_2 and IrO_2 are too expensive and scarce to be used in large scale applications.[102, 104] *3d* transition metal based materials, such as Fe, Ni and Co represent viable options for OER catalysis. Besides enhancing oxygen evolution, these materials are stable, relatively cheap, abundant, and, therefore suitable for industrial applications.

Moreover, the electrocatalysts composed of a combination of different metals can lead to a further reduction of the OER overpotential. Ma *et al.*[101] and Tolentino *et al.*[105] reported that the addition of iron (even at a very low concentration) improves nickel OER electrocatalytic properties. The specific mechanisms behind such synergistic effects are not yet fully understood.[105] Nevertheless, Ni-Fe compounds have been thoroughly studied as possible catalysts for OER applications. In this context, Ni-Fe LDH structure is highly attractive for electrochemical processes. The interlayer distance can be modified by anion exchange, thus making the structure more accessible to the electrolyte. In general, Ni-Fe based LDH lead to lower Tafel plots (the relationship between the rate of the electrochemical reaction and the overpotential), smaller overpotential values and stability in OER in comparison with other commercially available catalysts.[105] Due to the interesting and promising properties presented by single-layer materials, the exfoliation and synthesis of monolayer (or a few nanometers thick) Ni-Fe LDH has also been proposed and reported.[101, 103-105] As it happens for other layered materials, such as graphene, two-dimensional Ni-Fe LDH present an enhanced activity that strongly differs from their bulk counterparts. Regarding this, in the present work the synthesis of highly crystalline, thin Ni-Fe LDH nanoparticles was attempted and the details are described in the Chapter 4.

1.2 Semiconducting gallium chalcogenides

Gallium chalcogenides (GaS, GaSe and GaTe), so-called III-VI semiconducting compounds, present a layered structure and, like other layered materials, strong covalent bonds are in-plane while the layers are held together via weak van der Waals interactions. The structures of GaS and GaSe are similar, consisting of four-layered slabs, which contains two metal layers and two chalcogenide layers.[106, 107] In the case of GaS, hexagonal (β-type) and rhombohedral stacking are observed (Figure 1.2.1 a,b), while for GaSe hexagonal, ε-type GaSe polytype was reported, as presented in the Figure 1.2.1 c.[107]

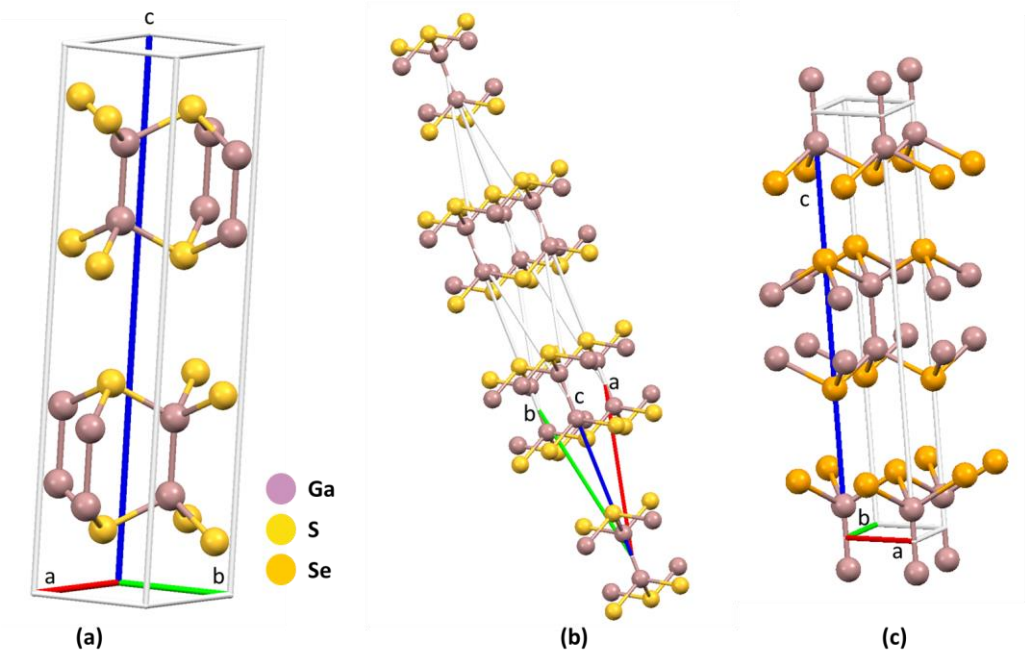

Figure 1.2.1 The structure of GaS/GaSe, a) the stacking sequence in hexagonal GaS, b) rhombohedral GaS and c) the stacking sequence in hexagonal GaSe. Structures were generated in Mercury software.

Unlike GaS and GaSe, the telluride derivative crystallizes in a monoclinic structure (Figure 1.2.2). The structural units are linked by Te – Ga – Ga – Te strips, where Ga – Ga bonds are at a right angle to the other Ga – Ga bonds.

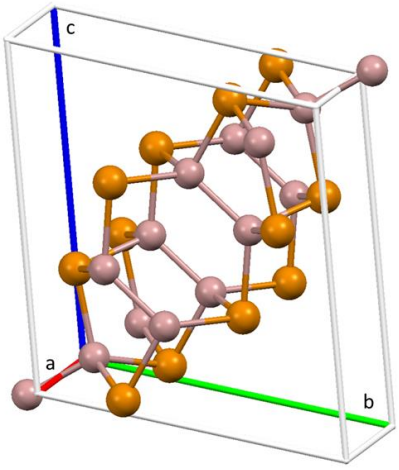

Figure 1.2.2 The structure of the monoclinic GaTe. Structure was generated in Mercury software.

As mentioned earlier, gallium chalcogenides are classified as semiconductors, in which the energy difference between valence and conduction band is relatively small so, when an external energy is applied, the electrons can promote to the conduction band. Differently, in insulators, the energy gap (E_g) between valence and conduction band is large, so the electrons which are occupying a valence band cannot be promoted to the higher energy level (conduction band). In contrast, for conductors the energy gap between valence and conduction band is very small or does not exist at all, so the electrons can freely flow (Figure 1.2.3).[108-110]

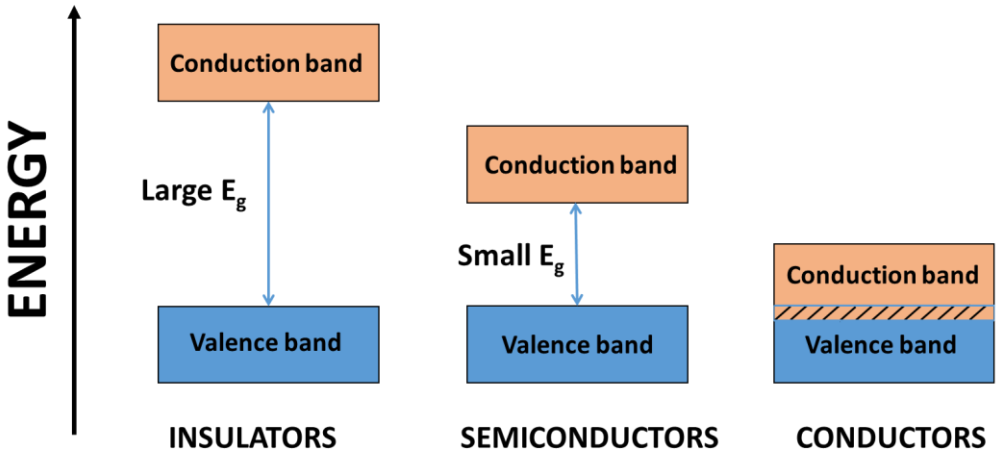

Figure 1.2.3 Energy diagram of materials with different electron conductivity.

In semiconducting materials, the band gap is the difference between the maximum energy of the valence band (E_v) and the minimum energy of the conduction

band (E_c). In a crystal, the electron can have only discrete values of energy which depends on its momentum (k).[108] If the maximum energy of the valence band and the minimum energy of the conduction band occur at the same k-values, the electron can jump between those bands without changing its momentum and the material is classified as a direct semiconductor. When the electron falls from conduction to valence band in direct semiconductors, the energy can be emitted in the form of a photon with an energy equal to the band gap. In contrast, when the maximum energy of the valence band and the minimum energy of the conduction band have a different momentum (indirect band gap semiconductor), the process when the electron comes back to the lower energy level requires a change in the momentum and usually the emission of a photon is not observed.[108] A schematic representation of direct and indirect semiconductors is presented in the Figure 1.2.4.

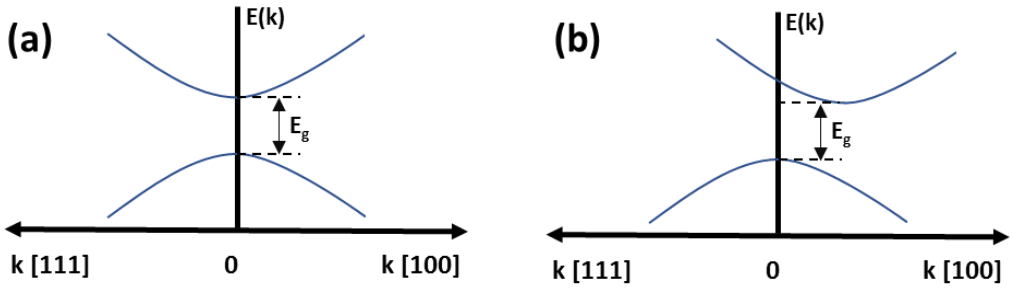

Figure 1.2.4 Energy vs momentum in a) direct and b) indirect band gap semiconductors (based on ref. 108).[108]

Moreover, the size and the shape of the semiconducting nanoparticles significantly influence their electronic properties. The density of the energy states (DOS, $\rho(E)$)[111] changes from continuous levels in bulk materials to the discrete states when the dimensionality is decreased, according to the relationship $\rho(E) \approx E^{D/2-1}$, where D is the dimensionality. Moreover, it was also observed that the band gap energy increases when the dimensionality and size are decreased (Figure 1.2.5).

The shape of the nanocrystal also influences the band gap energy, because quantum confinement effects depend on the diameter and the length of the nanocrystal,[111] as schematically presented in the Figure 1.2.6.

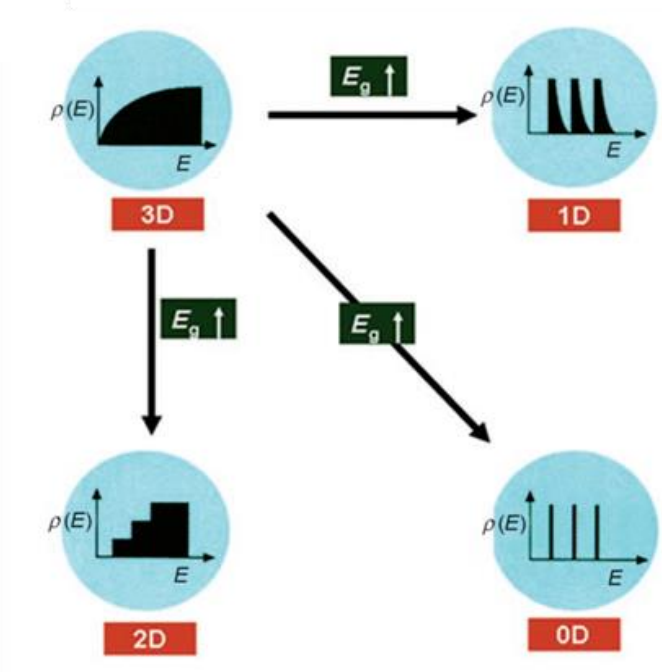

Figure 1.2.5 The plot of density of states vs energy for nanomaterials depending on the nanoparticles dimensionality. Adapted from ref 113. Copyright 2017 John Wiley and Sons (licence number 4118190688913).

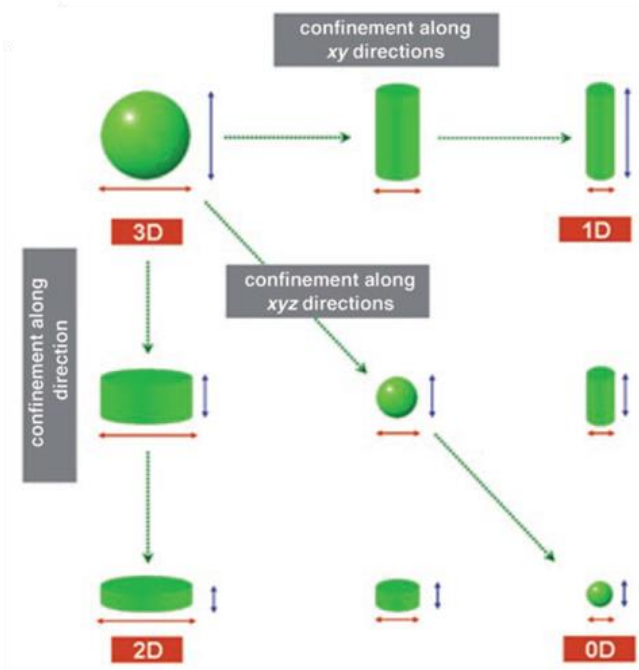

Figure 1.2.6 Quantum confinement of the 3D along z, xy and xyz directions. Adapted from ref 113. Copyright 2017 John Wiley and Sons (licence number 4118190688913).

1.2.1 GaS/Se-organic frameworks

Gallium chalcogenide-organic frameworks have attracted considerable interest, due to their distinctive topologic structures integrating unusual electronic, optical and semiconducting properties.[112, 113]

In 2002 Zheng *et al.* reported the synthesis of GaS/Se clusters with tetrahedrally coordinated gallium atoms.[114] Those clusters formed a 3D zeolite-type network, with the general framework composition AB_2, where A is a tetrahedral Ga and B is a bicoordinated S/Se. A few years later, it was proposed that GaS/Se clusters can be connected by organic moieties, which leads to organic-inorganic architectures presenting unique optical and photochemical properties.[115, 116] The chalcogenide atoms at the vertexes are replaced by organic molecules which results in the clusters' linkage and formation of the organic-inorganic frameworks, as presented in the Figure 1.2.7.

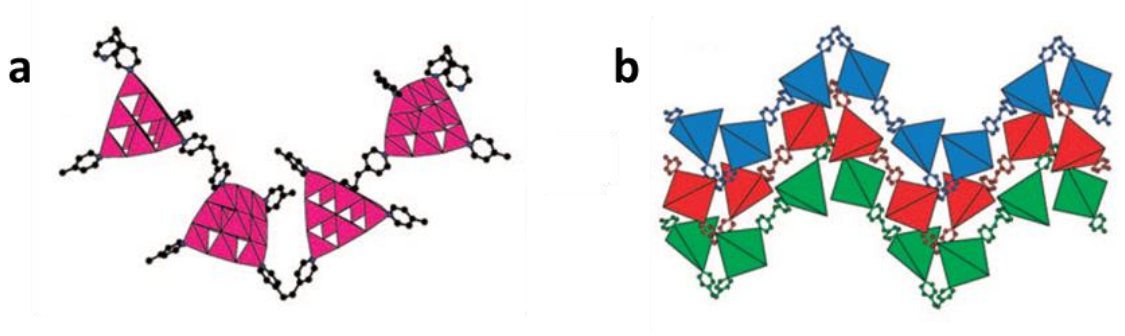

Figure 1.2.7 a) A one-dimensional $[Ga_{10}S_{16}(NC_6H_7)_2(N_2C_{12}H_{12})]_2^-$ chain and b) schematic representation of a layer made of it's clusters. Reprinted from ref. 116. Copyright 2017 American Chemical Society.

In these compounds, the gallium chalcogenide-organic framework is negatively charged, which is compensated by metal cations or protonated amines.[115, 117 112, 118]

These materials are especially attractive due to their interesting properties, such as a large surface-to-volume ratio,[106] tendency to self-assemble[119] and different electronic and optical properties in comparison to their higher-dimensional counterparts.[120 121]

The optical and electronic properties of GaS/Se-organic frameworks can be controlled by the cluster size, its composition and the interactions between them,[113, 116] which make them promising materials for opto-electronic applications. Moreover, open frameworks are promising building blocks for hybrid materials with high porosity.[114, 122]

The synthesis of inorganic-organic frameworks is usually performed by wet-chemistry methods in polar solvents (such as water, alcohol or organic amines).[112] The use of various organic amines,[123] (such as oleylamine[124] and octadecylamine[125]) have been reported in the preparation of gallium chalcogenide nanostructures. However, the use of hexadecylamine and dodecylamine (which have demonstrated a great potential in the templating the 1D growth of vanadium oxide,[126] vanadium sulfide[127] and copper sulfide[133]) still were not tested. In this work, the long-chain amines templated synthesis of gallium chalcogenide nanotubes is proposed. Then, in collaboration with John CF Zhang (researcher in the Prof. Nicolosi group), the obtained nanostructures were tested as active materials in lithium-ion battery anodes, which is described in the Chapter 5.

2 Experimental techniques

In this Chapter, the characterization techniques utilized in this work with a brief theoretical background and detailed experimental set-ups are presented.

2.1 Electron microscopy

A microscope is used to observe the object in its enlarged form. The resolution (R) of the microscope is inversely proportional to the light or electron's wavelength (λ),[128] according to Equation 2.1.1.

$$R \propto \frac{1}{\lambda} \qquad \textbf{Eq. 2.1.1}$$

The resolution provided by visible light is from 200 to 400 nm, which is not high enough for the imaging of nanomaterials under study and for this reason, electrons under a high acceleration voltage are required in order to observe morphological details and atom arrangements of nanomaterials. Theoretically, electrons accelerated at 100 kV provide a resolution as high as 2 pm, but the imperfections (aberrations) of the lenses usually hinder the real value.

When an electron beam hits the specimen, it can interact in different ways, generating signals presented in the Figure 2.1.1.

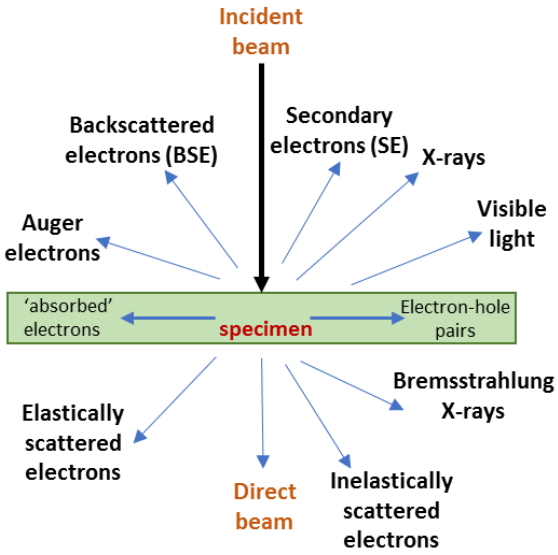

Figure 2.1.1 Possible signals generated after electron-specimen interaction (based on ref. 128).[128]

Some of these signals are used to define the topography and morphological properties of the sample (secondary electrons, elastically scattered electrons) and some are giving information about sample composition and crystallinity (X-rays, BSE Auger electrons, inelastically scattered electrons and Bremsstrahlung X-rays).

In the present work, two types of electron microscopes were used: scanning electron microscope (SEM) and transmission electron microscope (TEM). The main difference between them lies in the nature of the collected signals, as for SEM the image is constructed from 'reflected' electrons and 'transmitted' electrons are used for TEM imaging (Figure 2.1.2).

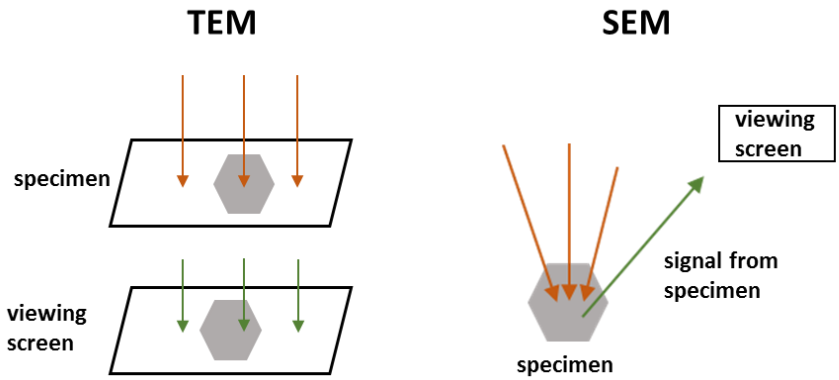

Figure 2.1.2 Signals collected for generating TEM and SEM images (based on ref. 129).[129]

SEM operates by scanning an electron beam across the sample surface. The region over which incident electrons interact with the sample is known as interaction volume which is schematically presented in the Figure 2.1.3.

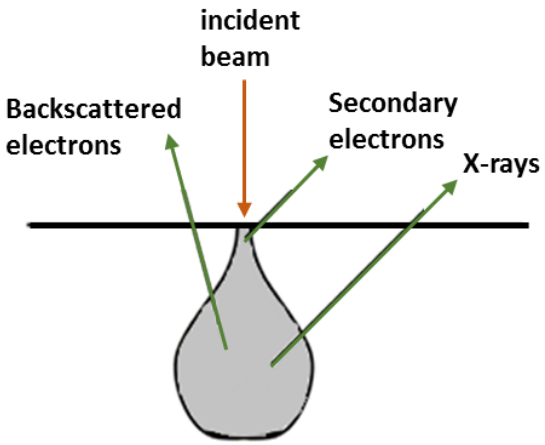

Figure 2.1.3 Signals generated after electron beam-sample interaction typical for SEM (based on ref. 130).[130]

The electron from the beam interacts with an atom in the sample in different ways, as shown in Figure 2.1.4.

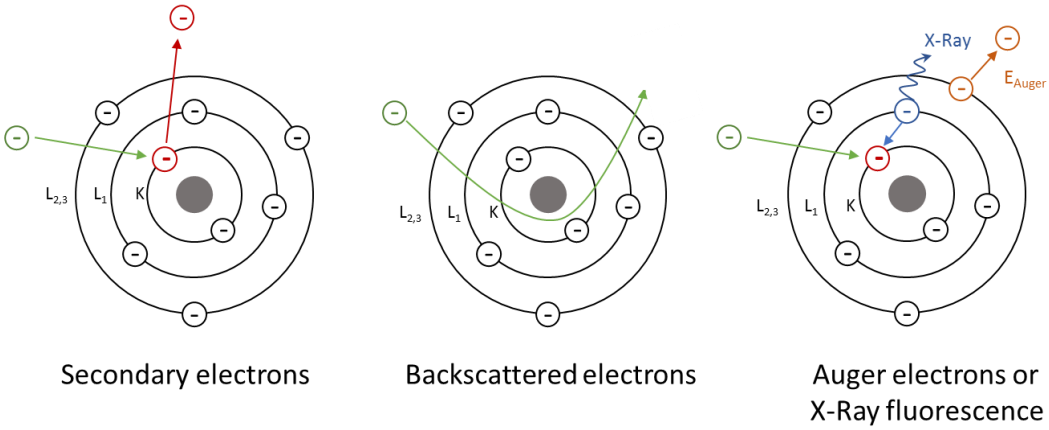

Figure 2.1.4 Electron beam-atom interactions.

Firstly, topographic information of the sample can be obtained from low-energy secondary electrons, which are ejected from the surface of the sample after the collision with the electrons from the beam. For optimal morphology information, a low acceleration voltage must be applied (2-5 keV), so all the electrons generated come from the most external atoms of the sample. Secondly, backscattered electrons are originated when some electrons from the beam are diverted by the atom nuclei, so their signal strongly depends on the atomic number. Therefore, this signal is mostly used to distinguish elements with different atomic weight in the sample, which is especially useful in analysing composites, although the resolution and contrast is usually not high. Moreover, some of the holes produced when the electrons are ejected in the secondary electron processes can be filled by electrons from the same atom with higher energies, thus producing X-rays during the electronic promotion with the characteristic energies of the atoms. This is the base of energy-dispersive X-ray spectroscopy (EDX), which can be used for qualitative analysis of the sample composition and also mapping distribution of the elements.[130]

In contrast, in TEM the electron beam interacts with the atomic nucleus and surrounding electron clouds (in a very thin sample) and the electrons are scattered, which lead to the formation of the TEM image (2D projection of a 3D specimen) and diffraction pattern.[128] These scattering events are controlled by many factors such as incident energy, atomic number, sample thickness and crystallinity.

The incident electrons can be scattered without changes in their kinetic energy (elastic scattering) or their kinetic energy after interacting with the sample might be different than initial (inelastic scattering) (Figure 2.1.1). Moreover, the transmitted electrons can remain in phase with each other (coherent) or they have no relationship (incoherent) after interaction with the specimen.[128] The nature of the scattered electrons depends on the angle at which they are scattered and the signals can be selectively collected by changing the microscope aperture and the "collection" detection.[128]

Diffraction pattern obtained from TEM is called selected area diffraction pattern (SAED), because it is strongly localized, which means that only the atoms which are in the "selected" part of the sample diffracts the electrons, if Bragg's condition ($n\lambda=2d\sin\Theta$, Subchapter 2.4) is satisfied. Moreover, electrons have a much shorter wavelength than X-Rays ($d << \lambda$), so the Bragg's law can be written as $n\lambda = 2d\Theta$.[128]

In the present work, SEM images were acquired using a Zeiss Ultra Plus field-emission microscope equipped with a Gemini® column and a secondary electron detector, working at acceleration voltages in the range of 2-5 keV. Samples were deposited by drop casting on an aluminium holder. TEM images were taken using a FEI Titan microscope operated at accelerating voltages of 100 or 80 keV. Samples were dropped onto 200 mesh copper TEM grids coated with Lacey Formvar Carbon. Aberration-corrected STEM imaging was performed using a NION Ultra STEM 200 which operates at 200 kV with a Bruker windowless EDX detector. EDX analyses were performed with the microscopes operating at 15 kV (SEM), 100 or 80 kV (TEM) and 200 kV (NION). TEM analyses are credited to Christopher Hobbs, while aberration-corrected STEM imaging was performed by Clive Downing.

TEM and STEM images were analysed by Digital Micrograph (DM Software) and the TEM-EDX by Analyses TIA (ES Vision); STEM-EDX and SEM-EDX were analysed by Bruker - ESPRIT 2.0.

2.2 Atomic force microscopy

Atomic force microscopy (AFM) was used to obtain a thickness profile of the samples by utilizing atomic interactions between the measurement tip and the sample surface.[131] AFM can operate in contact mode, where the scanning tip is in contact with the sample surface leading to strong interactions and at intermittent (tapping) mode, where molecular orbitals of the sharp tip and the surface overlap and interact

electrostatically. In the presented work tapping mode was used to avoid sample/tip damages. The tip is attached to the flexible cantilever spring, which bends under the influence of a nearby surface. This bending is measured by a laser beam which is transmitted to and reflected from the cantilever. The reflected laser beam is detected with a position-sensitive photodetector which is schematically presented in the Figure 2.2.1.

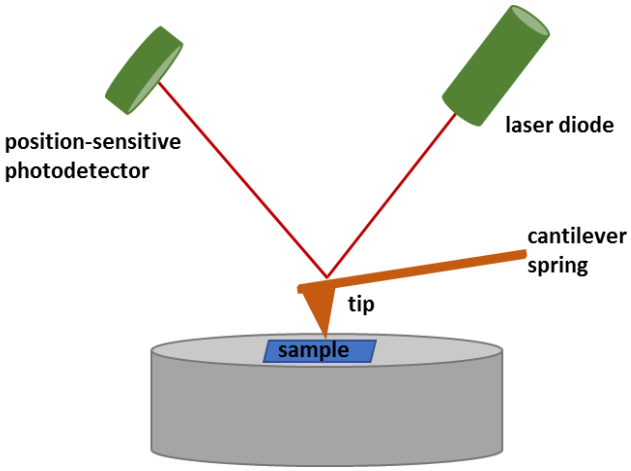

Figure 2.2.1 Schematic diagram of AFM (based on ref. 131).[131]

In all oscillating modes, the cantilever is oscillated with an additional piezoelectric element at its resonant frequency and when the oscillating probe approaches the sample, the oscillation changes because of the interaction of the probe and the force field from the sample. This affects the cantilever oscillation and results in a reduction of the frequency and amplitude, while the oscillation is monitored by the force transducer which keeps the tip-sample distance at the constant level. In the presented work, intermittent contact mode was used, where a large oscillation amplitude was applied which led to the tip-sample interactions passing from the "zero-force" regime through the attractive regime and to "repulsive regime", as schematically presented in the Figure 2.2.2.

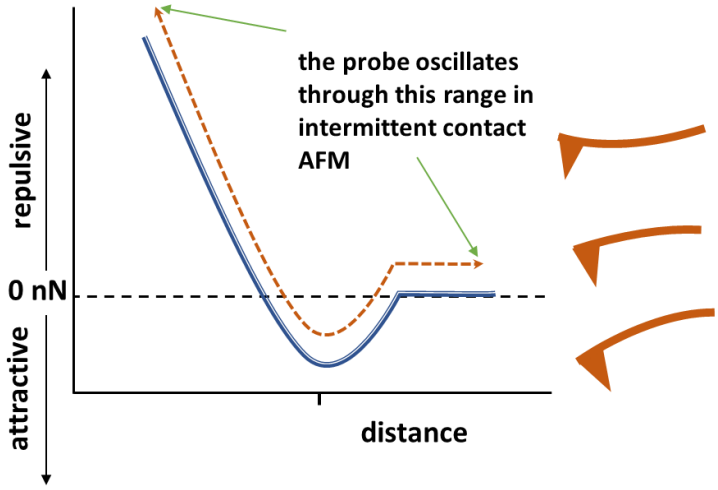

Figure 2.2.2 Intermittent-contact operating regime (based on ref. 132).[132]

The electrostatic interactions of the tip and the sample's surface change the resonance frequency, which influence the phase and the amplitude of the oscillation. The feedback system of the AFM controller uses the amplitude to control the cantilever oscillation at a constant value and by registering those changes the high profile is obtained.

AFM images were taken on an Asylum Research MFP 3D microscope working in a tapping mode. A silicon tip coated with aluminium from Budget Sensors and a nominal resonant frequency of 300 kHz was used. The images were acquired under ambient conditions at 22 °C with a scanning rate of 1 Hz. The data were processed with Gwyddion software.

2.3 Infrared Spectroscopy

Infrared spectroscopy (IR) is a technique which uses the vibrations of the bonds between atoms of a molecule to identify its chemical structure. In this method infrared radiation (14000 - 10 cm^{-1}) is passed through the sample and a fraction of this radiation is absorbed at specific frequencies which correspond to the respective vibrational frequencies of the bonds present in the sample.[133]

In infrared spectroscopy, when the molecule or it's component absorbs electromagnetic radiation, the molecule's energy level is changed to another quantized discrete energy level, which is schematically shown in the Figure 2.3.1.[134]

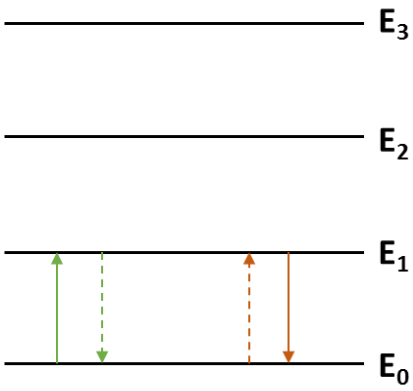

Figure 2.3.1 Illustration of quantized discrete energy level in the atom/molecule.

When the energy level is changed, a quantum of energy is emitted or absorbed and it is equal to

$$\Delta E = h\upsilon \qquad \textbf{Eq. 2.3.1}$$

Infrared absorption occurs only for molecules which change dipole moment during the vibration.[133] The molecule containing N atoms has 3N degrees of freedom in which 3 are translational and the other 3 are degrees of rotational freedom (for non-linear molecules; for linear molecules there are only 2 rotational degrees of freedom). Accordingly, there are 3N-6 or 3N-5 degrees of vibrational freedom for non-linear and linear molecules respectively.

The molecule absorbs IR radiation only when its frequency is the same as one of the fundamental modes of vibration of the molecule, which can be expressed as:

$$\upsilon = \left({}^{1}/_{2}\,\pi\right)\sqrt{\left({}^{k}/_{\mu}\right)} \qquad \textbf{Eq. 2.3.2}$$

where k is force constant (from Hook's law) and μ is a reduced mass. Therefore, a certain molecule absorbs IR light at specific frequencies and has its unique spectrum.

In a conventional Fourier Transform infrared spectroscopy (FT-IR) the light transmitted from the sample embedded in KBr is measured. However, this method is obsolescent nowadays, due to the emergence of methods that allow the direct measurement into the neat sample (reflectance techniques). FT-IR reflection techniques can be classified as internal - Attenuated Total Reflection (ATR), external - Specular Reflection) and a combination of both internal and external reflection - Diffuse Reflection (DRIFTs).[135] ATR method was used in a presented work.

In ATR technique, crystals with very high refractive index, such as Ge or ZnSe are in an optical contact with the sample. When the incident beam hits the ATR crystal at a certain angle, total internal reflection takes place (as presented in the Figure 2.3.2), but some part of this reflected light is absorbed by the sample leading to weakening this signal which is then used to construct the spectrum of the analysed material.

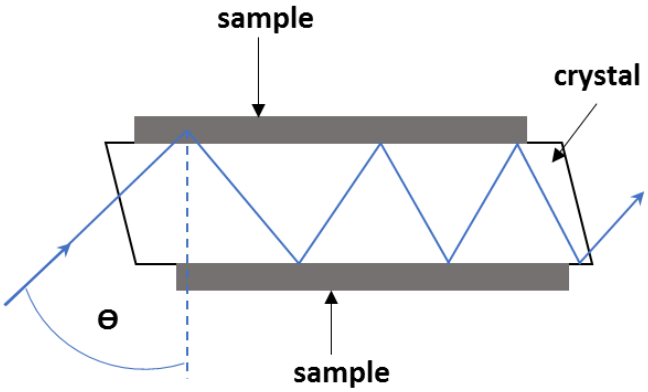

Figure 2.3.2 Schematic representation of ATR technique (based on ref. 133).[133]

In this work, FT-IR spectra were recorded in the range of 4000–550 cm^{-1} using a Perkin Elmer Spectrum 100 FT-IR spectrometer. Measurements were carried out by ATR method on the neat samples directly.

2.4 X-Ray diffraction

X-Ray diffraction is a technique broadly used to determine the crystallinity and composition of a sample. Crystals are regular arrays of atoms and they all have their characteristic interplanar distance (d), so the constructive diffraction only occurs at the certain wavelengths and incident beam angles (Θ) defined by the Bragg's law, schematically presented in the Figure 2.4.1.[136]

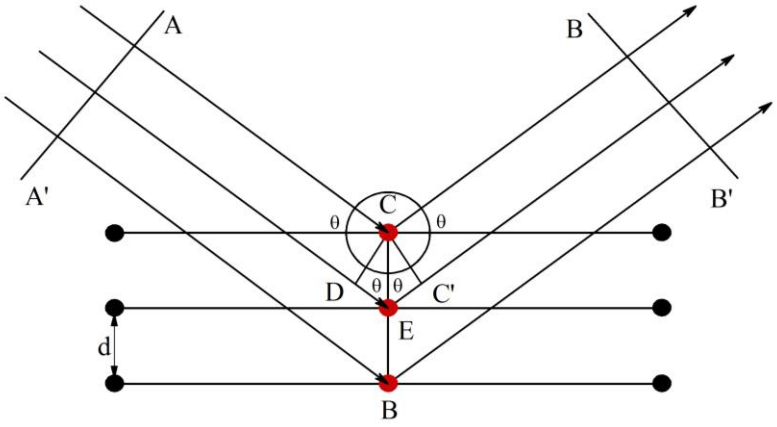

Figure 2.4.1 Schematic representation of the Bragg's law (based on ref. 136).[136]

First of all, the angle of the incident and reflected beam are the same and also the diffracted waves across a wavefront, (AA', BB') are all in phase, so the path lengths between wavefronts AA' and BB' differ by an integral (n) of wavelengths λ:[136]

$$\delta = n\lambda \qquad \textbf{Eq. 2.4.1}$$

Following this requirement, CC' and CD are wavefronts as well, so by simple trigonometry it is possible to define δ as:

$$\delta = DE + EC' = 2CE\sin\Theta \qquad \textbf{Eq. 2.4.2}$$

CE corresponds to interplanar distance, d, so when substituted giving:

$$\delta = 2d\sin\Theta \qquad \textbf{Eq. 2.4.3}$$

which in combination with Equation 2.4.1 gives the final form of the Bragg's law:

$$\mathbf{n\lambda = 2d\sin\Theta} \qquad \textbf{Eq. 2.4.4}$$

The positions of the diffraction peaks are determined by the distance between parallel planes of atoms and the Bragg's law determines where the constructive interference from X-rays scattered by those planes give rise to signals. Planes of atoms are described by Miller indices (hkl) and the d-spacing (d_{hkl}) is the vector extending from the origin to this plane (hkl) and is normal to (hkl). Moreover, d_{hkl} is a geometric function of the size and shape of the unit cell, so from the XRD measurement lattice parameters and crystal geometry can be calculated. It also gives information about the sample purity and phase composition, as all crystalline materials have their own unique

atomic arrangement, so their diffraction pattern is characteristic for the certain compound. Furthermore, by measuring the peaks broadening the crystallite size can be estimated.[137]

In the presented work Powder XRD was measured in a Bruker Advance Powder X-ray diffractometer equipped with a molybdenum-Kα emission source (λ= 0.7107 Å) in the Bragg-Brentano configuration. The finely ground samples were deposited in the XRD holder.

2.5 Inductively Coupled Plasma - Optical Emission Spectrometry

Inductively Coupled Plasma - Optical Emission Spectrometry (ICP-OES) is used to qualitatively and quantitatively analyse the sample. This method relies on measuring electromagnetic radiation which is absorbed or emitted from the elements in the material, so the sample molecules have to be firstly transformed to free atoms and then excited (nowadays this step is achieved by applying an inert gas plasma).[138] The qualitative information is obtained from the wavelengths at which the electromagnetic radiation is absorbed or emitted, while the quantitative analysis is given from the amount of this radiation.

To understand how ICP-OES works it is important to recall the Bohr model of an atom which is schematically presented in the Figure 2.5.1. Briefly, an atom consists of a positively charged nucleus surrounded by negatively charged electrons which are travelling on orbitals with certain energy.

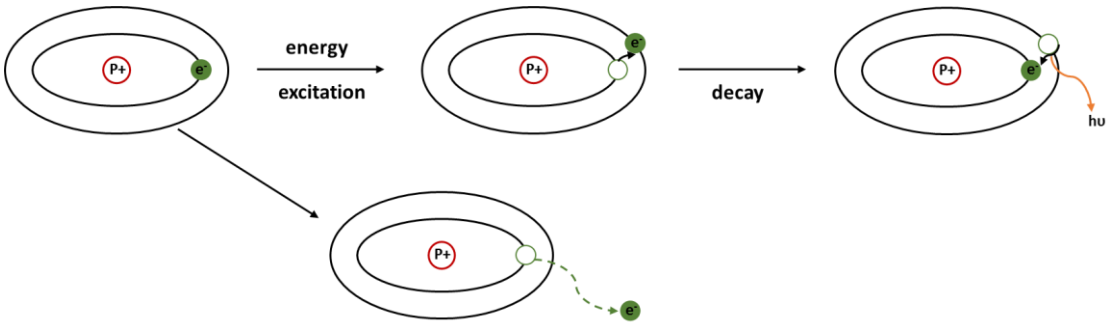

Figure 2.5.1 Schematic Bohr model of atom and possible electron excitation/decay process (based on ref. 139).[139]

When electromagnetic radiation is absorbed by the atom, an electron can be excited to the orbital with higher energy (excited state), which is unstable and

eventually decays back to the lower energy level by the emission of photon (hυ) whose wavelength is characteristic of each element. It also can happen, when the energy absorbed by an atom is high enough (known as ionisation potential), that an electron is completely dissociated from the atom leaving an ion with a net positive charge. This ion also has ground and excited states, so it can absorb and emit energy by the same excitation and decay processes as an atom.[139]

In this work, ICP-OES characterization was conducted using a Thermo Elemental IRIS intrepid spectrometer. Samples dispersed in water were bath sonicated for 10 min, and then dissolved in HCl to a concentration of 1 $mgml^{-1}$. The metal content was calculated by comparison with the calibration curves of the reference standards.

2.6 Elemental analysis

Elemental analysis gives quantitative information about the H, C and N content in the sample which allows to verify its molecular formula. In this technique, the sample is burned at very high temperature under excess of oxygen and the resulting combustion gases are analysed. Firstly, NO_x are reduced to N_2 with Cu powder, and subsequently the gases go to detectors and, on the basis of their amount, the percentage of the elements in the sample is calculated.[140]

In this work, HCN elemental analyses were carried out using an Exeter Analytical CE 440 elemental analyser. The samples were combusted in oxygen enriched helium (temperatures up to 1600 ^oC) and the percentage content was calculated by comparison with the reference standards.

2.7 Thermogravimetric analysis

Thermogravimetric analysis (TGA) is a technique in which the mass changes are monitored with respect to temperature and provides information about sample thermal stability and the percentage of volatiles (such as moisture) in the same. In TGA, the temperature is usually increased continuously with time while the sample weight changes are examined.[141] Thermal analysis can be performed in different atmospheres- under air which might result in sample oxidation or under inert gas.

TGA analyses were carried out using a Perkin Elmer Pyris 1 TGA, which had previously been calibrated with nickel and iron standards. Approximately 10 mg of

finely ground powder of the sample was heated to 850 °C (rate 5 / 10 °C min^{-1}) under air / N_2 atmosphere.

2.8 Ultraviolet–visible spectroscopy

Ultraviolet-visible spectroscopy (UV-Vis) was used for quantitative and qualitative analysis of the samples and also to estimate the band gap of semiconducting compounds. In this technique, light with higher electromagnetic radiation energy than IR but lower than X-Ray is used, typically 100-900 nm.

The total energy of a molecule (E_{tot}), can be expressed as:

$$E_{tot} = E_{elec} + E_{vib} + E_{rot} \qquad \textbf{Eq. 2.8.1}$$

where E_{elec} is electronic energy, E_{vib} is vibration energy, E_{rot} is rotation energy and $E_{elec} > E_{vib} > E_{rot}$.[140] Changes measured by UV-Vis are much more significant than IR, since UV-Vis can affect the electronic structure of the molecule. The most probable transition happens from the highest occupied molecular orbital (HOMO) to the lowest unoccupied molecular orbital (LUMO).[140] Electronic energy levels and possible transitions are presented in Figure 2.8.1.

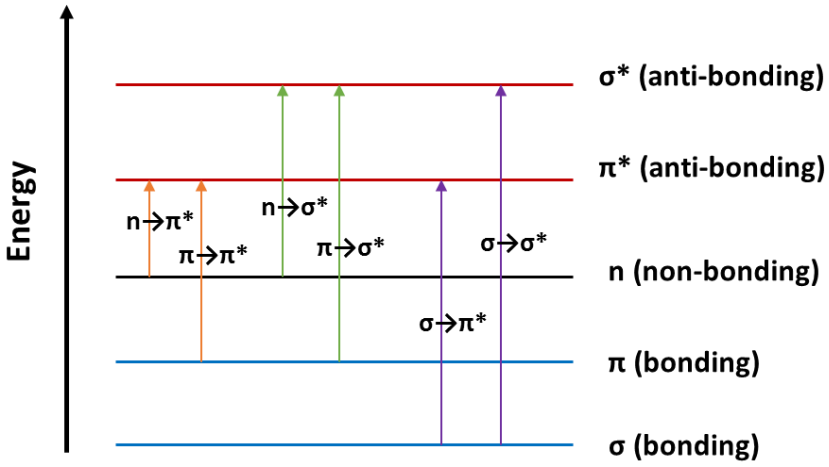

Figure 2.8.1 Electronic energy levels and possible transitions in UV-Vis spectroscopy (based on ref. 142).[142]

To briefly explain the diagram shown in the Figure 2.8.1 for most cases, the lowest occupied molecular orbitals are σ and corresponding σ bonds. Then, at slightly higher energy are π orbitals (π bonds) and then there are non-bonding n orbitals. At the highest energy are unoccupied anti-bonding π* and σ* orbitals. The transitions which

might occur after UV-Vis absorption are: n → π*, n → σ*, π → π*, π → σ*, σ → π*, σ → σ*. However, not all transitions are allowed and only when spin quantum number remains unchanged, the transitions are possible.[142]

UV-Vis spectroscopy can be used for both qualitative and quantitative analysis. Qualitative analysis is possible due to specific transitions characteristic of a certain compound, while quantitative analysis is made on the basis of Bouguer-Lambert-Beer law (Eq. 2.8.2).

$$A = \varepsilon l c \qquad \textbf{Eq. 2.8.2}$$

where A is absorbance, ε is the extinction coefficient (characteristic for the compound and solvent), l is the length of the sample cell and c is the sample concentration.[140]

Moreover, since UV-Vis spectroscopy measures electronic transitions, this technique can be also used to estimate the band gap in semiconducting materials by measuring the energy required to excite the electron from valence to conduction band.[108]

It is worth noting that the measurement of the UV-Vis spectrum of suspension samples is complicated because of the light scattering due to the particles in the solution, which prevents all light from reaching the detector.[143] To improve the detection of light, an integrating sphere which allows the absolute measurement of transmittance or reflectance can be used. The inside walls of an integrating sphere are coated with a material which distributes light evenly (Lambertian diffuser). The sphere has an entrance and symmetrically located sample and reference ports all centered on a great circle of the sphere. The exact position of the ports depends on the angle of incidence for which the reflectance and transimttance are determined, which is easily changed by rotating the sphere.[144] Thus, the absorbance of a dispersion of nanomaterials can be measured by the use of an integrating sphere.

The extinction spectrum (sum of absorbance and scattering) is measured without the use of the integrating sphere. The scattering spectrum can be calculated as the difference between extinction and absorbance.

In this work, UV-Vis measurement were conducted in the range of 200-900 nm using a Biochrom Libra S22 UV/Vis Spectrophotometer. To estimate the band gap, optical absorbance was measured from 220 to 800 nm on a Perkin Elmer 650 spectrometer using an integrating sphere.

2.9 Photoluminescence Spectroscopy

Luminescence is the phenomenon which occurs when electronically excited electrons emit photons when coming back to the ground state.[145] When the electrons are excited form the ground state (S_0) they can go to the singlet excited state (S_1) or to the triplet excited state (T_1) and depending on the excitation state of the photon, emission can be called fluorescence and phosphorescence respectively, as schematically shown in Jablonski diagram presented in the Figure 2.9.1.

To briefly explain, in a singlet excited state (S_1) the electron on the higher energy level has opposite spin orientation as the electron on the lower energy level (they are called paired), and when this excited electron is coming back from singlet excited state to the ground state it emits light known as fluorescence. On the other hand, when the electron is excited to a triplet state, its spin orientation is the same as the electron on the lower energy level (unpaired), so when it returns to the ground state, change in spin orientation is required and this light emission is called phosphorescence.[145]

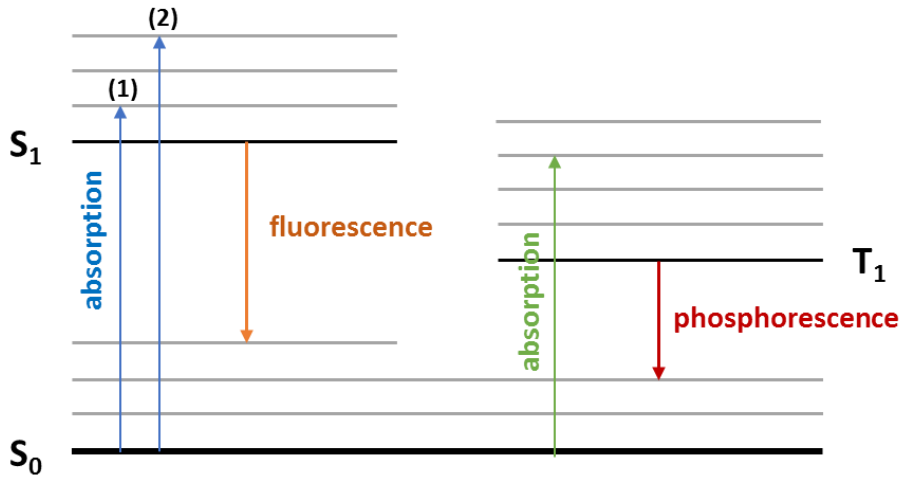

Figure 2.9.1 Joblonski diagram (based on ref. 146) representing difference between fluorescence and phosphorescence.[146]

The energy of the emitted light corresponds to the energy difference between excited and ground states.[147] The most common transition in semiconducting materials is between valence band and conduction band, thus photoluminescence spectroscopy (PL) gives a direct measure of the band gap. Moreover, direct and indirect semiconductors can be distinguished by PL due to the energy differences between photon and phonon emitted by semiconducting materials with direct and indirect band gap respectively.[108]

Photoluminescence of the sample was measured in quartz cuvettes using an Edinburgh Instruments FS920 PL spectrometer equipped with a xenon lamp (450 W) and a S900 photomultiplier tube detector. The contour plot was measured at room temperature using single monochromators to record the excitation and emission.

2.10 X-Ray Photoelectron Spectroscopy

X-Ray Photoelectron Spectroscopy (XPS) is a non-destructive, highly sensitive technique used to analyse the surface of solids, which provides information about the identity of the elements that comprise the sample and their chemical environment (bonding).[148] The fundamental principle of XPS is the photoelectric effect, schematically presented in the Figure 2.10.1.

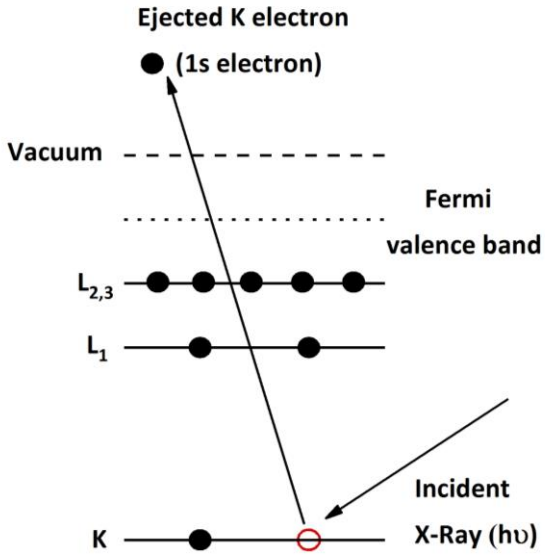

Figure 2.10.1 Schematic of the XPS process showing the ejection of a 1s electron after interaction with X-Ray (based on ref. 149).[149]

When X-Ray photons are absorbed by the atoms in the surface of the sample, their electrons can be ejected from the sample and emitted as photoelectrons, whose kinetic energy (E_k) can be measured by the XPS detector and is described by the following equation:

$$E_k = h\upsilon - E_B - \phi \qquad \textbf{Eq. 2.10.1}$$

where $h\upsilon$ is energy of the incident photon, E_B is the electron binding energy and ϕ is the work function (a correction factor of the instrument).[149] Since $h\upsilon$ and ϕ are known, the

binding energies can be easily calculated from the measured E_k by using the Equation 2.10.1. The XPS spectrum usually plots the binding energy of the electrons ejected from the surface without energy loss (X-axis) versus the counts per second (Y-axis) and is a fingerprint of the solid surface, providing information about the composition and the purity of the sample. Every element in the sample can be identified due to the set of peaks produced at the characteristic binding energies of its electrons.[149] Moreover, due to the high sensitivity of this technique, the different chemical environments of an element can be also determined by the deconvolution of the peaks which correspond to their outer orbitals.[109]

In the present study, XPS spectra were acquired using monochromated Al Kα X-rays from an Omicron XM1000 MkII X-ray source and an Omicron EA125 energy analyzer. The analyzer pass energies were 15 eV for the core-level spectra and 100 eV for the survey spectra. For charge compensation, an Omicron CN10 electron flood gun was used. After subtraction of a background, the core-level spectra were fitted with Gaussian–Lorentzian line shapes using the CasaXPS software.

2.11 X-ray fluorescence spectrometry

X-ray fluorescence is a non-destructive analytical method used to qualitatively and quantitatively determine the composition of the sample for elements between Si (Z=14) and U (Z=92). Similarly to XPS (Subchapter 2.10), the main principle of XRF is the photoelectric effect. However, in the case of XRF, the measured signal is the fluorescence of the sample (Subchapter 2.9).[140]

As described in Section 2.10, after sample-X-ray interaction, an electron from the inner shell is ejected, which leads to the ionization of the atom. To return to its ground state, the gap created in the core level can be filled by an electron from an outer shell, with the subsequent emission of a photon which has an energy equivalent to the energy difference between the inner and the outer shell (X-ray fluorescence radiation) presented in Figure 2.11.1 a. Noteworthy, the emitted photon might transfer its energy to another electron, which is then expelled (so-called Auger effect- Figure 2.11.1 b).[109]

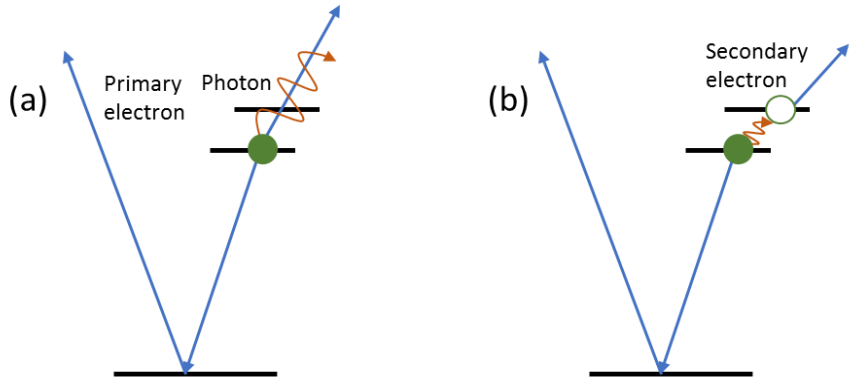

Figure 2.11.1 Schematic representation of a) photon emission and b) Auger effect (based on ref. 109).[109]

There are several types of XRF systems, such as: a wavelength-dispersive (WD-XRF), energy dispersive (ED-XRF), thickness/microspot XRF, handheld XRF, and total reflectance XRF (T-XRF),[140] which was used in the presented work. In T-XRF, the X-ray beam hits the surface of the sample at a very small glancing angle (< 0.1°),[150] which results in the total reflection of the X-rays,[151] thus leading to the enhancement of the signal-to-noise ratio.

T-XRF analysis was performed with a S2 PicoFox TXRF spectrometer from Bruker Nano GmbH, equipped with a molybdenum X-ray source working at 50 kV and 600 μA, a multilayer monochromator with 80% of reflectivity at 17.5 keV (Mo Kα), a XFlash SDD detector with an effective area of 30 mm^2 and an energy resolution better than 150 eV for Mn Kα. Cobalt was used as an internal standard.

2.12 Nuclear magnetic resonance

Nuclear magnetic resonance (NMR) is a spectroscopic technique mainly used for the elucidation of molecular structures, although it can also be used for quantitative, kinetics and thermodynamic studies. This technique is based on the ability of certain atomic nuclei (those with a magnetic moment distinct of zero) to absorb radiation in the radio-frequency region. Since the frequency of the absorbed radiation depends on the chemical environment of the atom, the number of magnetically distinct atoms and their associated chemical environment within a molecule can be determined.[140, 142]

The nuclear spin is a quantized property of the atom, and the number of possible spin states is 2I+1, (I is a nuclear spin quantum number). In the presence of an external magnetic field (B_0), the spins of the atomic nuclei align either in the same or the

opposite direction as the B_0. In these conditions, the spin states are not equivalent in energy and those aligned with the B_0 have a smaller energy and, for this reason, these states are slightly more populated.[142]

In modern NMR, the sample (in solution) is excited with a multi-frequency pulse of a very short duration. Usually, the range of used frequencies excites the whole range of frequencies of a certain nuclei (for example ^1H) to the upper energy spin situation (Figure 2.12.1). Then, these excited atoms return to their lower energy state by emitting energy with a frequency equal to the difference in energy between their upper and lower energy levels. The radiation emitted during the relaxation processes is measured by the NMR spectrometer and turned into frequencies by applying the Fourier Transform.

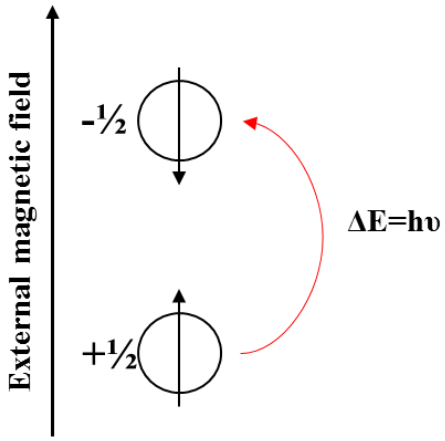

Figure 2.12.1 NMR absorption process for the proton (based on ref. 142),[142] a spin change after interaction with electromagnetic radiation.

The great versatility of NMR spectroscopy relies on the different resonant frequencies of the atoms with a different electronic environment, as valence-shell electron density varies from one atom to another depending on its chemical bonding, leading to shielding or deshielding the nucleus.[140] This shielding/deshielding effect is quantified by the shielding constant (σ), which connects the effective field reaching the nucleus (B_{eff}) and the external field (B_0) by Equation:

$$B_{eff} = B_0(1-\sigma) \qquad \textbf{Eq. 2.12.1}$$

The changes in the resonant frequency of the nucleus results in the phenomena called chemical shift. The different chemical environment (for example, ^1H in alkanes,

alkynes of aromatic molecules) present a different chemical shift, which allows the determination of the structure of the sample.[140]

Another important phenomena in NMR is the spin-spin splitting, which can be empirically explained by n+1 rule. In the molecule, each proton "senses" the number of the equivalent protons (n) bonded to the carbon atoms next to the one where the examined proton is bonded. As a result of this "sensing" its resonance peak is split in (n+1) components.[142]

In the present work, ^{1}H and ^{13}C NMR analyses were performed using Bruker Avance HD 400 NMR with BBFO probe (Broad Band Probe for observation of the nuclei from ^{31}P to ^{15}N and ^{19}F). Samples dissolved in D_2O with concentration of 10 $mgml^{-1}$ and 50 $mgml^{-1}$, for ^{1}H and ^{13}C respectively, were analysed and the data were processed by TopSpin software.

2.13 Gas absorption and BET

Physical gas absorption on the solid surface is used to determine the specific surface area of materials by applying BET theory. Generally, the amount of the adsorbed gas depends on temperature (T), pressure (p) and the interaction potential (E). The interactions between gas and solid surface can be both chemical and physical. Chemical interactions consist of bonds formation between gas (adsorbate) and solid (adsorbent) which results in irreversibility of this process. By chemisorption, the surface is covered by a single layer of adsorbate and activation energy is required to form chemical bonds. In contrast, physical adsorption does not make changes in an adsorbent surface and it is fully reversible. Differently to the chemisorption, physisorbed gas can form more than one layer.[152] As bond formation typically requires an activation energy, the measurements are performed at low temperature where only physisorption occurs.

Stephen Brunauer, Paul Hugh Emmett, and Edward Teller proposed a model (known as BET) which describes that the amount of a gas adsorbed (v) on a solid surface can be given by:

$$v = \frac{v_m c p}{(P_0 - P)[1+(c-1)\left(P/P_0\right)]} \qquad \textbf{Eq. 2.13.1}$$

where P/P_0 is the relative pressure, v and v_m correspond to the weight of the gas adsorbed and weight of the adsorbate respectively and c is a BET constant.

Taking into account that $P/v(P_0-P)$ against P/P_0 has a linear trend,[153] Eq. 2.13.1 is usually written as:

$$\frac{P}{v(P_0-P)} = \frac{1}{v_m c} + \frac{c-1}{v_m c}\frac{P}{P_0} \qquad \textbf{Eq. 2.13.2}$$

which results that:

$$Slope = \frac{c-1}{v_m c} \qquad \textbf{Eq. 2.13.3}$$

$$Intercept = \frac{1}{v_m c} \qquad \textbf{Eq. 2.13.4}$$

leading to simple calculation of v_m and c from the graph

$$v_m = \frac{1}{Slope+Intercept} \qquad \textbf{Eq. 2.13.5}$$

known as *Multi-Point BET*.

To further simplify, the intercept is ignored due to its small value (known as *Single-Point BET*), and the Eq. 2.13.2 is expressed:

$$v_m = v(1 - \frac{P}{P_0}) \qquad \textbf{Eq. 2.13.6}$$

Once the volume of the gas adsorbed is known, and knowing that the volume of a mole of gas (STP) is $22.4 \cdot 10^{-3}$ m^{-3}, the total surface area of the solid can be calculated from:

$$S_t = \frac{v_m N \sigma_a}{m \cdot 22.4 \cdot 10^{-3}} \qquad \textbf{Eq. 2.13.7}$$

where N is Avogadro's number, σ_a is adsorbate cross sectional area and m is mass of the adsorbate. Then a specific surface area is obtained by dividing S_t by the sample's weight.[152]

In presented work BET isotherms were acquired in a Quantachrome Nova 4200e station using nitrogen at 77 K. The specific surface area was obtained by applying the BET equation to the linear portion of the isotherm curves. All samples were outgased in a nitrogen atmosphere at 100 ^oC for 16 hours before the measurements.

Materials used in the syntheses

Aluminium nitrate nonahydrate ($Al(NO_3)_3 \cdot 9H_2O$, ≥ 98 %), aluminium chloride hexahydrate ($AlCl_3 \cdot 6H_2O$, 99 %), isopropyl alcohol-IPA (C_3H_8O, ≥ 99 %), hydrochloric acid (HCl, 37 %), sodium chloride (NaCl, ≥ 99.5 %), hexamethylenetetramine-HMT ($C_6H_{12}N_4$, ≥ 99 %), ethylene glycol-EG ($C_2H_6O_2$, ≥ 99.8 %), sodium hydroxide (NaOH, ≥97 %), sodium nitrate ($NaNO_3$, ≥99 %), iron(III) nitrate nonahydrate ($Fe(NO_3)_3 \cdot 9H_2O$, >98 %), citric acid trisodium salt anhydrous-TSC ($Na_3C_6H_5O_7$, 99 %), triethanolamine-TEA ($C_6H_{15}NO_3$, >99 %) gallium(III) acetylacetonate ($Ga(acac)_3$, > 99 %), sulfur (S, >99 %), selenium (Se, 99.5 %), hexadecylamine ($CH_3(CH_2)_{15}NH_2$, technical grade - 90%), dodecylamine ($CH_3(CH_2)_{11}NH_2$, 98%), toluene ($C_6H_5CH_3$, 99.8%, anhydrous), diphenyl disulphide-Ph_2S_2 ($C_{12}H_{10}S_2$ >99 %), debenzyl disulfide ($C_{14}H_{14}S_6$, 98%), diisopropyl disulfide ($C_6H_{14}S_2$, 96 %) and tellurium (Te, 99.8 %) were purchased from Sigma Aldrich.

Magnesium nitrate hexahydrate ($Mg(NO_3)_2 \cdot 6H_2O$, 99 %), ammonia solution (NH_3aq, 25 %) and magnesium chloride hexahydrate ($MgCl_2 \cdot 6H_2O$, 99 %), were purchased from Merk.

Urea (CH_4N_2O, ≥ 99.3 %) was ordered from Alfa Aesar.

Nickel(II) nitrate hexahydrate ($Ni(NO_3)_2 \cdot 9H_2O$, 99 %) was purchased from Fisher.

All chemicals were used as received without further purification. Deionized water was used in the experiments.

3 Synthesis of magnesium-aluminium layered double hydroxides with tailored size and crystallinity for biological applications

The primary aim of this project is the development of efficient methods to prepare Mg_xAl_y LDH nanoplatelets for their further use as a host for plasmid DNA (pDNA). These pDNA-LDH nanohybrids are expected to be applied in bone-repairing therapy. The main properties of the synthesized LDH particles for such application must be a low toxicity (Mg and Al have been selected as M^{2+} and M^{3+}, respectively, to overcome this problem) and also the dimensions in the range of 50-200 nm in order to be uptaken by a living cell in an endocytosis process.[81]

Moreover, it was recently reported that smaller LDH particles (~50 nm) have higher gene capacity than larger ones (>100 nm).[81, 84-87] Furthermore, counter anions which compensate a positive charge of the layers should be easily exchangeable to provide high yield in pDNA intercalation. On this regard, anions such as chloride or nitrate are optimum candidates due to their weaker bonding with the layers compared to the strongly bonded carbonate.[35]

In this Chapter, different methods to produce LDH were explored, which include precipitation at increasing pH (by thermal decomposition of urea or HMT), co-precipitation at fixed pH (at the isoelectric point of the LDH) and precipitation at decreasing pH. Moreover, ion-exchange process to exchange carbonate to chloride is also discussed.

The last part of this Chapter describes the preliminary results in the pDNA intercalation and cell uptake. Plasmid DNA-LDH nanohybrids were prepared from platelets with sizes below 50 nm by three different methods: direct synthesis, reconstruction procedure and ion-exchange. The latter are being currently tested as non-viral vectors for delivery of pDNA in collaboration with Prof. Fergal O'Brien's research group (RCSI).

3.1 Homogenous precipitation of Mg_xAl_y LDH at increasing pH by thermal decomposition of urea and HMT

Homogenous precipitation is a convenient method to obtain LDH based on the *in-situ* generation of the precipitating agent (OH^-) by thermal decomposition of weak bases, like urea (CH_4N_2O) or HMT ($C_6H_{12}N_4$). The hydrolysis of these compounds at elevated temperatures results in the slow release of ammonia, which acts as a source of OH^- (Eq. 3.1.1 and 3.1.2). The slow increase in OH^- concentration results in a slow nucleation rate and the further growth of particles with well-defined shapes and good crystallinity.

$$CH_4N_2O + 3\ H_2O \rightarrow 2\ NH_4OH + CO_2 \qquad \textbf{Eq. 3.1.1}$$

$$C_6H_{12}N_4 + 10\ H_2O \rightarrow 4NH_4OH + 6CH_2O \qquad \textbf{Eq. 3.1.2}$$

During the slow pH increase, the Al^{3+} precipitates first as $Al(OH)_3$, and once Al^{3+} is completely consumed, Mg^{2+} is incorporated within the structure via a dissolution/precipitation mechanism, which results in the formation of Mg^{2+}-Al^{3+} LDH. The urea or HMT hydrolysis rate and therefore the rate of formation of LDH particles can be controlled by the temperature:[154] at lower temperatures less crystal nuclei formation leads to the growth of bigger particles, while at higher temperature, the higher OH^- production leads to the conditions of supersaturation, which cause that more crystals nuclei to be formed and the obtained particles are smaller in size (so-called LaMer theory).[155]

Moreover, the addition of an organic solvent can also be used to inhibit the particles growth via the adsorption of the solvent molecules on the growing surfaces, as will be described later for mixtures of water/ethylene glycol (EG).[154]

As mentioned above, the particle size and the metals ratio can be controlled by changing the reaction temperature, time, solvent polarity and also the nature of the ammonia-releasing agent.[154] In order to check the influence of those parameters on the final particle size and composition, a set of experiments was carried out.

Experimental Section:

The synthesis of Mg_xAl_y LDH was performed according to the recipe described by Adachi-Pagano;[154] the modification of the recipe included a change from urea to HMT and the reaction temperature up to 110 ^oC. Briefly, 10 ml of a solution containing $Mg(NO_3)_2 \cdot 6H_2O$ (0.0075 mol), $Al(NO_3)_3 \cdot 9H_2O$ (0.0025 mol) and urea or HMT (0.1

mol) were diluted in 50 ml of deionised water and then stirred for 30 minutes at room temperature (RT) in a round bottom flask. Then, the flask was immersed in an oil bath at a certain temperature (65 ^{o}C, 80 ^{o}C, 90 ^{o}C, 100 ^{o}C or 110 ^{o}C) and continuously stirred for 24 hours under reflux. Additional samples produced at 90 °C were stirred for 48 and 72 h (in total). After this time, the flask was cooled in a water bath for 30 minutes, and the precipitate was separated by centrifugation (3000 rpm/10 minutes) and washed three times with water. The syntheses were performed at temperatures of 65 ^{o}C, 80 ^{o}C, 90 ^{o}C, 100 ^{o}C or 110 ^{o}C using urea as ammonia source and at 80 ^{o}C, 100 ^{o}C and 110 ^{o}C using HMT. Additionally, the study of the solvent polarity on the size/shape of the particles was performed at 80 ^{o}C, using the same reactants concentration and a mixture of EG and water in ratios 1/1, 2/1 and 4/1 (v/v %) as a solvent.

The pH of the solution was measured by pH-Meter Jenway 3510 previously calibrated by 3 points methods, using buffer solutions (pH of 2, 7 and 10). The elemental formula of the samples was determined based on the metals ratio measured by ICP-OES, CHN content and then related to the general formula of the LDH ($[M^{II}_{1-x}M^{III}_{x}(OH)_2]^{x+}[A^{n-}_{x/n}\cdot yH_2O]^{x-}$).

3.1.1 Temperature effect

3.1.1.1 Synthesis with urea

The materials obtained at temperatures in the range of 80-110 ^{o}C from urea as an ammonia releasing agent are shown in Figure 3.1.1. Well defined flakes with rounded edges and 2-3 μm in diameter were produced at 80, 90 and 100 ^{o}C (Figure 3.1.1 a-c), while smaller, sharp platelets were obtained at 110 ^{o}C (Figure 3.1.1 d), which is in a good agreement with theoretical predictions.[154]

During the study of the reaction temperature effect on the $Mg_xAl_y(OH)_2(CO_3)_{y/2}\cdot nH_2O$ properties, it was observed that urea did not hydrolyse at 65 °C and, therefore, the formation of a precipitate was not observed.

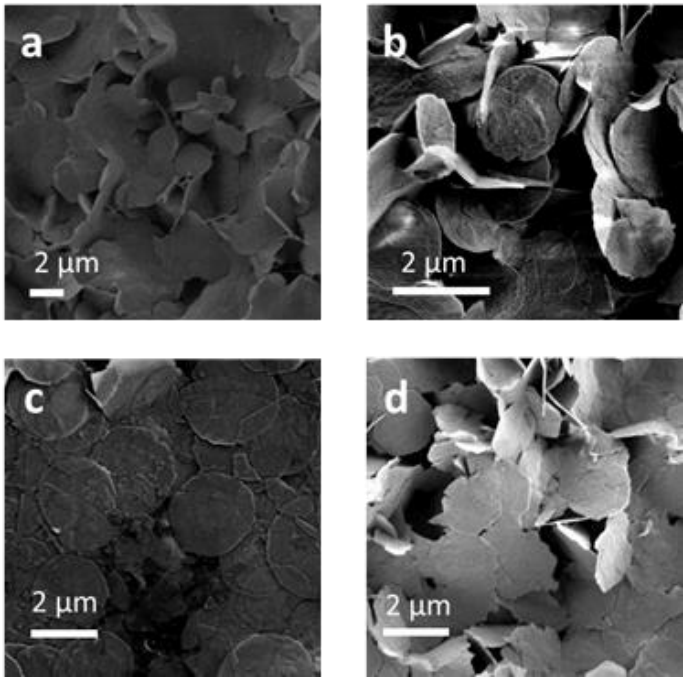

Figure 3.1.1 SEM micrograph of $Mg_xAl_y(OH)_2(CO_3)_{y/2}\cdot nH_2O$ obtained at a) 80 °C, b) 90 °C, c) 100 °C and d) 110 °C.

3.1.1.2 Synthesis with HMT

The nature of the precipitating agent was changed from urea to HMT and the reaction was run at 80 °C, 100 °C and 110 °C for 24 h. The reaction performed at 80 °C did not lead to formation of precipitate, which suggested that this temperature was not high enough to cause the thermal decomposition of HMT.

At 100 °C and 110 °C material made of much smaller platelets with irregular shapes (Figure 3.1.2), in comparison to material obtained when using urea (Figure 3.1.1 c, d) was formed. Those differences in morphology most probably resulted from the higher release of ammonia during thermal decomposition of HMT compared to urea (Eq. 3.1.1 and 3.1.2). This caused a faster increase of the pH of the reaction mixture and thus, an increasing in the nucleation rate, so the flakes precipitated faster forming more crystal nuclei.[156]

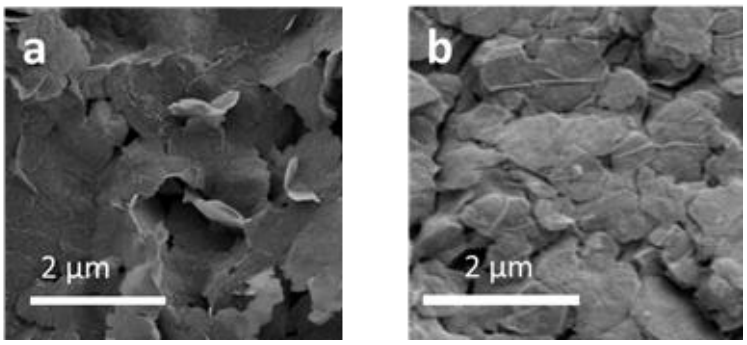

Figure 3.1.2 SEM micrograph of $Mg_xAl_y(OH)_2(CO_3)_{y/2}\cdot nH_2O$ obtained from HMT decomposition at a) 100 ºC and b) 110 ºC after 24 h.

Since much more regular flakes were obtained when using urea, in comparison to HMT, the urea precursor was chosen as a more promising one. Nonetheless, no major differences were observed between the sizes and shapes of the particles at temperatures from 80 ºC to 100 ºC and 90 ºC was set as reaction temperature to study the influence of the reaction time.

3.1.2 Reaction time

Several syntheses were carried out for 24, 48 and 72 hours at 90 °C. SEM images showed that the samples obtained after 24 hours (Figure 3.1.1 b) and 48 hours (Figure 3.1.3 a) were very similar, which is consistent with the results previously described in the literature.[156] However, when the reaction time was extended up to 72 hours (Figure 3.1.3 b) smaller particles were observed, probably due to the breaking of the flakes due to the excess of stirring.

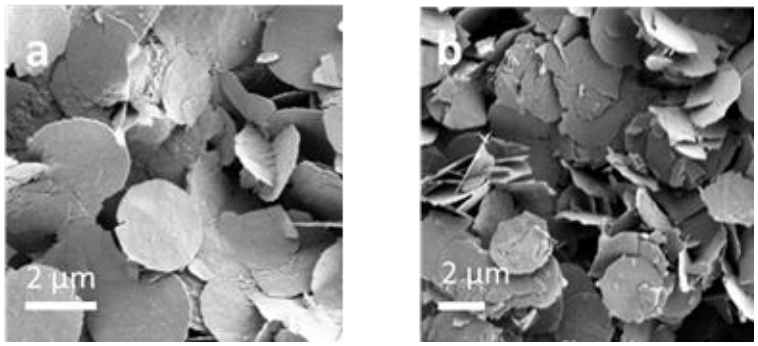

Figure 3.1.3 SEM micrograph of $Mg_xAl_y(OH)_2(CO_3)_{y/2}\cdot nH_2O$ obtained at 90ºC after a) 48 and b) 72 hours.

3.1.3 Encapsulation effect of organic solvents

In order to check the effect of the addition of an organic solvent to the reaction mixture over the particle size, shape and composition, several mixtures of EG and water in ratios 1:1, 2:1 and 4:1 were studied as a solvent.[154] SEM images of the materials obtained in different EG/water ratios are shown in Figure 3.1.4.

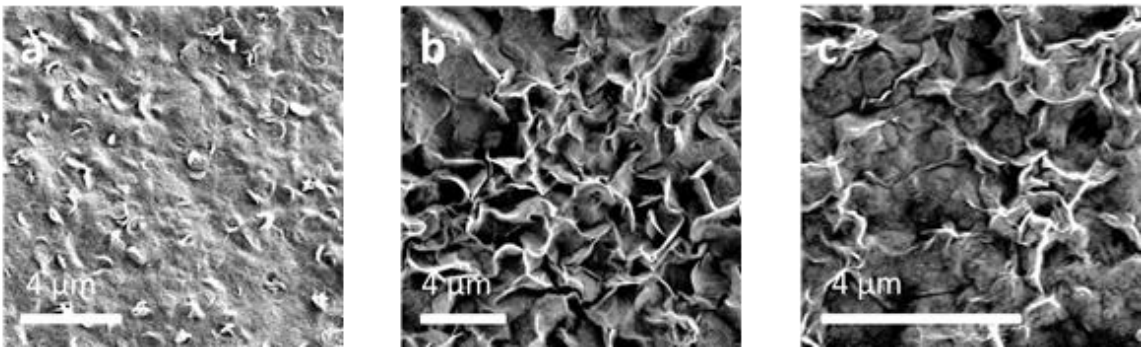

Figure 3.1.4 SEM micrograph of $Mg_xAl_y(OH)_2(CO_3)_{y/2}\cdot nH_2O$ obtained at 80 ºC in a) EG/water (1:1), b) EG/water (2:1) and c) EG/water (4:1).

When comparing these results with flakes obtained in pure water at the same temperature (Figure 3.1.1. a) it was observed that EG addition inhibited the crystal growth of the particles and the size of the platelets was effectively decreased, although those flakes were still bigger than the desired 50-100 nm and their shape was highly irregular. For this reason, no further experiments were carried out using this method.

3.1.4 Compositional and structural characterization

The samples were analysed by ICP-OES in order to obtain the real Mg^{2+}/Al^{3+} ratio of the synthesized materials. Moreover, to check samples purity and homogeneity of the counter anions (carbonate, nitrate), the produced materials were also characterized by elemental analysis. The results, together with pH value after the reaction, are presented in Table 3.1.1.

Table 3.1.1 Composition of the $Mg_xAl_y(OH)_2(CO_3)_{y/2}\cdot nH_2O$ produced by homogeneous precipitation, as obtained by ICP-OES and elemental analysis.

Solvent/ ammonia precursor	**Tempe-rature [^{o}C]**	**Time [h]**	**Mg^{2+}/Al^{3+} (*starting ratio 3:1)**	**pH after reaction**	**C [%]**	**N [%]**
Water/ Urea	**65**	24	-	5.34	-	-
	80	24	**0.0037**	8.11	6.05	0.84
	90	**24**	1.1720	8.31	4.49	0.73
	90	**48**	1.8353	8.22	2.70	0.00
	90	**72**	1.9305	8.33	2.68	0.00
	100	24	1.3513	8.50	4.09	0.11
	110	24	**2.0966**	8.37	2.75	0.00
EG/water (**1:1** v/v %)/ Urea	80	24	0.1686	7.96	5.98	2.37
EG/water (**2:1** v/v %)/ Urea	80	24	0.4884	8.03	5.70	0.83
EG/ water (**4:1** v/v %)/ Urea	80	24	1.4130	8.12	5.32	8.49
Water/ HMT	**80**	24	-	6.50	-	-
	100	24	1.2579	7.27	6.86	8.84
	110	24	**2.1411**	8.26	2.23	1.03

The real Mg^{2+}/Al^{3+} ratio of the obtained materials was usually below the starting ratio (3:1), similarly as previously reported.[157] The lowest Mg^{2+}/Al^{3+} ratio was observed at temperatures of 80 ^{o}C (0.0037), which meant that the production of OH^- ions was enough to precipitate Al^{3+} but only a small fraction of Mg^{2+} was incorporated to the platelets. In contrast, at 90 ^{o}C the amount of hydroxide ions increased and a higher fraction of Mg^{2+} was precipitated, reaching a higher Mg^{2+}/Al^{3+} ratio (1.17), but still lower than the starting ratio of 3. When the reaction time was extended up to 3 days, more Mg^{2+} was incorporated within the structure, reaching a metals ratio of 1.93, but at the same time the flakes quality was lower, as was seen by SEM (Figure 3.1.3 b).

The optimum time at 90 ºC was 48 hours, since the produced flakes had regular round shape (Figure 3.1.3 a) and the metals ratio equals to 1.84. When the temperature was further increased to 110 ºC (24 h), the Mg^{2+}/Al^{3+} ratio was the highest when using urea, but the flakes obtained were smaller (Figure 3.1.1 d). Moreover, materials obtained in a mixture of water and EG, presented higher Mg^{2+} content which proved the EG adsorption on the $Al(OH)_3$ surface which enabled magnesium substitution which was consistent with the literature,[154] but due to the poor quality of the obtained flakes (Figure 3.1.4), no further experiments were carried out with this solvent mixture, as mentioned before. The reaction performed with HMT at 110 ºC led to the synthesis of the material presenting the highest Mg^{2+}/Al^{3+} ratio (2.14).

Elemental analysis results showed that some materials produced with urea contained nitrogen, which proved that the nitrate anion (from the metal salts used as metal precursors), was partially incorporated. This was in good agreement with the results found in the literature;[99] the presence of adsorbed/intercalated urea as a nitrogen source was excluded on the basis of FT-IR (Figure 3.1.5). It was observed that when increasing the reaction time to 48 and 72 hours or the increase of the temperature to 110 ºC, led to the decrease of nitrogen content, which most probably was related to a total substitution by carbonate anions formed during thermal urea decomposition. Relatively large amounts of nitrogen were found in the samples produced in a mixture of EG and water, where most probably nitrate anions balanced the positive charge of the layers. Furthermore, when using HMT, the presence of nitrogen was also related to the presence of adsorbed HMT, as was further checked by FT-IR spectroscopy (Figure 3.1.5 j and k).

Typically, the FT-IR spectra of the samples (Figure 3.1.5) contained three signals characteristic of LDH: broad band at 3350 cm^{-1} was related to symmetric and asymmetric stretching of ν_{O-H} coming from hydroxide groups in LDH and also interlayer and adsorbed water. The water molecules gave rise to another sharp peak at 1640 cm^{-1} assigned as a bending mode. Sharp peaks at 1350 cm^{-1} together with 780 cm^{-1} were usually attributed to C-O asymmetric stretching vibrations of CO_3^{2-}, which is the main counter anion when urea hydrolysis is used as OH^- source.[36, 99, 154, 158] Typical lattice vibrations (ν_{O-M}) at 678 cm^{-1} were present only in the spectra of the samples prepared at 90 ºC, 100 ºC, 110 ºC when using urea and for the sample obtained from HMT decomposition at 110 ºC (Figure 3.1.5 b, c, d, e, f, k). For the samples synthesised in a mixture of EG and water additional signals at 1220 cm^{-1} and 1740 cm^{-1} were present

in the spectra. Those peaks are characteristic of the functional group of carboxylic acid and it is possible that ethylene glycol was oxidized to carboxylic acid at elevated temperatures and further incorporated to the LDH.[159] The relatively low pH value after the reaction with HMT at 100 ^{o}C together with the extra peaks observed in FT-IR spectrum (Figure 3.1.5 j) suggested that amine was not completely hydrolysed at 100 ^{o}C and $C_6H_{12}N_4$ molecules were intercalated in the interlammelar space or adsorbed on the surface.[158] Those signals related to the presence of HMT disappeared when performing the reaction at 110 ^{o}C (Figure 3.1.5 k), which suggested that 110 ^{o}C was the lowest temperature to precipitate pure LDH flakes by HMT hydrolysis.

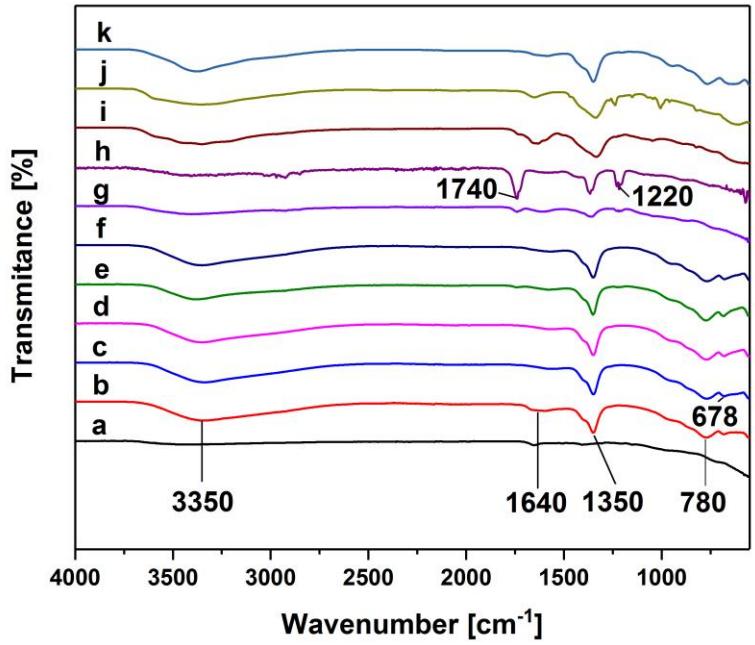

Figure 3.1.5 FT-IR spectra of $Mg_xAl_y(OH)_2(CO_3)_{y/2}\cdot nH_2O$ obtained at a) 80 ^{o}C, b) 90 ^{o}C, c) 90 ^{o}C after 48 h, d) 90 ^{o}C after 72h, e) 100 ^{o}C, f) 110 ^{o}C, g) 80 ^{o}C in a mixture EG/water-1:1), h) 80 ^{o}C in a mixture EG/water-2:1, i) 80 ^{o}C in a mixture EG/water-4:1, j) 100 ^{o}C from HMT and k) 110 ^{o}C from HMT.

The XRD analyses confirmed the FT-IR results, showing that the materials obtained in a mixture of EG and water (Figure 3.1.6 g-i) were not pure layered double hydroxides. LDH phases were identified for the samples produced in the solvents mixture in ratios 1:1 and 1:2 (Figure 3.1.6 g, h), but not for 4:1 (Figure 3.1.6 i). Despite the presence of LDH phase, an undefined peak at 4.8 Å appeared as a contamination. Similarly, material synthesized from HMT at 100 ^{o}C (Figure 3.1.6 j) was

not LDH, since none of the characteristic signals were found, and only a sharp peak at 4.95 Å (from HMT)[160] was observed. Moreover, for samples obtained with urea in water (Figure 3.1.6 a-f) and for the sample formed at 110 ºC with HMT (Figure 3.1.6 k) pure LDH with high crystallinity was obtained. A series of strong basal reflections which corresponded to the successive (00l) harmonics of the interlayer spacing[26] were observed and the patterns were indexed as rhombohedral symmetry (space group R-3m; a = 3.05 Å, c = 22.70 Å, JCPDS card 01-089-5434), characteristic for Mg-Al layered double hydroxides in the carbonate form. [26,161,99]

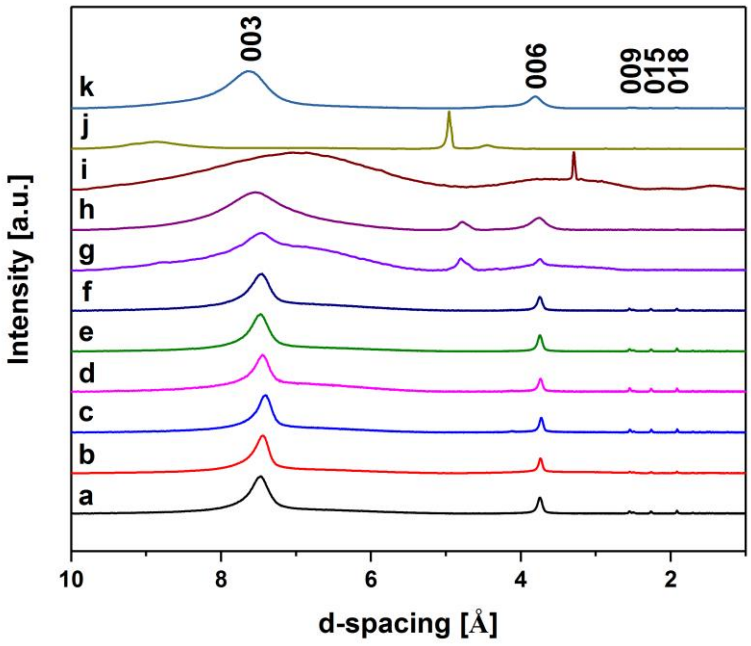

Figure 3.1.6 XRD patterns of $Mg_xAl_y(OH)_2(CO_3)_{y/2}\cdot nH_2O$ obtained at a) 80 ºC, b) 90 ºC, c) 90 ºC after 48 h, d) 90 ºC after 72h, e) 100 ºC, f) 110 ºC, g) 80 ºC in a mixture EG/water-1:1), h) 80 ºC in a mixture EG/water-2:1, i) 80 ºC in a mixture EG/water-4:1, j) 100 ºC from HMT and k) 110 ºC from HMT.

The obtained $Mg_xAl_y(OH)_2(CO_3)_y\cdot nH_2O$ flakes presented a variety of sizes and shapes, however their size was not suitable for biological applications, as they were too big to be uptaken via endocytosis.[86] Nevertheless, a possible application of these materials might be their use as catalysts[33] or as a substrate directing nanotubes growth.[162] Since the catalytic activity is strongly related to the surface area,[99, 163] which dramatically increases for single or few layers platelets,[164] exfoliation of these materials is proposed as a route to improve their performance in those applications. However,

exfoliation of layered double hydroxides is a special case of the delamination process, because as well as van der Waals forces and hydrogen bonds, electrostatic interactions also need to be broken to separate single sheets.[19, 163] To facilitate and improve their exfoliation, carbonate to chloride ion-exchange was performed and the details are described in the next section.

3.1.5 Ion exchange

Ion exchange is one of the most common modification processes used to increase the distance between layers and also weaken the forces keeping the sheets together. This technique relies on the exchange of the original ions for "new" counter anions, which are bigger, present a smaller charge and usually are more able to create hydrogen bonds.[12, 16, 50-55] LDH present a very high affinity to carbonate ions as a result of the very strong interactions between brucite-like layers and oxygen atoms in CO_3^{2-}, which form hydrogen bonds with OH^- in the layers. Additionally, the parallel orientation of planar carbonate anions causes electrostatic interactions which are even stronger, and interlamellar distance is minimized.[26, 163] In the present work, the ion-exchange of carbonate to chloride was attempted for the material obtained by thermal decomposition of urea at 90 ºC. This new anion is expected to decrease the strength of the interactions that maintain the layers stacked and facilitate the penetration of solvent molecules, thus leading to swelling which facilitates exfoliation.[54]

The ion-exchange process was performed in an acid-salt mixed solution.[36] The acid protonates the carbonate, simplifying decarbonisation, without reacting with the hydroxyl groups of the LDH. This change from di- to monovalent counter anion causes an electrical charge imbalance and the chloride anions present in solution in high concentration are immediately incorporated between the layers.[36] As LDH are dissolved in acidic environments by neutralization reactions, the acid must be diluted (concentration below 0.005 M) to avoid changing of the material shape and structure.

Experimental Section:

The ion-exchange was performed as described in literature.[163] 100 mg of $Mg_{0.65}Al_{0.35}(OH)_2(CO_3)_{0.175}{\cdot}nH_2O$ obtained at 90 ºC after 48 h were dispersed in 100 ml of an aqueous solution of NaCl (1M) and HCl (3.3 mM). The mixture was purged with N_2 for 1 h and then sealed and kept at ambient temperature for 24 hours without stirring. After this time, the precipitate was centrifuged (3000 rpm, 5 min) and washed three

times with decarbonated water. The whole procedure was repeated three times and samples were analysed by FT-IR, XRD and SEM every 24 hours.

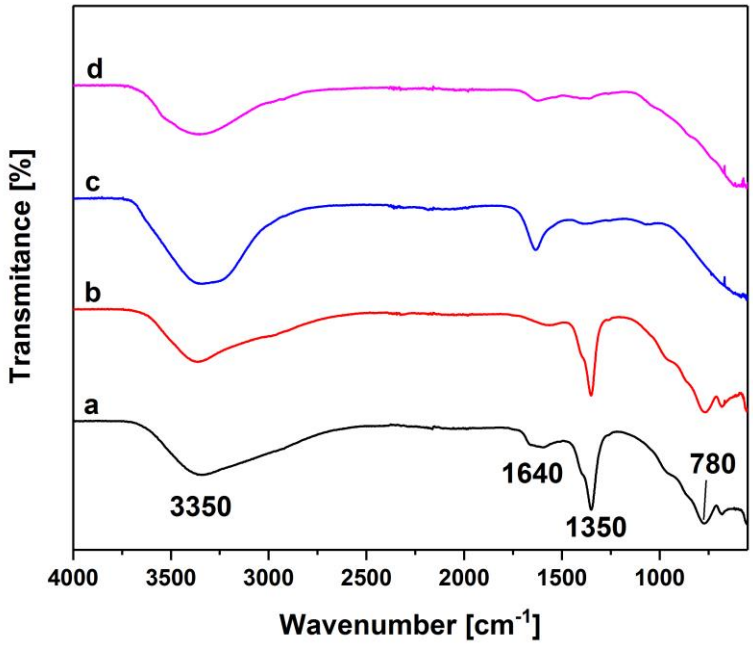

Figure 3.1.7 FT-IR spectra of $Mg_{0.65}Al_{0.35}(OH)_2(CO_3)_{0.175}{\cdot}nH_2O$ a) before acid-salt treatment, b) after treatment for 24 hours, c) after 48 hours and d) after 72 hours.

FT-IR spectroscopy (Figure 3.1.7 a-d) evidenced that carbonate anions were successfully removed from interlayer space by acid-salt treatment, as the peaks at 1350 and 780 cm^{-1}, previously assigned as the υ_3 vibration and bending modes of CO_3^{2-} respectively, disappeared after 48 hours of ion-exchange, while they were still present when the sample was treated for only 24 hours.

During the ion exchange procedure, the interlayer space varied from 7.49Å (carbonate form) to 7.53 Å after 72 hours (chloride form), as presented in the Figure 3.1.8. Moreover, in the XRD pattern of the sample kept in the acid-salt mixture for 72 hours, the peaks at lower d-values disappeared, which was most probably related to the damage of the flakes which was observed under SEM (Figure 3.1.9 d). In contrast, for samples treated by acid-salt solution for 24 and 48 hours no structural or morphological changes were detected, but a low intensity peak at 4.14 Å, related to the contamination of NaCl, was observed (Figure 3.1.9 b and c).

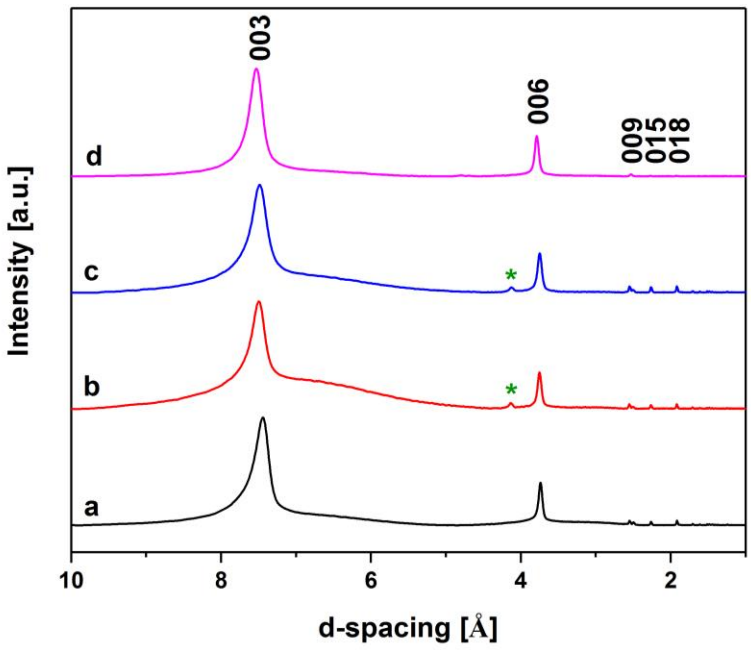

Figure 3.1.8 XRD pattern of $Mg_{0.65}Al_{0.35}(OH)_2(CO_3)_{0.175}{\cdot}nH_2O$ a) before acid-salt treatment, b) after treatment for 24 hours, c) after 48 hours and d) after 72 hours. Peaks marked by green * are related to the contamination of NaCl.

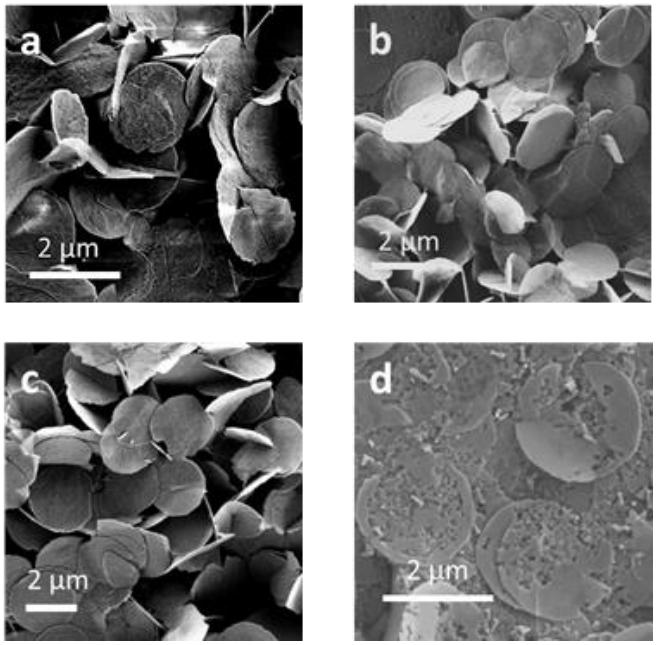

Figure 3.1.9 SEM micrograph of $Mg_{0.65}Al_{0.35}(OH)_2(CO_3)_{0.175}{\cdot}nH_2O$ a) before acid-salt treatment, b) after treatment for 24 hours, c) after 48 hours and d) after 72 hours.

By combining these results, the optimum time for exchanging carbonate to chloride was set as 48 hours and this sample was additionally characterized by thermogravimetric analysis (TGA) (Figure 3.1.10).

The TGA showed a 41.60 % total mass loss for both samples-before and after ion exchange procedure. The TGA curves were typical for LDH materials,[165] showing a two-step decomposition: firstly (at temperatures below 200 ^{o}C), the adsorbed and intermolecular water was lost. Secondly (up to 800 ^{o}C), dehydroxylation of the brucite-like layers and decomposition of interlamellar anions took place leading to the final product, identified as magnesium-aluminium spinel[165, 166] as proved by XRD analysis of the residue (Figure 3.1.11), by comparison to JCPDS card 00-021-1152. The differences in a mass loss between chloride and carbonate forms during first step (14.42 % and 16.45 % respectively) indicated that those materials contained slightly different amounts of water, which might have been a result of changes in interlamellar space after anion exchange. During the second step, where the counter anions were removed, it was observed that the carbonate anion was more difficult to remove than chloride, since higher temperature was required to get spinel.

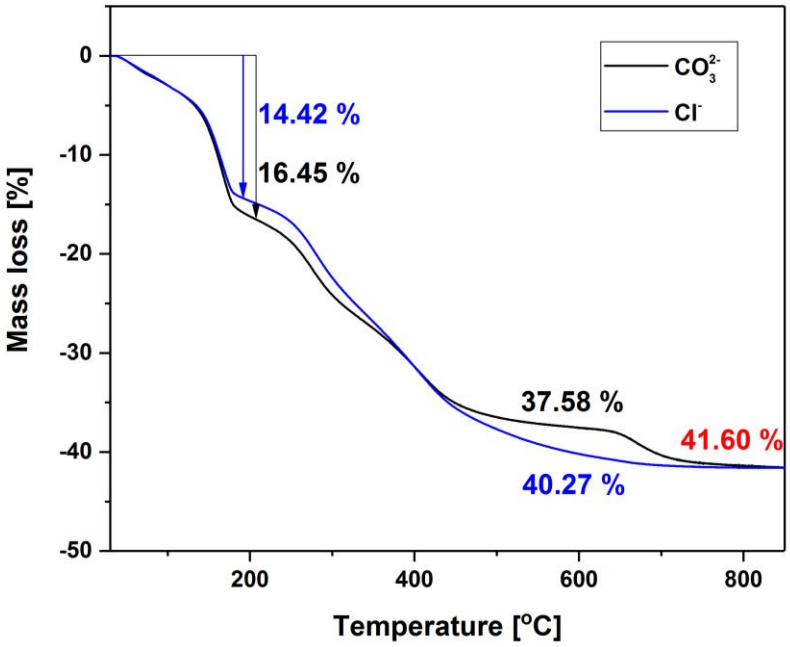

Figure 3.1.10 TGA analysis of $Mg_{0.65}Al_{0.35}(OH)_2(CO_3)_{0.175}/(Cl)_{0.35}\cdot nH_2O$ corresponding to the samples before and after ion-exchange.

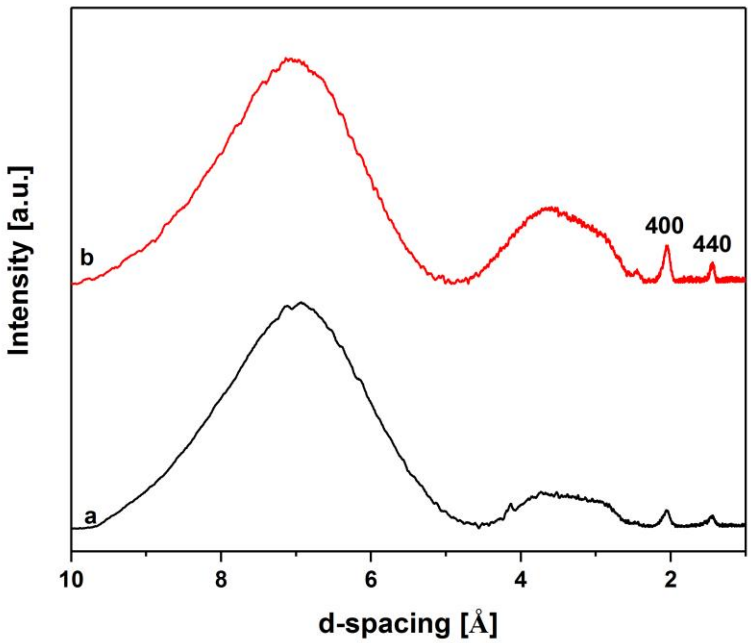

Figure 3.1.11 XRD pattern of the residue after thermogravimetric analysis of a) $Mg_{0.65}Al_{0.35}(OH)_2(Cl)_{0.35}\cdot nH_2O$ and b) $Mg_{0.65}Al_{0.35}(OH)_2(CO_3)_{0.175}\cdot nH_2O$.

The liquid phase exfoliation of $Mg_{0.65}Al_{0.35}(OH)_2(Cl)_{0.35}\cdot nH_2O$ is currently the focus of ongoing research in the project of a visitor student in Prof. Nicolosi group (Gabriele Bianca).

3.2 Precipitation of $Mg_xAl_y(NO_3)_y\cdot nH_2O$ at constant pH

The precipitation at constant pH is a very common method to obtain LDH in which the pH of the solution is kept constant by adding the metals salts solution and the base solution simultaneously. One of the biggest advantages of this method is that the material with the desired counter anion can be obtained in a single step if the synthesis is performed in a CO_2-free environment.[161]

The pH of the reaction must be suitably chosen to provide the precipitation of both metals at the same time.[24, 26] In the case of the Mg-Al LDH, the pH should be kept at a value of 10,[73, 154, 161] which is equivalent to the isoelectric point (IEP) of the particles (the pH at which their surface is electrically neutral).[167] In contrast to the precipitation at increasing pH described in the previous section, in this procedure, both M^{2+} and M^{3+} precipitate at the same time, so their final ratio in the LDH is expected to be close to the starting metals ratio in the solution.[168] Noteworthy, the reaction

temperature is also an important factor in this synthesis, as studies performed by Li *et al.*[169] showed that the precipitation performed at elevated temperature leads to formation of nanoparticles with higher interlayer spacing, but, at the same time their crystallinity is lower. Taking into account previous experiments described in the literature, the synthesis of $Mg_xAl_y(NO_3)_y{\cdot}nH_2O$ was accomplished at room temperature at a constant pH of 10.[161]

Experimental Section:

The precipitation of $Mg_xAl_y(NO_3)_y{\cdot}nH_2O$ at constant pH of 10 was performed according to the recipe described in the literature.[161] A mixture of $Mg(NO_3)_2{\cdot}6H_2O$ (0.22 mol) and $Al(NO_3)_3{\cdot}9H_2O$ (0.11 mol) was dissolved in 125 ml of decarbonated water (previously boiled for 1 hour under N_2 purging in order to remove CO_2). Then, this solution was added dropwise to a 250 ml of ammonia solution previously adjusted to pH 10 under vigorous stirring and N_2 bubbling. During the precipitation reaction the pH was maintained at 10 by adding ammonia solution (12 M) when needed. The resulting suspension was stirred for 1 h under N_2 bubbling at room temperature. Then, the precipitate was centrifuged (3000 rpm/20 min) and washed three times with decarbonated water to remove the excess of reactants.

The pH of the solution was continuously measured by pH-Meter Jenway 3510 previously calibrated by 3 points methods, using buffer solutions (pH of 2, 7 and 10). The elemental formula of the sample was determined based on the metals ratio measured by ICP-OES, CHN content and then related to the general formula of LDH ($[M^{II}_{1-x}M^{III}_{x}(OH)_2]^{x+}[A^{n-}_{x/n}\cdot yH_2O]^{x-}$).

The analysis of the samples by ICP-OES led to a Mg^{2+}/Al^{3+} metals ratio of 1.8, close to the starting value of 2, thus showing an improvement in the incorporation of Mg^{2+} with respect the processes described in the previous section. The slightly lower amount of Mg^{2+} could have been due to a lower rate of mixing or lack of ageing time, which might have resulted in not all Mg^{2+} being incorporated within the structure.[26] By combining this result with the elemental analysis, the molecular formula was calculated as $Mg_{0.645}Al_{0.355}(OH)_2(NO_3)_{0.317}(CO_3)_{0.019}{\cdot}nH_2O$, which effectively confirmed the incorporation of nitrate as counter anion.

The obtained particles presented a layered structure under SEM, although the lack of a well-defined size and shape (Figure 3.2.1 a). The FT-IR spectrum (Figure 3.2.1 b) was similar to those previously reported,[99, 161] presenting vibration modes

characteristic for LDHs: a wide band around 3400 cm^{-1}, which corresponded to the ν_{O-H} mode of hydroxyl groups in brucite-like layers and interlayer/adsorbed water, peaks at 1640 cm^{-1} and 1350 cm^{-1} were related to the interlayer/adsorbed water and to the asymmetric stretching modes of the nitrate ion, respectively.[99, 161] The XRD pattern showed that the material presented a low degree of crystallinity, similarly to other materials produced by precipitation methods without any additional aging treatment, showing only the (00l) reflections (l is a multiple of 3) typical for $Mg_xAl_y(OH)_2(NO_3)_y{\cdot}nH_2O$ (Figure 3.2.1 c).[161, 170]

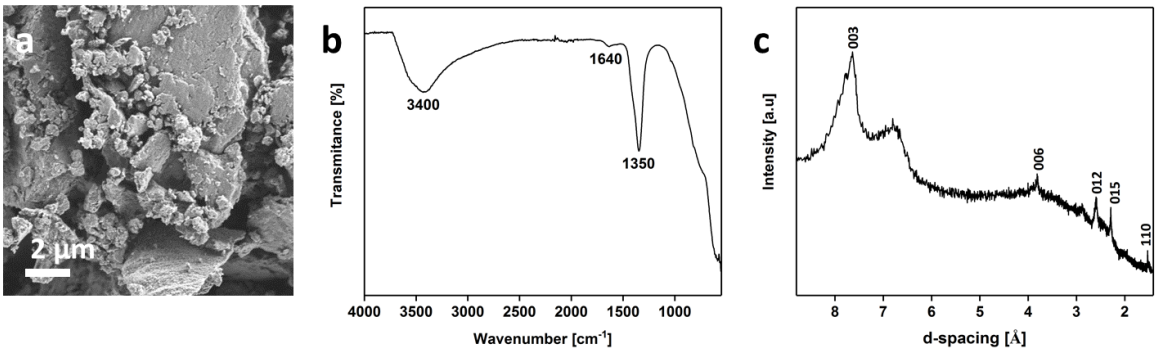

Figure 3.2.1 a) SEM micrograph, b) FT-IR spectrum and c) XRD pattern of $Mg_{0.645}Al_{0.355}(OH)_2(NO_3)_{0.317}(CO_3)_{0.019}{\cdot}nH_2O$ obtained at constant pH.

$Mg_{0.645}Al_{0.355}(OH)_2(NO_3)_{0.317}(CO_3)_{0.019}{\cdot}nH_2O$ obtained at constant pH had the desired composition, but heterogeneous size distribution and irregular shape made it unsuitable for biological applications. For this reason, an alternative synthesis approach which consisted of the precipitation at decreasing pH was proposed and it is developed in the next section.

3.3 Precipitation of $Mg_xAl_y(OH)_2(NO_3)_y{\cdot}nH_2O$ at decreasing pH

The synthesis of $Mg_xAl_y(OH)_2(A)^{n-}_{y/n}{\cdot}nH_2O$ performed at pH > 10 results in the fast precipitation of both metals at the same time, so in the end the metals ratio is closer to the initially used.[155, 168] Furthermore, when the pH of the solution is different than the IEP of the primarily formed nanoparticles, those are charged and therefore agglomeration does not occur due to electrostatic repulsion.[168] Moreover, it was also reported that the formation of M-OH covalent bonds along x and y axes is more

thermodynamically favoured than stacking along z axis by electrostatic interactions, which requires at least one more step (anions adsorption on the hydroxide layers).[171]

Stable dispersions of Mg_xAl_y LDH nanoparticles presenting a narrow size distribution, with diameters ~50 nm and nitrate as a counter anion were previously formed in a non-aqueous solvents (usually alcohols) with additional hydrothermal treatment, while the similar procedure in aqueous environment resulted in bigger particles formation ~110 nm, as reported by Dong *et.al*.[78, 86]

In the present study, particles of Mg_xAl_y LDH with nitrate as the counter anion with different Mg^{2+}/Al^{3+} ratio were produced in an aqueous solution using a similar route to the one proposed by Mourad *et.al*.[40] To check the influence of the aging parameters on the particles formation/growth process, the obtained raw precipitate was then aged in different conditions (temperature, time, solvent and concentration).

Experimental Section:

The precipitation of the starting colloidal solution was performed according to the recipe described by Mourad *et al*.[40] Briefly, the precursors solution was prepared by dissolving a required amount of $Mg(NO_3)_2 \cdot 6H_2O$ and $Al(NO_3) \cdot 9H_2O$ in 100 ml of decarbonated water. The Mg^{2+}/Al^{3+} ratios studied were 2:1, 3:1 and 4:1, with the total metals concentration equal to 0.5 M. Then, the metal salts solution was drop added to an equal volume (calculated in relation to the required amount of OH^-) of 1.1 M NaOH containing 0.15 M $NaNO_3$ under vigorous stirring and N_2 bubbling. After the precipitation procedure, the raw precipitate was centrifuged (3000 rpm/20 min) and re-dispersed in water. Then 85 ml of the colloidal solutions were aged at different conditions presented in Table 3.3.1. The samples aged at RT, 50 ^oC, 85 ^oC and 115 ^oC were transferred to the glass bottles and kept in an oil bath previously heated to required temperature, while the samples aged at 150 ^oC were poured to a 125 ml stainless-steel Teflon-lined autoclave and placed in an oven heated to 150 ^oC. The modifications of the Mourad's procedure included aging at RT, 50 ^oC and 115 ^oC (EG/water mixture).

Similarly, as in the previous section the elemental formulas were determined based on the metals ratio measured by ICP-OES, CHN content and then related to the general formula of LDH ($[M^{II}_{1-x}M^{III}_{x}(OH)_2]^{x+}[A^{n-}_{x/n} \cdot yH_2O]^{x-}$). The size of the particles was determined with imaging software (*ImageJ*) by manual measurement of the platelets diameter. The size distribution histograms were plotted based on the diameter of around 100 platelets. In order to minimize the error, the data for statistical analysis

was obtained from 5 different images acquired in the various sample regions. The samples thickness was estimated based on the height profiles measured by AFM and analysed by *Gwyddion* software.

Table 3.3.1 Aging conditions of Mg_xAl_y LDH nitrate form with various starting Mg^{2+}/Al^{3+} ratios.

Mg^{2+}/Al^{3+} ratio	**sample**	**Temperature [^oC]**	**solvent**
2:1	A	150	water
	B	RT	water
	C	115	EG/water (4:1 v/v %)
4:1	D	85	water
3:1	E	RT	water
	F	50	water
	G	85	water
	H	115	EG/water (4:1 v/v %)
	I	150	water

3.3.1 Characterization of $Mg_xAl_y(OH)_2(NO_3)_y \cdot nH_2O$ with initial Mg^{2+}/Al^{3+} ratio 2:1 – Temperature effect

ICP-OES of the raw (non-aged) $Mg_xAl_y(OH)_2(NO_3)_y \cdot nH_2O$ precipitate (initial metals ratio of 2:1) showed a real Mg^{2+}/Al^{3+} = 1.5. The obtained precipitate was hydrothermally treated at 150 ^oC, in a refluxing mixture of EG/water (4:1 v/v %) at 115 ^oC and RT for 3 days (a procedure known as aging).[40]

Compared to the materials reported by Mourad *et al.*,[40] where hexagonal platelets, homogenous in size of mean diameter of 146 nm were reported after aging at 150 ^oC, in this study, the obtained LDH nanoparticles (sample A) presented larger particle diameter, a broader size distribution (50-300 nm) and the edges of the particles were visibly jagged. In contrast, flakes with sharp edges presenting regular shape were produced in the sample aged at room temperature in this work (sample B). The aging performed in EG/water - 4:1 mixture (sample C) resulted in formation of platelets with

diameter below 100 nm with rounded edges, proving that the organic solvent addition significantly inhibited the crystal growth (Figure 3.3.1 c).[154] Both magnesium and aluminium were detected by EDX in all samples and a representative spectrum is shown in the Figure 3.3.1 d.

These experiments showed that precipitation at decreasing pH leads to formation of $Mg_{0.6}Al_{0.4}(NO_3)_{0.4}{\cdot}nH_2O$ platelets whose size can be controlled by changing the aging temperature and solvent. Bigger platelets were formed at higher temperature, since higher temperatures enhance the Brownian motion of the particles which in turn prevents aggregation and then individual crystallites grow via the Ostwald ripening.[171] In the next section, the synthesis of platelets with different metals ratio (Mg^{2+}/Al^{3+} = 4:1) is described and the influence of the concentration of the initially formed precipitate on the structure of the obtained particles is investigated.

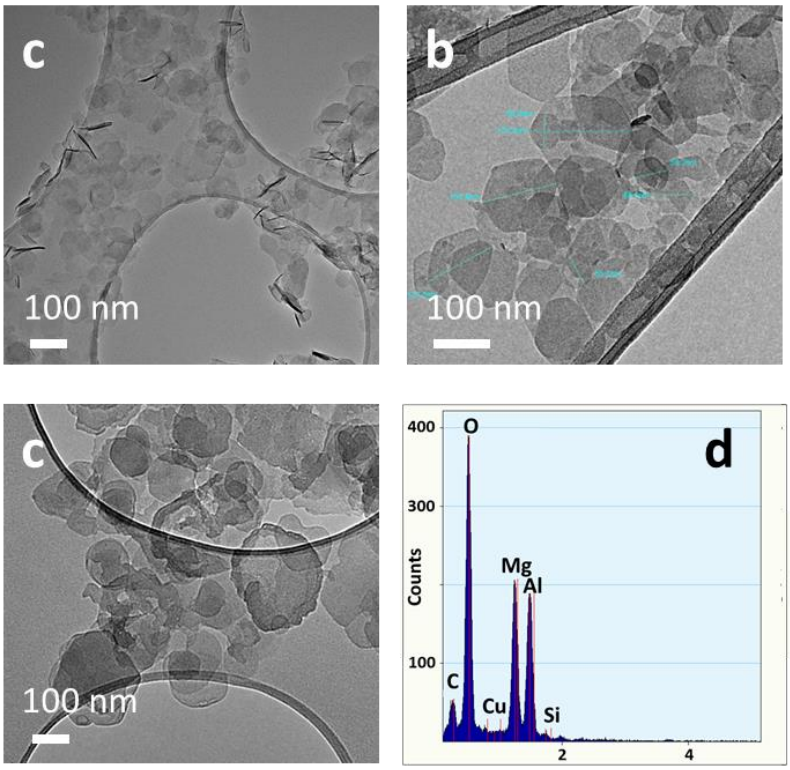

Figure 3.3.1 TEM micrograph of $Mg_{0.6}Al_{0.4}(NO_3)_{0.4}{\cdot}nH_2O$ aged at a) water at 150 ^oC, b) water at RT and c) EG/water (4:1) - 115 ^oC); d) EDX results of sample aged at RT.

3.3.2 Characterization of $Mg_xAl_y(OH)_2(NO_3)_y \cdot nH_2O$ with initial Mg^{2+}/Al^{3+} ratio 4:1 – Concentration effect during aging

$Mg_xAl_y(OH)_2(NO_3)_y \cdot nH_2O$ with an initial Mg^{2+}/Al^{3+} metals ratio equal to 4 (sample D) was precipitated and further aged at 85 ^oC. The influence of the concentration of the starting precipitate on the particles growth was checked by comparing the sample aged without any dilution with the suspension diluted 1:10 in deionized water. In both cases flakes with rounded corners below 100 nm in diameter were obtained (Figure 3.3.2) which meant that the dilution did not have a significant influence, which is consistent with the previous results described in the literature.[171]

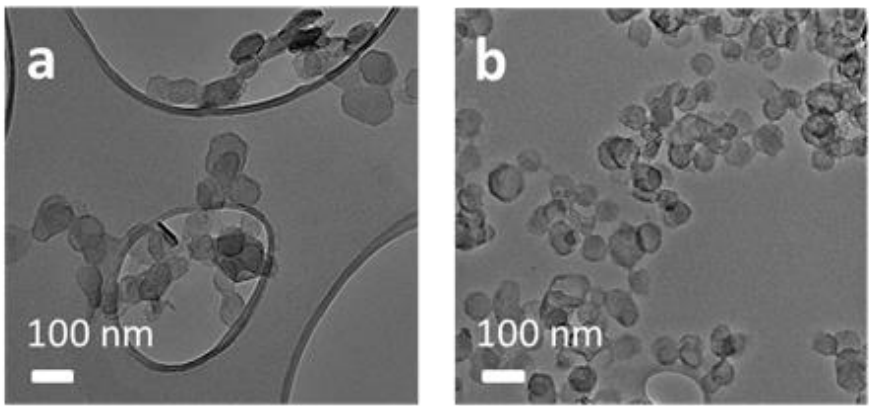

Figure 3.3.2 TEM micrograph of $Mg_{0.78}Al_{0.22}(NO_3)_{0.22} \cdot nH_2O$ aged at 85 ^oC a) without dilution, b) diluted 1:10.

The Mg^{2+}/Al^{3+} ratio was calculated as 3.6 on the basis of ICP-OES, close to the starting ratio of 4. This observation caused that the initially precipitated nanoparticles were aged without dilution in further experiments.

3.3.3 Characterization of $Mg_xAl_y(OH)_2(NO_3)_y \cdot nH_2O$ with initial Mg^{2+}/Al^{3+} ratio 3:1 – Temperature and time effect during aging

A more detailed study of the effect of the aging temperature and aging time was performed in the samples prepared from an initial Mg^{2+}/Al^{3+} ratio of 3.

Firstly, ICP-OES analysis of the freshly precipitated $Mg_xAl_y(OH)_2(NO_3)_y \cdot nH_2O$ with initial $Mg^{2+}/Al^{3+} = 3$ showed that the real metals ratio was 2.7, thus leading to the formula $Mg_{0.73}Al_{0.27}(NO_3)_{0.27} \cdot nH_2O$. Different aging conditions (Table 3.3.1, samples E-I) were applied and the samples were analysed by TEM and XRD.

The TEM micrographs (Figure 3.3.3 a-f) and platelets diameter distribution analysis (Figure 3.3.3 a'-f') for the samples aged for three days at different temperatures (RT, 50 ^{o}C, 85 ^{o}C, 115 ^{o}C (EG/water, 4:1) and 150 ^{o}C) showed that the aging temperature has an important effect on the particles shape and size, which is consistent with the previous results obtained for the materials with initial metals ratio equal to 2 (Section 3.3.1). The raw precipitate (Figure 3.3.3 a) did not show any consistent platelet or crystalline structure formation, however, after aging for three days it was possible to distinguish nanoparticles and their size and shape were observed to depend on the aging

temperature: the observed trend was that the higher the temperature, the higher the particle size, since the crystal growth rate is proportional to the reaction temperature if the other parameters are kept constant.[171]

Interestingly, at RT, 50 ^{o}C and 85 ^{o}C (Figure 3.3.3 c and d respectively) sharp edges were observed, while at higher temperatures only flakes with rounded corners were present. This phenomena might be explained by the fact that, at higher temperature, the initially formed gel-like particles incorporated a high number of substitutional defects during the first (re)crystallization steps, which further caused the imperfect platelets edges.[171]

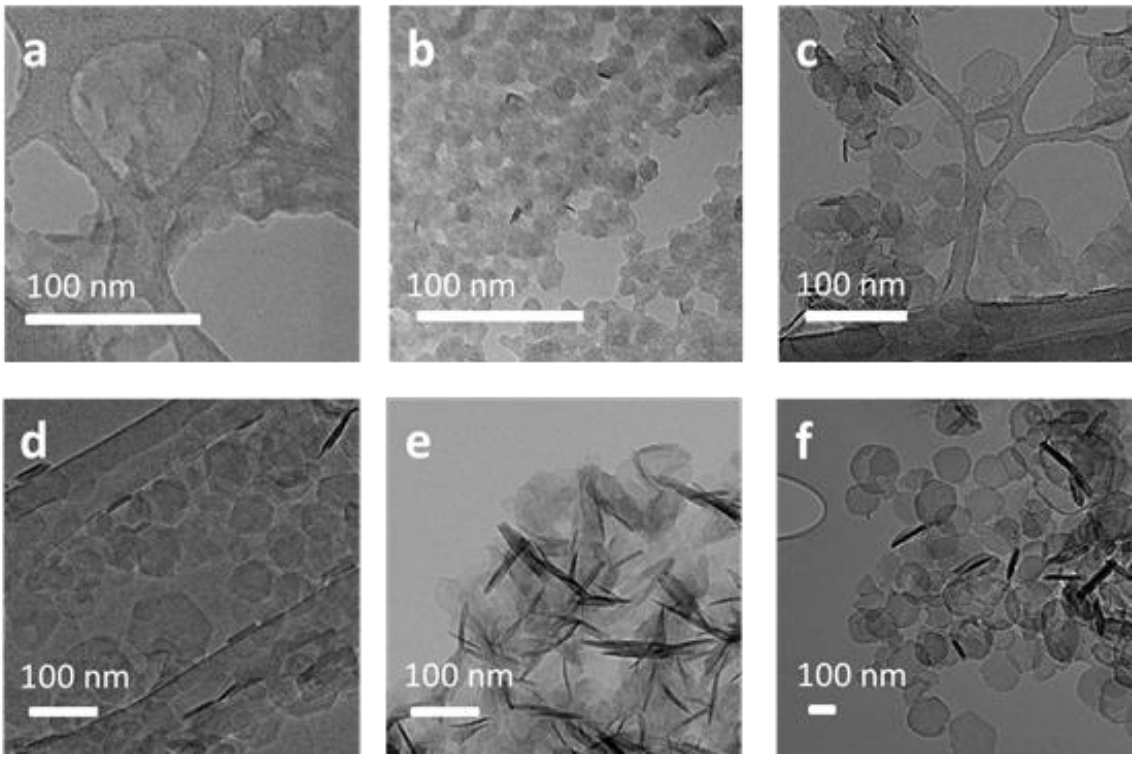

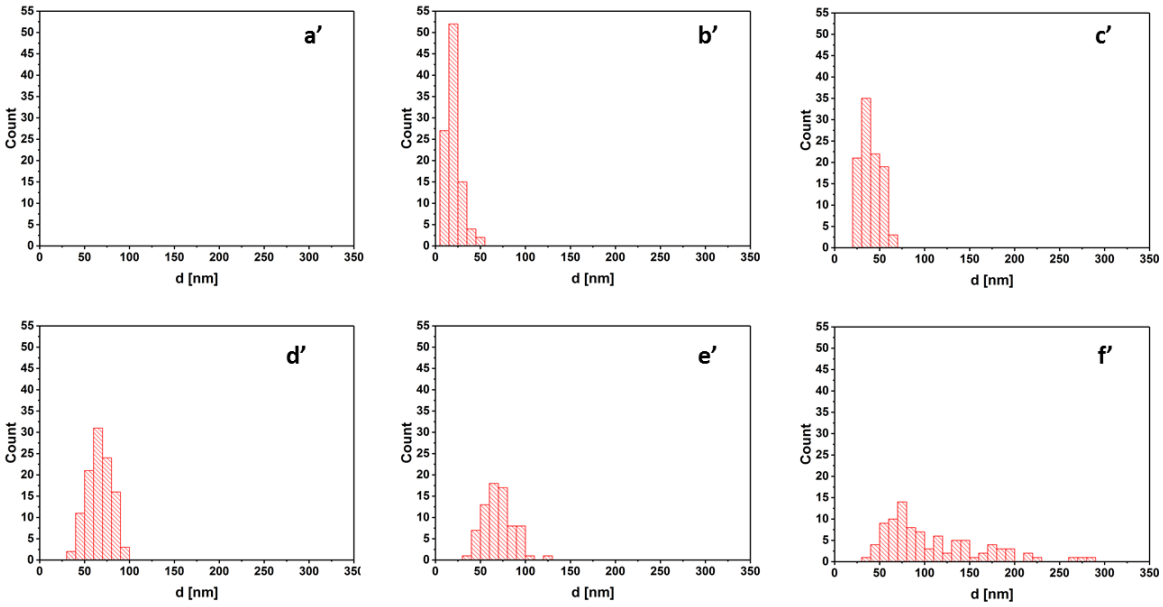

Figure 3.3.3 TEM micrograph (a-f) and corresponding particles diameter histograms (a'-f') of $Mg_{0.73}Al_{0.27}(NO_3)_{0.27}\cdot nH_2O$ a) without aging, b) aged for 3 days at RT, c) aged for 3 days at 50 ^oC, d) aged for 3 days at 85 ^oC, e) aged for 3 days at 115 ^oC (EG:H_2O-4:1) and f) aged for 3 days at 150 ^oC.

Further aging of the samples up to seven days in total performed at RT, 50 ^oC and 85 ^oC (Figure 3.3.4) showed no relevant differences in the size of the particles. However, the edges changed their shape significantly, as hexagons were formed at RT and 50 ^oC, while at 85 ^oC previously observed sharp corners visible after 3 days disappeared. Changes in the shape of the LDH platelets might be explained by the so-called 3-D process (dissociation, deposition and diffusion). Firstly, during the dissociation step, the gel-like precipitate formed straight after precipitation (Figure 3.3.3 a) is dissolved. Then, a diffusion process makes the metals to distribute more homogenously within the layers, which rearrange to form regular hexagons (Figure 3.3.3 d). When the particles are dispersed in a solvent for longer time periods, the smaller crystallites present in solution dissolve and deposit onto the bigger crystallites via process known as Ostwald ripening.[171, 172] The 3-D process explains well the formation of platelets with sharp edges, but does not really fit to the observed corners damaging at 85 ^oC after 7 days, which still remains a challenge for the author. Although, it might have been related to an increase in the defects density by a constant effect of the relatively high temperature and the breaking due to the magnetic stirring.

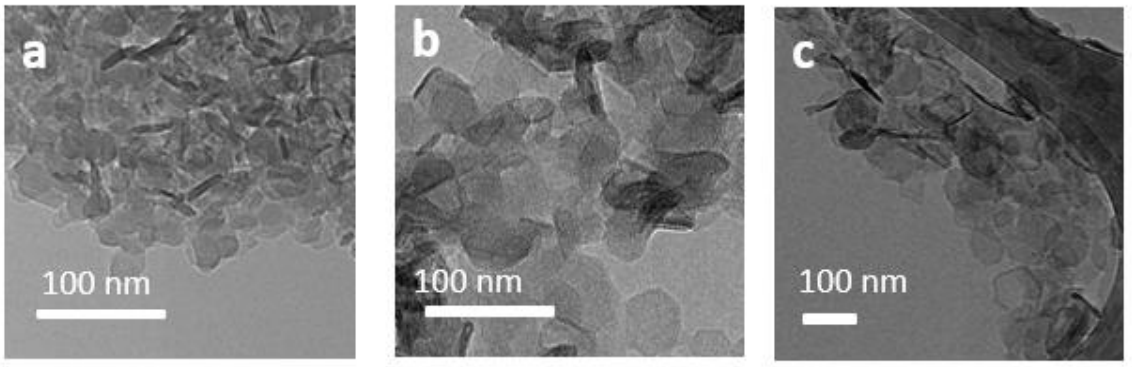

Figure 3.3.4 TEM micrograph of $Mg_{0.73}Al_{0.27}(NO_3)_{0.27}\cdot nH_2O$ aged for 7 days at a) RT, b) 50 ^oC, c) 85 ^oC.

The promising results of the sample aged in water at room temperature (sample E) caused that further studies of the evolution of the platelets morphology for longer periods of time (up to 6 weeks) were performed. The TEM micrographs are shown in the Figure 3.3.5. The particle size did not vary with time and in all cases the flakes presented diameters below 50 nm. Moreover, after fourteen days almost all platelets were hexagons and kept this shape with time, up to 6 weeks.

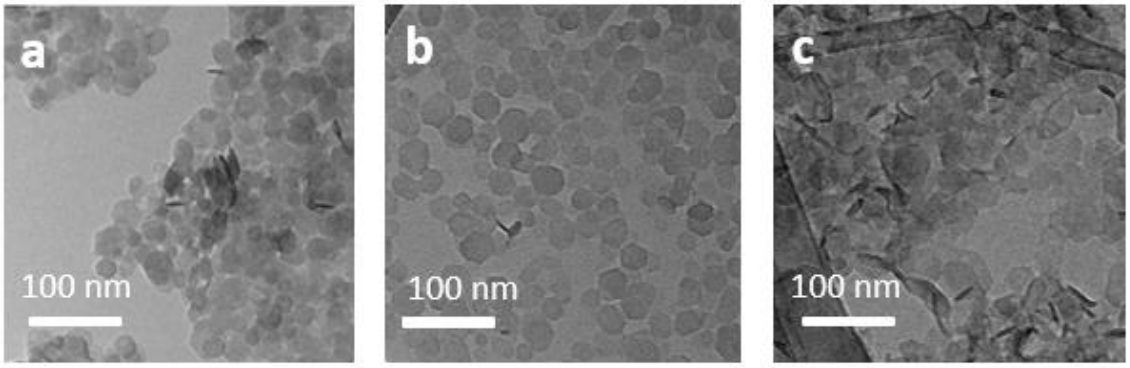

Figure 3.3.5 TEM micrograph of $Mg_{0.73}Al_{0.27}(NO_3)_{0.27}\cdot nH_2O$ kept at RT for a) 14 days, b) 28 days, c) 42 days.

The sample aged at RT for 7 days was additionally analysed by AFM. Representative image and thickness profiles are presented in the Figure 3.3.6. The analyzed flakes had thickness from 2 to 10 nm, but also flakes with heights below 1 nm, which is typical of single layered LDH[104, 173] were found.

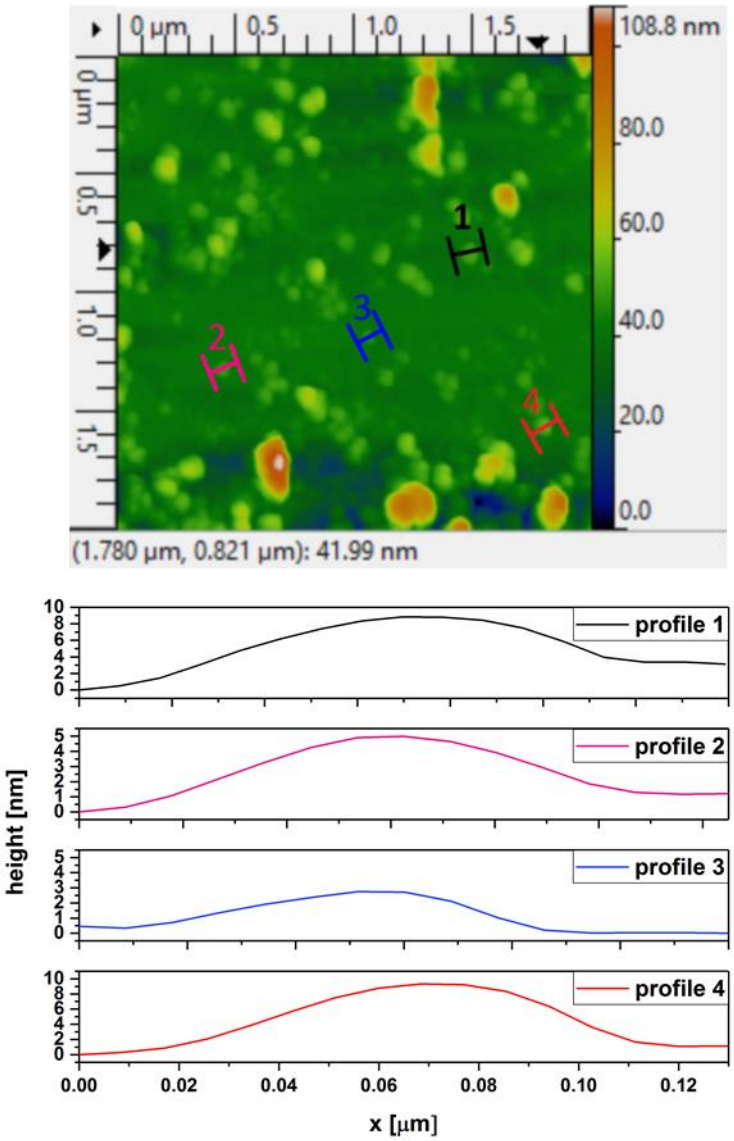

Figure 3.3.6 AFM image and height profile of $Mg_{0.73}Al_{0.27}(NO_3)_{0.27}\cdot nH_2O$ kept at RT for 7 days. The profiles 1, 2, 3 and 4 correspond to the numbered lines in the AFM image.

The structural characterization of $Mg_{0.73}Al_{0.27}(NO_3)_{0.27}\cdot nH_2O$ aged at different temperatures was performed by XRD. Figure 3.3.7 a-f shows the XRD patterns of the samples aged for 3 days at RT, 50 ºC, 85 ºC, 115 ºC and 150 ºC, respectively. In all cases, the reflections (003), (006), (012), (015) and (110) were found, which is in good agreement with results reported in literature.[161] In order to check the importance of the washing step, XRD of the non-washed material aged for 3 days at RT was also recorded. Many reflections observed in the diffractogram of the sample aged without washing (Figure 3.3.7 a) confirmed that the sample was a mixture of different

compounds, including LDH and the metal hydroxides. During the washing step extra electrolytes are removed and purer LDH can be obtained (Figure 3.3.7 b) – a similar observation was reported by Xu *et al.*[171] where the washing procedure was crucial to obtain stable dispersion of pure and homogeneous in size LDH particles.

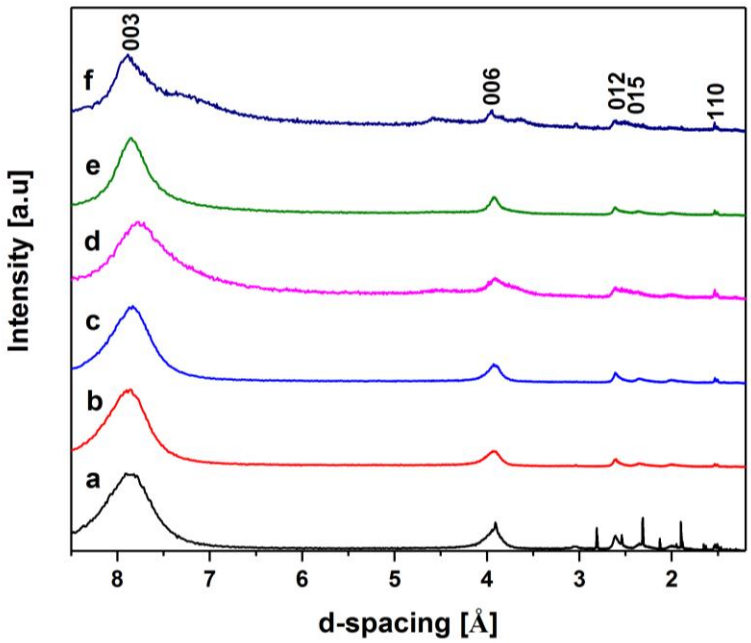

Figure 3.3.7 XRD pattern of $Mg_{0.73}Al_{0.27}(NO_3)_{0.27}{\cdot}nH_2O$ aged for 3 days at a) RT without washing, b) RT washed, c) 50 ºC, d) 85 ºC, e) 115 ºC (EG/water-4:1) and f) 150 ºC.

Furthermore, this very simple method to obtain small $Mg_{0.73}Al_{0.27}(NO_3)_{0.27}{\cdot}nH_2O$ platelets was also expanded to the synthesis of the chloride form of $Mg_xAl_yCl_y{\cdot}nH_2O$, showing similar results (supplementary information, Figure S1). The process was succesfully scaled up (20 g of nanoparticles dispersed in 1 L of water) without any differences in comparison to the small (100 ml) laboratory scale (supplementary information, Figure S2).

As far as the author is concerned, this is the first time that a straightforward synthesis in water and aging the precipitate at room temperature had resulted in the production of small, hexagonal LDH platelets. The charge of the nanosheets, which results from the M^{2+}/M^{3+} metals ratio, was controlled by changing the initial M^{2+}/M^{3+} ratio, and also counter anion balancing this charge could be selectively chosen.

Moreover, aging at RT was fully scaleable, reproducable and did not require special equipment to provide homogeneous heat distribution. The $Mg_{0.73}Al_{0.27}(NO_3)_{0.27}\cdot nH_2O$ material aged at room temperature was chosen as a sample suitable for the pDNA intercalation process described in the next section.

3.4 Plasmid DNA intercalation

As it was previously mentioned in Chapter 1, the intercalation of negatively charged molecules between the LDH layers protects them from decomposition within a living organism and permits their safe transport to the cells.[74, 75, 77] Moreover, the hydroxide layers can be easily dissolved by the acidic media within the cell, thus releasing the biomolecules.[24, 74, 81, 87]

One of the methods to introduce the negatively charged biomolecules between the layers is direct synthesis, where metals salt solution is drop-added to the base solution containing them. When the LDH nanoparticles are precipitated, those biomolecules are automatically intercalated between the layers to neutralize the positive charge generated in the layers by the trivalent cations, so the biomolecule-LDH hybrid is produced in a single step.[77, 174]

Another procedure to create these nanohybrids is ion-exchange, where the negatively charged biomolecules replace the original counter anions, according to the mechanism shown in Figure 3.4.1.[77, 83, 175] In this procedure of intercalation, since the biomolecules are usually larger than the original inorganic counter-anion, the basal spacing is increased, which causes an interlamellar swelling.

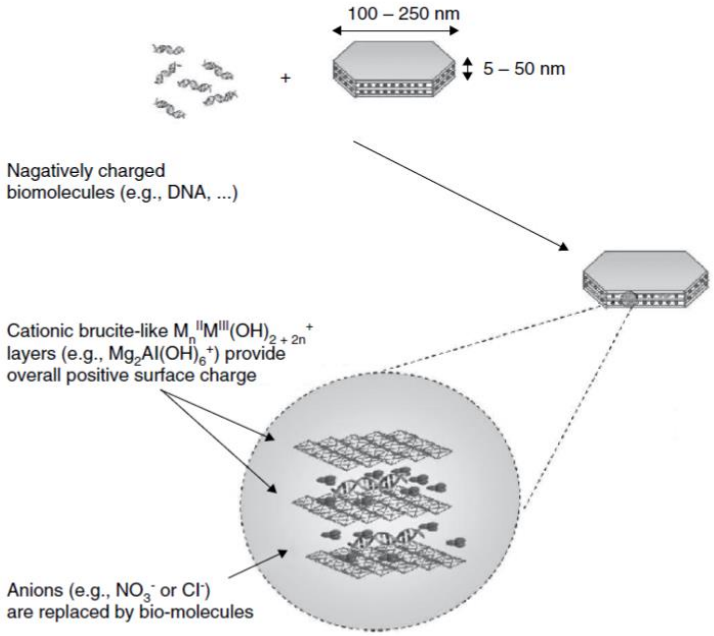

Figure 3.4.1 The intercalation mechanism of DNA into LDH via ion-exchange mechanism. Adapted from ref 83.[83] Copyright 2017 Taylor & Francis.

Thirdly, biomolecule-LDH nanohybrids can be also produced by making use of the LDH "memory-effect", where layered double oxides (LDO) formed by thermal decomposition of LDH reconstruct their hydrated structure when exposed to water and preferred anions[26, 77, 175] which is schematically presented in the Figure 3.4.2.[176]

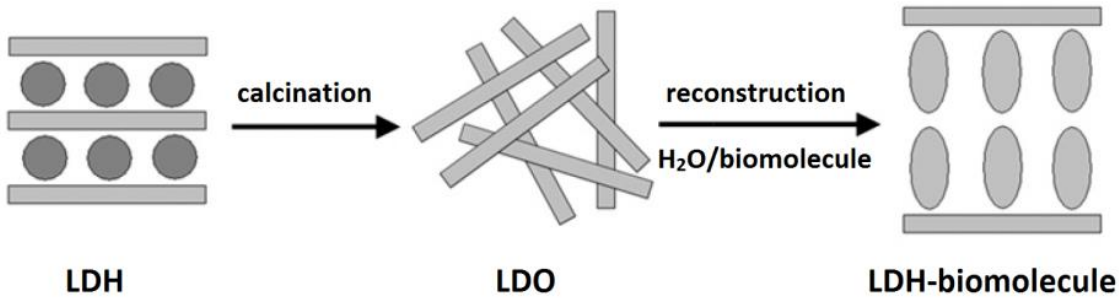

Figure 3.4.2 Schematic representation of reconstruction method. Adapted from ref. 176 (licence number 4119400879469).[176]

In the present study, all three techniques (direct synthesis, ion-exchange and reconstruction) were applied to form pDNA-LDH nanohybrids, which are being used as non-viral vectors for delivery of pDNA as a part of bone-repairing therapy in an

ongoing research project in collaboration with bioengineers from Prof. Fergal O'Brien's group from RCSI.

Experimental Section:

Direct synthesis of the pDNA-LDH nanohybrid was performed analogously to the method described in a previous Chapter (Section 3.3), but due to very small amount of pDNA available and impossibility of performing the experiment in µl scale the substrate concentration was decreased ten times. Briefly, 6 ml of 0.05 M aqueous solution of $Mg(NO_3)_2 \cdot 6H_2O$ and $Al(NO_3)_3 \cdot 9H_2O$ was drop-added to 6.1 ml of aqueous solution of 0.11 M NaOH containing 0.15 µmol pDNA. The obtained mixture was kept in the mother liquid for one week, centrifuged (3000 rpm/5 min) and washed 3 times with decarbonated water. The sample obtained by this method was labelled as A1.

Secondly, the intercalation of pDNA by an ion-exchange reaction into material synthesised by precipitation at decreasing pH (described in the previous Section) was carried out according to the recipe described in the literature.[175] 50 µg of LDH nanoflakes were mixed with 25 µg of pDNA and additional 250 µL of decarbonated water giving the final concentration equal to 0.166 and 0.083 $\mu g \mu l^{-1}$ for LDH and pDNA respectively. The pH of the dispersion was adjusted to 8 by addition of citric acid. The obtained slurry was continuously stirred at 37 ^oC for 30 min. After that the sample was centrifuged (3000 rpm/5 min) and washed 3 times with water. Material was called A2.

Finally, LDO used in the reconstruction method were produced by calcination of previously synthesized LDH nanoflakes at 500 ^oC for 4 h.

The reference reaction (LDH→LDO→LDH) with addition of $NaNO_3$ was performed in order to check LDO ability to reconstruct their hydrated structure. To do so, 11.45 mg of LDO were mixed with 11.45 mg $NaNO_3$ and 2.7 ml H_2O and kept at room temperature for 3 days. After this time, the precipitate was centrifuged (3000 rpm/5 min) and washed 3 times with water.

In case of the intercalation of pDNA, the concentration of LDO and pDNA were the same as in ion-exchange procedure (0.166 and 0.083 $\mu g \mu l^{-1}$, respectively) and the mixture was kept at ambient temperature for 1 week. Sample was named A3.

3.4.1 LDH – LDO – LDH reconstruction with $NaNO_3$

Prior to the pDNA intercalation, the reconstruction of the LDH structure from LDO was studied in the presence of $NaNO_3$. LDO with a formula of $Mg_{0.73}Al_{0.27}O_{1.27}$ was produced by calcination of $Mg_{0.73}Al_{0.27}(NO_3)_{0.27}\cdot nH_2O$ (Section 3.4), as confirmed by XRD (Figure 3.4.3 b, JSPD card 00-047-0254). When comparing the diffraction patterns of directly synthesised LDH (sample B1) and the material obtained by reconstruction method (labelled as sample B2), different planes, both typical for Mg_xAl_y LDH (JSPD card 00-014-0191), were observed. Reflections (006), (009) and (113) were identified in both materials (Figure 3.4.3 a, c), but planes (015), (018) and (110) were detected only in B1 (Figure 3.4.3 a), while (0111) and (205) appeared in the diffractogram of B2 (Figure 3.4.3 c).

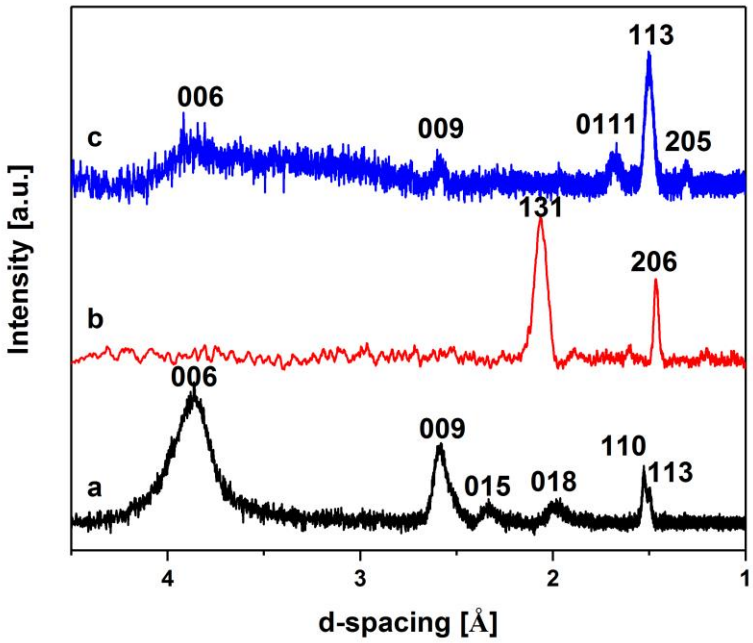

Figure 3.4.3 XRD diffractogram of a) B1, b) LDO and c) B2.

FT-IR analysis (Figure 3.4.4) confirmed the XRD results, proving that the LDO was successfully produced by thermal decomposition of LDH, as peaks related to O-H stretching modes at 3400 cm^{-1} and 1640 cm^{-1} did not appear (Figure 3.4.4 b) and only a weak signal from counter anion at 1350 cm^{-1} and peaks related to the lattice vibrations below 1000 cm^{-1} were observed, which indicated that, most probably, some nitrate anions remained within the structure after the thermal treatment. Moreover, the FT-IR

spectra of B1 (Figure 3.4.4 a) and B2 (Figure 3.4.4 c) were very similar, although, a shift upon reconstruction of 15 cm^{-1} for the absorption bands at 1350 cm^{-1} was indicative of the different location of nitrate anion in the interlayer of samples B1 and B2.[177]

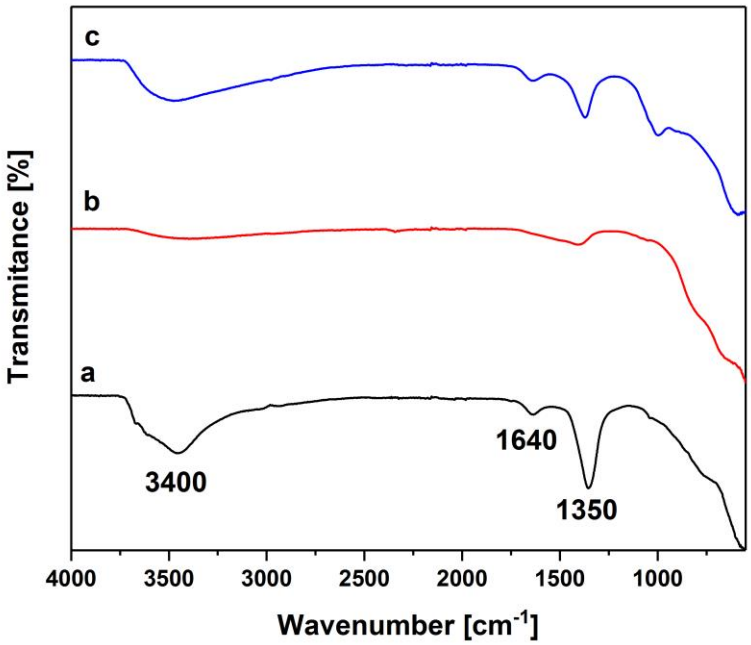

Figure 3.4.4 FT-IR spectrum of a) B1, b) LDO and c) B2.

The differences in the diffraction patterns and FT-IR spectra of B1 and B2 suggested modifications in the nanoparticles' morphology. SEM micrographs of B1, LDO and reconstructed B2 are presented in the Figure 3.4.5. B1 as well as LDO (Figure 3.4.5 a, b) did not have a well-defined geometry visible under SEM and individual crystallites were undistinguishable by this technique. In contrast, material $Mg_{0.73}Al_{0.27}(NO_3)_{0.27}{\cdot}nH_2O$ produced by reconstruction method (B2) consisted of regular platelets with round edges and diameters around 200 nm. This improvement in crystallinity was previously described and most probably it was related to a dissolution-recrystallization mechanism.[58, 165, 177, 178]

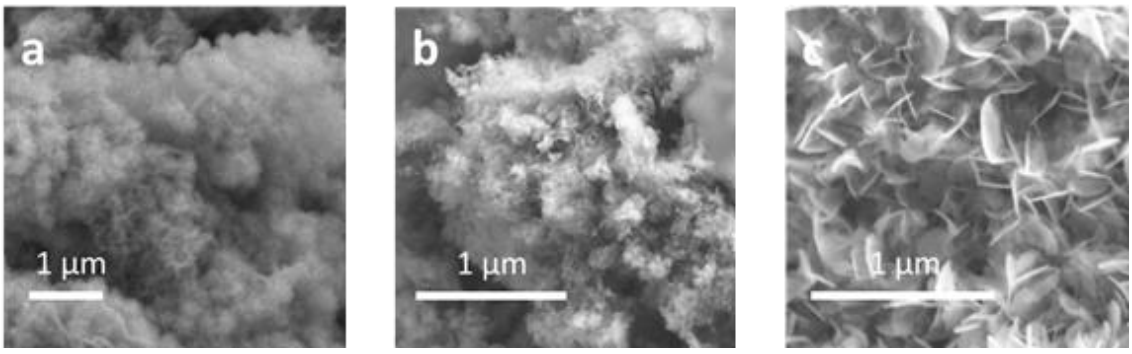

Figure 3.4.5 SEM micrograph of a) B1, b) LDO and c) B2.

3.4.2 Synthesis of pDNA-LDH nanohybrids

Plasmid DNA-LDH nanohybrids were prepared by the 3 methods previously mentioned (A1, A2 and A3). The samples were analysed by FT-IR spectroscopy and compared to the spectrum of the neat LDH (sample B1), as shown in the Figure 3.4.6.

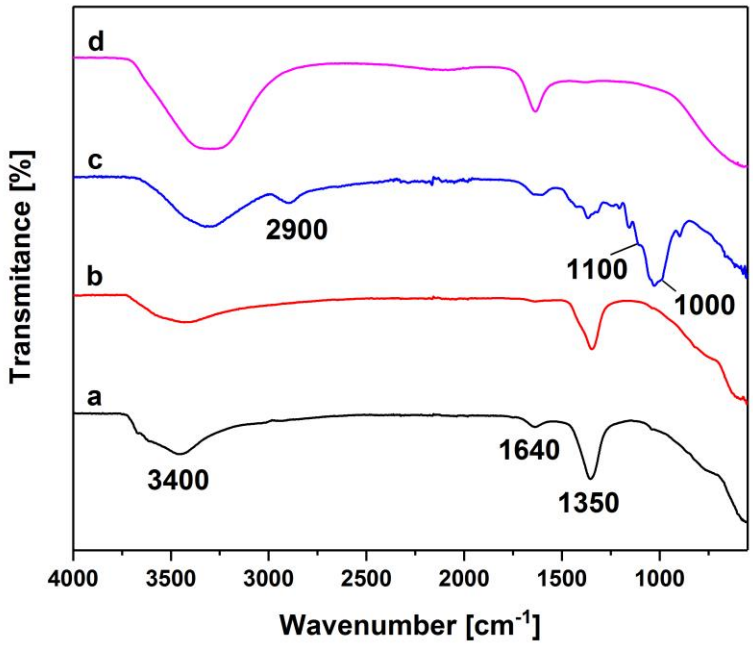

Figure 3.4.6 FT-IR spectrum of a) B1, b) A1, c) A2 and d) A3.

FT-IR analysis showed that pDNA intercalation took place only in the hybrid produced by ion-exchange method (A2), as the intensity of the peak related to the stretching mode of nitrate anion at 1350 cm^{-1} significantly decreased (Figure 3.4.6 c), suggesting that this anion was partially replaced by the biomolecule or attached to the nanoparticles surface. Moreover, the absorption bands at ~2900 cm^{-1} and at 1000-1100

cm^{-1}, ascribed as C-H and P-O vibrations in the pDNA, respectively were observed in the spectra of A2.[73, 179]

In contrast, the spectra of the samples A1 and A3 did not give any evidence of DNA intercalation or attachment: spectrum A1 was the same as B1, while in the spectrum of A3 only peaks related to the O-H group and interlayer/adsorbed water were present (Figure 3.4.6 b and d respectively).

Due to the very small amount of the material available it was not possible to analyse the sample by XRD, and the A2 nanohybrid was additionally characterized by STEM and STEM-EDX microscopy (credited to Christopher Hobbs) presented in the Figure 3.4.7.

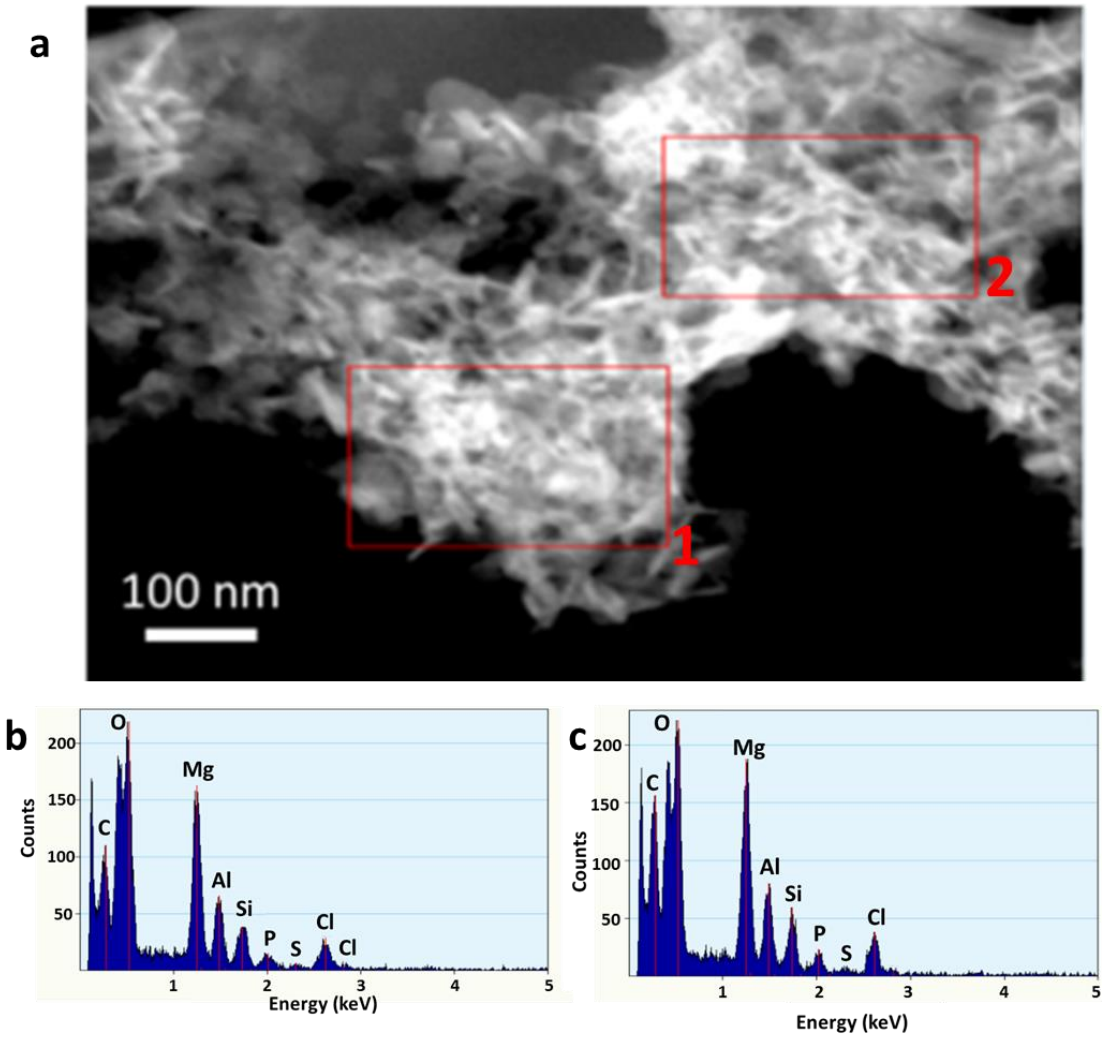

Figure 3.4.7 a) STEM and b, c) STEM-EDX analysis of A2.

The STEM micrograph (Figure 3.4.7 a) showed that $Mg_{0.73}Al_{0.27}(NO_3)_{0.27}{\cdot}nH_2O$ platelets agglomerated and the nanohybrid size was in the range of several hundred

nanometres. The phosphorus signal observed in the STEM-EDX spectra taken in two different regions (Figure 3.4.7 b, c) confirmed the presence of pDNA, consistently with FT-IR results. This pDNA-LDH nanohybrid was too big to be uptaken by the cell in an endocytosis process, therefore mild sonication in an ultrasonic bath was applied leading to the breaking of the agglomerate into smaller particles suitable for endocytosis.[81]

3.4.3 Testing of the LDH as pDNA delivery agent

The pDNA-LDH nanohybrids prepared by ion-exchange method were exposed to the cells cultured in 6-well plates for 28 days in order to check LDH ability to deliver pDNA. STEM and STEM-EDX analyses showed pDNA-LDH nanohybrid inside the cell as presented in the Figure 3.4.8.

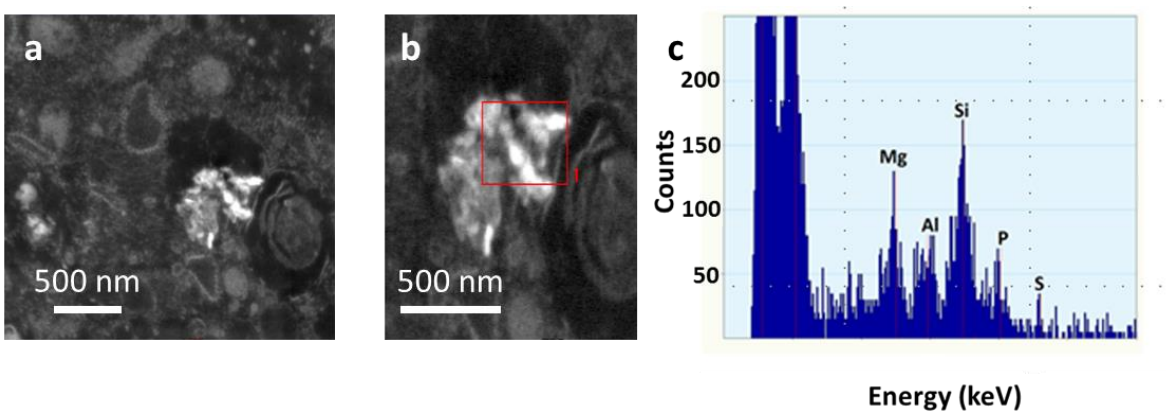

Figure 3.4.8 a) STEM micrograph, b) Zoomed-in STEM micrograph and c) STEM-EDX spectrum of the pDNA-LDH nanohybrid inside the cell.

The detection of pDNA-LDH inside the cell suggested that produced LDH nanoparticles can be potentially used as pDNA delivery agents. However, these were only preliminary tests and still detailed analysis of the uptake mechanism is required. Nevertheless, these first results strongly indicated the potential of the obtained material in biological applications and their use can be also potentially extended to the delivery of other negatively charged molecules, such as drugs[80, 84, 85] or quantum dots.[180]

3.5 Conclusions

This work describes the preparation of pDNA-LDH nanohybrids having size below 200 nm, suitable for endocytosis, as a part of a bone-repairing therapy project. Different LDH synthetic approaches were explored, resulting in the preparation of Mg_xAl_y LDH nanoplatelets with diameters between 3 μm and 20 nm.

A first synthesis method, where the pH was gradually increasing due to the thermal decomposition of urea or HMT, led to the formation of $Mg_xAl_y(OH)_2(CO_3)_{y/2}{\cdot}nH_2O$ particles with sizes in the range of 300 nm to 3 μm and high crystallinity. The particle size was controlled by the temperature and the nature of the ammonia releasing agent, although remarkable differences were only observed for temperatures in the range of 100-110 ºC in the case of urea (the flakes diameter decrease from 2 to 1 μm). In contrast, the reactions carried out with HMT resulted in the formation of smaller platelets (< 0.5 μm). The temperature and the reaction time mostly affected the particles composition, defining the Mg^{2+}/Al^{3+} ratio and the homogeneity of the interlayer anion.

Moreover, the strongly bonded carbonate anion located between the layers of these LDH was successfully exchanged to chloride by a simple acid-salt treatment. The LDH nanoparticles with chloride as a counter anion are expected to be easier to exfoliate than those having carbonate, due to the weakening of the forces which keep the layers together, and these materials are currently the focus of an ongoing project of liquid phase exfoliation in the Nicolosi group. Even though the platelets formed by homogeneous precipitation were too big for biological applications, single- or few-layer nanosheets might be promising materials for catalysis,[33] flame-retardant agents[69] or substrates to direct the growth of nanotubes,[162] and their applications in these fields will be tested in the future.

Secondly, co-precipitation of LDH at constant pH resulted in the formation of nanoparticles without a well-defined size and shape, but with a more controllable metals ratio compared to the previous method. However, the size of the nanoparticles (reaching several microns) and the observed agglomeration of the same due to the pH conditions (isoelectric point) suggested the use of a new synthetic method at higher pH, described below.

The last synthesis approach, precipitation at RT at a pH higher than the $Mg_xAl_y(NO_3)_y{\cdot}nH_2O$ isoelectric point, led to the formation of non-aggregated

nanoplatelets with a highly controllable composition and an appropriate size for endocytosis. The nanoparticles geometry was successfully controlled by the addition of an aging step. The diameter of the obtained flakes depended on the temperature at which the dispersions were aged: < 50 nm at RT, 25-75 nm at 50 ^{o}C, 40-100 nm at 85 ^{o}C, 50-125 nm at 115 ^{o}C and 50-275 nm at 150 ^{o}C, as a result of the temperature dependence of the Brownian motions (which prevent the particles aggregation) and the particles growth via Ostwald ripening. The AFM characterisation of the flakes produced by aging at RT showed a platelets thickness in the range of 3-10 nm. It was also found that the aging time affects the shape of the nanoflakes, while their size remains unchanged. Moreover, the nanoparticles concentration had a negligible influence on the final morphology of the platelets and this synthesis method was also successfully scaled up to 20 g of the nanoparticles dispersed in 1 L of water. For the first time, a straightforward precipitation at decreasing pH and subsequent aging the colloidal solution at room temperature resulted in the formation of small (<50 nm) Mg_xAl_y LDH platelets.

The preparation of the pDNA-LDH nanohybrids was attempted by three different approaches: direct synthesis, ion-exchange and reconstruction method. Plasmid DNA was intercalated between the $Mg_xAl_y(NO_3)_y{\cdot}nH_2O$ layers only via ion-exchange approach, since direct synthesis and reconstruction methods did not lead to the intercalation of pDNA between the LDH layers. The hybrids produced by ion-exchange, composed by an aggregation of platelets, as was seen by STEM, were easily re-dispersed into smaller particles suitable for endocytosis by mild sonication. Finally, the well-dispersed pDNA-LDH nanohybrids were exposed to the cells and STEM microscopy suggested their uptake. Although, these were only preliminary tests and further experiments are required to confirm the ability of LDH platelets (obtained in this work) to deliver genes to the cell. The optimization of the cell-uptake process and final application of these nanohybrids in bone-regeneration therapy process is an ongoing project currently realized in RCSI.

4 Synthesis of nickel-iron layered double hydroxides and their application as catalysts for oxygen evolution reaction

Recent studies have revealed that Ni_xFe_y LDH are promising electrocatalysts in OER (Section 1.1.2).[103-105] Their high surface area and also a high number of open coordination sites at the edges[104] (which most probably act as the active sites for water oxidation), have caused these materials to be intensively studied in recent years. Despite several techniques which have been used to prepare Ni_xFe_y LDH platelets,[173, 181] the obtained materials did not present a well-defined morphology. Therefore, the development of wet-chemistry routes to prepare thin Ni_xFe_y LDH flakes with regular shape and good crystallinity still remains a challenge in the field.

The difficulty of synthesizing these materials lies in the fact that, in aqueous solution, Fe^{3+} precipitates as a gel-like $Fe(OH)_3$ at pH above 2, which impedes further incorporation of Ni^{2+} within its structure.[182] The substitution of Fe^{3+} by Ni^{2+} and the precipitation of $Ni(OH)_2$ start at a very similar pH, so Ni_xFe_y LDH is usually contaminated with nickel hydroxide, because the formation of $Ni(OH)_2$ is thermodynamically more favourable than the substitution of Fe^{3+} within $Fe(OH)_3$.[181, 183]

Several synthetic routes have been used to produce Ni_xFe_y LDH, such as reversed co-precipitation,[184] ball milling,[185] Fe^{2+} oxidation techniques[186] or co-precipitation with the use of a long-chain organic acid.[187] Nonetheless, in the last few years special attention has been placed on the use of capping agents which coordinate Fe^{3+}, thus preventing the formation of $Fe(OH)_3$ and at the same time facilitating the combination with Ni^{2+}.[173, 181]

In this Chapter, homogeneous precipitation methods (described in Chapter 3.1) were explored to prepare Ni_xFe_y LDH with a good crystallinity and high purity. The influence of the addition of two different capping agents, trisodium citrate (TSC) and triethanolamine (TEA) was studied. Then, in collaboration with Joao Coelho (researcher in Prof. Nicolosi group), the obtained materials were tested as electrocatalysts in OER.

4.1 Synthesis of Ni_xFe_y LDH using trisodium citrate as capping agent

TSC is a very common capping agent widely used in the synthesis of various noble metals nanoparticles.[188, 189] Moreover, this organic salt can also be applied in the preparation of transition metals LDH, where citrate anions act as a tetradentate ligands and chelate trivalent cations.[181] In the case of Ni_xFe_y LDH, citrate anions chelate Fe^{3+} in aqueous solution and form soluble in water iron-citrate complexes (Eq. 4.1.1),[190] in which Fe^{3+} is octahedrally coordinated to two tetra-ionized citrate ligands.

$$Fe^{3+} + 2C_6H_5O_7^{4-} \leftrightarrow [Fe(C_6H_5O_7)_2]^{5-} \qquad \textbf{Eq. 4.1.1}$$

Moreover, the coordination of Ni^{2+} ions by citrate ligands leads to the formation of very unstable coordination compounds, so nickel is present in the solution in its unbounded ionic form or aquo complex.[191]

When an ammonia releasing agent (like urea) is added to the reaction mixture and it is heated up to induce its thermal decomposition, the OH^- released combine with Ni^{2+} and displace citrate in the $[Fe(C_6H_5O_7)_2]^{5-}$, which results in formation of pure Ni_xFe_y LDH (Eq. 4.1.2). These reaction mechanism is similar to the homogeneous precipitation described in Chapter 3, section 3.1.

$$2[Fe(C_6H_5O_7)_2]^{5-} + 6Ni^{2+} + CO_3^{2-} + 6OH^- + 7H_2O \rightarrow$$

$$\rightarrow [Ni_6Fe_2(OH)_{16}](CO_3) \cdot 5H_2O + 2C_6H_5O_7^{3-} \qquad \textbf{Eq. 4.1.2}$$

To form LDH with an ordered structure it is necessary to control the nucleation, growth and termination steps, which indeed depend on reactants concentration, pH[192] and the reaction time.[186, 193]

In this work, the influence of TSC concentration on the Ni_xFe_y LDH particles formation was checked at different temperatures (100 and 150 ^oC) at TSC:Fe^{3+} ratios of 2:1, 1:1, 1:2 and 1:20. The concentration of Ni^{2+}, Fe^{3+} and urea were used as described in the literature,[181] while the modifications of the recipe included various TSC concentration and the reaction temperature. The changes of the amount of the capping agent resulted from the uncompleted studies performed by Han *et al.*[181]

Experimental Section:

100 ml of an aqueous solution of $Ni(NO_3)_2 \cdot 6H_2O$ (15 mM), $Fe(NO_3)_3 \cdot 9H_2O$ (5 mM) and urea (35 mM) was prepared, following the recipe described in the literature.[181] Then, TSC in different amounts was introduced into the above aqueous solution to reach a final concentration of 10, 5, 2.5 and 0.25 mM and magnetically stirred for 1

hour. 80 ml of the solution were either transferred to a 100 ml round bottom flask connected to a condenser and magnetically stirred at 100 ºC for 48 hours or poured to a 125 ml stainless-steel Teflon-lined autoclave and heated in the oven at 150 ºC for 48 hours without stirring. All reactions were carried out under air atmosphere. After this, both systems were naturally cooled down to room temperature and the resulting precipitate was collected by centrifugation (3000 rpm/ 10 min) and washed with water three times. Experimental details of the syntheses are summarized in the Table 4.1.1.

Table 4.1.1 Experimental details of the syntheses of Ni_xFe_y LDH with the addition of TSC.

Sample	Temperature [ºC]	TSC concentration [mM]	Fe:TSC ratio
S1	100	10	1:2
S2		5	1:1
S3		2.5	2:1
S4		0.25	20:1
S5	150	10	1:2
S6		**5**	**1:1**
S7		2.5	2:1
S8		0.25	20:1

SEM micrographs of the samples obtained at 100 ºC and 150 ºC with different TSC:Fe^{3+} ratio are presented in the Figure 4.1.1. The SEM images of the materials obtained without capping agent in relation to Fe^{3+} performed at 100 ºC and 150 ºC are available in supplementary information (Figure S3).

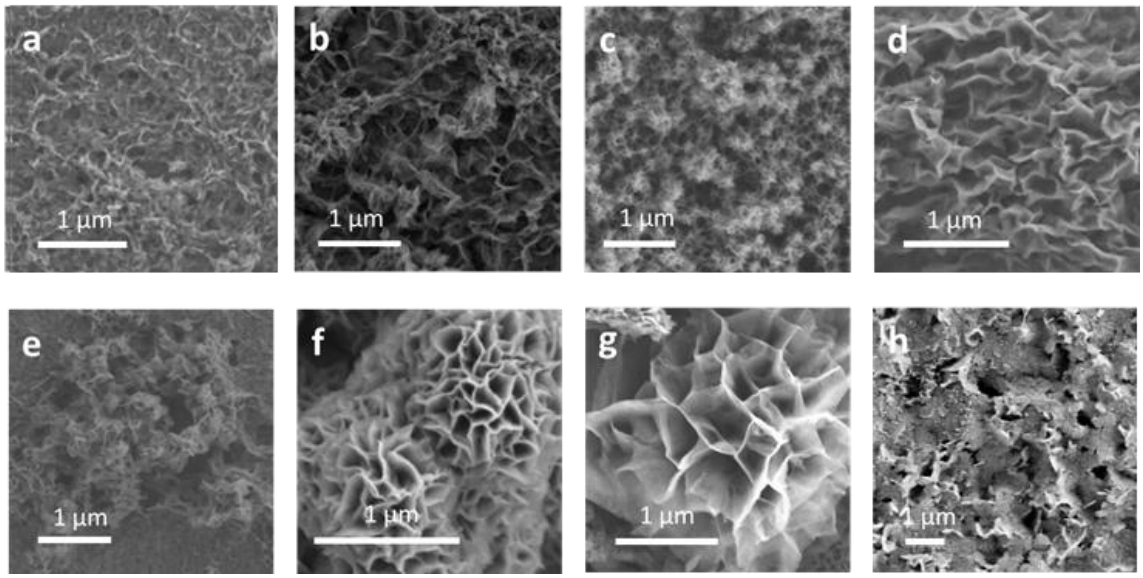

Figure 4.1.1 SEM micrographs of a) S1, b) S2, c) S3, d) S4, e) S5, f) S6, g) S7 and h) S8.

The geometry of the particles was defined by the temperature and the capping agent concentration, which is consistent with the results presented in the literature.[181] All the reactions performed at 100 ^{o}C did not lead to formation of regular crystals and only small irregular nanoparticles were obtained (Figure 4.1.1 a-d). In contrast, when the reaction was accomplished at 150 ^{o}C, the nanoparticles morphology depended on the TSC concentration. When a stoichiometric amount of TSC in relation to Fe^{3+} (Eq. 4.1.1) was used, very small (<50 nm) agglomerated flakes were formed (Figure 4.1.1 e). However, when not all Fe^{3+} ions were complexed by TSC (Fe^{3+}/TSC ratio < 2), the obtained flakes were bigger (0.5-1 µm in diameter) and their edges were sharper (Figure 4.1.1 f-h). Interestingly, for TSC:Fe^{3+} ratios of 1:1 (Figure 4.1.1 f) and 1:2 (Figure 4.1.1 g), the produced flakes tended to intergrow and form flower-like structures, which differ from the results presented by Han *et al.*,[181] who obtained regular platelets using the same reaction conditions. When the TSC amount was reduced ten times, the obtained flakes were thicker and visibly separated (Figure 4.1.1 h). On the basis of the SEM analysis, it was verified that the reactions with the use of TSC required temperatures higher than 100 ^{o}C to produce Ni_xFe_y LDH with regular geometry.

Typically, a flower-like morphology of Ni_xFe_y LDH provides a high surface area and good ion-permeability,[194] hence those kind of nanostructures found many applications, such as gas sensors,[194] supercapacitors[192] and catalysts.[195]

Another advantage of flower-like structures is their easy exfoliation by ultrasound irradiation,[196] which results in obtaining dispersions of flakes in a suitable solvent.[2] For these reasons, the flower-like material obtained at 150 ºC with the TSC:Fe^{3+} ratio of 1:1 (Figure 4.1.1 f) was further characterized by elemental analysis, FT-IR, XRD and BET, and the results are described in the next section.

4.1.1 Characterization of flower-like Ni_xFe_y LDH synthesised at 150 ºC with TSC:Fe^{3+} ratio of 1:1

FT-IR spectra of the sample and TSC are presented in Figure 4.1.2 a for comparison. In both spectra, a broad signal around 3350 cm^{-1} was attributed to the stretching mode of OH groups in the brucite-like layers of the LDH and also proved the presence of OH groups in the spectrum of TSC.[186] Signals at 1562 cm^{-1} and 1582 cm^{-1} in the spectra of Ni_xFe_y LDH and TSC respectively (green label) were assigned to asymmetric stretching vibrations of carboxyl group, υ_{as} (COO^-). The corresponding symmetric stretches, υ_s (COO^-) appeared at 1389 cm^{-1} and 1395 cm^{-1} for LDH and TSC, respectively (blue label). The shift of these signals to the lower wavenumber observed in the spectrum of Ni_xFe_y LDH in comparison to TSC, was previously observed for the Fe^{3+}-TSC complex.[190] The difference between the symmetric and asymmetric stretches $\Delta(\upsilon_{as\ (COO-)} - \upsilon_{s(COO-)})$ was 173 cm^{-1}, which indicated that COO^- ligands were either free or monodentally bonded.[190] Due to strong affinity of LDH to carbonate anions,[163] those were most probably intercalated between the layers together with citrate anions, but their characteristic signals in the FT-IR spectrum (at 1350 cm^{-1} and 780 cm^{-1}) were masked by the peaks from TSC. The citrate and carbonate loading of the LDH could not be determined, since FT-IR is not a quantitative technique. The other signals in the Ni_xFe_y LDH spectrum fitted well with the TCS, thus confirming the presence of the citrate anions. The signal at 678 cm^{-1} (purple label) in the Ni_xFe_y LDH spectrum was related to the lattice vibration υ_{M-O} and it is characteristic of LDH.[186]

XRD analysis (Figure 4.1.2 b) showed the typical pattern of Ni_xFe_y LDH, which was indexed as hexagonal symmetry (JSPDS card 00-049-0188) where planes (003), (006), (101) and (110) were assigned. The broad peak around 7 Å ascribed as (003) plane, which corresponds to the distance between the layers, was not well defined, most probably due to the heterogeneous nature of the intercalated anions. Moreover, a weak signal at d-spacing values of 2.0 and 1.3 Å (labelled as *) were most probably related to the presence of $NiFe_2O_4$[197] as an impurity in the synthesized sample.

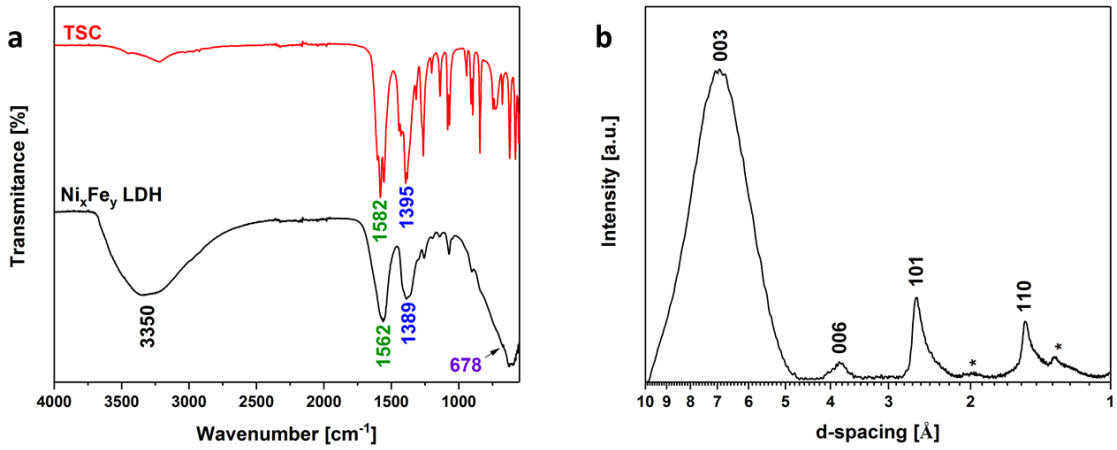

Figure 4.1.2 a) FT-IR spectra and b) XRD of TSC and $Ni_{0.75}Fe_{0.25}(OH)_2(C_6H_5O_7)_x(CO_3)_y{\cdot}nH_2O$. Peaks marked as * are attributed to the contamination of $NiFe_2O_4$.

The Ni^{2+}/Fe^{3+} ratio was found to be 3:1, as initially used. The elemental analysis showed C, H and N contents of 3.18 %, 1.86 % and 0 %, respectively. Taking into account the heterogeneous nature of the counter anion, the formula of the considered compound can be written as $Ni_{0.75}Fe_{0.25}(OH)_2(C_6H_5O_7)_x(CO_3)_y{\cdot}nH_2O$. The surface area, measured by nitrogen absorption, was 130.61 m^2/g, which was higher than the value previously reported for flower-like Ni_xFe_y LDH (70.3 m^2/g).[186] The synthesis of flower-like Ni_xFe_y LDH previously described in the literature[186] consisted of homogeneous precipitation of Ni^{2+}-Fe^{2+} and then subsequent oxidation of Fe^{2+} to Fe^{3+} in ethylene glycol under elevated temperature and pressure, which is more complicated technique in comparison to the method presented in this Thesis.

Finally, $Ni_{0.75}Fe_{0.25}(OH)_2(C_6H_5O_7)_x(CO_3)_y{\cdot}nH_2O$ presenting a flower-like morphology was tested as an electrocatalyst in the OER, which is described in the Section 4.3.

4.2 Synthesis Ni_xFe_y LDH with triethanolamine as capping agent

Another capping agent that can be used in the synthesis of Ni_xFe_y LDH is triethanolamine, TEA, ($C_6H_{15}NO_3$) which behaves like a tri- (N, O, O') or tetradentate (N, O, O', O'') ligand[198] and form weak cationic metal complexes with several transition metals like Ni^{2+} and Fe^{3+}. When TEA acts as tetradentate ligand, the formed

complex is known as "atrane",[199] which is a tricyclic system with intramolecular coordination N→E (E = metal) inert to hydrolysis at neutral pH (Figure 4.2.1).[200]

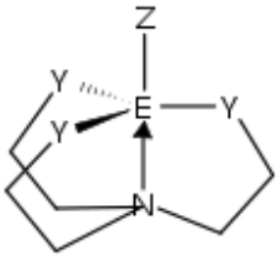

Figure 4.2.1 Schematic representation of an atrane structure.

This inertness is controllable by pH and temperature, so when those are increasing (for example, by urea decomposition at elevated temperature releasing ammonia (Chapter 3.1)),[154] the metal-TEA complex decomposes. Then, the metal released form the complex, recombines with OH^- ions present in the solution and precipitate with other cations to form mixed-metals LDH.[173] According to the literature,[173] the Ni_xFe_y LDH formation mechanism is similar to that previously described with the use of TSC, through an Fe^{3+} coordination compound.

The results previously obtained with the use of TSC, described in the Subchapter 4.1.1, showed that the capping agent concentration and the temperature applied during homogenous precipitation play a key role in the Ni_xFe_y LDH nanoparticle formation,[181, 201] which aimed to use the performance of similar experiments to study the effect of the synthesis parameters with TEA. The syntheses of Ni_xFe_y LDH with different TEA:Fe^{3+} ratios (1:2, 1:1, 2:1, 4:1) were performed at 100 ºC and 150 ºC by combining the recipes described in the literature.[104, 181] Significant changes of those recipes included decreasing the reaction temperature from 150 ºC to 100 ºC, which would dramatically reduce the synthesis cost, and also facilitate its scalability. Moreover, the concentration of the capping agent was increased, due to the TEA ability to coordinate both Ni^{2+} and Fe^{3+}.

Experimental Section:

A mixture of $Ni(NO_3)_2{\cdot}6H_2O$, $Fe(NO_3)_3{\cdot}9H_2O$ and urea was dissolved in 400 ml of deionized water, giving the final concentration of 7.5, 2.5 and 17.5 mM respectively. Then, different amounts of TEA with respect to Fe^{3+} (TEA:Fe^{3+} molar ratios of 1:2, 1:1, 2:1, 4:1 and only at 100 ºC 6:1 and 8:1) were added (see experimental conditions in

Table 4.2.1). After stirring the solutions for 24 hours at RT, 80 ml of the reaction mixture were either transferred to a 100 ml round bottom flask and heated at 100 ^{o}C under reflux system and magnetic stirring for 48 h or poured into a 125 ml stainless-steel Teflon-lined autoclave and heated at 150 ^{o}C for 48 hours. Both systems were naturally cooled down to room temperature and the precipitate was collected by centrifugation (3000 rpm/ 10 min) and washed with water three times.

A reference reaction, where TEA was replaced by NaOH to get a solution with a starting pH of 6.6, was made only at 100 ^{o}C (sample NF9). The synthesis was performed analogically as the procedure described above, but in this case TEA was not added to the reaction mixture. Briefly, $Ni(NO_3)_2 \cdot 6H_2O$, $Fe(NO_3)_3 \cdot 9H_2O$ and urea were dissolved in 400 ml of deionized water, giving the concentration of 7.5, 2.5 and 17.5 mM respectively. Then the pH of the solution was adjusted to 6.6 by the addition of NaOH and the reaction mixture was stirred for 24 hours and then subsequently heated to 100 ^{o}C for 48 hours.

TEA is a strong base, so the starting pH of the solution strongly depended on the TEA:Fe^{3+} ratio. Moreover, due to high concentration of the OH^- even before heating (pH_0), the formation of precipitate was observed in some cases as presented in the Table 4.2.1; pH after heating (pH_e) was also checked.

The pH of the solution was measured by pH-Meter Jenway 3510 previously calibrated by 3 points methods, using buffer solutions (pH of 2, 7 and 10). The elemental formula of the sample was determined based on the metals ratio measured by ICP-OES, CHN content and then related to the general formula of LDH ($[M^{II}_{1-x}M^{III}_{x}(OH)_2]^{x+}[A^{n-}_{x/n} \cdot yH_2O]^{x-}$). The amount of water was estimated based on the TGA analysis.

Table 4.2.1 Synthesis conditions and pH of the reaction mixture before and after heating.

TEA:Fe^{3+}	Sample	Temperature [ºC]	pH_0	pH_e	Precipitate at RT
1:2	NF1	100	2.4	7.0	No
	NF2	150		8.1	
1:1	NF3	100	2.7	7.3	No
	NF4	150		8.2	
2:1	NF5	100	2.8	8.2	No
	NF6	150		8.2	
4:1	**NF7**	**100**	6.6	8.1	Yes
	NF8	150		8.1	
0:1	NF9	100	6.6	8.2	Yes
6:1	NF10	100	7.2	8.3	Yes
8:1	NF11	100	7.6	8.4	Yes

SEM micrographs of Ni_xFe_y LDH formed by homogeneous precipitation at 100 ºC and 150 ºC with different TEA concentrations are presented in the Figure 4.2.2.

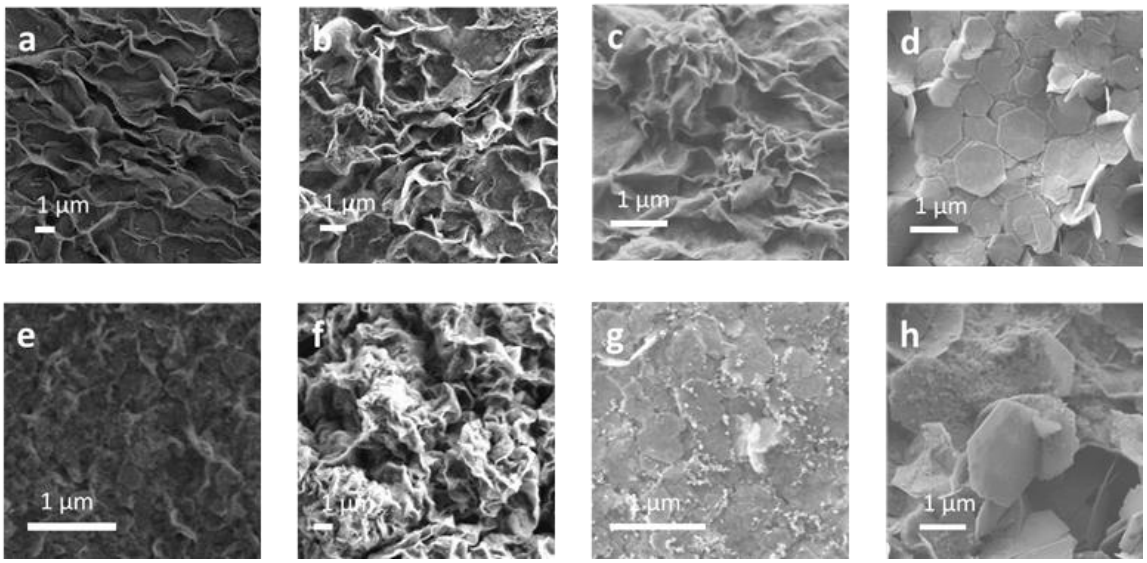

Figure 4.2.2 SEM micrographs of samples a) NF1, b) NF3, c) NF5, d) NF7, e) NF2, f) NF4, g) NF6 and h) NF8.

Regular hexagonal platelets were formed at a TEA:Fe^{3+} ratio of 4:1 (samples NF7 and NF8 in Figure 4.2.2 d and h), although when the reaction was performed at 150 °C (Figure 4.2.2 h) an additional contamination coexisted with the hexagons. This contamination was most probably insoluble nickel/iron carbonate,[202] which was formed only in the sealed autoclave and that was not observed in the sample heated at 100 °C, where the excess of CO_3^{2-} was removed as CO_2 from the reaction flask. At lower TEA:Fe^{3+} ratios (1:2, 1:1 and 2:1) flake-like particles were produced at 100 °C (samples NF1, NF3, NF5, Figure 4.2.2 a-c), but their geometry was not well-defined. The reactions performed at 150 °C led to formation of irregular platelets at TEA:Fe^{3+} ratio of 2:1 (sample NF6, Figure 4.2.2 g) while under other conditions (samples NF2 and NF4, Figure 4.2.2 e and f) it was not possible to distinguish individual particles under SEM.

The reference reaction NF9 (NaOH was added instead of TEA to reach a starting pH value of 6.6, similar as the starting pH of the reaction NF7) resulted in the formation of Ni_xFe_y LDH, although the quality of the flakes was much lower when compared to the sample NF7 produced with the addition of TEA. An SEM micrograph and the XRD pattern of NF9 are presented in the Figure 4.2.3.

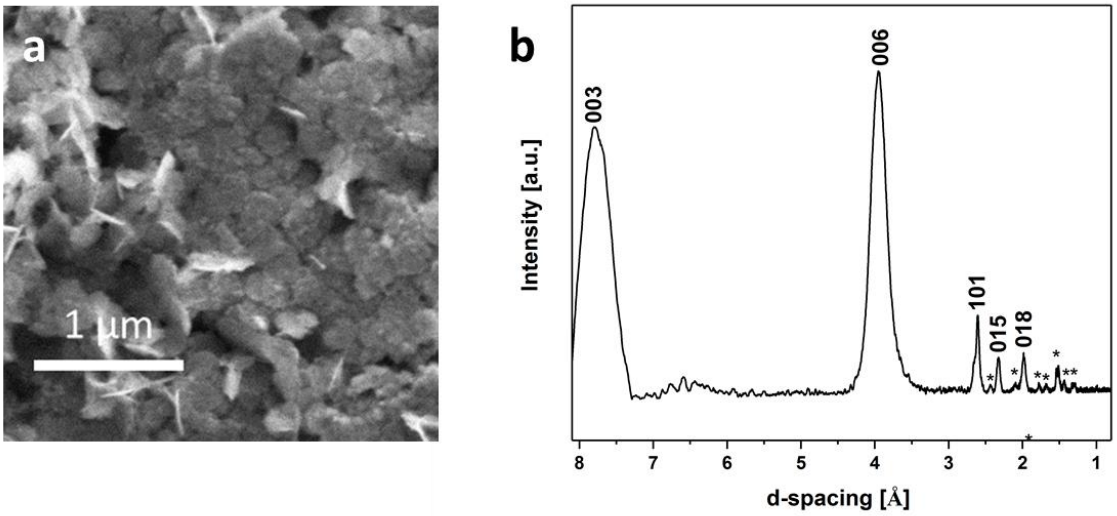

Figure 4.2.3 a) SEM micrograph and b) XRD pattern of the sample NF9. Peaks marked by * have been attributed to the contamination of iron(III) oxides and hydroxides.

XRD analysis showed the characteristic pattern of Ni_xFe_y LDH mixed with additional peaks ascribed to iron(III) oxides and hydroxides[203] (labelled as * in the Figure 4.2.3 b). These contaminations suggested that the synthesis of hexagonal

platelets cannot be performed with the use of NaOH and no further experiments were performed with the use of this chemical. This indicated that not only the starting pH was important for the synthesis of hexagonal flakes, but also the presence of TEA in the solution was required.

Since hexagonal flakes were obtained at 100 ºC with a TEA:Fe^{3+} ratio of 4:1, additional syntheses with a higher starting capping agent concentration (TEA:Fe^{3+} = 6 and 8, samples NF10 and NF11 respectively) were also accomplished. The SEM images of these samples are presented in Figure 4.2.4, showing that further increase of TEA:Fe^{3+} ratio did not result in the formation of hexagonal platelets. Just a few flakes were observed in the sample NF10, although they were smaller in size and irregular in shape compared to those observed in the sample NF7.

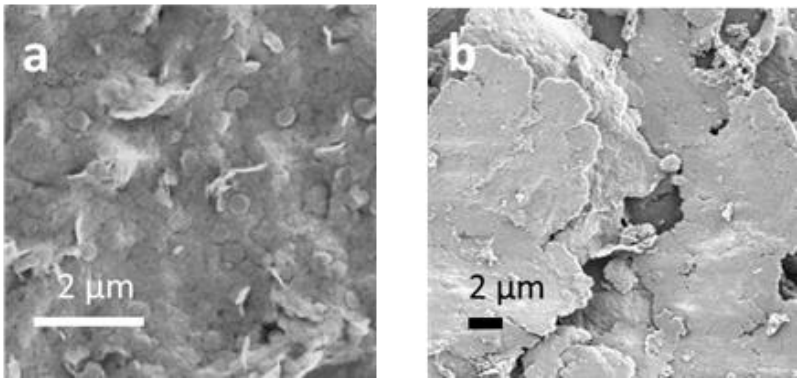

Figure 4.2.4 SEM micrograph of a) NF10 and b) NF11.

4.2.1 Characterization of Ni_xFe_y LDH obtained by homogeneous precipitation at 100 ºC with a TEA:Fe^{3+} ratio of 4:1 (sample NF7)

The Ni^{2+} to Fe^{3+} ratio was found to be 3.54, which is slightly higher than the starting value of 3, suggesting that not all the Fe^{3+} was incorporated to the LDH. Moreover, the C, H and N contents were 1.53, 2.67 and 0.21 in weight %, respectively, thus, the general formula of the Ni:Fe LDH can be estimated as $Ni_{0.78}Fe_{0.22}(OH)_2A_x{\cdot}nH_2O$ (A= counter anions). The presence of N could have been related to the partial compensation of the positive charge of the layers by nitrate anions or by the adsorbtion/intercalation of TEA molecules. The presence of TEA in the sample was further confirmed by FT-IR spectroscopy. The spectrum, presented in the Figure 4.2.5 a, showed weak peaks at 1155 cm^{-1} and 1040 cm^{-1} (green labels) which are characteristic for C-N stretching mode in tertiary amines.[204] However, the presence of

nitrate anions could not be excluded since the vibration peaks of NO_3^- overlap with the stretching mode of CO_3^{2-}(observed at 1350 cm^{-1}), which most probably was incorporated between the layers.[26] The broad band at 3450 cm^{-1} was related to OH stretching mode in brucite-like layers and also interlayer and absorbed water, which gave rise to another peak at 1645 cm^{-1}.[99, 161] The strong absorption band centred at 695 cm^{-1} is typical for LDHs and it was attributed to the lattice vibration υ_{M-O}.[26]

The XRD pattern (Figure 4.2.5 b) was typical of LDH, [26, 173] and it was indexed as hexagonal symmetry (a= 3.08 Å, c=23.55 Å). No additional peaks were observed, thus confirming the high quality of the material.

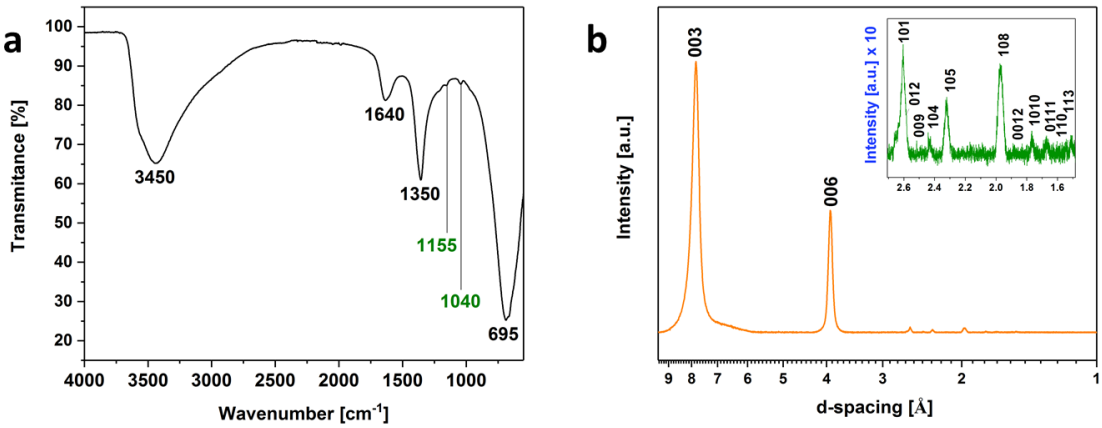

Figure 4.2.5 a) FT-IR spectrum and b) X-Ray diffraction pattern of $Ni_{0.78}Fe_{0.22}(OH)_2A_x{\cdot}nH_2O$. In the inset it is shown the zoomed d-spacing region of 1.5-2.7 Å.

The TGA analysis (Figure 4.2.6) showed a 30 % mass loss which, as expected for LDH materials, took place in a two-step process.[173] First, in the temperature range of 30-200 ^oC, the adsorbed and interlamellar water was removed (10 % mass loss), which allowed to calculate the amount of water in the sample (n value) of 0.6, yielding the formula $Ni_{0.78}Fe_{0.22}(OH)_2A_x{\cdot}0.6H_2O$. Then, at higher temperatures (200-800 ^oC) the weight loss was due to the dehydroxylation of the brucite-like layers and the decomposition of the counter anions.[26]

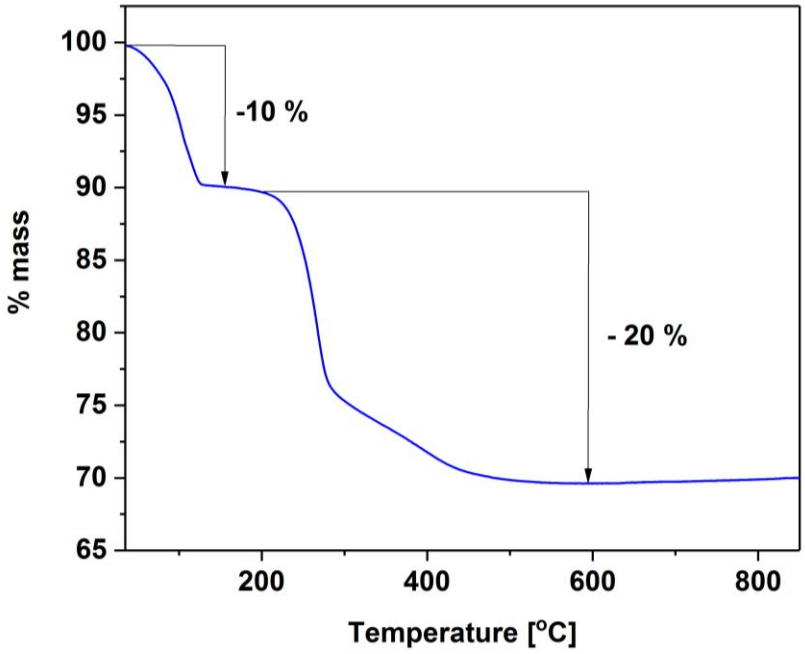

Figure 4.2.6 TGA analysis of $Ni_{0.78}Fe_{0.22}(OH)_2A_x{\cdot}0.6H_2O$.

The BET surface area of $Ni_{0.78}Fe_{0.22}(OH)_2A_x{\cdot}0.6H_2O$ hexagonal platelets was 27.5 m^2/g, which is almost five times lower in comparison to the value obtained for the flowers (130.61 m^2/g), described in the previous Section. This difference was most probably the result of a strong agglomeration of the hexagons after drying, which was required to perform the BET measurement.

TEM analysis (Figure 4.2.7 a) showed hexagonal platelets with diameters around 1 μm and below, with well-defined and sharp edges. The weak homogenous contrast observed in the images suggested a uniform thickness of the single flakes. Moreover, SAED (Figure 4.2.7 b) showed a hexagonal arrangement of diffracted peaks, typical for in-plane symmetry in LDH,[26] the spots were indexed to the plane family of (110), (100) and (300).[104, 205]

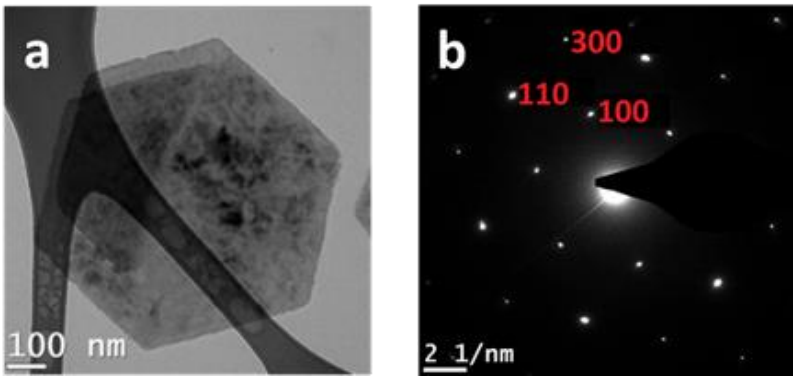

Figure 4.2.7 a) TEM micrograph and b) SAED of $Ni_{0.78}Fe_{0.22}(OH)_2A_x{\cdot}0.6H_2O$.

$Ni_{0.78}Fe_{0.22}(OH)_2A_x{\cdot}0.6H_2O$ flakes were further analysed by AFM. A typical tapping-mode AFM image showed two-dimensional hexagons (Figure 4.2.8). The height profiles revealed that the platelets had a flat terrace and a typical height of the representative flake was around 18 nm, which is consistent with a thickness of around 20 layers.[104, 173]

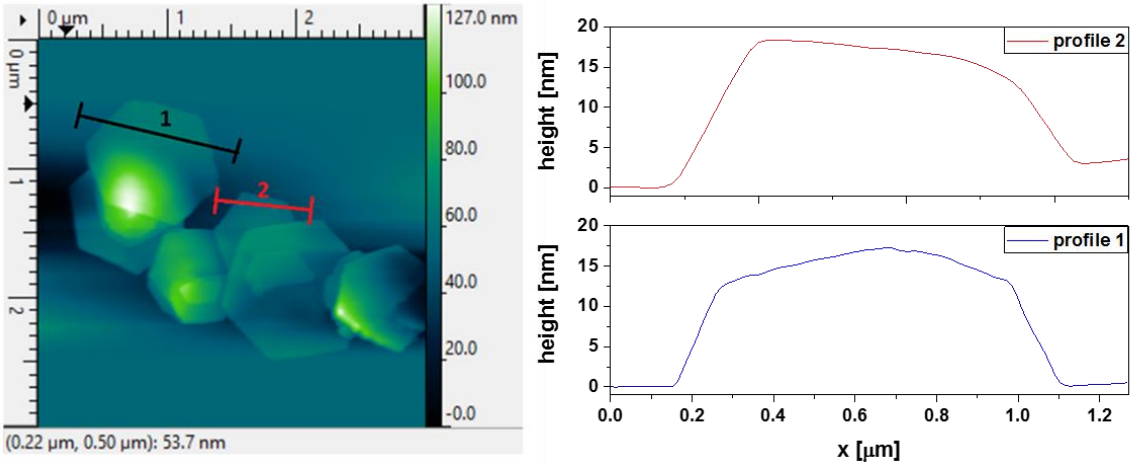

Figure 4.2.8 AFM image and height profiles of $Ni_{0.78}Fe_{0.22}(OH)_2A_x{\cdot}0.6H_2O$.

The homogeneous distribution of the metal cations within the LDH structure[26] was checked by EDX mapping performed under SEM (Figure 4.2.9). Nickel, iron and oxygen were evenly spread in the flakes, which indicated the consistent substitution of Fe^{3+} in the brucite-like layers of $Ni(OH)_2$.

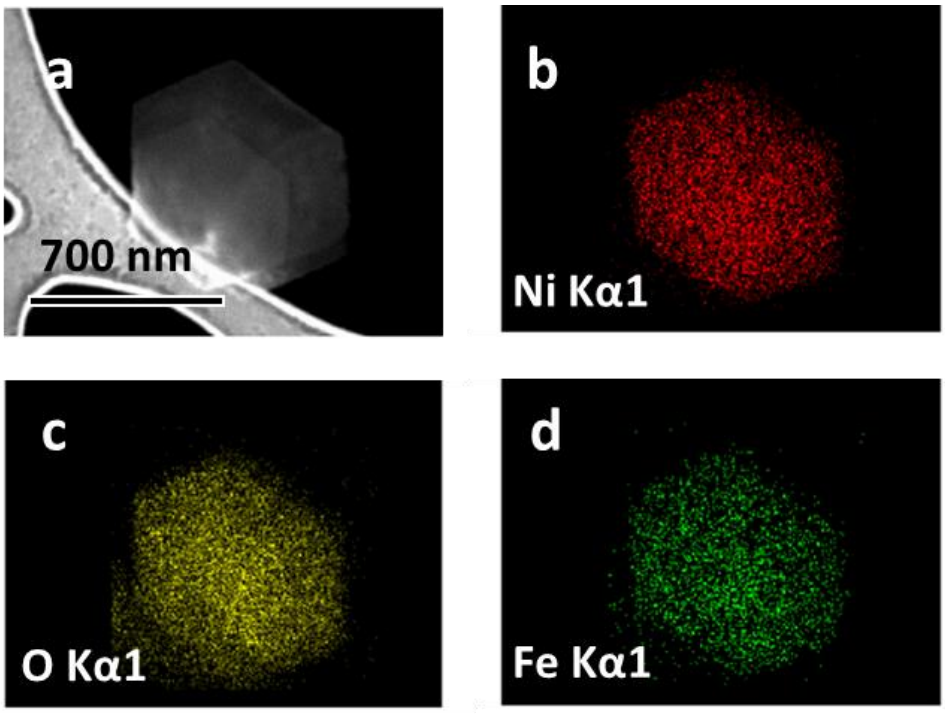

Figure 4.2.9 a) SEM electron image and distribution of b) nickel, c) iron and d) oxygen within a $Ni_{0.78}Fe_{0.22}(OH)_2A_x \cdot 0.6H_2O$ flake.

4.2.2 $Ni_{0.78}Fe_{0.22}(OH)_2A_x \cdot 0.6H_2O$ formation mechanism

As mentioned in the beginning of this Chapter, the main difficulty in the synthesis of Fe^{3+}-containing LDH is the fast precipitation of insoluble $Fe(OH)_3$ when the pH is above 2.[181, 182] However, in the present study, a highly crystalline and pure material was obtained starting from a pH as high as 6.6. Since the formation of a gel-like brown precipitate during the initial mixing step at RT was observed, a detailed study was performed in order to understand the reaction mechanism for the synthesis of $Ni_{0.78}Fe_{0.22}(OH)_2A_x \cdot 0.6H_2O$.

The brown precipitate was isolated by centrifugation, washed several times with water and analysed by FT-IR, XRD and TEM.

In the FT-IR spectrum (Figure 4.2.10 a) a broad absorption band with a maximum at 3270 cm^{-1} was attributed to υ_{O-H} stretching mode, which is typical for hydroxides and also to the structural/adsorbed water. Additionally, a peak at 1640 cm^{-1} confirmed the presence of water. Moreover, the peaks at 1470 cm^{-1} and 1360 cm^{-1} were assigned to the Fe-O and Fe-OH, respectively, which suggested that the precipitate was most probably one of the forms of ferric hydroxide or oxyhydroxide.[206, 207] Furthermore, a very strong inflection at about 1000 cm^{-1} could be explained by the deformation

vibration of surface OH groups in ferric hydroxides.[207] Weak absorption bands at the region of 1200-1000 cm^{-1} might have been related to the partial complexation of Fe^{3+} by TEA molecules.[199]

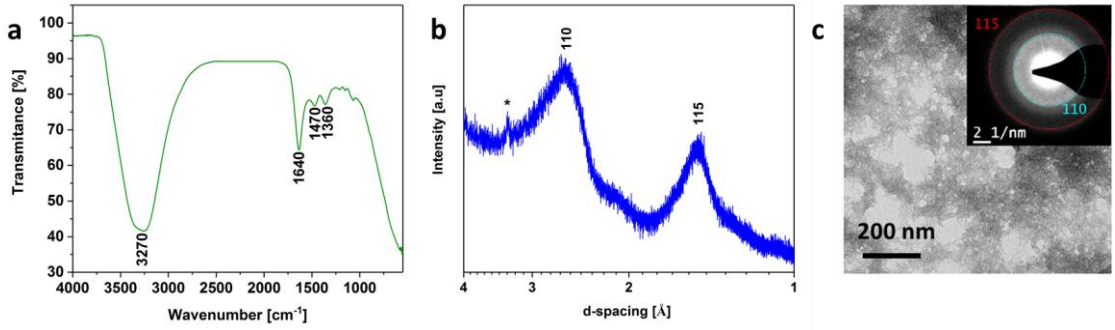

Figure 4.2.10 a) FT-IR spectrum, b) XRD pattern and c) TEM micrograph and SAED (in the inset) of the precipitate formed at RT.

The XRD pattern of the precipitate showed that the material presented a low degree of crystallinity, as only two broad peaks at about 2.6 Å and 1.5 Å were detected (Figure 4.2.10 b). Low crystallinity is typical for ferric oxyhydroxides,[208] and a similar XRD pattern was previously observed in the literature[209] for two-line ferrihydrite (JCPDS card 29-0712). The weak signal at a d-spacing of 3.3 Å (labelled as *) was most probably related to the partial formation of six-line ferrihydrite.[210]

The precipitate formed at RT, identified as two-line ferrihydrite on the basis of XRD, was additionally characterized by TEM microscopy (Figure 4.2.10 c). The material did not present a defined morphology and it was composed of nanoparticles with a very small size which were strongly agglomerated (Figure 4.2.10 c). In the SAED (inset in the Figure 4.2.10 c) two bright, diffused rings were observed and their positions fitted well to the pattern obtained by XRD (Figure 4.2.10 b). TEM results were in a good agreement with those found in the literature confirming that the precipitate was two-line ferrihydrite.[211]

Two-line ferrihydrite is a poorly crystalline and thermodynamically unstable Fe^{3+} oxide which finally transforms to more crystalline forms,[212, 213] depending on the temperature and pH. Considering that those parameters were both changing during thermal decomposition of urea (see Chapter 3.1), the author suspect, in the presence of Ni^{2+} and CO_3^{2-}, the two-line ferrihydrite transformed into Ni_xFe_y LDH. Regarding this, the mechanism and kinetics of the two steps that comprised the synthesis (stirring at RT,

where two-line ferrihydrite was formed, and the second step at 100 °C, when Ni_xFe_y LDH was obtained) were studied by time-controlled UV-Vis measurements (Section 4.2.2.1 and 4.2.2.3).

4.2.2.1 Time-controlled precipitation of two-line ferrihydrite at RT

Time-controlled UV-Vis measurements at RT were performed in order to follow the kinetics of the Fe^{3+} precipitation in the starting solution by monitoring the absorbance of the supernatant. Since the unbound Fe^{3+} has a strong broad absorbance in the range of 250-400 nm, the absorbance at 350 nm was chosen to observe the changes in Fe^{3+} concentration.

Time-dependent measurements showed a linear decrease during the first two hours and then more than 2/3 of the starting Fe^{3+} amount precipitated within the following hour. In the next hours of stirring the reaction mixture at RT, the Fe^{3+} ions formed two-line ferrihydrite at a slower rate. The measurements were performed for 9 hours and after this time the absorbance remained constant, which indicated that the precipitation of the Fe^{3+} was completed. The pH of the solution was also checked, and persisted at a constant value of 6.6 during the whole process.

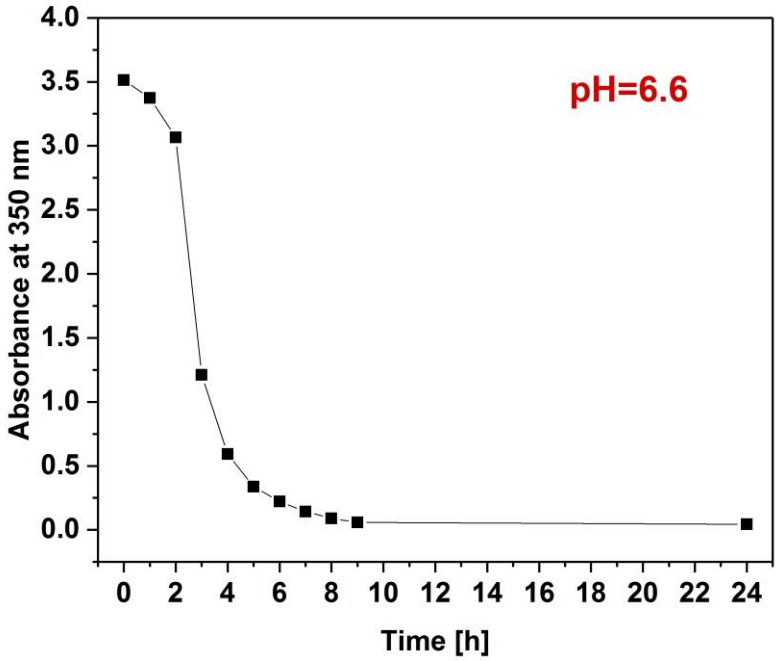

Figure 4.2.11 Absorbance at 350 nm of the supernatant of the reaction mixture after different stirring time at RT.

4.2.2.2 Ni^{2+} complex in the reaction mixture at RT

As described above, the Fe^{3+} precipitated as two-line ferrihydrite, so the remaining solution must have been composed of Ni^{2+}, NO_3^-, TEA and urea. Several coordination compounds of Ni-TEA-NO_3^- have been described[205, 214] in the form of blue crystals, which differ from the clear, pale green/blue solution obtained in the present study. This difference was most probably the result of an insufficient amount of TEA in relation to Ni^{2+}, since the TEA:Ni^{2+} ratio was 4:3 and should have been 2:1 to form $[Ni(TEA)_2](NO_3)_2$ crystals. In order to define the coordination of Ni^{2+}, the reaction mixture was analysed by UV-Vis and NMR spectroscopy and compared to the spectrum of pure $Ni(NO_3)_2$ and TEA.

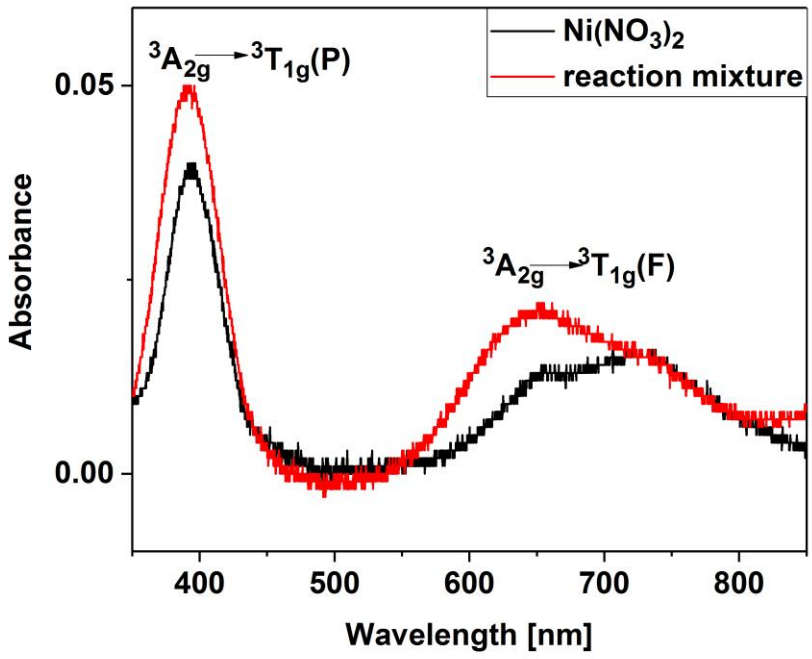

Figure 4.2.12 UV-Vis spectrum of $Ni(NO_3)_2$ and the reaction mixture.

The absorption spectra of both $Ni(NO_3)_2$ and the reaction mixture (Figure 4.2.12) showed two weak bands assigned to d-d transitions corresponding to an octahedral coordination geometry of Ni^{2+}.[205, 215, 216] The sharp peak centred at 390 nm was assigned to the $^3A_{2g}\rightarrow{}^3T_{1g}(P)$ transition in both cases,[205, 215] although the absorbance was higher for the reaction mixture. Moreover, the doublet with maxima at 656 nm and 726 nm, which was ascribed to the $^3A_{2g}\rightarrow{}^3T_{1g}(F)$ transition (observed in the spectrum of $Ni(NO_3)_2$, typical of nickel(II) aqua complex ($[Ni(H_2O)_6]^{2+}$),[216, 217] was

slightly shifted towards lower wavelengths in the reaction mixture. Similar results (higher absorbance of the peak at 390 nm and a blue shift at 656-720 nm) were previously observed by Agarwala *et al.*[217] for various Ni-TEA complexes in solution, including $[Ni(TEA)_2]^{2+}$, $[Ni(TEA)_2(OH)_2]^{2+}$ and $[Ni(TEA)]^{2+}$ although, at this stage, it was not possible to unambiguously define the form of the Ni-TEA complex, which most probably consisted of a mixture of Ni:TEA compounds with different stoichiometries.

The reaction mixture was also characterized by ^{1}H and ^{13}C NMR spectroscopy and compared to the spectrum of pure TEA (Figure 4.2.13). The changes in both proton and carbon environment were clearly visible which indicated formation of Ni-TEA coordinative compound. The ^{1}H NMR spectrum of pure TEA showed two triplets for NCH_2 and OCH_2 which were also observed in the spectrum of the reaction mixture, but those were broadened and moved downfield in the presence of Ni^{2+}, which was in good agreement with the theoretical predictions, suggesting that the loss of electron-density upon coordination to the metal results in shifts to higher frequency of the adjacent ligand protons and the signals broadening.[218] Differently, in the ^{13}C NMR spectrum the trend was not observed: OCH_2 singlet was shifted upfield, which was also previously observed in metal-organic compounds,[219] while the signal from NCH_2 was slightly shifted downfield.

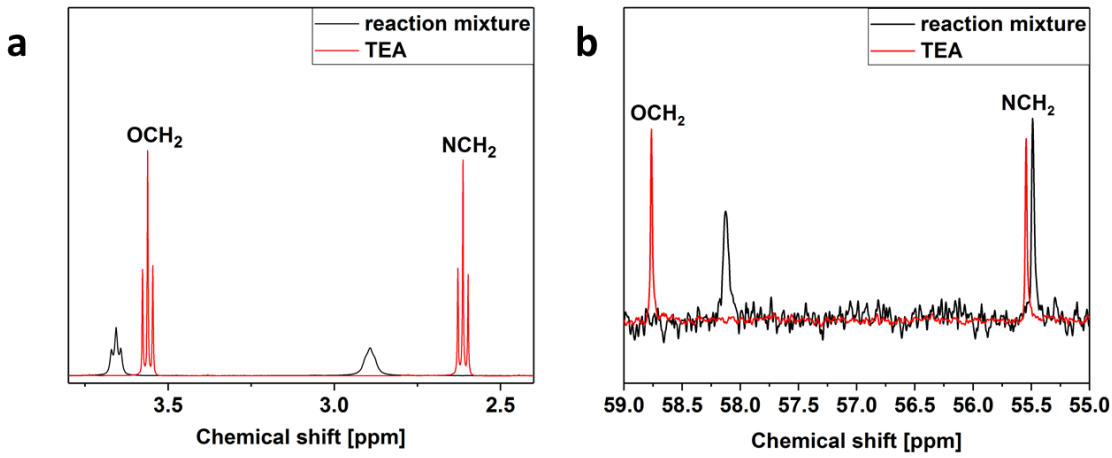

Figure 4.2.13 Comparison of the a) ^{1}H and b) ^{13}C NMR spectrum of the reaction mixture and TEA.

To summarize, on the basis of UV-Vis and NMR spectroscopy, nickel(II) was present in the reaction mixture as an octahedral Ni-TEA complex, however its chemical formula could not be accurately defined, due to the many possibilities of ligand

coordination,[217, 220] and most probably it consisted of a mixture of Ni-TEA coordination compounds in quick kinetic equilibrium.

4.2.2.3 Ni_xFe_y LDH formation by thermal decomposition of urea at 100 °C

As explained in Chapter 3.1, heating the reaction mixture to 100 °C led to the thermal decomposition of urea and the subsequent pH increase. Then, the Fe^{3+} and Ni^{2+} were released and, in the presence of OH^- and CO_3^{2-} the ions precipitated as Ni_xFe_y LDH. The changes in the pH and the absorbance at 350 nm, related to the Fe^{3+} concentration in the supernatant are presented in Figure 4.2.14. Within the first 4 hours of heating the mixture, a dramatic raise of Fe^{3+} concentration was observed, suggesting the decomposition of two-line ferrihydrite. In the next 4 hours, Fe^{3+} concentration continued to raise, but between the 8th and the 12th hour of the experiment it started to drop and this trend sustained till the end of the measurements, which were performed for the next 36 hours. Further heating and stirring resulted in a decrease of the quality of the flakes. The pH increased almost linearly during the first 12 hours of heating and after this time period the changes were slower.

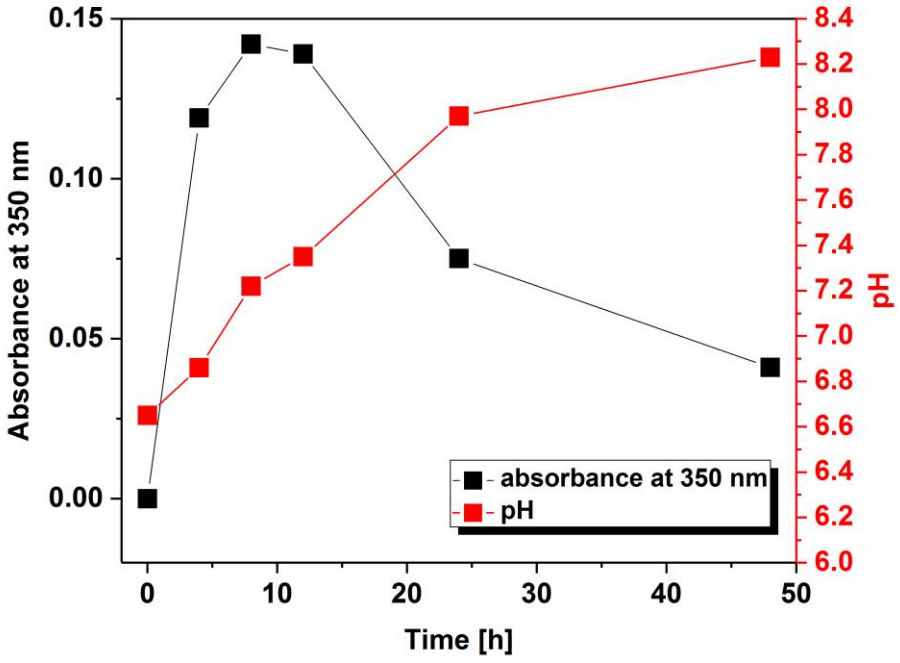

Figure 4.2.14 Evolution of the Fe^{3+} concentration and the pH value within 48 hours of heating the reaction mixture.

The precipitate formed after 4, 12 and 24 hours of heating the reaction mixture was analysed by SEM as presented in the Figure 4.2.15.

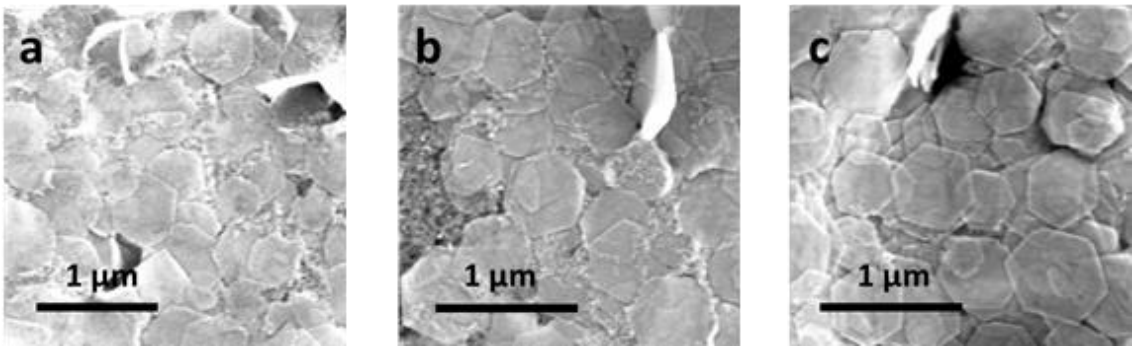

Figure 4.2.15 SEM micrographs of Ni_xFe_y LDH formed after a) 4 hours, b) 12 hours and c) 24 hours of heating the reaction mixture at 100 ^oC.

Hexagonal flakes with slightly jagged edges and diameters around 0.5 µm were obtained after 4 hours of heating (Figure 4.2.15 a). Nevertheless, these flakes co-existed with a precipitate which was, most probably, remaining two-line ferrihydrite and it was observed even after 12 hours of heating (Figure 4.2.15 b). Subsequent heating for additional 12 hours (Figure 4.2.15 c) led to the complete consumption of two-line ferrihydrite and only hexagonal platelets were visible under SEM. The amount of the obtained material after 24 hours of the reaction was 60 mg. However, by extending the reaction time for another 24 hours the reaction yield increased by an additional 30 %, up to 80 mg, while flakes geometry remained unchanged. Most probably, after 24 hours of heating, all two-line ferrihydrite decomposed releasing Fe^{3+} ions to the solution (Figure 4.2.14) and only part of those ions precipitated as Ni_xFe_y LDH. When the heating was continued for 24 hours more, another fraction of Fe^{3+} ions formed LDH, which resulted in lowering the absorbance at 350 nm (Figure 4.2.14) and increasing the reaction yield.

To the best of the author's knowledge, this is the first time when regular hexagonal platelets of Ni_xFe_y LDH were produced in a two-step process. During the first step thermodynamically unstable iron oxyhydroxide and Ni-TEA complex were formed at room temperature. Subsequently, the second step relied on heating the reaction mixture to 100 ^oC, which caused thermal decomposition of urea leading to pH increase, which resulted in recombination of the reaction intermediates and formation of Ni_xFe_y LDH. Moreover, the formation mechanism of those platelets was carefully studied.

4.3 Electrocatalytic activity in OER

Finally, the electrocatalytic activity in OER of both Ni_xFe_y LDH (the nanoflowers described in section 4.1 and the hexagonal platelets described in section 4.2) (see section 1.1.3.1),[101, 103-105] was tested (credited to Joao Coelho).

Experimental Section:

The samples were dispersed in water and deposited onto nickel foam substrates by ultrasonic spray deposition (USI Prism Ultracoat 300). The spray head was moved at a constant spray height (35 mm) and speed (100 $mm \cdot s^{-1}$) by an automated gantry in x and y directions drawing a previously designed and specified spray pattern that produced a uniform film. Electrochemical measurements were conducted in a BioLogic VMP 300. 1 M KOH was used as electrolyte and platinum wire and Ag/AgCl were used as counter and reference electrodes, respectively. Both cyclic and linear sweep voltammetry curves were acquired in the range from 0 V to 0.6 V at a scan rate of 5 $mV \cdot s^{-1}$ against Ag/AgCl. All the potentials were calibrated with respect to a reversible hydrogen electrode (RHE) reference as follows:[105] $V_{RHE} = V_{Ag/AgCl} + V/AgCl(vsRHE) + (0.059 \times pH)$. All voltammetry curves are shown with compensated cell resistance (iR).

It can be seen from the Figure 4.3.1 that the synthesized Ni_xFe_y LDH materials presented an electrocatalytic activity towards OER. In the present study, it was assumed that the resulting high current densities resulted from oxygen evolution.[105, 221] The required experimental verification could not be performed, due to the lack of adequate equipment. However, the curves presented in Figure 4.3.1 have been reported several times in the literature as resulting from OER.[101, 104, 105] Moreover, the cyclic voltammetry curves (inset in Figure 4.3.1) revealed well defined cathodic and anodic peaks at 1.35 V/RHE and 1.46 V/RHE, respectively. These peaks are usually associated with the Ni^{2+}/Ni^{3+} redox couple and the overall electrochemical process can be described by:

$$Ni^{2+} - Fe + OH^- = Ni^{3+}(OH^-) - Fe + e^-$$

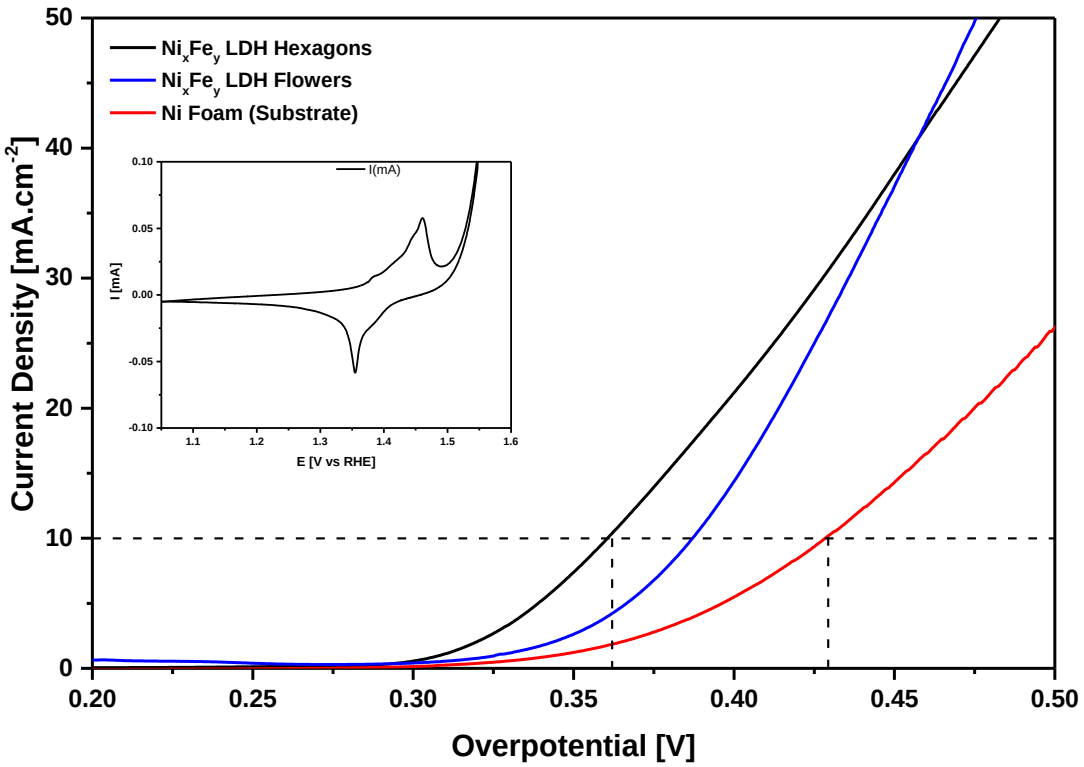

Figure 4.3.1 Linear sweep voltammetry curves for the Ni_xFe_y LDH hexagons, flowers and Ni foam at a scan rate of 5mVs^{-1} in 1M KOH. The horizontal dashed lines indicate the overpotential required to obtain a current density of 10 mA·cm^{-2}. This value corresponds to a 10 % efficient solar water-splitting device and it has been commonly accepted as the figure of merit for OER catalysts.[221] In the inset it is shown a voltammogram revealing the typical peaks for the Ni^{3+}/Ni^{2+} redox couple.

In a very simple way, nickel sites change their oxidation states due to insertion/desertion of OH^- ions from the structure interlayer spacing.[105] So far, it has been shown that the prepared Ni_xFe_y LDH can in fact be used as catalysts for the oxygen evolution reaction. However, it is quite important to place the obtained results in a much broader context. The overpotential values of as-synthesised Ni_xFe_y LDH flowers and hexagons were compared with other similar samples reported in the literature (Table 4.3.1).

Table 4.3.1 Comparative table of the overpotential of synthesized Ni_xFe_y LDH versus other Ni_xFe_y LDH catalysts reported in the literature.

Material	OER Overpotential [V]	Mass load [mg]	Conditions
Ni_xFe_y LDH flowers (this work)	0.39	0.25	5mV·s^{-1} in 1 M KOH
Ni_xFe_y LDH hexagons (this work)	0.36	0.25	5mV·s^{-1} in 1 M KOH
Ni foam (this work)	0.43	-	5mV·s^{-1} in 1 M KOH
Topochemical oxidation route[101]	0.37	0.25	5mV·s^{-1} in 0.1 M KOH
Cheng Tang[221]	0.46	0.25	1 M KOH
Fang Song *et al*[104]	0.30	0.07	5mV·s^{-1} in 1 M KOH

It was clear that the overpotential obtained in this study was consistent with other published work. The observed variations in the OER overpotential among different samples were likely to be a consequence of the LDH thickness, substrate and solution concentration.[105] In spite of presenting the same chemical composition of their bulk counterparts, monolayer LDH are always prefered as their catalytic activity is higher due to more accessible active sites being a result of an increased surface area.[33, 103] Higher electrolyte concentrations can also positively impact the OER activity of Ni_xFe_y LDH.[222] Currently, the state of the art of these catalysts rely on ultrathin 2D materials combined with carbon materials.[101] The synergistic effect resulting from the LDH-carbon combination has allowed to reduce the OER overpotentials to values as low as 0.30 V.[104] Therefore, the optimization of the OER catalytic properties of the LDH presented in this study would be considered for future work.

4.4 Conclusions

The work presented in this Chapter describes the synthesis of Ni_xFe_y LDH by homogeneous precipitation methods with the use of TSC and TEA as capping agents. In the optimization procedure, different concentrations of the capping agents (in relation to

Fe^{3+}) were used and the reactions were performed at 100 ºC and 150 ºC. The formation mechanism of hexagonal platelets of Ni:Fe LDH with TEA was carefully studied.

The synthesis with addition of TSC led to formation of flower-like $Ni_{0.75}Fe_{0.25}(OH)_2(C_6H_5O_7)_x(CO_3)_y{\cdot}nH_2O$ LDH nanoparticles at 150 ºC at Fe^{3+}:TSC ratios of 1:1 and 2:1. The heterogeneous nature of the counter anion compensating the positive charge of the layers was confirmed by FT-IR spectroscopy and XRD analysis. Surface area of the flowers was 130.61 m^2g^{-1}. As far as the author is concerned, this is the first time when the flower-like nanostructures of Ni:Fe LDH were synthesised by homogeneous precipitation in the presence of TSC.

On the contrary, the synthesis with TEA resulted in the formation of hexagonal platelets with sharp edges presenting lateral sizes from 0.5 to 1 μm and thicknesses around 18 nm. The TEA concentration drastically changed the particles geometry, and only when TEA:Fe^{3+} was 4:1, regular hexagons were obtained at both temperatures (100 ºC and 150 ºC), although at 150 ºC the hexagons were contaminated with impurities in the form of small particles. The real Ni^{2+}:Fe^{3+} ratio was slightly higher than the starting value, and some TEA molecules and/or nitrate anions were intercalated or adsorbed within the LDH structure leading to the formula $Ni_{0.78}Fe_{0.22}(OH)_2(A)_x{\cdot}0.6H_2O$. Nevertheless, the obtained flakes presented a high degree of crystallinity showing sharp, symmetric peaks in the XRD pattern. EDX analysis performed under SEM showed the homogeneous distribution of Ni, Fe and O within the platelets.

The formation mechanism of the hexagonal flakes was analysed by splitting the synthesis procedure into two steps: at RT and at 100 ºC. At RT, the reaction mixture consisted of a brown precipitate of two-line ferrihydrite and a pale green/blue solution of the mixture of Ni-TEA complexes with different stoichiometries. When the reaction mixture was heated to 100 ºC, Fe^{3+} and Ni^{2+}were gradually released, combined and reacted with OH^- and CO_3^{2-}, thus forming the Ni_xFe_y LDH hexagonal platelets. The synthesis of Ni-Fe LDH in a two-step process is a novel method, which was not previously described in the literature.

Both nanostructures were tested as catalysts in OER giving the overpotential values of 0.39 V and 0.36 V for the flowers and hexagons, respectively. Those results are typical of Ni_xFe_y LDH and probably, by exfoliation to single layer nanosheets, the overpotential can be reduced, which is considered as a future work.

5 Synthesis of Amine-Templated Gallium Chalcogenide Nanotubes

1D gallium chalcogenide nanostructures have shown a great potential in several applications varying from optoelectronic devices to biological fields.[111, 120, 223] Similarly to other semiconductors,[224] when the particle size is reduced to the nanoscale, materials with different optical, electronic and mechanical properties arise.[224] Moreover, the small size of the active components might lead to the development of smaller and more effective devices that could make a valuable contribution to the semiconductors industry. Despite several synthesis methods, which have been widely used to obtain semiconducting 1D nanoparticles, most of these processes, due to their high cost and complexity, are not applicable in industry. Therefore, there is an urgent need to develop simple and affordable methods to allow industrial scale fabrication of semiconducting nanomaterials. Regarding this, special attention has been placed on wet-chemistry methods, which have shown their great potential for the preparation of nanostructures with controlled geometry.

Moreover, wet-chemistry synthesis using long-chain amines was successfully applied to prepare several anisotropic-shaped nanomaterials,[124, 225] including 1D nanostructures of vanadium oxide,[126] vanadium sulfide[127] and copper sulfide.[226] Long-chain amines are particularly interesting in the synthesis of nanoparticles due to their multiple role: as a solvent (reaction media), surfactant (stabilizer)[124] and as a template (directing the nanostructures formation by controlling nucleation and growth processes).[227, 228]

Long-chain amines have relatively high boiling point (ranging from 259 ^{o}C of dodecylamine to 323 ^{o}C of hexadecylamine, used in the current work), which allows to carry out reactions at temperatures high enough to induce decomposition of metal and chalcogen precursors and their further reaction at atmospheric pressure.[124] Moreover, long-chain amines act as an electron donor at elevated temperatures.[124, 125] Recent studies performed on the system sulfur-oleylamine suggested formation of alkylammonium polysulfides at relatively low temperatures, which upon temperature increase reacted with an excess of amines and released H_2S that combined with the metal precursor forming metal sulfide.[229]

Furthermore, the role of long-chain amines as a surfactant and a template prevents agglomeration and also enables crystal growth in a certain direction, as schematically presented in the Figure 5.1. In the case of long-chain amines such templates are formed due to amines self-assembly properties.[230]

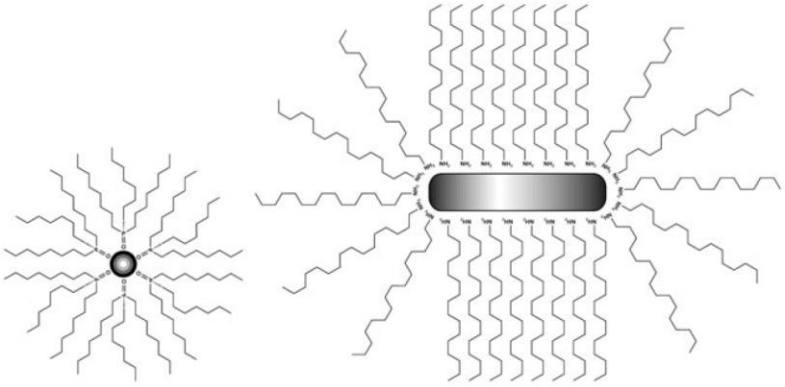

Figure 5.1 A Schematic template mechanism for nanoparticles growth with the use of surfactant/template. Adapted from ref. 227.[227] Copyright 2017 John Wiley and Sons (licence number 4119410018096).

In such surfactant/template systems, initially formed crystal nuclei are surrounded by surfactant molecules, which limits their growth.[227]

In this work, a heating-up synthesis method with the use of long-chain amines is proposed for the preparation of gallium chalcogenide nanotubes. This heating-up method relies on mixing all substrates at room temperature and then, due to a gradual temperature increase, nucleation and growth of the nanocrystals is induced. Firstly, at low temperatures the reaction mixture is comprised of precursors dissolved in amines, but when the temperature is increased, those precursors decompose and release monomers which combine to form crystal nuclei and finally nanocrystals.[231] In the presence of a surfactant or template it is possible to direct the anisotropic growth of these nanocrystals in a certain direction.[227]

In this work, a heating-up procedure was applied to obtain amine-templated gallium chalcogenide (sulfur, selenium and tellurium) nanotubes, abbreviated as $A_tGa(S/Se/Te)_{x/y/z}$ NT. The synthesis conditions were studied and optimized to obtain the nanotubes in maximum quality and quantity. The nanostructures were further tested as active materials for electrodes of lithium ion battery, in collaboration with John CF Zhang (researcher in the Prof. Nicolosi group). The methodology used this chapter was

novel and the results were published in *Nanoscale,* 2016, 8, 11698-11706 (DOI:10.1039/C6NR01663D).[228]

Experimental Section:

In the optimized synthesis procedure, 1 mmol of gallium(III) acetylacetonate [$Ga(acac)_3$], 2 mmol of sulfur or 1.5 mmol of selenium were added to a two-neck flask containing a degassed mixture of 100 mmol of hexadecylamine and 20 mmol of dodecylamine. The mixture was heated to 150 °C under nitrogen atmosphere and reflux system and maintained at this temperature for 1 h in order to completely remove oxygen and moisture. After this time, the temperature was increased to 200 ºC and the reaction was carried out for 24 and 72 hours for sulfur and selenium precursor, respectively. The setup used in the synthesis is presented in the Figure 5.2.

After the reaction time, the system naturally cooled down, 10 ml of toluene were added to facilitate the washing procedure, and the formed precipitate was washed three times with warm (70 ºC) isopropyl alcohol (IPA). Colloidal suspensions of a white material in IPA were obtained in both cases.

The reaction yield was calculated in relation to the starting amount of gallium.

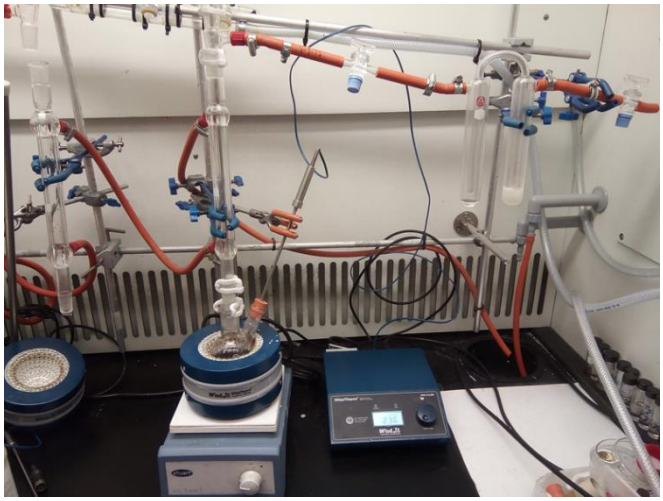

Figure 5.2 The setup used in the heating-up synthesis in long-chain amines.

5.1 Optimization of the synthesis of A_tGaS_x NT

The synthesis of A_tGaS_x NT was optimized by carrying out a set of reactions under different synthesis conditions by changing several parameters, including the temperature, sulfur to gallium ratio, reaction time and sulfur precursor (elemental sulfur,

diphenyl disulphide-Ph_2S_2, dibenzyl disulphide-Bz_2S_2 and di-isopropyl disulphide-$_iPr_2S_2$), as summarized in the Table 5.1.1.

Table 5.1.1 Optimization of the synthesis conditions of A_tGaS_x NT: temperature study (samples A-E), gallium to sulfur molar ratio study (samples C, F and G), time optimization (samples G-K) and study of disulfides as alternative sulfur precursors (samples L-N).

Sample	Sulfur precursor	Temperature [°C]	Ga : S molar ratio	Reaction time [h]	Yield [%]
A	S	**150**	1:1	144	-
B	S	**175**	1:1	144	n.a.
C	S	**200**	**1:1**	144	1.0
D	S	**225**	1:1	144	-
E	S	**250**	1:1	144	-
F	S	200	**1:1.5**	144	62.0
G	S	200	**1:2**	**144**	70.4
H	S	200	1:2	**6**	55.2
I	S	200	1:2	**12**	64.4
J	**S**	**200**	**1:2**	**24**	**70.8**
K	S	200	1:2	**72**	69.2
L	**Ph_2S_2**	200	1:2	144	-
M	**Bz_2S_2**	200	1:2	144	-
N	**$_iPr_2S_2$**	200	1:2	144	46.5

Firstly, 1 mmol of $Ga(acac)_3$ and 1 mmol of elemental sulfur reacted at different temperatures for 144 h (150–250 °C at intervals of 25 °C, Table 5.1.1, samples A–E). A colour change from pale yellow to transparent and the subsequent formation of a white precipitate were observed at 175 and 200 °C, which is the temperature range where the thermal decomposition/sublimation of $Ga(acac)_3$ occurs.[232] No precipitate was formed at 150 °C, most probably due to the slow kinetics. The synthesized materials were stable

in the solution up to 220 ºC, since the white precipitate obtained at 200 ºC dissolved at temperatures above 220-225 ºC.

The precipitates formed at 175 ºC and 200 ºC were characterized by SEM, which showed relevant differences between those materials: spheres with a diameter of several microns composed of intergrown nanotubes were produced at 175 ºC, whereas tubular hollow structures with lengths of 100-500 nm and diameters of tens of nanometres were obtained at 200 °C (Figure 5.1.1 a and b respectively). To improve the quality and yield of the tubular structures, the temperature was set to 200 °C in further experiments.

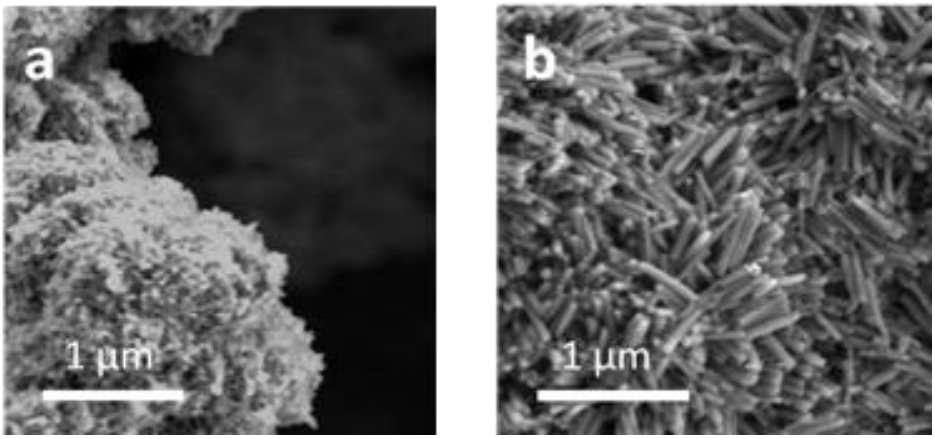

Figure 5.1.1 SEM micrograph of the materials obtained at a) 175 ºC and b) 200 ºC.

The effect of the molar ratio of the precursors was studied by adjusting initial gallium to sulfur molar ratio to 1:1, 1:1.5 and 1:2 (Table 5.1.1, samples C, F and G, respectively). The SEM analysis did not show any differences between the materials obtained when using different precursors ratios, but the reaction yield significantly increased when sulfur was used in excess, as presented in Table 5.1.1. Moreover, the time required for the white precipitate formation decreased from 72 h when using 1:1 ratio to 24 h and 2 h at 1:1.5 and 1:2 ratios, respectively. Thus, a gallium to sulfur ratio of 1:2 was selected to maximise the yield and reduce the reaction time.

The optimum reaction time was defined by measuring the amount of the precipitate formed after 6, 12, 24, 72 and 144 hours (Table 5.1.1, samples H, I, J, K and G, respectively). The maximum amount of the nanotubes was reached after 24 h of reaction.

Finally, alternative sulfur precursors, including Ph_2S_2, $_iPr_2S_2$ and Bz_2S_2 (Table 5.1.1 samples L–M, respectively), were explored in the synthesis of A_tGaS_x NT. In

these reactions, 1 mmol of $Ga(acac)_3$ was heated with 2 mmol of R_2S_2 (R = $_i$Pr, Ph, Bz) at 200 ºC for 144 hours. Nanotubes were only obtained when using Bz_2S_2 as a precursor showing a structure similar to the material produced with the use of elemental sulfur (Figure 5.1.1 and Figure 5.1.2), demonstrating that Bz_2S_2 can be also used as a suitable sulfur precursor for the synthesis of A_tGaS_x NT.

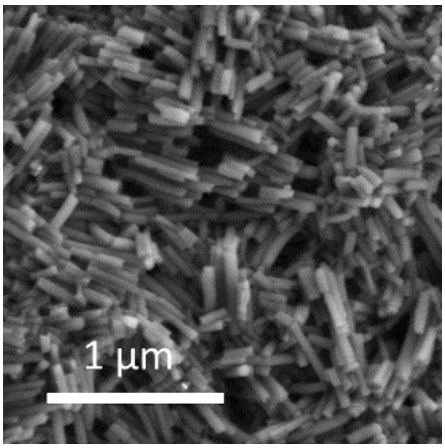

Figure 5.1.2 SEM image of A_tGaS_x NT obtained from Bz_2S_2.

The reactivity of the organic disulfides follows the trend Bz_2S_2 > $_i$Pr$_2S_2$ > Ph_2S_2.[233] In the presented study, only Bz_2S_2 seemed to be reactive enough at 200 ºC to release S^{2-} and produce nanotubes under the reaction conditions. Nevertheless, significantly lower amounts of the precipitate were obtained when using this precursor in comparison to sulfur (Table 5.1.1), so the latter was maintained as the preferred precursor for this reaction.

To sum up, the optimum reaction parameters for the synthesis of A_tGaS_x NT were found to be: 1 mmol of $Ga(acac)_3$ and 2 mmol of elemental sulfur reacted at 200 °C for 24 h.

5.2 Optimization of the synthesis of A_tGaSe_y NT

A similar procedure to that described for the synthesis optimization of A_tGaS_x NT was performed for A_tGaSe_y NT (see reaction parameters in Table 5.2.1).

Table 5.2.1 Optimization of the synthesis conditions of A_tGaSe_y NT: temperature study (samples O-S), gallium to selenium molar ratio study (samples Q, T and U), time optimization (samples Q and V-Y) and study of diselenides as alternative selenium precursors (samples Z and AA).

Sample	Selenium precursor	Temperature [ºC]	Ga : Se molar ratio	Reaction time [h]	Yield [%]
O	Se	**150**	1:1	144	-
P	Se	**175**	1:1	144	16.7
Q	Se	**200**	**1:1**	144	27.2
R	Se	**225**	1:1	144	32.2
S	Se	**250**	1:1	144	-
T	Se	200	**1:1.5**	**144**	74.0
U	Se	200	**1:2**	144	75.1
V	Se	200	1:1.5	**12**	1.2
W	Se	200	1:1.5	**24**	58.4
X	**Se**	**200**	**1:1.5**	**72**	**72.8**
Y	Se	200	1:1.5	**120**	73.9
Z	**Ph_2S_2**	200	1:1.5	144	-
AA	**Bz_2S_2**	200	1:1.5	144	-

In the synthesis of A_tGaSe_y NT, a white precipitate was formed at temperatures varying from 175 ºC to 225 °C (samples P, Q and R), showing that the range of temperatures for the synthesis of these nanotubes was broader in comparison to sulfur. Nanotubes synthesized at 175 °C (Figure 5.2.1 a) were smaller in size than those prepared at 200 °C (Figure 5.2.1 b), which indicated that the average size of the nanotubes can be controlled by the temperature at which the synthesis is performed. Moreover, SEM analysis of the sample synthesized at 225 °C showed a high number of

impurities (Figure 5.2.1 c), thus, 200 °C was selected as optimum synthesis temperature in order to maximize the size and quality of the nanotubes.

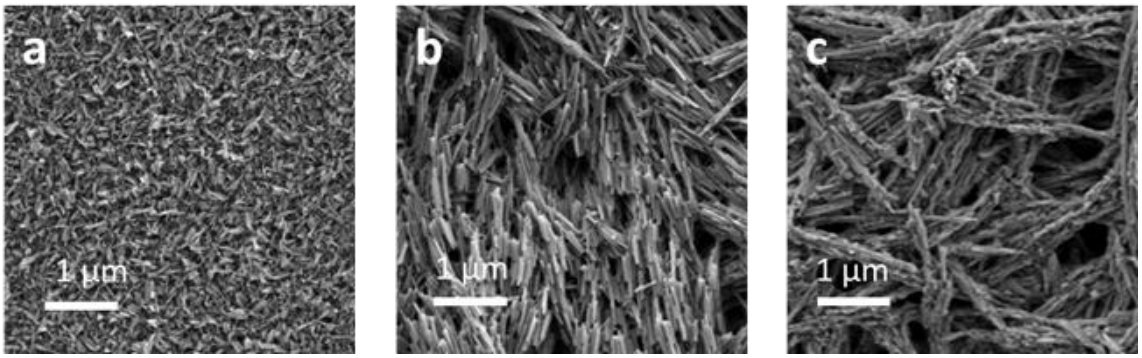

Figure 5.2.1 SEM micrograph of A_tGaSe_y NT synthesised at a) 175 °C, b) 200 °C and c) 225 °C.

Nanotubes produced at higher Ga:Se starting ratios resulted in formation of materials with the same morphology, although the amount of the obtained precipitate increased, as shown in the Table 5.2.1 (samples Q, T and U). The yield of the reactions with Ga:Se ratio of 1:1.5 and 1:2 was similar, so the ratio of 1:1.5 was selected in order to minimize the usage of selenium precursor.

Moreover, different reaction time (Table 5.2.1, samples T, V-Y) showed that the nanotubes are formed within 24 hours, while the maximum yield was reached after 3 days.

Alternative selenium precursors (Ph_2Se_2 and Bz_2Se_2) were also explored in the synthesis of the nanotubes (Table 5.2.1, samples Z and AA), but the formation of a precipitate was not observed in any case, which indicated that the reactivity of diselenides was not high enough to produce the nanotubes or other compounds at 200 °C. Regarding this, no further experiments were carried out with these chemicals.

In summary, the optimum conditions for the synthesis of A_tGaSe_y NTs were 200 °C during 72 h, using $Ga(acac)_3$ and elemental selenium in a molar ratio of 1:1.5.

5.3 Synthesis of A_tGaTe_z NT

The preparation of amine-templated gallium telluride nanotubes was also undertaken. However, the synthesis was not feasible in similar conditions to those described for sulfur and selenium derivatives. One of the possible reasons might have been a high melting point of tellurium (449.5 °C), in comparison to sulfur (115.2 °C)

and selenium (220.8 ^{o}C). All the syntheses were run for 144 hours and details are summarized in the Table 5.3.1.

Table 5.3.1 Parameters changed during synthesis of A_tGaTe_z NT: reactions with elemental tellurium at different temperatures (sample BB-FF) and various Ga:Te molar ratio (samples GG and HH), temperature study with the use of Bz_2Te_2 (samples II-NN).

Sample	Selenium precursor	Temperature [^{o}C]	Ga : Se molar ratio
BB	**Te**	**150**	1:1
CC	Te	**175**	1:1
DD	Te	**200**	**1:1**
EE	Te	**225**	1:1
FF	Te	**250**	1:1
GG	Te	200	**1:1.5**
HH	Te	200	**1:2**
II	**Bz_2Te_2**	**200**	1:2
JJ	Bz_2Te_2	**220**	1:2
KK	Bz_2Te_2	**230**	1:2
LL	Bz_2Te_2	**240**	1:2
MM	Bz_2Te_2	**265**	1:2
NN	Bz_2Te_2	**300**	1:2

Reactions performed between $Ga(acac)_3$ and elemental tellurium (BB to HH) did not show the formation of any precipitate and it was observed that, differently to sulfur and selenium, tellurium was not dissolved in the mixture of amines in the temperature range under study, as SEM and EDX analysis of the solid isolated after the reaction showed only the presence of small nanoparticles without a defined geometry identified as tellurium by EDX (Figure 5.3.1 a and b respectively).

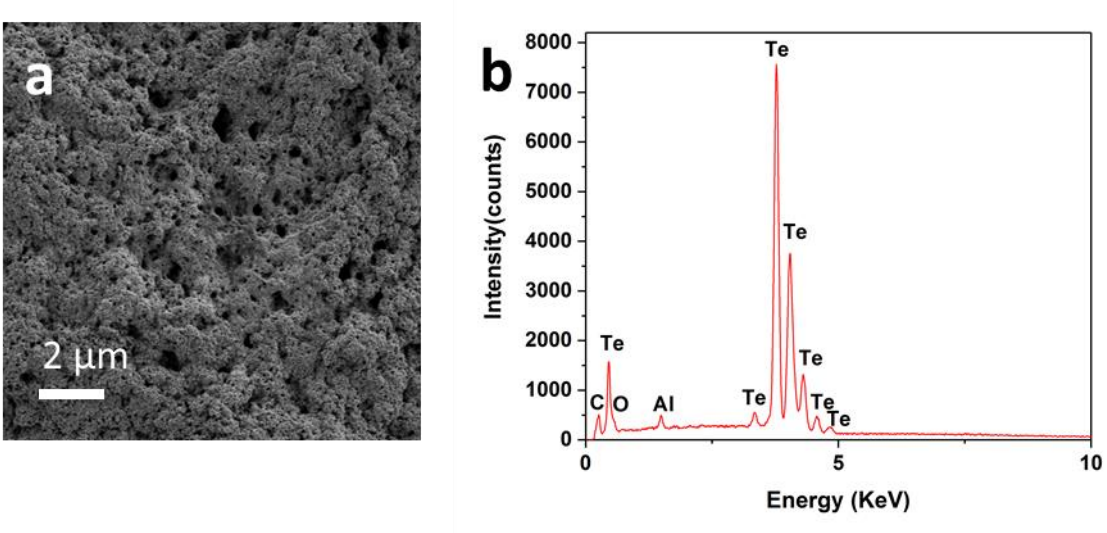

Figure 5.3.1 a) SEM micrograph and b) EDX spectrum of the precipitate isolated from the reaction FF, EDX signals of C, O and Al come from the SEM stub.

In contrast to the elemental tellurium, Bz_2Te_2 dissolved in the amines mixture at the temperatures under study and the formation of a precipitate was observed at the temperatures above 240 ^oC. SEM analysis of the solid showed that it consisted of polyhedral, needle-like particles reaching several microns in length which were identified as trigonal tellurium by XRD (Figure 5.3.2 a and b respectively).[234]

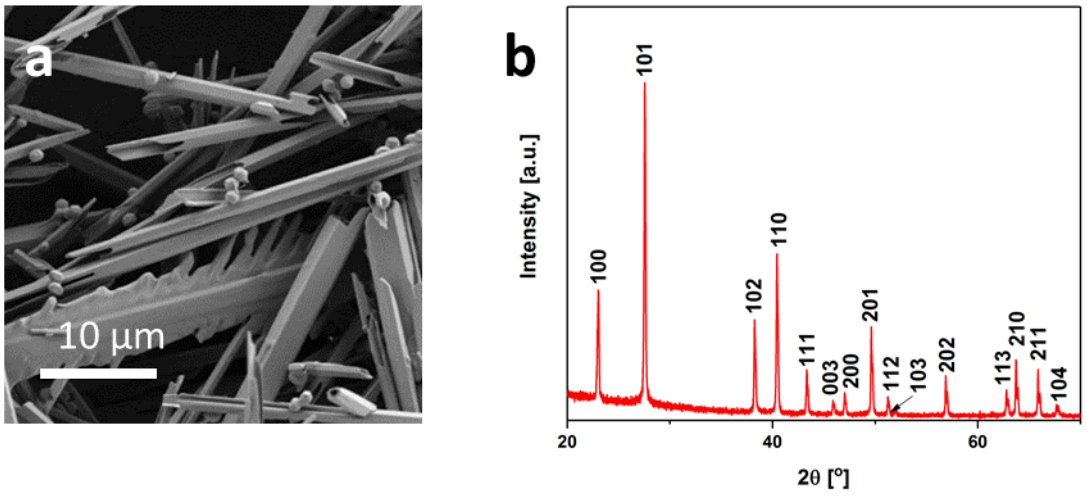

Figure 5.3.2 a) SEM image and b) XRD pattern of the sample MM.

These results showed that the amine templated gallium telluride nanotubes cannot be produced by heating-up synthesis in long-chain amines at 150-300 ^oC. Further

experiments to prepare these materials by a different chemical route should be considered.

5.4 Characterisation of A_tGaS_x and A_tGaSe_y NT

SEM analysis and low-magnification TEM showed hollow-core nanotubes with lengths in the range of 100-500 nm and 0.1-2 μm for A_tGaS_x NT and A_tGaSe_y NT, respectively (Figure 5.4.1). In most cases, the nanotubes had open caps, terminating in a circular shape and sometimes they showed a slit on the end side of the tube.

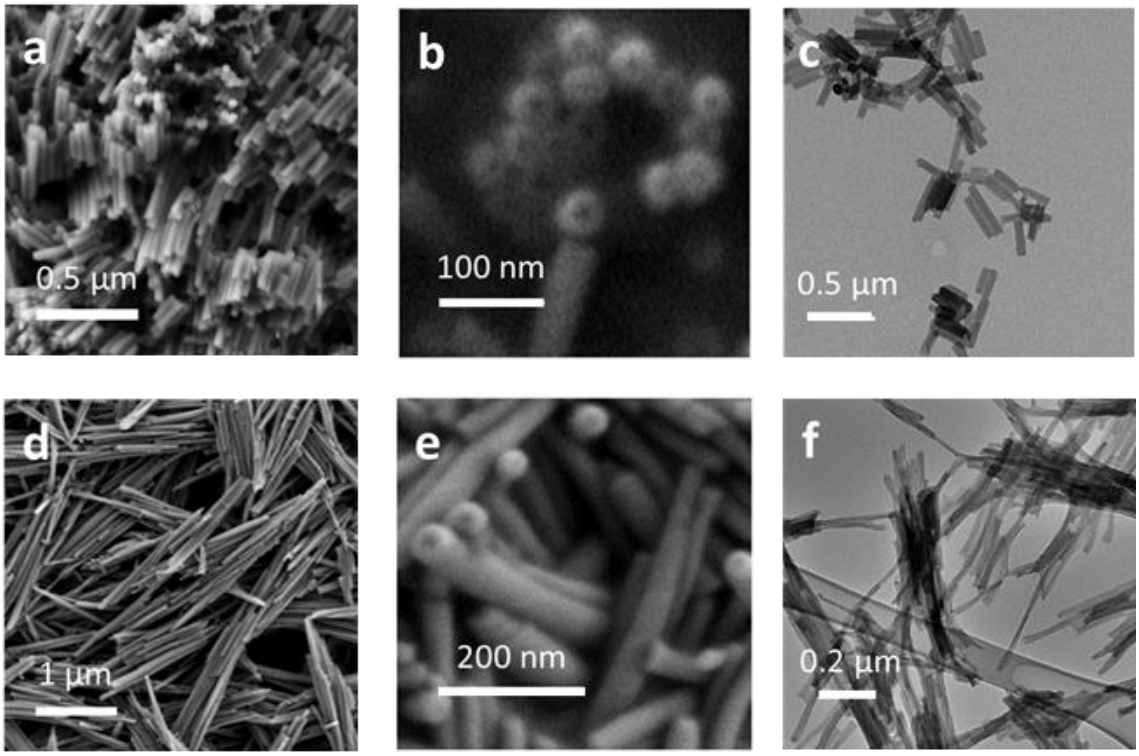

Figure 5.4.1 SEM and low magnification TEM micrographs of A_tGaS_x NT (a, b, c) and A_tGaSe_y NT (d, e, f).

TEM imaging showed that the tubes had a layered nature (Figure 5.4.2). The distance between the layers had been measured with the intensity profiles along the nanotubes in the places marked by red lines (Figure 5.4.2 a and b) giving values of 29.1 Å and 25.0 Å for A_tGaS_x NT and A_tGaSe_y NT, respectively. Those interlayer distances were higher than the typical values of gallium chalcogenide described in the literature,[235, 236] but similar to those found for amine-capped layered materials with long-chain amines between the layers.[237] Most probably, the amines (hexadecylamine and dodecylamine) used as a solvent were incorporated into the nanotubes structure and

acted as a template directing their growth, similarly as observed in the synthesis of vanadium oxide,[126] vanadium sulfide[238] and metallophosphate[230] nanotubes previously reported.

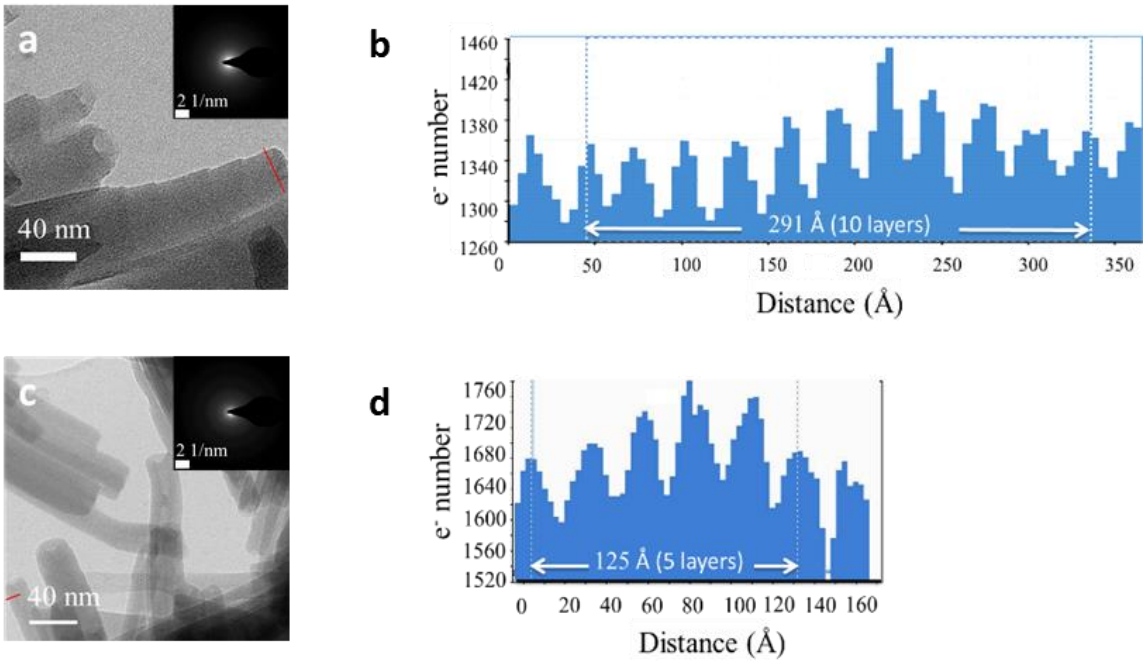

Figure 5.4.2 TEM micrographs and corresponding intensity profiles taken in the places marked by a red line for a, b) A_tGaS_x NT and c, d) A_tGaSe_y NT. The insets in a and b show SAED taken in the places marked by red lines.

The nanotubes interlayer distance was also calculated on the basis of XRD, which gave a value of 34.1 Å and 30.3 Å for A_tGaS_x NT and A_tGaSe_y NT, respectively. These values were slightly higher than those obtained from TEM, which most probably was a result of the nanotubes sensitivity to the electron beam, since a noticeable shrinkage and structural damages were observed within seconds after exposure (insets in the Figure 5.4.2 a and c).

The XRD patterns of both A_tGaS_x NT and A_tGaSe_y NT (Figure 5.4.3) showed, in addition to the multiple (00l) reflections (which were used to calculate the basal spacing), broad peaks in the region of 3.7-4.6 Å, which might be attributed to a liquid crystal arrangement of the long chain amines.[239, 240] The low intensity broad peaks at a d-spacing of 3.05 Å and 3.20 Å for A_tGaS_x NT and A_tGaSe_y NT, respectively were probably related to the Ga-Ga atoms distance in the nanotubes, since similar values were observed for Ga-Ga bonds in other GaS nanostructures.[241] Additionally, a broad

peak observed at 2.00 Å in the pattern of the A_tGaSe_y NT was ascribed to an interatomic distance reported for Ga-N bonding in amine-stabilized gallium chalcogenides.[235, 236]

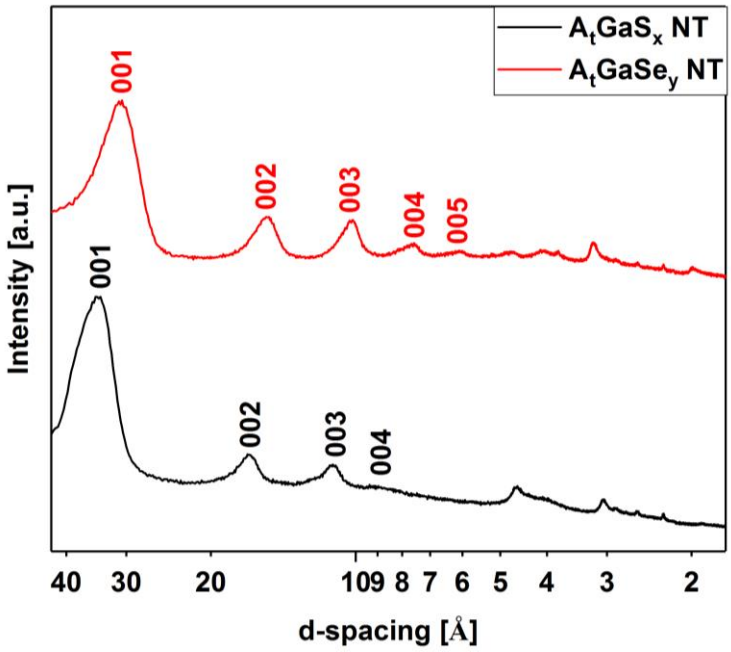

Figure 5.4.3 XRD patterns of A_tGaS_x NT (black) and A_tGaSe_y NT (red).

5.4.1 Distribution of elements within the nanotubes

The distribution of elements within the nanotubes was analyzed by EDX mapping performed under SEM. Moreover, carbon, gallium and sulfur/selenium distribution was also checked within a single nanotube by high-resolution aberration-corrected STEM-EDX (credited to Clive Downing).

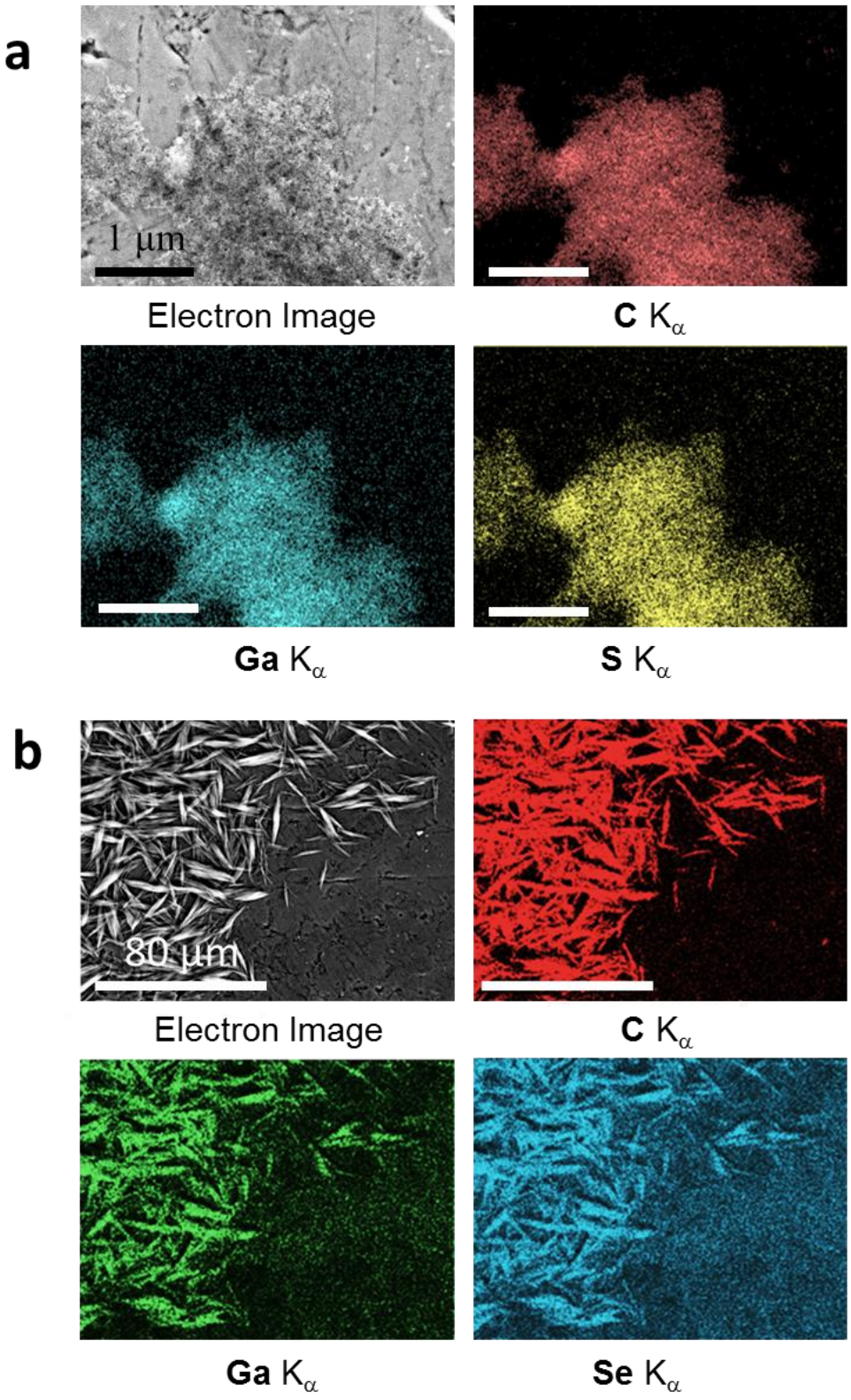

Figure 5.4.4 EDX mapping performed under SEM of a) A_tGaS_x NT and b) A_tGaSe_y NT.

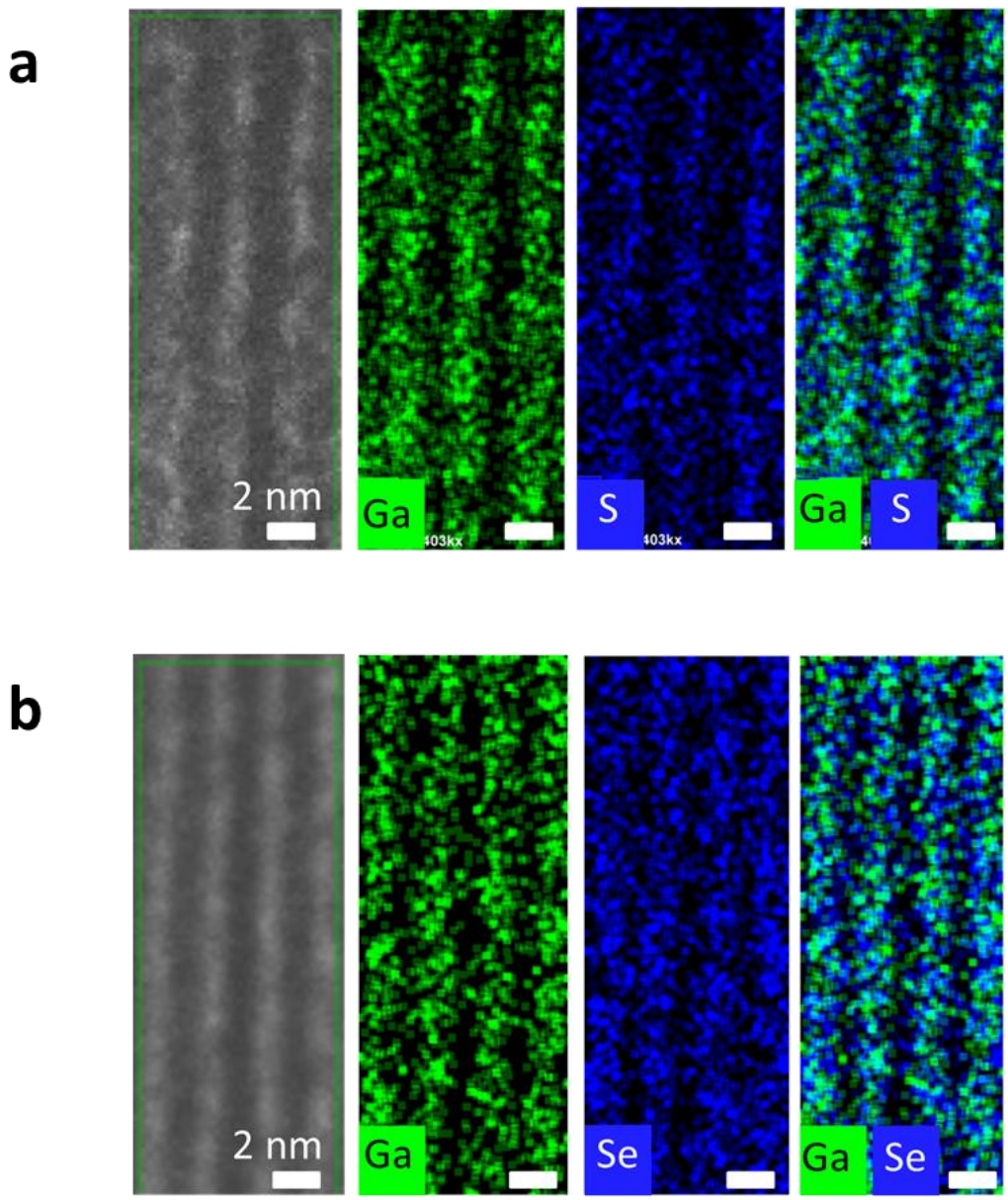

Figure 5.4.5 EDX mapping performed under high-resolution aberration-corrected STEM of a) A_tGaS_x NT and b) A_tGaSe_y NT.

SEM-EDX mapping confirmed homogeneous distribution of carbon, gallium and sulfur/selenium within the nanotubes (Figure 5.4.4 a and b for A_tGaS_x NT and A_tGaSe_y NT, respectively). Furthermore, EDX mapping performed under high-resolution aberration-corrected STEM clearly demonstrated that the structure of the nanotubes consisted of alternate stacked layers of gallium chalcogenides and amines (Figure 5.4.5 a and b for A_tGaS_x NT and A_tGaSe_y NT, respectively).

5.4.2 Composition of amine templated A_tGaS_x and A_tGaSe_y nanotubes

The EDX (TEM) analysis of A_tGaS_x NT and A_tGaSe_y NT proved presence of carbon gallium and sulfur/selenium (Figure 5.4.6).

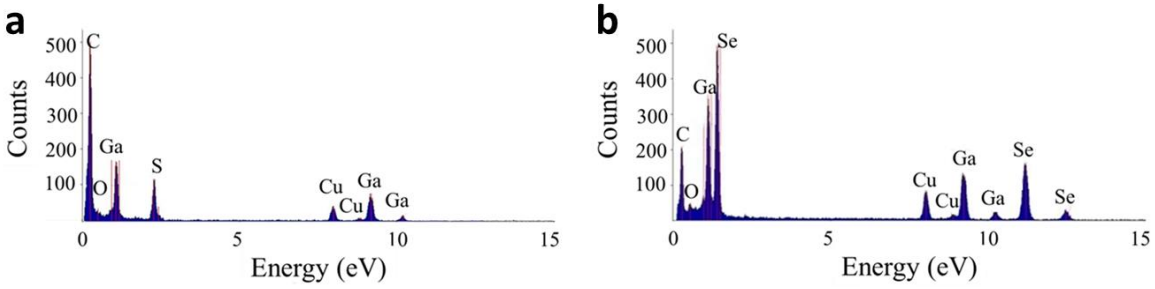

Figure 5.4.6 EDX (TEM) spectra of a) A_tGaS_x NT and b) A_tGaSe_y NT.

Furthermore, the EDX spectra (TEM) showed low intensity signals from oxygen, in both materials (Figure 5.4.6.), which might have been due to the incorporation of this element or partial oxidation of the nanotubes during post-synthesis processing.

FT-IR spectroscopy confirmed the presence of long-chain amines within the nanotubes structure, by comparing the spectra of neat hexadecylamine and dodecylamine with the spectra of A_tGaS_x NT and A_tGaSe_y NT (Figure 5.4.7). To simplify the analysis, the bands were split up into two groups: vibrational modes involving the hydrocarbon backbone and peaks related to presence of amino group.

Firstly, in the region of 2957-2850 cm^{-1}, vibrations ascribed as methylene and methyl stretching were detected. Additionally, the bending modes were assigned at 1470 cm^{-1}, 1375 cm^{-1} and 1360 cm^{-1} and the rocking vibrations at 720 cm^{-1}.[242] All those signals, attributed to vibrations of the hydrocarbon backbone were present in the spectra of amines and nanotubes and their positions remained unchanged.

Secondly, in the spectra of pure amines, bands at 3333 cm^{-1}, 3258 cm^{-1} and 3172 cm^{-1} were attributed to the asymmetric and symmetric N-H stretching modes and to the symmetric stretching mode interacting with the amine group bending mode, respectively. Moreover, a scissoring bending mode and a N-H wagging mode were observed at 1609 cm^{-1} and around 925 cm^{-1}, respectively.[237, 243] Interestingly, in the spectra of A_tGaS_x NT and A_tGaSe_y NT, the bands ascribed to stretching and scissoring vibrations were broadened and shifted to a lower wavenumber, while the wagging mode was not observed. These changes in the spectra of gallium chalcogenide nanotubes

suggested that the interactions between the amines and gallium chalcogenide happened through the amino groups.[237, 242, 243]

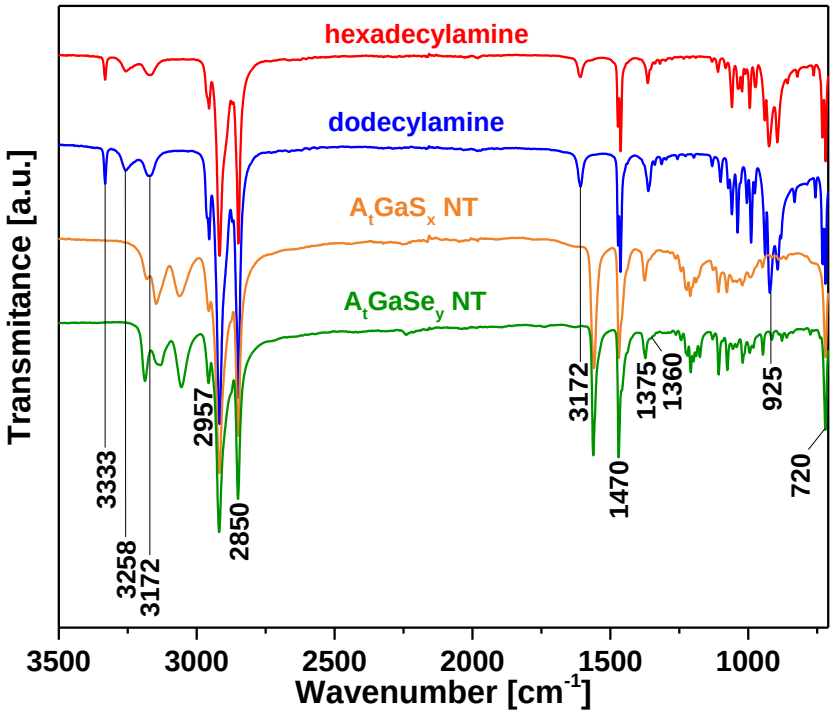

Figure 5.4.7 FT-IR spectra of hexadecylamine, dodecylamine, A_tGaS_x NT and A_tGaSe_y NT.

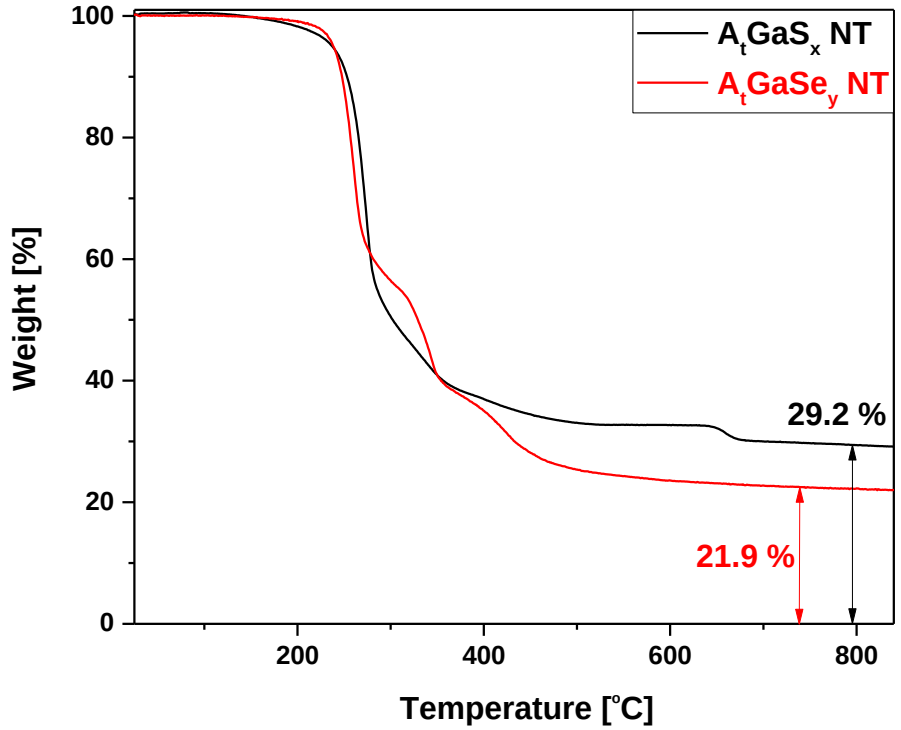

Figure 5.4.8 TGA curve of A_tGaS_x NT (black line) and A_tGaSe_y NT (red line).

In order to estimate the gallium content in the nanotubes, TGA analysis was performed by heating the samples up to 850 ^{o}C under air atmosphere (heating rate 10 ^{o}C/min). The observed weight loss was 70.8 % and 78.1 % for A_tGaS_x NT and A_tGaSe_y NT, respectively (Figure 5.4.8).

The XRD patterns of the residues (indexed as monoclinic gallium(III) oxide in both cases (Figure 5.4.9 c, d), and the EDX (SEM) analysis (which showed only O and Ga, Figure 5.4.9 a, b), confirmed the total removal of amines and chalcogens. According to TGA results, the gallium content in the nanotubes was calculated as 21.7% and 16.3 % in weight, for A_tGaS_x NT and A_tGaSe_y NT, respectively.

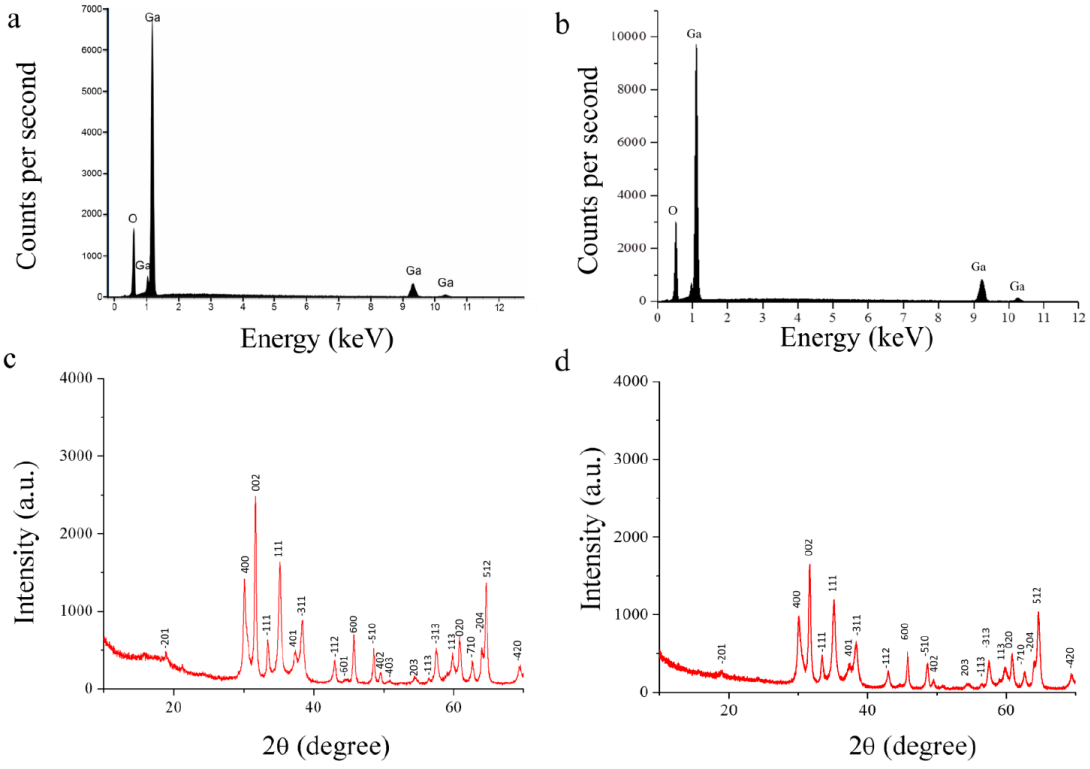

Figure 5.4.9 EDX (SEM) and XRD of the TGA residue of a, c) A_tGaS_x NT and b, d) A_tGaSe_y NT respectively.

The gallium to chalcogen ratio was calculated on the basis of T-XRF using cobalt as an internal standard (Figure 5.4.10). The amount of the elements in the sample was calculated by integrating the area of the peaks after subtracting the background,[151] leading to the approximate weight content of the chalcogens in the nanotubes of 12.7 % sulfur and 27.6 % selenium, respectively. In the case of A_tGaS_x NT, bromine was detected as a contamination.

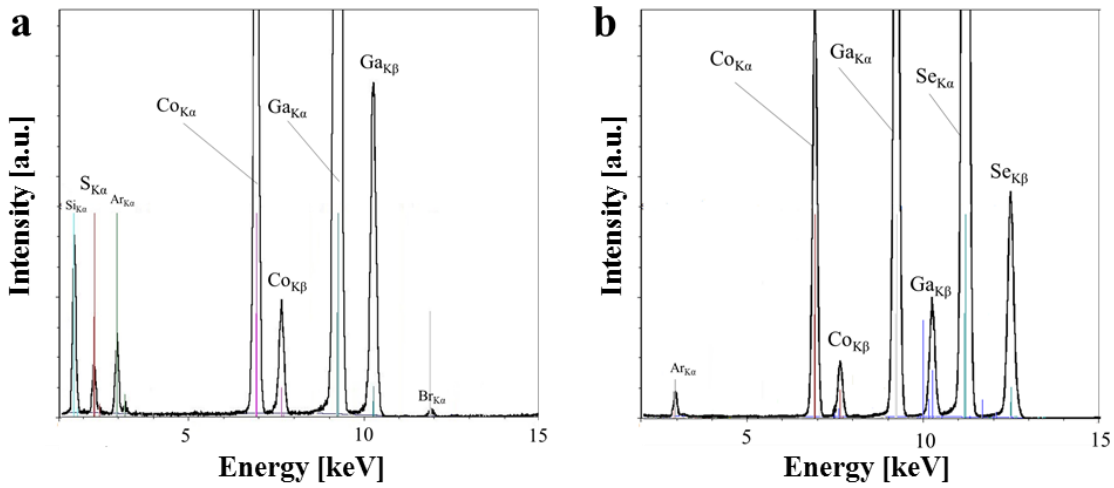

Figure 5.4.10 T-XRF spectrum of a) A_tGaS_x NT and b) A_tGaSe_y NT.

The nanotubes were also characterized by XPS, which showed the presence of Ga, C, N, O and the corresponding chalcogenide (S or Se). The survey spectra are presented in the Figure 5.4.11.

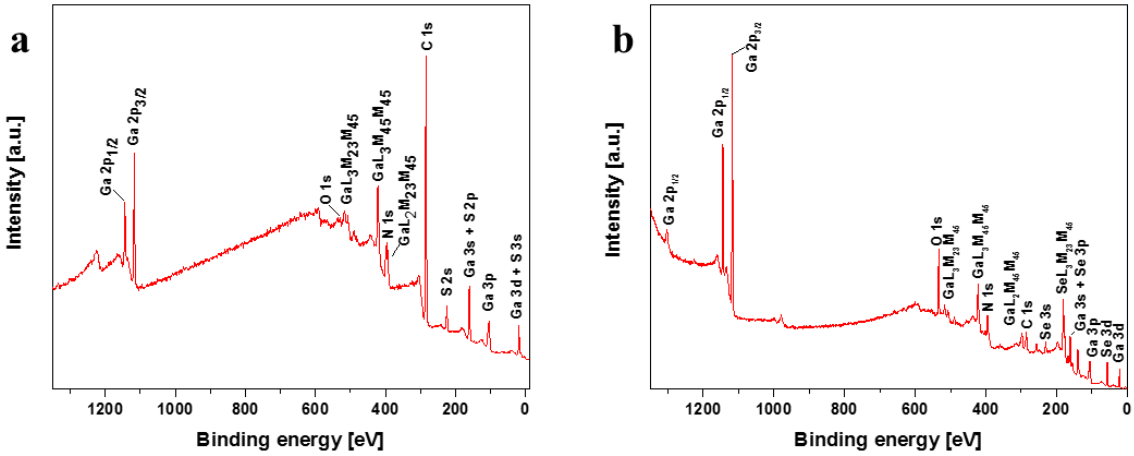

Figure 5.4.11 XPS spectra of a) A_tGaS_x NT and b) A_tGaSe_y NT.

The nitrogen peak observed at a binding energy of 399.9 eV, detected in both cases (A_tGaS_x NT and A_tGaSe_y NT) is typical for amines (399.9 eV). In order to analyze the chemical bonding environment of nitrogen, gallium and chalcogens, the N 1s, Ga 3d, S 2p and Se 3d core level regions were acquired at high resolution (Figure 5.4.12). A small contribution from protonated amines was detected in the A_tGaSe_y NT, at a binding energy of 401.1 eV (Figure 5.4.12 a).[244]

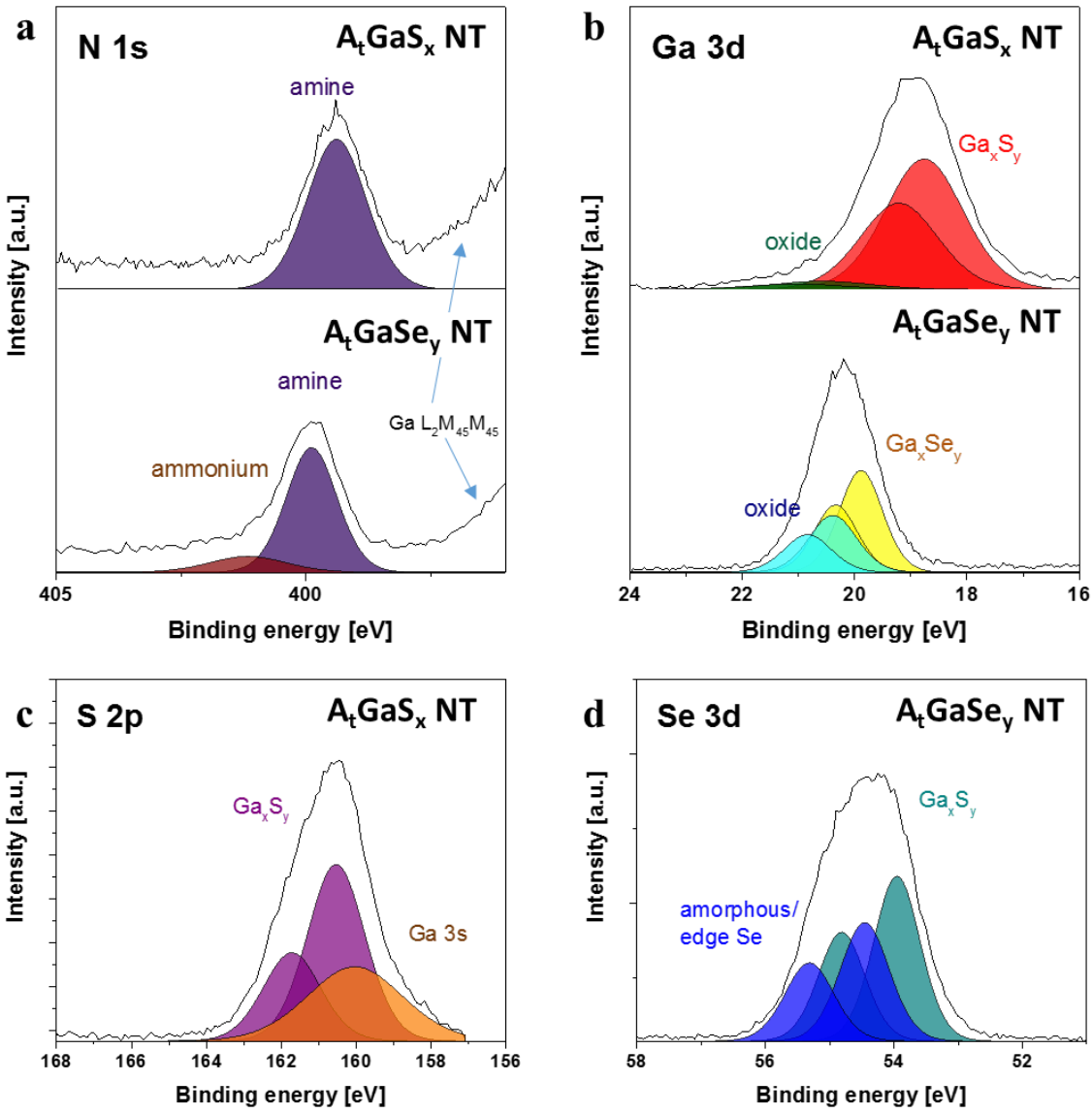

Figure 5.4.12 XPS of a) N 1s, b) Ga 3d, c) S 2p and d) Se 3d regions of A_tGaS_x NT and b) A_tGaSe_y NT.

The Ga 3d peak was fitted with two doublets in both samples (Figure 5.4.12 b), with binding energies of 18.8 eV and 20.6 eV for the sulfur-based sample and 19.9 eV and 20.4 eV for the selenium derivative. All these components had a full width at half maximum (FWHM) much higher than the resolution of the XPS system, which suggested that each of them comprised a variety of slightly different chemical species. The signals at lower binding energies were most probably associated with gallium bonded to the respective chalcogen,[245] while the higher binding energy region was characteristic of gallium oxide.[246] The presence of gallium oxide was most probably the result of a partial oxidation of the sample's surface, and the more intense peak observed

in the spectrum of A_tGaSe_y NT suggested that this sample was more sensitive to air and moisture than the sulfur-based counterpart.

The S 2p core-level line overlapped with the Ga 3s peak in the A_tGaS_x NT spectrum, so the S 2p and Ga 3s region yielded a good fit for only one discernible sulfur component associated with Ga_xS_y species (Figure 5.4.12 c). The Se 3d region in the A_tGaSe_y NT showed a broad peak which was fitted to two doublets with binding energies centered at 53.9 eV and 54.4 eV. The first peak (at 53.9 eV) was most probably related to Ga_xSe_y species, while the second one (at 54.4 eV) was associated with edge effects or the presence of selenium-enriched regions in the sample surface (Figure 5.4.12 d).

The amine-stabilized gallium chalcogenides were previously studied[113, 247, 248] and usually presented an open-framework structure consisting of the assembly of building blocks composed of corned-linked chains or clusters of the type $[Ga_{10}S_{18}]^{6-}$, $[Ga_{20}S_{35.5}(S_3)_{0.5}O]^{12-}$ or $[GaSe_2]^{-n}$, among others. The charge of the clusters or chains was usually compensated with metal cations or protonated amines.[115, 117] Moreover, direct bonding between gallium and nitrogen atoms was reported in some of these clusters, when sulfur in tetrahedral "GaS_4" units has been partially substituted by a nitrogen from amine ligands to form "GaS_3N" or "GaS_2N_2" units.[117] Furthermore, some of these compounds were found to be stabilized by the presence of sulfur-sulfur or selenium-selenium bridges.[113, 248]

In the present study, a structure of layers of polymeric gallium sulfide/selenide alternating with long-chain amine layers is proposed. The amines acted as a template and scaffold for the nanotube formation and interacted with the gallium chalcogenide through the amino group, stabilizing the whole structure in a tubular shape resulting in the observed discrete units of multi-walled nanotubes. The gallium chalcogenide layers presented a complex structure which resulted in a low crystallinity and incorporation of some oxygen, at least in the sample surface.

In order to further study the stability of A_tGaSe_y NT in air, the sample was exposed to the ambient conditions for certain periods of time and then characterized by SEM. It is seen at a glance that this material turned reddish within a few hours (insets in the Figure 5.4.13).

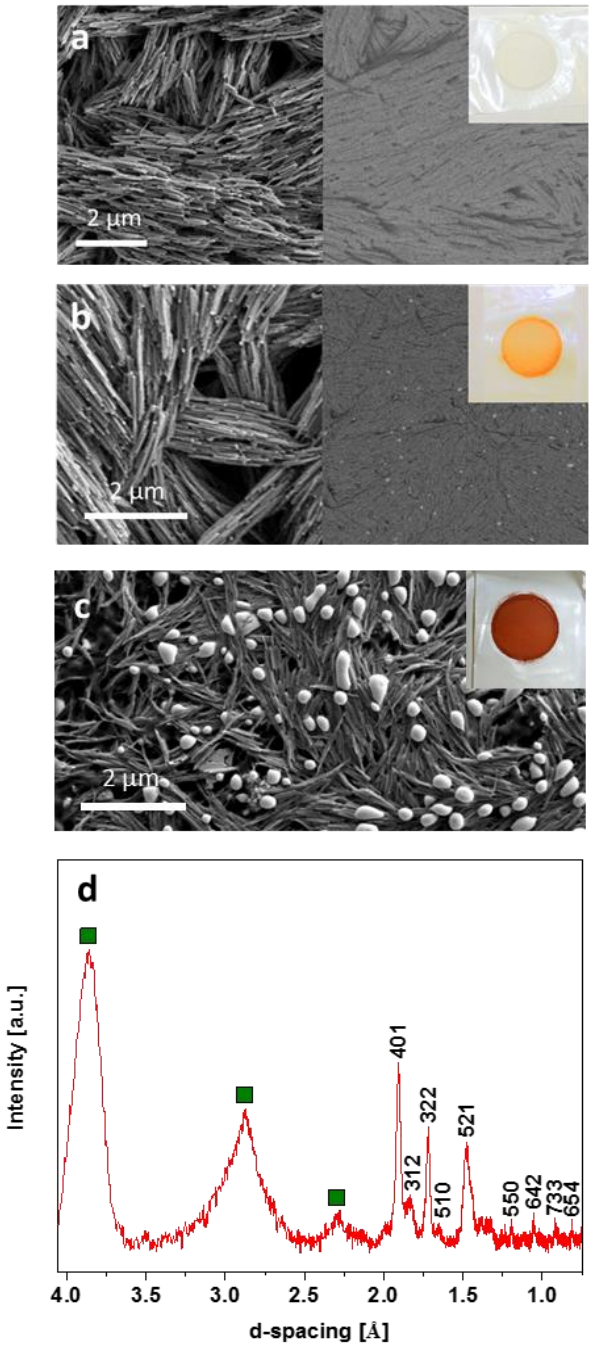

Figure 5.4.13 SEM micrographs (left-SE and right BSE detector) of A_tGaSe_y NT a) fresh, b) after 1 day under air and c) after 1 week under air and d) XRD pattern of the sample kept for 1 week under air; peaks marked by green square are ascribed to the nanotubes. In the insets in the right corners it is shown the color changes of the samples after exposure to ambient conditions.

SEM analysis showed that the A_tGaSe_y NT produced spherical selenium oxide particles, as confirmed by XRD (Figure 5.4.13 d, peaks marked by green square were

ascribed to the nanotubes), when exposed to air, which caused the reddish color of the sample.

5.4.3 Optical properties of A_tGaS_x NT and A_tGaSe_y NT

The optical properties of the nanotubes were analyzed by UV-Vis (using an integrating sphere in the transmission mode) and also by PL spectroscopy. The use of an integrating sphere was necessary, due to the light scattering by the nanoparticles in the solution, which prevents all light from reaching the detector (see Section 2.8). The absorption spectra are presented on the energy scale in Figure 5.4.14 a and b. The scattering spectra were obtained by subtracting the absorbance spectrum from the extinction spectrum.

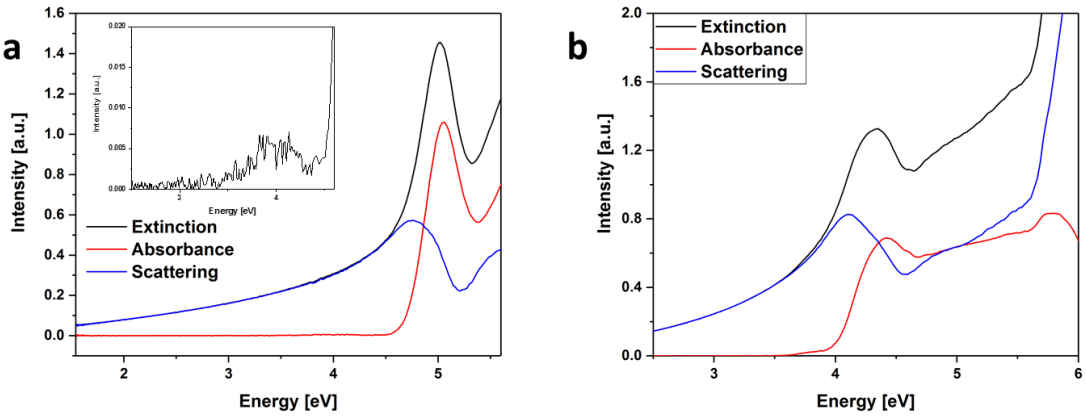

Figure 5.4.14 UV-Vis spectrum of a) A_tGaS_x NT and b) A_tGaSe_y NT dispersed in IPA; absorbance-red, extinction-black and scattering-blue. In the inset it is shown the zoomed in spectrum of A_tGaS_x NT in the region 2.5-4.5 eV.

The absorbance spectrum of A_tGaS_x NT showed two bands: a high-intensity band, with the maximum absorption at 5.2 eV (Figure 5.4.14 a), and the second low-intensity at 3.8 eV. In case of A_tGaSe_y NT, a series of peaks at energies greater than 4 eV were observed (Figure 5.4.14 b) with the lowest energy absorbance feature centred at 4.4 eV. No residual absorbance was detected in the visible region in either samples, and all the signals in the extinction spectra were due to the scattering.

The spectra of both A_tGaS_x NT and A_tGaSe_y NT were similar to the spectra previously reported for gallium(II) chalcogenide nanosheets,[143, 249] although the transitions were observed to be shifted to higher energies, and similarly to the two-dimensional analogues, the optical absorbance was probably related to excitonic

transitions.[143, 250] Since it was not possible to estimate the typical binding energies of the excitons, the real band gap was not extracted from the optical spectra. However, it must have been larger than the energy of the highest energy transition observed, e.g. > 5.2 eV for the A_tGaS_x NT and > 4.4 eV for the A_tGaSe_y NT, which was larger than the band gap of bulk gallium chalcogenides (typically 2.1-3.3 eV)[249, 251] and of amine-stabilized gallium chalcogenides (2.6–4.2 eV for gallium sulfides[115, 248, 252] and 1.4-2.4 eV for gallium selenides).[235, 236] The increase in the band gap, observed for the nanotubes is in good agreement with the results reported for other long-chain amine-intercalated semiconductors, which presented a strong structure-induced quantum confinement leading to a blue-shift in comparison to their bulk counterparts.[253, 254]

In order to check whether the materials are direct band gap semiconductors, the dispersion was subjected to PL spectroscopy, and luminescence was observed in both samples (Figure 5.4.15).

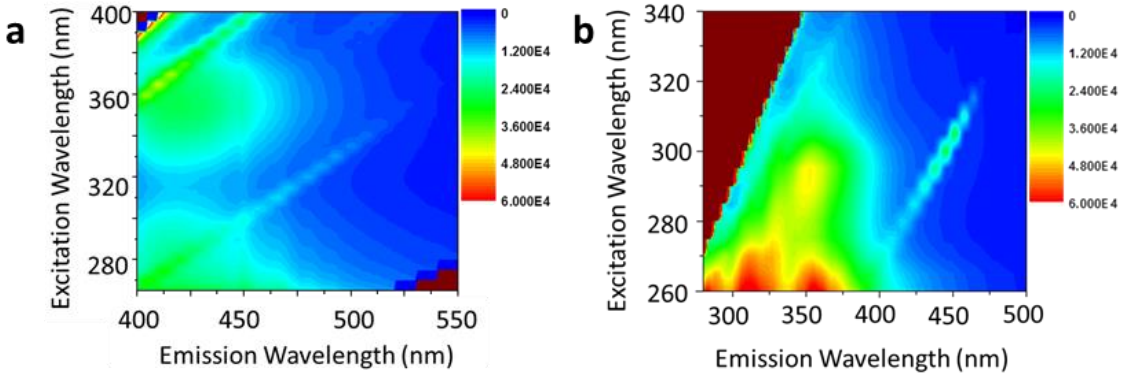

Figure 5.4.15 Photoluminescence (PL) excitation-emission contour plot of a) A_tGaS_x NT and b) A_tGaSe_y NT.

A_tGaS_x NT showed an emission centered at 425 nm (2.92 eV), which is consistent with the absorbance spectrum, with a red shift of ~0.2 eV. Therefore, significantly greater luminescence would be expected when exciting further in the UV region where the main absorbance band is centered, but, due to the restrictions of the excitation source (450 W Xenon arc lamp covering a range of 250-1000 nm), this could not be experimentally confirmed. The A_tGaSe_y NT presented multiple emissions features at excitations < 300 nm (4 eV) showing the main emissions at ~290, 315 and 350 nm (4.3, 3.9 and 3.5 eV) which were red-shifted in comparison to the absorbance. The emission wavelengths of the tested materials were similar to that of open-

framework amine-templated gallium chalcogenides, which are typically luminescent in the range of 440–500 nm.[113]

To summarize, both A_tGaS_x NT and A_tGaSe_y NT were tentatively classified as direct large band gap semiconductors, with excitonic transitions in the UV region.

5.5 Testing of the nanotubes as active materials for lithium ion battery anodes

A_tGaS_x NT and A_tGaSe_y NT were processed into composite electrodes and tested as lithium ion battery anodes (credited to John CF Zhang). In order to improve the conductivity of the electrodes, the nanotubes were mixed with single-walled carbon nanotubes (SWCNT).

Experimental Section:

The A_tGaS_x NT/A_tGaSe_y NT - SWCNT composite was made by mixing 12 mg of gallium chalcogenide nanotubes (dispersed in isopropyl alcohol, achieved by 30 minutes of bath sonication) and 2.6 mg of SWCNT (dispersed in isopropyl alcohol, concentration of 0.1 $mgml^{-1}$). The mixture was bath sonicated for an additional 5 minutes to ensure complete mixing. A free standing electrode was prepared by vacuum-filtration of the mixture through Celgard K2045 membrane (Coated PP, Celgard LLC, Charlotte, NC) and dried overnight at 100 ^oC under vacuum. The dried electrode was then cut into square stripes (0.7 x 0.7 cm) with a thickness of 10 μm and a mass of 0.6 mg. To compare the composite performance to the activity of each component, free standing electrodes of SWCNT were prepared using the same procedure as for the composite. The electrode made of amines mixture was prepared by mixing 1.0 mmol of hexadecylamine and 0.2 mmol of dodecylamine with polyvinylidene fluoride in N-methyl pyrolidinone. The homogeneous slurry was cast onto a copper foil, dried under vacuum and cut into an electrode with diameter of 12 mm and thickness of 20 μm (excluding the thickness of a copper foil). CR2032 coin-type cells were assembled using the composite as a working electrode and lithium metal foil as counter and reference electrodes. A porous propylene membrane (Celgard K2045) was used as a separator. The electrolyte was 1 M lithium hexafluorophosphate/ethylene carbonate/diethyl carbonate. The galvanostatic charge/discharge tests were carried out on an Arbin Potentiostat (BT2145, USA) between 0.01-2 V (*vs.* Li/Li^+) at current densities varying from 10 mAg^{-1} to 500 mAg^{-1}. The cell was cycled five times under each current density and the discharge capacity at the fifth cycle was chosen as a stable value.

The pictures of a free standing, flexible electrode prepared by vacuum filtration of the composite are presented in the Figure 5.5.1. SEM analyses of the same showed homogeneous mixing of SWCNT with gallium chalcogenide nanotubes (Figure 5.5.1 a and b for A_tGaSe_y NT/SWCNT and A_tGaS_x NT/SWCNT respectively).

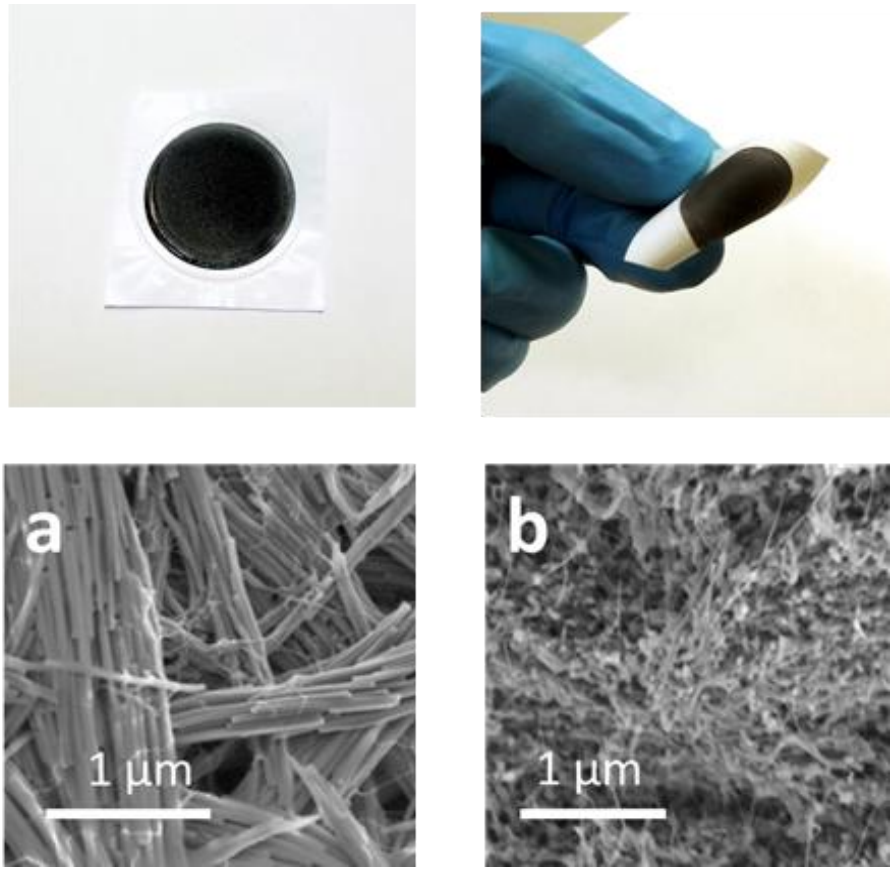

Figure 5.5.1 Pictures of free standing electrodes and SEM micrograph of a) A_tGaSe_y NT/SWCNT and b) A_tGaS_x NT/SWCNT.

The galvanostatic charge/discharge tests showed initial discharge capacities of 190 $mAhg^{-1}$ and 164 $mAhg^{-1}$ for A_tGaS_x NT/SWCNT and A_tGaSe_y NT/SWCNT, respectively (Figure 5.5.2). However, at the fifth cycle the capacity of both composites decreased, which was most probably due to the irreversible formation of a solid-electrolyte interface layer leading to the consumption of the electrolyte and the formation of a passive layer, thus lowering the coulombic efficiency.[255]

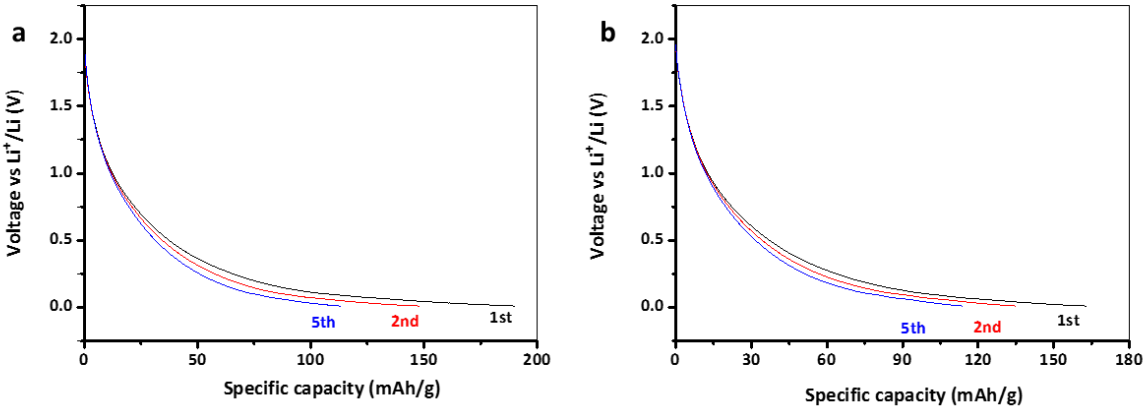

Figure 5.5.2 Discharge curve of a) A_tGaS_x NT/SWCNT and b) A_tGaSe_y NT/SWCNT.

The rate performance of A_tGaS_x NT/SWCNT and A_tGaSe_y NT/SWCNT composites at various current densities is presented in the Figure 5.5.3. The capacities of the composite films were higher than SWCNT and amine electrodes at all current densities.

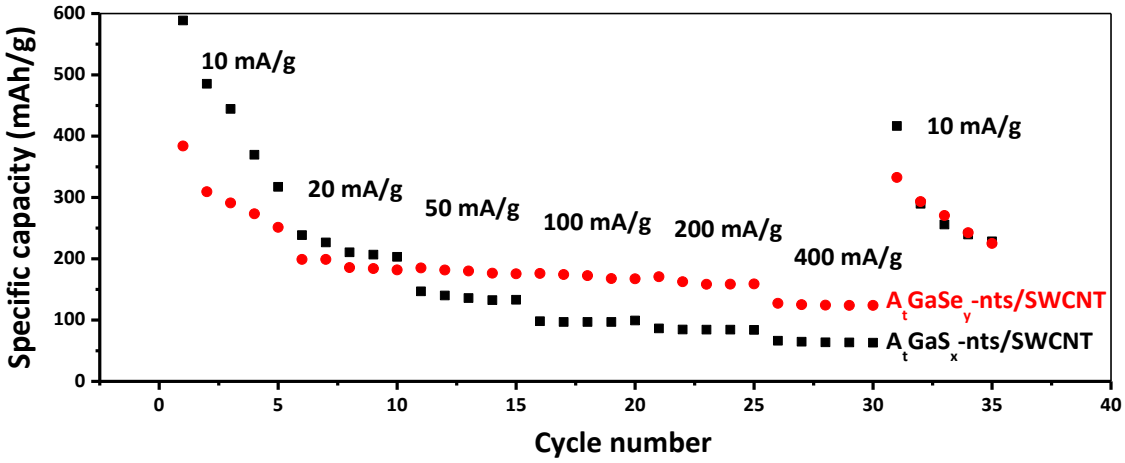

Figure 5.5.3 Rate performance of A_tGaS_x NT/SWCNT (black) and A_tGaSe_y NT/SWCNT (red).

The specific capacity of the gallium chalcogenide fraction of the nanotubes was quantitatively determined by subtracting the contribution of SWCNT and amine, giving the value of 317 $mAhg^{-1}$ and 251 $mAhg^{-1}$ at 10 mAg^{-1} for A_tGaS_x NT/SWCNT and A_tGaSe_y NT/SWCNT, respectively. At 400 mAg^{-1}, the selenide derivative reached capacity of 124 $mAhg^{-1}$, which was much higher than for sulfur-based composite (63 $mAhg^{-1}$). Those values were lower than the results previously described in the literature for a similar system (reaching up to 575 $mAhg^{-1}$ at a current density of 120 $mAhg^{-1}$ in a

voltage window of 0.01-2 V).[256] Most probably, the lower capacity was a result of the presence of encapsulating amines, which might have hinder the charge and ion exchange between the gallium chalcogenide layers. Nonetheless, these results are only preliminarily tests and further optimization of the performance of the nanotubes might give improved results.

5.6 Conclusions

The work presented in this Chapter describes the use of a heating-up method with the use of long-chain amines as a template in the synthesis of gallium chalcogenide nanotubes. The methodology used in this project was novel, and similar synthesis methods were not described in the literature.

The synthesis of A_tGaS_x NT and A_tGaSe_y NT has been studied and optimized. To do so, different sulfur/selenium/tellurium precursors reacted with $Ga(acac)_3$ in different ratios at temperatures in the range of 150-300 ^oC for 6-144 hours. The sulfur-based compound was obtained with the maximum yield (71 %) with the use of elemental sulfur in its double excess in relation to Ga at 200 ^oC within 24 h. Similarly, A_tGaSe_y NT were produced with the use of elemental selenium (Ga:Se=1.5) at 200 ^oC within 72 h with a yield as high as 73 %. The preparation of amine-templated gallium telluride nanotubes could not be achieved by this method.

A_tGaS_x NT and A_tGaSe_y NT presented a hollow tubular structure with the maximum length of 500 nm for A_tGaS_x NT and 2 μm for A_tGaSe_y NT. Both materials were low crystalline, and the nanotubes consisted of polymeric gallium sulfide/selenide alternating with long-chain amines layers. The amines acted as a template and scaffold stabilizing the whole structure. The sulfur-based compound contained 21.7 % of Ga and 12.7 % of S, while selenium derivative consisted of 16.3 % of Ga and 27.6 % of Se. A_tGaSe_y NT was air-sensitive leading to formation of selenium oxide when exposed to ambient conditions.

Optical characterization indicated that both compounds were tentatively classified as direct large band gap semiconductors with excitionic transitions in the UV region.

Finally, A_tGaS_x NT and A_tGaSe_y NT were tested as lithium ion battery anodes and their performance was in the range of 251-317 $mAhg^{-1}$ at 10 mAg^{-1}, which is lower

than typical values reported in the literature. Nevertheless, both materials are promising candidates for electro-optical applications.

6 Conclusions and future work

This Thesis describes the synthesis of 2D LDH (Mg_xAl_y and Ni_xFe_y) and 1D layered gallium chalcogenides by wet chemical methods. The geometry, purity and crystallinity of those nanomaterials were suitably controlled by adjusting the reaction parameters, and their further applications were tested: small (< 50 nm) hexagonal platelets of Mg_xAl_y LDH were used as a delivery agents of pDNA to the cells, as a part of an ongoing bone-repairing therapy; flower-like and large hexagonal flakes (~ 1μm) of Ni_xFe_y LDH were applied as electrocatalysts in water splitting; and 1D gallium chalcogenides (S, Se) were tested as active materials in LiB anodes. It was demonstrated, that wet-chemistry methods are versatile, cost-effective and potentially scalable techniques to produce the compounds under study.

Mg_xAl_y LDH were obtained by three different synthetic methods (homogeneous precipitation, co-precipitation at constant pH and precipitation at decreasing pH), which resulted in the formation of flakes with diameters varying from 3 μm to 20 nm.

The largest flakes, obtained by thermal decomposition of urea or HMT (homogeneous precipitation) were obtained following the recipe described in the literature. The size of the platelets was not suitable for biological applications, but when exfoliated to single- or few-layer nanosheets this material might be promising catalyst. In order to facilitate its exfoliation, the interlayer space was modified by changing the anions from the strongly bonded carbonate to the easily exchangeable chloride, which is expected to weaken the electrostatic interactions which keep the layers together. The liquid-phase exfoliation of this material is an ongoing project in the Prof. Nicolosi group and the testing of the exfoliated nanosheets in the mentioned applications will be carried out in the future.

The smallest flakes of Mg_xAl_y LDH (< 50 nm) were obtained by precipitation at decreasing pH with additional aging at RT for 1 week. As far as the author is concerned, it was the first time when straightforward synthesis and aging the colloidal suspension at RT resulted in formation of non-agglomerated hexagonal platelets. Those were used to prepare pDNA-LDH nanohybrids by ion-exchange and after exposure to the cells, their successive uptake was observed under STEM. However, those were only

preliminary tests and proper analysis of the pDNA intercalation, agglomeration of the platelets, their stability inside the cell and the pDNA release profile need to be studied which is an ongoing work in the Nicolosi group in collaboration with Prof. Fergal O'Brien (RCSI). The final step of this project is the performance of the pDNA-LDH nanohybrids in bone-regeneration therapy. Furthermore, the obtained Mg_xAl_y LDH nanoplatelets can be also used to deliver negatively charged drugs or quantum dots.

The second synthesized material was Ni_xFe_y LDH in the form of platelets and nanoflowers and their application as electrocatalysts in water splitting reaction. The synthesis relied on the homogeneous precipitation with the use of two different capping agents (TSC and TEA). Firstly, Ni_xFe_y LDH nanoparticles presenting a flower-like morphology were obtained when TSC was added to the reaction mixture, which was a novel discovery. Secondly, regular hexagons of Ni_xFe_y LDH were produced with the use of TEA. The formation mechanism of the reaction with TEA was studied; the Ni_xFe_y LDH hexagons were formed from a two-line ferrihydrite and Ni-TEA complex mixture upon heating and pH increase. The synthesis of hexagonal Ni_xFe_y LDH in a two-step process was an innovative approach discovered by the author. Both materials (flower-like and flakes of Ni_xFe_y LDH) were tested in OER, which provided results typical for this kind of Ni-Fe compounds.

The synthesis of Ni_xFe_y LDH was optimized and the possible formation mechanism was proposed, but there is still significant room for improvements to be made. For instance, the synthesis conditions were optimized only for the Ni^{2+}:Fe^{3+} ratio of 3, while LDH structure can be formed with the Ni^{2+}:Fe^{3+} ratio varying from 1.5 to 4.0. The synthesis of the materials with different Fe^{3+} content should be considered, as it is known that the electrocatalytic activity in OER is strongly related to the amount of iron. Moreover, since the catalytic activity depends on the surface area, the exfoliation of the obtained materials to single layers nanosheets is already one of the ongoing projects in the Nicolosi group. Another approach to get higher surface area is the reduction of the particles size. Theoretically, this could be achieved by formation of more crystal nuclei, which should happen in the conditions of higher supersaturation of OH^- ions (higher initial concentration of urea or its replacement by HMT). The advantage of using smaller platelets over exfoliated nanosheets is a higher number of available edges, which is expected to reduce the overpotential value in OER.

In a more general content, the synthesis methods to obtain LDH developed in the presented Thesis can be expanded to the other LDH with different metal/anions combinations presenting various properties.

The last project concerned the synthesis of amine-templated gallium chalcogenide nanotubes by a heating-up method using long-chain amines. By this technique, sulfur and selenium derivatives were obtained, while the preparation of gallium telluride nanotubular materials were observed not to be feasible under the studied conditions. A_tGaS_x NT and A_tGaSe_y NT presented a layered, hollow, tubular structure with a maximum length of 500 nm for A_tGaS_x NT and 2 μm for A_tGaSe_y NT. Both materials had a low crystallinity, and the nanotubes consisted of polymeric gallium sulfide/selenide layers alternating with long-chain amines layers. The amines acted as a template and scaffold, stabilizing the whole structure. Both materials were tentatively classified as direct large band gap semiconductors, although further characterization with the use of the excitation lamp in the region < 250 nm is required to estimate the real band gap. Both kinds of nanotubes were mixed with SWCNT and tested as active materials for LiB anodes. The specific capacity of the composites was lower than for bulk gallium chalcogenides.

The synthesis of gallium telluride nanotubes was unsuccessful by the heating-up method in a mixture of hexadecylamine and dodecylamine. To obtain this material another technique should be considered, and maybe by changing the amines to the compounds with higher boiling point, the decomposition of the tellurium precursor might be achieved. Moreover, the preparation of the electrodes should be optimized to improve the performance of the obtained nanostructures as LiB anodes.

In summary, the results presented in this Thesis prove the great versatility of wet-chemistry methods for the synthesis of nanostructured materials. By simple modifications of commonly used synthetic approaches, the morphology of the obtained nanoparticles was controlled, which might enhance their properties and expand their applications to the new fields. Moreover, the amount of the nanoparticles obtained was in the range of tens to hundreds of milligrams and all the processes are potentially scalable. Finally, the preliminary tests of the synthesized materials gave promising results proving that the compounds under study satisfy the requirements for certain applications.

7 Supplementary information

7.1 Chapter 3

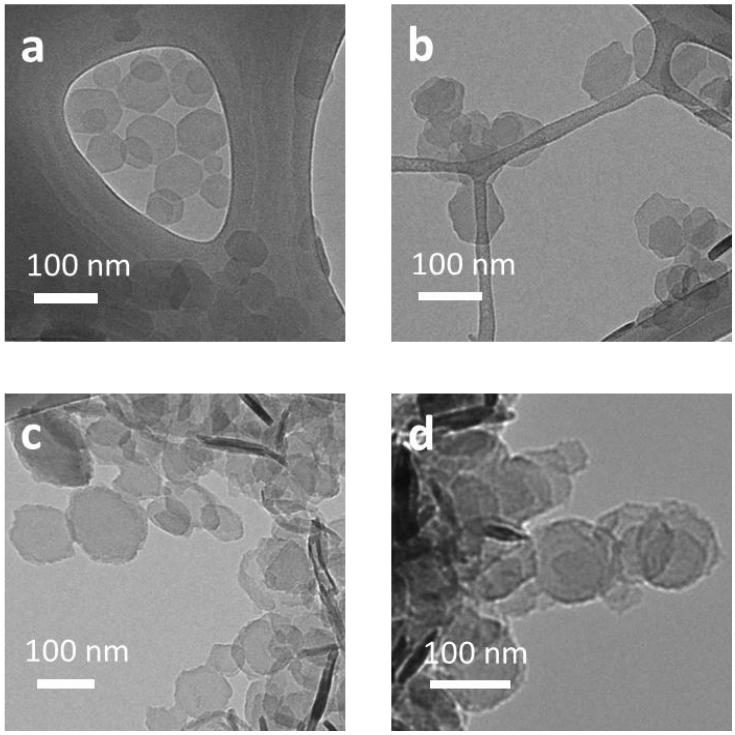

Figure S 1 TEM micrograph of $Mg_xAl_yCl_y \cdot nH_2O$ aged for 7 days at a) RT, b) 50 ºC, c) 85 ºC and d) 115 ºC.

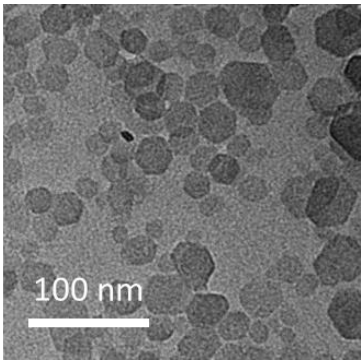

Figure S 2 TEM micrograph of $Mg_xAl_yCl_y \cdot nH_2O$ obtained in large-scale (20 g, 1 L of dispersion) process.

7.2 Chapter 4

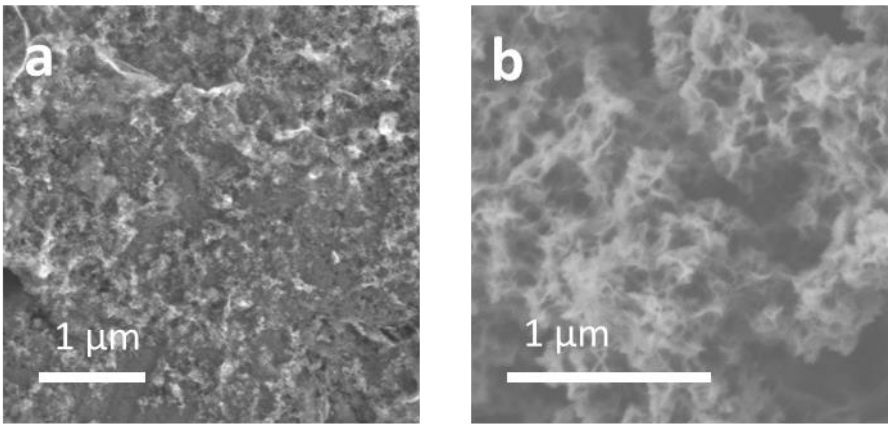

Figure S 3 SEM micrograph of Ni_xFe_y LDH obtained at a) 100 ºC and b) 150 ºC without capping agent.

8 References

1. K. S. Novoselov, A. K. G., S. V. Morozov, D. Jiang, Y. Zhang, S. V. Dubonos, I. V. Grigorieva, A. A. Firsov. *Science* **2004,** 306, 666-669.
2. Nicolosi, V.; Chhowalla, M.; Kanatzidis, M. G.; Strano, M. S.; Coleman, J. N. *Science* **2013,** 340, (6139), 1226419.
3. Shi, Y.; Li, H.; Li, L.-J. *Chemical Society Reviews* **2015**.
4. Lei, B.; Cui, J.; Xiang, Z.; Shang, C.; Wang, N.; Ye, G.; Luo, X.; Wu, T.; Sun, Z.; Chen, X. *Physical review letters* **2016,** 116, (7), 077002.
5. Sun, Y.; Wang, D.; Shuai, Z. *The Journal of Physical Chemistry C* **2016,** 120, (38), 21866-21870.
6. Miró, P.; Audiffred, M.; Heine, T. *Chemical Society Reviews* **2014,** 43, (18), 6537-6554.
7. Yenny Hernandez, V. N., Mustafa Lotya, Fiona M.Blighe, Zhenyu Sun, Sukanta De, I. T. McGovern, Brendan Holland, Michele Byrne, Youri K. Gun'ko, John J. Boland, Peter Niraj, Georg Duesberg, Satheesh Krishnamurthy, Robbie Goodhue, John Hutchison, Vittorio Scardaci, Andrea C. Ferrari and Jonathan N. Coleman. *Nature nanotechnology* **2008,** 3, 563-568.
8. Kaul, A. B. *Journal of Materials Research* **2014,** 29, (03), 348-361.
9. Ellis, J. K.; Lucero, M. J.; Scuseria, G. E. *Applied Physics Letters* **2011,** 99, (26), 261908.
10. Chhowalla, M.; Shin, H. S.; Eda, G.; Li, L.-J.; Loh, K. P.; Zhang, H. *Nature chemistry* **2013,** 5, (4), 263-275.
11. Li, H.; Wu, J.; Yin, Z.; Zhang, H. *Accounts of chemical research* **2014,** 47, (4), 1067-1075.
12. Ma, R.; Sasaki, T. *Advanced materials* **2010,** 22, (45), 5082-5104.
13. Keith R. Paton, E. V., Claudia Backes, Ronan J. Smith, Umar Khan, Arlene O'Neill, Conor Boland,; Mustafa Lotya, O. M. I., Paul King, Tom Higgins, Sebastian Barwich, Peter May, Pawel Puczkarski,; Iftikhar Ahmed, M. M., Henrik Pettersson, Edmund Long, João Coelho, Sean E. O'Brien,; Eva K. McGuire, B. M. S., Georg S. Duesberg, Niall McEvoy, Timothy J. Pennycook,; Clive Downing, A. C., Valeria Nicolosi and Jonathan N. Coleman. *Nature Materials* **2014,** 13, 624-630.
14. Pang, X.; Sun, M.; Ma, X.; Hou, W. *Journal of Solid State Chemistry* **2014,** 210, (1), 111-115.
15. Butler, S. Z.; Hollen, S. M.; Cao, L.; Cui, Y.; Gupta, J. A.; Gutierrez, H. R.; Heinz, T. F.; Hong, S. S.; Huang, J.; Ismach, A. F. *ACS nano* **2013,** 7, (4), 2898-2926.
16. Sun, Z.; Liao, T.; Dou, Y.; Hwang, S. M.; Park, M.-S.; Jiang, L.; Kim, J. H.; Dou, S. X. *Nature communications* **2014,** 5.
17. Hu, G.; Wang, N.; O'Hare, D.; Davis, J. *Chemical communications* **2006**, (3), 287-289.
18. Hu, G.; Wang, N.; O'Hare, D.; Davis, J. *Journal of Materials Chemistry* **2007,** 17, (21), 2257-2266.

19. Ma, R.; Sasaki, T. *Nanotubes and Nanosheets: Functionalization and Applications of Boron Nitride and Other Nanomaterials* **2015**, 113.
20. Son, J. S.; Yu, J. H.; Kwon, S. G.; Lee, J.; Joo, J.; Hyeon, T. *Advanced Materials* **2011,** 23, (28), 3214-3219.
21. Polte, J. *CrystEngComm* **2015,** 17, (36), 6809-6830.
22. Nasilowski, M.; Mahler, B.; Lhuillier, E.; Ithurria, S.; Dubertret, B. *Chemical Reviews* **2016,** 116, (18), 10934-10982.
23. Xia, Y.; Xiong, Y.; Lim, B.; Skrabalak, S. E. *Angewandte Chemie International Edition* **2009,** 48, (1), 60-103.
24. Rives, V., *Layered double hydroxides: present and future*. Nova Publishers: 2001.
25. Feitknecht, W.; Fischer, G.; Helu, G. *Helv. Chim. Acta* **1935,** 18, 555-569.
26. Auerbach, S. M.; Carrado, K. A.; Dutta, P. K., *Handbook of layered materials*. CRC Press: 2004.
27. Salomao, R.; Milena, L.; Wakamatsu, M.; Pandolfelli, V. C. *Ceramics International* **2011,** 37, (8), 3063-3070.
28. Cavani, F.; Trifirò, F.; Vaccari, A. *Catalysis today* **1991,** 11, (2), 173-301.
29. Radha, A.; Kamath, P. V.; Shivakumara, C. *Acta Crystallographica Section B: Structural Science* **2007,** 63, (2), 243-250.
30. Rodrigues, E.; Pereira, P.; Martins, T.; Vargas, F.; Scheller, T.; Correa, J.; Del Nero, J.; Moreira, S.; Ertel-Ingrisch, W.; De Campos, C. *Materials Letters* **2012,** 78, 195-198.
31. Chang, Z.; Evans, D.; Duan, X.; Boutinaud, P.; De Roy, M.; Forano, C. *Journal of Physics and Chemistry of Solids* **2006,** 67, (5), 1054-1057.
32. Intissar, M.; Jumas, J.-C.; Besse, J.-P.; Leroux, F. *Chemistry of materials* **2003,** 15, (24), 4625-4632.
33. Fan, G.; Li, F.; Evans, D. G.; Duan, X. *Chemical Society Reviews* **2014,** 43, (20), 7040-7066.
34. Khan, A. I.; O'Hare, D. *Journal of Materials Chemistry* **2002,** 12, (11), 3191-3198.
35. Miyata, S. *Clays Clay Miner* **1983,** 31, (4), 305-311.
36. Iyi, N.; Matsumoto, T.; Kaneko, Y.; Kitamura, K. *Chemistry of materials* **2004,** 16, (15), 2926-2932.
37. Erickson, K. L.; Bostrom, T. E.; Frost, R. L. *Materials Letters* **2005,** 59, (2), 226-229.
38. Chubar, N.; Gerda, V.; Megantari, O.; Mičušík, M.; Omastova, M.; Heister, K.; Man, P.; Fraissard, J. *Chemical Engineering Journal* **2013,** 234, 284-299.
39. Gonzalez, A. R.; Asencios, Y. J.; Assaf, E. M.; Assaf, J. M. *Applied Surface Science* **2013,** 280, 876-887.
40. Maurice C. D. Mourad, E. J. D., Matti M. van Schooneveld, Chantal Vonk, and; Lekkerkerker, H. N. W. *J. Phys. Chem. B* **2008,** 112, 10142–10152.
41. Kovanda, F.; Koloušek, D.; Cílová, Z.; Hulínský, V. *Applied Clay Science* **2005,** 28, (1), 101-109.
42. Sharma, S. K.; Kushwaha, P. K.; Srivastava, V. K.; Bhatt, S. D.; Jasra, R. V. *Industrial & engineering chemistry research* **2007,** 46, (14), 4856-4865.
43. Kannan, S.; Jasra, R. V. *Journal of Materials Chemistry* **2000,** 10, (10), 2311-2314.
44. Bergada, O.; Vicente, I.; Salagre, P.; Cesteros, Y.; Medina, F.; Sueiras, J. E. *Microporous and Mesoporous Materials* **2007,** 101, (3), 363-373.

45. Benito, P.; Labajos, F. M.; Rives, V. *Pure and Applied Chemistry* **2009,** 81, (8), 1459-1471.
46. Chitrakar, R.; Makita, Y.; Sonoda, A.; Hirotsu, T. *Journal of hazardous materials* **2011,** 185, (2), 1435-1439.
47. Tao, Q.; Zhang, Y.; Zhang, X.; Yuan, P.; He, H. *Journal of Solid State Chemistry* **2006,** 179, (3), 708-715.
48. Pérez-Ramírez, J.; Abelló, S.; van der Pers, N. M. *Chemistry-A European Journal* **2007,** 13, (3), 870-878.
49. Liu, J.; Yu, L.; Zhang, Y. *Desalination* **2014,** 335, (1), 78-86.
50. Wang, Q.; O'Hare, D. *Chemical reviews* **2012,** 112, (7), 4124-4155.
51. Hibino, T.; Jones, W. *J. Mater. Chem.* **2001,** 11, (5), 1321-1323.
52. Adachi-Pagano, M.; Forano, C.; Besse, J.-P. *Chemical Communications* **2000**, (1), 91-92.
53. Hibino, T. *Chemistry of materials* **2004,** 16, (25), 5482-5488.
54. Ma, R.; Liu, Z.; Li, L.; Iyi, N.; Sasaki, T. *Journal of Materials Chemistry* **2006,** 16, (39), 3809-3813.
55. Gordijo, C. R.; Constantino, V. R. L.; de Oliveira Silva, D. *Journal of Solid State Chemistry* **2007,** 180, (7), 1967-1976.
56. Parashar, P.; Sharma, V.; Agarwal, D. D.; Richhariya, N. *Materials Letters* **2012,** 74, 93-95.
57. Peterson, C. L.; Perry, D. L.; Masood, H.; Lin, H.; White, J. L.; Hem, S. L.; Fritsch, C.; Haeusler, F. *Pharmaceutical research* **1993,** 10, (7), 998-1004.
58. Ulibarri, M.; Pavlovic, I.; Barriga, C.; Hermosın, M.; Cornejo, J. *Applied Clay Science* **2001,** 18, (1), 17-27.
59. Yong, Z.; Rodrigues, A. r. E. *Energy conversion and management* **2002,** 43, (14), 1865-1876.
60. Othman, M.; Helwani, Z.; Fernando, W. *Applied Organometallic Chemistry* **2009,** 23, (9), 335-346.
61. Choy, J.-H.; Choi, S.-J.; Oh, J.-M.; Park, T. *Applied Clay Science* **2007,** 36, (1), 122-132.
62. Yuan, Y.; Shi, W. *Applied Clay Science* **2012,** 67, 83-90.
63. Xu, Y.; Liu, X.; Ding, Y.; Luo, L.; Wang, Y.; Zhang, Y.; Xu, Y. *Applied Clay Science* **2011,** 52, (3), 322-327.
64. Forano, C.; Vial, S.; Mousty, C. *Current Nanoscience* **2006,** 2, (3), 283-294.
65. Shan, D.; Cosnier, S.; Mousty, C. *Analytical chemistry* **2003,** 75, (15), 3872-3879.
66. Basu, D.; Das, A.; Stöckelhuber, K. W.; Wagenknecht, U.; Heinrich, G. *Progress in Polymer Science* **2014,** 39, (3), 594-626.
67. Jing Leng, P. J. P., Nianjun Kang, De-Yi Wang, Jana Falkenhagen,; Franziska Emmerling, A. F. T., Andreas Schönhals. *European Polymer Journal* **2015**.
68. Salomão, R.; Dias, I. M.; Arruda, C. C. In *Hydrotalcite (Mg6Al2 (OH) 16 (CO3)· 4H2O): A Potentially Useful RAW Material for Refractories*, Proceedings of the Unified International Technical Conference on Refractories (UNITECR 2013), Wiley Online Library: pp 1151-1156.
69. Shabanian, M.; Basaki, N.; Khonakdar, H. A.; Jafari, S. H.; Hedayati, K.; Wagenknecht, U. *Applied Clay Science* **2014,** 90, 101-108.
70. Elbasuney, S. *Powder Technology* **2015,** 277, 63-73.
71. Gualandi, I.; Scavetta, E.; Zappoli, S.; Tonelli, D. *Biosensors and Bioelectronics* **2011,** 26, (7), 3200-3206.

72. Cai, X.; Shen, X.; Ma, L.; Ji, Z.; Xu, C.; Yuan, A. *Chemical Engineering Journal* **2015,** 268, 251-259.
73. Choy, J.-H.; Kwak, S.-Y.; Park, J.-S.; Jeong, Y.-J.; Portier, J. *Journal of the American Chemical Society* **1999,** 121, (6), 1399-1400.
74. Nalawade, P.; Aware, B.; Kadam, V.; Hirlekar, R. *J. Sci. Ind. Res* **2009,** 68, (4), 2674272.
75. Costantino, U.; Ambrogi, V.; Nocchetti, M.; Perioli, L. *Microporous and Mesoporous Materials* **2008,** 107, (1), 149-160.
76. Tamura, H.; Chiba, J.; Ito, M.; Takeda, T.; Kikkawa, S.; Mawatari, Y.; Tabata, M. *Journal of colloid and interface science* **2006,** 300, (2), 648-654.
77. Rives, V.; del Arco, M.; Martín, C. *Applied Clay Science* **2014,** 88, 239-269.
78. Dong, H.; Chen, M.; Rahman, S.; Parekh, H. S.; Cooper, H. M.; Xu, Z. P. *Applied Clay Science* **2014,** 100, 66-75.
79. Kim, T.-H.; Lee, G. J.; Kang, J.-H.; Kim, H.-J.; Kim, T.-i.; Oh, J.-M. *BioMed research international* **2014,** 2014.
80. Chakraborty, J.; Roychowdhury, S.; Sengupta, S.; Ghosh, S. *Materials Science and Engineering: C* **2013,** 33, (4), 2168-2174.
81. Canton, I.; Battaglia, G. *Chemical Society Reviews* **2012,** 41, (7), 2718-2739.
82. Xu, Z. P.; Zeng, Q. H.; Lu, G. Q.; Yu, A. B. *Chemical Engineering Science* **2006,** 61, (3), 1027-1040.
83. Zhang, K.; Xu, Z. P.; Lu, J.; Tang, Z. Y.; Zhao, H. J.; Good, D. A.; Wei, M. Q. *International journal of molecular sciences* **2014,** 15, (5), 7409-7428.
84. Choi, S.-J.; Choy, J.-H. *Nanomedicine* **2011,** 6, (5), 803-814.
85. Chandra, S.; Barick, K.; Bahadur, D. *Advanced drug delivery reviews* **2011,** 63, (14), 1267-1281.
86. Dong, H.; Parekh, H. S.; Xu, Z. P. *Journal of colloid and interface science* **2015,** 437, 10-16.
87. Chen, M.; Cooper, H. M.; Zhou, J. Z.; Bartlett, P. F.; Xu, Z. P. *Journal of colloid and interface science* **2013,** 390, (1), 275-281.
88. Friedmann, T.; Roblin, R. *Science* **1972,** 175, (4025), 949-955.
89. Wirth, T.; Parker, N.; Ylä-Herttuala, S. *Gene* **2013,** 525, (2), 162-169.
90. Nayerossadat, N.; Maedeh, T.; Ali, P. A. *Advanced biomedical research* **2012,** 1.
91. Luo, J.; Sun, M. H.; Kang, Q.; Peng, Y.; Jiang, W.; Luu, H. H.; Luo, Q.; Park, J. Y.; Li, Y.; Haydon, R. C. *Current gene therapy* **2005,** 5, (2), 167-179.
92. Curtin, C. M.; Cunniffe, G. M.; Lyons, F. G.; Bessho, K.; Dickson, G. R.; Duffy, G. P.; O'Brien, F. J. *Advanced Materials* **2012,** 24, (6), 749-754.
93. Zelinsky, N.; Kommarewsky, W. *Berichte der deutschen chemischen Gesellschaft (A and B Series)* **1924,** 57, (4), 667-669.
94. Molstad, M. C.; Dodge, B. F. *Industrial & Engineering Chemistry* **1935,** 27, (2), 134-140.
95. Centi, G.; Perathoner, S. *Microporous and mesoporous materials* **2008,** 107, (1), 3-15.
96. Kannan, S. *Catalysis Surveys from Asia* **2006,** 10, (3-4), 117-137.
97. Nishimura, S.; Takagaki, A.; Ebitani, K. *Green Chemistry* **2013,** 15, (8), 2026-2042.
98. Chmielarz, L.; Jabłońska, M.; Strumiński, A.; Piwowarska, Z.; Węgrzyn, A.; Witkowski, S.; Michalik, M. *Applied Catalysis B: Environmental* **2013,** 130, 152-162.

99. Kuśtrowski, P.; Sułkowska, D.; Chmielarz, L.; Rafalska-Łasocha, A.; Dudek, B.; Dziembaj, R. *Microporous and Mesoporous Materials* **2005,** 78, (1), 11-22.
100. Marschall, R.; Wang, L. *Catalysis Today* **2014,** 225, 111-135.
101. Ma, W.; Ma, R.; Wang, C.; Liang, J.; Liu, X.; Zhou, K.; Sasaki, T. *ACS nano* **2015,** 9, (2), 1977-1984.
102. Doyle, R. L.; Lyons, M. E., The Oxygen Evolution Reaction: Mechanistic Concepts and Catalyst Design. In *Photoelectrochemical Solar Fuel Production*, Springer: 2016; pp 41-104.
103. Gong, M.; Dai, H. *Nano Research* **2015,** 8, (1), 23-39.
104. Song, F.; Hu, X. *Nature communications* **2014,** 5.
105. Oliver-Tolentino, M. A.; Vázquez-Samperio, J.; Manzo-Robledo, A.; Gonzalez-Huerta, R. D. G.; Flores-Moreno, J. L.; Ramírez-Rosales, D.; Guzmán-Vargas, A. *The Journal of Physical Chemistry C* **2014,** 118, (39), 22432-22438.
106. Shen, G.; Chen, D.; Chen, P.-C.; Zhou, C. *Acs Nano* **2009,** 3, (5), 1115-1120.
107. Oswald, H.; Asper, R.; Lieth, R. *Reidel, Dordrecht* **1977**, 122.
108. Colinge, J.-P.; Colinge, C. A., *Physics of semiconductor devices*. Springer Science & Business Media: 2005.
109. Atkins, P.; de Paula, J., *Atkins' Physical Chemistry*. OUP Oxford: 2010.
110. Gupta, K.; Gupta, N., *Advanced Semiconducting Materials and Devices*. Springer: 2016.
111. Jun, Y. w.; Choi, J. s.; Cheon, J. *Angewandte Chemie International Edition* **2006,** 45, (21), 3414-3439.
112. Zhou, J.; Dai, J.; Bian, G.-Q.; Li, C.-Y. *Coordination chemistry reviews* **2009,** 253, (9), 1221-1247.
113. Zheng, N.; Bu, X.; Feng, P. *Journal of the American Chemical Society* **2003,** 125, (5), 1138-1139.
114. Zheng, N.; Bu, X.; Wang, B.; Feng, P. *Science* **2002,** 298, (5602), 2366-2369.
115. Vaqueiro, P.; Romero, M. L. *Journal of the American Chemical Society* **2008,** 130, (30), 9630-9631.
116. Vaqueiro, P.; Romero, M. L.; Rowan, B. C.; Richards, B. S. *Chemistry-A European Journal* **2010,** 16, (15), 4462-4465.
117. Vaqueiro, P. *Inorganic chemistry* **2006,** 45, (10), 4150-4156.
118. Zhu, Q.-Y.; Dai, J. *Coordination Chemistry Reviews* **2017,** 330, 95-109.
119. Huang, Y.; Duan, X.; Wei, Q.; Lieber, C. M. *Science* **2001,** 291, (5504), 630-633.
120. Xia, Y.; Yang, P.; Sun, Y.; Wu, Y.; Mayers, B.; Gates, B.; Yin, Y.; Kim, F.; Yan, H. *Advanced materials* **2003,** 15, (5), 353-389.
121. Datta, A.; Sinha, G.; Panda, S. K. *Journal of Crystal Growth* **2013,** 368, 87-91.
122. Zheng, N.; Bu, X.; Lauda, J.; Feng, P. *Chemistry of materials* **2006,** 18, (18), 4307-4311.
123. Lin, Y.; Kong, C.; Chen, L. *RSC Advances* **2016,** 6, (39), 32598-32614.
124. Mourdikoudis, S.; Liz-Marzán, L. M. *Chemistry of Materials* **2013,** 25, (9), 1465-1476.
125. Wang, D.; Li, Y. *Inorganic chemistry* **2011,** 50, (11), 5196-5202.
126. Spahr, M. E.; Bitterli, P.; Nesper, R.; Müller, M.; Krumeich, F.; Nissen, H. U. *Angewandte Chemie International Edition* **1998,** 37, (9), 1263-1265.
127. Krumeich, F.; Muhr, H.-J.; Niederberger, M.; Bieri, F.; Schnyder, B.; Nesper, R. *Journal of the American Chemical Society* **1999,** 121, (36), 8324-8331.
128. Williams, D. B.; Carter, C. B. *Springer Science+ Business Media, New York, USA* **2009**.

129. Bozzola, J. J.; Russell, L. D., *Electron microscopy: principles and techniques for biologists*. Jones & Bartlett Learning: 1999.
130. Committee, E. D. F. A. S. D. R., *Microelectronics failure analysis: desk reference*. Asm Intl: 2004.
131. Haugstad, G., *Atomic force microscopy: understanding basic modes and advanced applications*. John Wiley & Sons: 2012.
132. Eaton, P.; West, P., *Atomic force microscopy*. Oxford University Press: 2010.
133. Stuart, B., *Infrared spectroscopy*. Wiley Online Library: 2005.
134. Smith, B. C., *Fundamentals of Fourier transform infrared spectroscopy*. CRC press: 2011.
135. Kaplan, S.; Hanssen, L.; Early, E.; Nadal, M.; Allen, D. *Metrologia* **2002,** 39, (2), 157.
136. Suryanarayana, C.; Norton, M. G., *X-ray diffraction: a practical approach*. Springer Science & Business Media: 2013.
137. Waseda, Y.; Matsubara, E.; Shinoda, K., *X-ray diffraction crystallography: introduction, examples and solved problems*. Springer Science & Business Media: 2011.
138. Pereiro-GarcÝa, R.; Medel, A. S.; Costa-Fernßndez, J. M.; Tomßs-Morer, X.; Fernßndez-Ruano, L.; FerrÚ-Baldrich, J.; Gmez-Carracedo, M. P.; BoquÚ-MartÝ, R.; Gonzßlez-SabatÚ, L.; Carlosena-Zubieta, A., *Basic chemometric techniques in atomic spectroscopy*. Royal Society of Chemistry: 2013.
139. Cazes, J., *Analytical instrumentation handbook*. CRC Press: 2004.
140. Rouessac, F.; Rouessac, A., *Chemical analysis: modern instrumentation methods and techniques*. John Wiley & Sons: 2013.
141. Khopkar, S. M., *Basic concepts of analytical chemistry*. New Age International: 1998.
142. Pavia, D. L.; Lampman, G. M.; Kriz, G. S.; Vyvyan, J. A., *Introduction to spectroscopy*. Cengage Learning: 2008.
143. Harvey, A.; Backes, C.; Gholamvand, Z.; Hanlon, D.; McAteer, D.; Nerl, H. C.; McGuire, E.; Seral-Ascaso, A. s.; Ramasse, Q. M.; McEvoy, N. *Chemistry of Materials* **2015,** 27, (9), 3483-3493.
144. Hanssen, L. *Applied Optics* **2001,** 40, (19), 3196-3204.
145. Lakowicz, J. R., *Principles of fluorescence spectroscopy*. Springer Science & Business Media: 2013.
146. Goldys, E. M., *Fluorescence applications in biotechnology and life sciences*. John Wiley & Sons: 2009.
147. Ueda, O.; Pearton, S. J., *Materials and reliability handbook for semiconductor optical and electron devices*. Springer Science & Business Media: 2012.
148. Hofmann, S., *Auger-and X-ray photoelectron spectroscopy in materials science: a user-oriented guide*. Springer Science & Business Media: 2012; Vol. 49.
149. Watts, J. F.; Wolstenholme, J. *An Introduction to Surface Analysis by XPS and AES, by John F. Watts, John Wolstenholme, pp. 224. ISBN 0-470-84713-1. Wiley-VCH, May 2003.* **2003**, 224.
150. Klockenkàmper, R.; Knoth, J.; Prange, A.; Schwenke, H. *Analytical Chemistry* **1992,** 64, (23), 1115A-1123A.
151. von Bohlen, A. *e-Preservation Science* **2004**, (1), 23-34.
152. Lowell, S.; Shields, J. E.; Thomas, M. A.; Thommes, M., *Characterization of porous solids and powders: surface area, pore size and density*. Springer Science & Business Media: 2012; Vol. 16.

153. Brunauer, S.; Emmett, P. H.; Teller, E. *Journal of the American chemical society* **1938,** 60, (2), 309-319.
154. Mariko Adachi-Pagano, C. F. a. J.-P. B. *J. Mater. Chem.* **2003,** 13, 1988–1993.
155. Oh, J.-M.; Hwang, S.-H.; Choy, J.-H. *Solid State Ionics* **2002,** 151, (1), 285-291.
156. Okamoto, K.; Iyi, N.; Sasaki, T. *Applied Clay Science* **2007,** 37, (1), 23-31.
157. Costantino, U.; Marmottini, F.; Nocchetti, M.; Vivani, R. *European Journal of Inorganic Chemistry* **1998,** 1998, (10), 1439-1446.
158. Nobuo Iyi, T. M., y Yoshiro Kaneko, and Kenji Kitamura. *Chemistry Letters* **2004,** 33, (9).
159. Sels, B. F.; De Vos, D. E.; Jacobs, P. A. *Catalysis Reviews* **2001,** 43, (4), 443-488.
160. Stevens, E.; Hope, H. *Acta Crystallographica Section A: Crystal Physics, Diffraction, Theoretical and General Crystallography* **1975,** 31, (4), 494-498.
161. María Dolores Ureña-Amate, N. D. B.; María del Mar Socias-Viciana, E. G.-P. *Applied Clay Science* **2011,** 52, (4), 368-373.
162. Zhang, Q.; Zhao, M. Q.; Tang, D. M.; Li, F.; Huang, J. Q.; Liu, B.; Zhu, W. C.; Zhang, Y. H.; Wei, F. *Angewandte Chemie* **2010,** 122, (21), 3724-3727.
163. Liu, Z.; Ma, R.; Osada, M.; Iyi, N.; Ebina, Y.; Takada, K.; Sasaki, T. *Journal of the American Chemical Society* **2006,** 128, (14), 4872-4880.
164. Coleman, J. N.; Lotya, M.; O'Neill, A.; Bergin, S. D.; King, P. J.; Khan, U.; Young, K.; Gaucher, A.; De, S.; Smith, R. J. *Science* **2011,** 331, (6017), 568-571.
165. Stanimirova, T.; Piperov, N.; Petrova, N.; Kirov, G. *Clay Minerals* **2004,** 39, (2), 177-191.
166. Constantino, V. R.; Pinnavaia, T. J. *Inorganic Chemistry* **1995,** 34, (4), 883-892.
167. Chang, C.-T.; Liaw, B.-J.; Huang, C.-T.; Chen, Y.-Z. *Applied Catalysis A: General* **2007,** 332, (2), 216-224.
168. Wang, Q.; Tay, H. H.; Guo, Z.; Chen, L.; Liu, Y.; Chang, J.; Zhong, Z.; Luo, J.; Borgna, A. *Applied Clay Science* **2012,** 55, 18-26.
169. Li, S. P.; Zhou, Z. P. *Journal of dispersion science and technology* **2006,** 27, (8), 1079-1084.
170. Olfs, H.-W.; Torres-Dorante, L.; Eckelt, R.; Kosslick, H. *Applied clay science* **2009,** 43, (3), 459-464.
171. Xu, Z. P.; Stevenson, G.; Lu, C.-Q.; Lu, G. Q. *The Journal of Physical Chemistry B* **2006,** 110, (34), 16923-16929.
172. Ladewig, K.; Niebert, M.; Xu, Z. P.; Gray, P. P.; Lu, G. Q. M. *Applied Clay Science* **2010,** 48, (1), 280-289.
173. Abellán, G.; Coronado, E.; Martí-Gastaldo, C.; Pinilla-Cienfuegos, E.; Ribera, A. *Journal of Materials Chemistry* **2010,** 20, (35), 7451-7455.
174. Choi, G.; Kwon, O.-J.; Oh, Y.; Yun, C.-O.; Choy, J.-H. *Scientific reports* **2014,** 4.
175. Nakayama, H.; Hatakeyama, A.; Tsuhako, M. *International journal of pharmaceutics* **2010,** 393, (1), 105-112.
176. Pan, D.; Zhang, H.; Zhang, T.; Duan, X. *Chemical Engineering Science* **2010,** 65, (12), 3762-3771.
177. Pavel, O.; Bîrjega, R.; Che, M.; Costentin, G.; Angelescu, E.; Şerban, S. *Catalysis Communications* **2008,** 9, (10), 1974-1978.
178. Takehira, K.; Shishido, T.; Shouro, D.; Murakami, K.; Honda, M.; Kawabata, T.; Takaki, K. *Applied Catalysis A: General* **2005,** 279, (1), 41-51.

179. Qiu, L.; Wang, Z.; Liu, P.; Liu, R.; Cai, C.; Fan, S. *Spectroscopy Letters* **2015,** 48, (2), 120-127.
180. Chen, C.; Yee, L. K.; Gong, H.; Zhang, Y.; Xu, R. *Nanoscale* **2013,** 5, (10), 4314-4320.
181. Han, Y.; Liu, Z.-H.; Yang, Z.; Wang, Z.; Tang, X.; Wang, T.; Fan, L.; Ooi, K. *Chemistry of Materials* **2007,** 20, (2), 360-363.
182. Ma, R.; Liu, Z.; Takada, K.; Iyi, N.; Bando, Y.; Sasaki, T. *Journal of the American Chemical Society* **2007,** 129, (16), 5257-5263.
183. Gayer, K.; Woontner, L. *The Journal of Physical Chemistry* **1956,** 60, (11), 1569-1571.
184. Li, F.; Liu, J.; Evans, D. G.; Duan, X. *Chemistry of Materials* **2004,** 16, (8), 1597-1602.
185. Iwasaki, T.; Yoshii, H.; Nakamura, H.; Watano, S. *Applied Clay Science* **2012,** 58, 120-124.
186. Xiao, T.; Tang, Y.; Jia, Z.; Li, D.; Hu, X.; Li, B.; Luo, L. *Nanotechnology* **2009,** 20, (47), 475603.
187. Hou, W.; Kang, L.; Sun, R.; Liu, Z.-H. *Colloids and Surfaces A: Physicochemical and Engineering Aspects* **2008,** 312, (2), 92-98.
188. Li, N.; Zhao, P.; Astruc, D. *Angewandte Chemie International Edition* **2014,** 53, (7), 1756-1789.
189. Sau, T. K.; Rogach, A. L. *Advanced Materials* **2010,** 22, (16), 1781-1804.
190. Matzapetakis, M.; Raptopoulou, C.; Tsohos, A.; Papaefthymiou, V.; Moon, N.; Salifoglou, A. *Journal of the American Chemical Society* **1998,** 120, (50), 13266-13267.
191. Furia, T. E., *CRC handbook of food additives*. CRC press: 1973; Vol. 1.
192. Li, T.; Li, G.; Li, L.; Liu, L.; Xu, Y.; Ding, H.; Zhang, T. *ACS applied materials & interfaces* **2016,** 8, (4), 2562-2572.
193. Parveen, N.; Cho, M. H. *Scientific reports* **2016,** 6, 27318.
194. Sun, H.; Chu, Z.; Hong, D.; Zhang, G.; Xie, Y.; Li, L.; Shi, K. *Journal of Alloys and Compounds* **2016,** 658, 561-568.
195. Du, Y.; Jin, Q.; Feng, J.; Zhang, N.; He, Y.; Li, D. *Catalysis Science & Technology* **2015,** 5, (6), 3216-3225.
196. Coelho, J.; Mendoza-Sánchez, B.; Pettersson, H.; Pokle, A.; McGuire, E. K.; Long, E.; McKeon, L.; Bell, A. P.; Nicolosi, V. *2D Materials* **2015,** 2, (2), 025005.
197. Shanmugavel, T.; Raj, S. G.; Kumar, G. R.; Rajarajan, G.; Saravanan, D. *Journal of King Saud University-Science* **2015,** 27, (2), 176-181.
198. Topcu, Y.; Andac, O.; Yilmaz, V.; Harrison, W. *Journal of Coordination Chemistry* **2002,** 55, (7), 805-815.
199. Naiini, A. A.; Young, V.; Verkade, J. G. *Polyhedron* **1995,** 14, (3), 393-400.
200. Cabrera, S.; El Haskouri, J.; Guillem, C.; Latorre, J.; Beltrán-Porter, A.; Beltrán-Porter, D.; Marcos, M. D.; Amoros, P. *Solid State Sciences* **2000,** 2, (4), 405-420.
201. Abellán, G.; Coronado, E.; Martí-Gastaldo, C.; Waerenborgh, J.; Ribera, A. *Inorganic chemistry* **2013,** 52, (17), 10147-10157.
202. Lide, D. R., *CRC handbook of chemistry and physics*. CRC press: 2004; Vol. 85.
203. Yan, W.; Liu, H.; Chen, R.; Xie, J.; Wei, Y. *RSC Advances* **2015,** 5, (129), 106396-106399.
204. Coates, J. *Encyclopedia of analytical chemistry* **2000**.

205. Hughes, M.; Rutt, K. *Journal of the Chemical Society A: Inorganic, Physical, Theoretical* **1968**, 2788-2790.
206. Xu, Z.; Yu, J.; Xiao, W. *Chemistry–A European Journal* **2013,** 19, (29), 9592-9598.
207. Russell, J. *Clay Miner* **1979,** 14, (2), 109.
208. Vodyanitskii, Y. N. *Eurasian Soil Science* **2010,** 43, (11), 1244-1254.
209. Rout, K.; Mohapatra, M.; Anand, S. *Dalton Transactions* **2012,** 41, (11), 3302-3312.
210. Michel, F.; Ehm, L.; Liu, G.; Han, W.; Antao, S.; Chupas, P.; Lee, P.; Knorr, K.; Eulert, H.; Kim, J. *Chemistry of Materials* **2007,** 19, (6), 1489-1496.
211. Janney, D. E.; Cowley, J. M.; Buseck, P. R. *Clays and Clay Minerals* **2000,** 48, (1), 111-119.
212. Kukkadapu, R. K.; Zachara, J. M.; Fredrickson, J. K.; Smith, S. C.; Dohnalkova, A. C.; Russell, C. K. *American Mineralogist* **2003,** 88, (11-12), 1903-1914.
213. Das, S.; Hendry, M. J.; Essilfie-Dughan, J. *Environmental science & technology* **2010,** 45, (1), 268-275.
214. Nielsen, K.; Hazell, R. G.; Rasmussen, S. *Acta Chem. Scand* **1972,** 26, (3), 3.
215. Yeşilel, O.; Ölmez, H. *Journal of thermal analysis and calorimetry* **2006,** 89, (1), 261-265.
216. Hausinger, R. P., *Biochemistry of nickel*. Springer Science & Business Media: 2013; Vol. 12.
217. Agarwala, G., Bardi Vishal, Bjerrum, Jannik. *Acta Chemica Scandinavia A* **1982,** 36, (5), 459-464.
218. Pastor, A.; Martínez-Viviente, E. *Coordination Chemistry Reviews* **2008,** 252, (21), 2314-2345.
219. Fang, J.; Wei, X.; Sapp, J. B.; Deng, Y. *Inorganica Chimica Acta* **2014,** 411, 5-10.
220. Cazacu, M.; Bargan, A.; Shova, S.; Turta, C. *Polyhedron* **2013,** 50, (1), 255-263.
221. Tang, C.; Wang, H. S.; Wang, H. F.; Zhang, Q.; Tian, G. L.; Nie, J. Q.; Wei, F. *Advanced Materials* **2015,** 27, (30), 4516-4522.
222. Li, X.; Walsh, F. C.; Pletcher, D. *Physical Chemistry Chemical Physics* **2011,** 13, (3), 1162-1167.
223. Dasgupta, N. P.; Sun, J.; Liu, C.; Brittman, S.; Andrews, S. C.; Lim, J.; Gao, H.; Yan, R.; Yang, P. *Advanced materials* **2014,** 26, (14), 2137-2184.
224. Suresh, S. *Nanoscience and Nanotechnology* **2013,** 3, (3), 62-74.
225. Green, M., *Semiconductor Quantum Dots: Organometallic and Inorganic Synthesis*. Royal Society of Chemistry: 2014; Vol. 33.
226. Lu, Q.; Gao, F.; Zhao, D. *Nano Letters* **2002,** 2, (7), 725-728.
227. Kumar, S.; Nann, T. *Small* **2006,** 2, (3), 316-329.
228. Seral-Ascaso, A.; Metel, S.; Pokle, A.; Backes, C.; Zhang, C.; Nerl, H.; Rode, K.; Berner, N.; Downing, C.; McEvoy, N. *Nanoscale* **2016,** 8, (22), 11698-11706.
229. Thomson, J. W.; Nagashima, K.; Macdonald, P. M.; Ozin, G. A. *Journal of the American Chemical Society* **2011,** 133, (13), 5036-5041.
230. Guo, X.; Guo, X.; Tao, W.; Chen, L.; Peng, L.; Ding, W. *Chemical Communications* **2011,** 47, (36), 10061-10063.
231. van Embden, J.; Chesman, A. S.; Jasieniak, J. J. *Chemistry of Materials* **2015,** 27, (7), 2246-2285.
232. Mahfouz, R. M.; Al-Khamis, K. M.; Siddiqui, M. R. H.; Al-Hokbany, N. S.; Warad, I.; Al-Andis, N. M. *Prog React Kinet Mec* **2012,** 37, (3), 249-262.

233. Alvarado, S. R.; Guo, Y. J.; Ruberu, T. P. A.; Tavasoli, E.; Vela, J. *Coordination Chemistry Reviews* **2014,** 263, 182-196.
234. Mayers, B.; Xia, Y. *Journal of Materials Chemistry* **2002,** 12, (6), 1875-1881.
235. Ewing, S. J.; Vaqueiro, P. *Inorganic chemistry* **2014,** 53, (17), 8845-8847.
236. Dong, Y.; Peng, Q.; Wang, R.; Li, Y. *Inorganic chemistry* **2003,** 42, (6), 1794-1796.
237. Cooper, J. K.; Franco, A. M.; Gul, S.; Corrado, C.; Zhang, J. Z. *Langmuir* **2011,** 27, (13), 8486-8493.
238. Therese, H. A.; Rocker, F.; Reiber, A.; Li, J.; Stepputat, M.; Glasser, G.; Kolb, U.; Tremel, W. *Angewandte Chemie International Edition* **2005,** 44, (2), 262-265.
239. Wortham, E.; Bonnet, B.; Jones, D. J.; Rozière, J.; Burns, G. R. *Journal of Materials Chemistry* **2004,** 14, (1), 121-126.
240. Ozin, G. *Journal of Materials Chemistry* **1997,** 7, (11), 2213-2222.
241. Vaqueiro, P. *Journal of Solid State Chemistry* **2006,** 179, (1), 302-307.
242. Silverstein, R. M.; Webster, F. X.; Kiemle, D. J.; Bryce, D. L., *Spectrometric identification of organic compounds*. John wiley & sons: 2014.
243. Meyers, R. A., *Encyclopedia of analytical chemistry*. John Wiley & Sons: 2011.
244. Graf, N.; Yegen, E.; Gross, T.; Lippitz, A.; Weigel, W.; Krakert, S.; Terfort, A.; Unger, W. E. *Surface Science* **2009,** 603, (18), 2849-2860.
245. Shepherd, F.; Williams, P. *Physical Review B* **1975,** 12, (12), 5705.
246. Carli, R.; Bianchi, C. *Applied surface science* **1994,** 74, (1), 99-102.
247. Zhou, J.; Zhang, Y.; Bian, G.-Q.; Li, C.-Y.; Chen, X.-X.; Dai, J. *Crystal Growth and Design* **2008,** 8, (7), 2235-2240.
248. Vaqueiro, P.; Romero, M. L. *Journal of Physics and Chemistry of Solids* **2007,** 68, (5), 1239-1243.
249. Allakhverdiev, K.; Hagen, J.; Salaeva, Z. *physica status solidi (a)* **1997,** 163, (1), 121-127.
250. Ho, C.; Lin, S. *Journal of applied physics* **2006,** 100, (8), 083508.
251. Springford, M. *Proceedings of the Physical Society* **1963,** 82, (6), 1020.
252. Vaqueiro, P.; Romero, M. L. *Inorganic chemistry* **2008,** 48, (3), 810-812.
253. Huang, X.; Li, J.; Zhang, Y.; Mascarenhas, A. *Journal of the American Chemical Society* **2003,** 125, (23), 7049-7055.
254. Zhang, X.; Hejazi, M.; Thiagarajan, S. J.; Woerner, W. R.; Banerjee, D.; Emge, T. J.; Xu, W.; Teat, S. J.; Gong, Q.; Safari, A. *Journal of the American Chemical Society* **2013,** 135, (46), 17401-17407.
255. Wei, Y.; Tao, Y.; Zhang, C.; Wang, J.; Qiao, W.; Ling, L.; Long, D. *Electrochimica Acta* **2016,** 188, 385-392.
256. Meng, X.; He, K.; Su, D.; Zhang, X.; Sun, C.; Ren, Y.; Wang, H. H.; Weng, W.; Trahey, L.; Canlas, C. P. *Advanced Functional Materials* **2014,** 24, (34), 5435-5442.